UNIVERSITAT POLITÈCNICA DE CATALUNYA BARCELONATECH

Zero-thickness interface elements in petroleum geomechanics: sand production and hydraulic fracture

Daniel Garolera Vinent

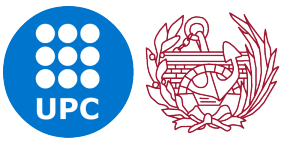

School of Civil Engineering of Barcelona
UPC BARCELONATECH

Zero-thickness interface elements in petroleum geomechanics: sand production and hydraulic fracture

Doctoral Thesis submitted by:

Daniel Garolera Vinent

Supervised by:

Ignacio Carol

Doctoral Program in Civil Engineering

Division of Geotechnical Engineering and Geosciences

Barcelona, July 2017

Agraïments

En primer lloc voldria agrair la tasca del director de la Tesi doctoral, el professor Ignasi Carol. Sense la seva ajuda i recolzament aquest treball no hauria sigut possible: els consells, valuosos i encertats; la paciència, sempre trobant el temps per explicar el que calgués; i l'ajuda, sobretot en aquells moments de dubtes. Gràcies.

Voldria agrair també l'ajuda dels professors Pere Prat i Carlos Maria López, que en molts moments també han actuat com a codirectors, ajudant, donant idees, corregint documents, en resum fent més fàcil el que a vegades sembla difícil.

Com es comenta en el document, l'inici d'aquest treball va partir de tres treballs anteriors del grup MECMAT. Agrair a l'Olga Roa el treball del generador de microestructures. A l'Antonio Caballero, l'ajuda en la llei constitutiva i els solvers... però sobretot el seu sentit de l'humor. Gràcies també a en Josep Maria Segura, doncs la transmissió del seu treball ha sigut clau pel resultat final.

També voldria tenir un agraïment especial per en Lakshmikantha. Sincerament dubto que sense ell, aquest viatge hagués començat i acabat. Primer, la sort de compartir els primers anys de doctorat, i després, en una segona etapa, la confiança dipositada.

También quiero agradecer la colaboración de los miembros del grupo de geomecánica de Repsol, en particular a José Alvarellos, a Nubia González, a Pablo Vargas y Enric Ibàñez. Gracias por las discusiones que han enriquezido notablemente el trabajo.

Mencionar la ayuda del MEC en forma de beca FPU durante la primera fase del doctorado.

El meu agraïment també pels membres actuals del grup de recerca MECMAT, i en particular en Joaquin i l'Adrià. Els dos en la darrera fase de doctorat. Amb el primer ens han unit moltes hores de discussions tècniques i filosòfiques; amb el segon hem col · laborat en un gruix important del treball de paral · lelització de codi.

En general, i fa de mal dir per no deixar-me ningú, gràcies a tots aquells que hem compartit algun moment en el departament, ja sigui al despatx o fent el tupper: l'Abel, l'Alessandra, l'Andrés, l'Anna, en Benoit, en Cristian, la Daniela, en Fermín, l'Ignasi, la Lola, la Marianna, la Núria i la Tere.

Per la família també voldria tenir un agraïment per la seva comprensió i suport. Aquí voldria tenir un record molt especial per en Joan Ignasi, el meu germà, doncs potser l'únic retret que em faig d'aquest treball és que no l'hagi pogut veure acabar.

Finalment voldria agrair la paciència infinita i el recolzament incondicional a la Glòria. Malgrat que a vegades m'hagi sigut difícil explicar-li el dia a dia de la feina o que m'hagi vist preocupat perquè alguna cosa no acabava de rutllar, sempre m'ha fet costat. Vaig començar el doctorat quan feia poc que havíem anat a viure junts, i l'he acabat amb la Berta, l'Aloma i l'Aniol. Un regal.

Daniel Garolera, Alella 12 juliol 2017

A la meva dona, la Glòria

A la memòria d'en Joan Ignasi.

Abstract

This thesis describes the extension of the Finite Element Method with zero-thickness interface elements (FEM+z) to 3D, large and complex problems in geomaterials, with special interest in petroleum geomechanics. This general objective has led to specific developments and applications such as the 3D code implementations and parallelization, and the specific petroleum geomechanics studies, both the macroscale (hydraulic fracture) and microscale (sand production).

The extension to 3D of the hydro-mechanical formulation of double node zero-thickness interface elements proposed earlier, has been developed and implemented in the computer code, with satisfactory results in the verification examples. From the theoretical viewpoint, the formulation is generalized via the definition of "transport" matrices for both mechanical and hydraulic formulations, so that the two levels of the formulation can be separated: the nodal variables of the interface element, and the mid-plane variables. The formulation described is successfully validated with benchmarking examples based on analytical expressions of a hydraulic fracture.

The parallelization of the code DRAC is achieved through the implementation of public domain library PETSc. The new code structure is conceived to perform a correct subdivision of tasks associated to each processor. For this purpose, a domain decomposition strategy has been implemented, which is crucial for an efficient matrix generation and assembly. The results obtained show a good degree of parallelization, demonstrated with a cube benchmark test.

The applications to hydraulic fracture have served a dual purpose. First, the examples of a single fracture have been used to validate the proposed formulation, since it has been possible to compare the results with the predictions of analytical expressions such as GDK or PKN, and to other numerical results from the literature. Second, the examples of multiple interacting fractures have shown the capabilities to analyze large and complex cases. The studies performed have shown a number of relevant aspects of multiple fracturing such as the effect of geometry (distance between injections) and the effect of *in situ* stresses.

Finally the thesis is devoted to the micromechanical analysis of sand production, including the generation and testing of micromechanical models based on the use of zero-thickness interface elements. Micromechanical (mesoscopic level) analysis with FEM+z has been successfully used to model the mechanical behavior of rock materials, using a similar approach as used previously for other heterogeneous materials. The rock grains are modeled as a group of continuum elastic elements and the cement (or matrix) is modeled with zero-thickness interfaces. This kind of modeling has been successfully used in uniaxial and triaxial compression test simulations. These numerical tests have been used for calibration purposes, comparing the macroscopic results obtained with the existing laboratory data. Due to the availability of experimental

data, the simulation of sand production has been focused on the modeling of the hollow cylinder test. The simulations have been divided into two parts. First, using a prototype material, the sensitivity of the method to geometric and microstructural variations has been analyzed, and the effect of the perforation size is clearly observed. The second part deals with the analysis of a real case of rock sanding, that includes micromechanical tests for parameter calibration and the simulation of sand production. The results, despite the intrinsic variability of the samples, have shown a satisfactory agreement with average experimental results, both in terms of the initiation and the production of sand.

Resum

En aquesta tesi es presenta l'extensió del mètode d'elements finits amb elements junta d'espessor zero (FEM+z) a casos en 3D, per geometries grans i amb fenòmens complexos de fracturació per geomaterials, amb especial interès en la geomecànica del petroli.

Aquest objectiu general ha donat lloc al desenvolupament i la generació d'aplicacions específiques, com ara les implementacions del codi a 3D i la paral · lelització, i els estudis específics de geomecànica del petroli, tant a macroescala (fractura hidràulica) com a microescala (producció de sorra).

L'extensió a 3D de la formulació hidromecànica d'elements junta de doble nus proposada anteriorment, s'ha desenvolupat i implementat en el codi de càlcul, amb resultats satisfactoris en els exemples de verificació. Des del punt de vista teòric, la formulació s'ha generalitzat mitjançant la definició de matrius de transport per les dues formulacions, la mecànica i la hidràulica, de manera que es poden separar els dos nivells de la formulació: les variables nodals de l'element junta i les variables del pla mig.

La paral · lelització del codi DRAC s'ha assolit mitjançant la implementació de la llibreria en codi lliure PETSc. La nova estructura del codi s'ha concebut per tal de realitzar una subdivisió correcta de les tasques associades a cada processador. Així, s'ha implementat una estratègia de descomposició de dominis, que és fonamental per a la generació i assemblatge de matrius de manera eficient. Els resultats obtinguts mostren un bon grau de paral · lelització.

Les aplicacions de fractura hidràulica han tingut un doble propòsit. En primer lloc, s'han utilitzat els exemples d'una sola fractura per tal de validar la formulació proposada, ja que s'han pogut comparar els resultats amb les prediccions d'expressions analítiques com GDK o PKN i altres resultats numèrics de la literatura. En segon lloc, els exemples d'interacció entre fractures múltiples han demostrat la capacitat d'analitzar casos grans i complexos. Els estudis realitzats han mostrat una sèrie d'aspectes rellevants de la fractura múltiple, com l'efecte de la geometria (distància entre les injeccions) i l'efecte de les tensions *in situ*.

Per finalitzar, la tesi presenta l'anàlisi micromecànica de la producció de sorra, que inclou la generació i la verificació dels models micromecànics basats en l'ús d'elements junta d'espessor zero. L'anàlisi micromecànica (nivell mesoscòpic) feta amb FEM+z s'ha utilitzat amb èxit per modelitzar el comportament mecànic de les roques. Els grans de roca es modelen com un grup d'elements elàstics de continu i el ciment (o matriu) es modelitza amb les juntes d'espessor zero. Aquest tipus de modelització s'ha utilitzat amb èxit en les simulacions d'assaigs a compressió uniaxial i triaxial. Les simulacions numèriques han servit per calibrar els paràmetres del model, comparant els resultats macroscòpics obtinguts amb les dades del laboratori existents. Degut a la

disponibilitat de dades experimentals, la simulació de la producció de sorra s'ha centrat en la modelització de l'assaig de cilindres buits.

Les simulacions s'han dividit en dues parts. En primer lloc, mitjançant l'ús d'un material prototip, s'ha analitzat la sensibilitat del mètode a les variacions geomètriques i microestructurals, on s'observa clarament l'efecte de mida de la perforació. La segona part ha tractat l'anàlisi d'un cas real de producció de sorra, que inclou assaigs micromecànics per la cal · libració dels paràmetres i la simulació de la producció de sorra. Els resultats, tot i la variabilitat intrínseca de les mostres, han demostrat una semblança satisfactòria amb els resultats experimentals, tant pel que fa a la iniciació com a la producció de sorra.

Contents

Chapter 1

Introduction

Contents

1.1 Geomechanics in petroleum engineering

Geomechanics is becoming a subject of growing interest in Petroleum Engineering. Progressive exhaustion of traditional oil fields and increase in oil price motivates the interest for optimal extraction of those fields, and also for consideration of more unconventional reservoirs. The exploitation of those reservoirs often forces engineers to face non-trivial technical challenges, and the prediction of the mechanical behavior of the rock formation becomes a key element for a proper understanding and exploitation strategy. Nearly depleted reservoirs or deep reservoirs are good examples of the importance of Geomechanics in oil exploitation.

In this context, advanced Geomechanics numerical models become an important tool to quantify and predict the behavior of the rock mass: stress-strain states, porosity changes, fracture opening/closures or fracture propagation, wellbore failures, sand production, etc. which may be relevant or even crucial in both well completion or production phases. Such models must describe properly the mechanical behavior of the geological materials, perhaps also the casing materials, their interfaces, the subsequent variation of flow/transport properties at any time, and all be compatible with appropriate reservoir models.

It has been common practice in petroleum engineering to consider the reservoir skeleton as an infinitely rigid (non-deformable) matrix (continuum), and focus on the flow problem exclusively. Solid deformability may be introduced as a first approach by means of elasticity or poroelasticity, although in general this does not lead to a realistic description of field deformations or stress states. Non-linear models in the form of Mohr-Coulomb or more sophisticated forms of elasto-plasticity may also be used, although the precise type of nonlinear model that may be adequate depends very

much on the particular geo-material (sand, rock), porosity level, degree of fracturing, existence of faults or localized discontinuities, etc. and also on the information available. And, last but not least, the initial stress state also generally plays an essential role, especially if plasticity or fracture behavior is involved.

Nowadays Geomechanics is applied to a large variety of problems, including for instance:

1. Wellbore stability problems: determination of breakout conditions due to *in situ* stress values (Bradley, 1979, Aadnoy, 2003).
2. Solid production management. (Papanastasiou and Vardoulakis, 1992, Vardoulakis et al., 1996, van den Hoek et al., 2000, Vaziri et al., 2002).
3. Hydraulic fracture: prediction of fracture geometry in hydraulic fracture, etc. (Nordgren, 1972, Sarris and Papanastasiou, 2012, Secchi and Schrefler, 2012).
4. CO_2 storage. Study of injection conditions and study of reservoir sealing conditions (Rutqvist, 2012, Vilarrasa et al., 2010).
5. Matured (depleted) reservoirs. Determination of stresses and surface subsidences (Gambolati et al., 2001).

1.2 Motivation and objectives

Some of the more difficult problems described above have in common the treatment of discontinuities/fractures. Fractures can be introduced for a precise structural description (eg, contacts between layers, faults, etc.) or due to material behavior (the simulation of brittle materials). In the literature there are multiple methods to take into account discontinuities, that can be grouped into: i) Methods based on a continuum approach, using special constitutive laws models (eg. multilaminate law (Zienkiewicz and Pande, 1977)), or enriched formulations, (eg *Cosserat* continuum (Mühlhaus, 1993)) etc.; ii) Methods based on a discrete approach, for instance Distinct Element Method (DEM) (Cundall, 1971). Very satisfactory results have been achieved with all these numerical methods. However, due to the high computational cost of some of them, or the intrinsic assumptions of others, very few of them are available for a wide range of applications in petroleum geomechanics.

In this context, the main objective of this thesis is to show the applicability of zero-thickness interfaces to a wide range of geomaterials problems, and in particular to oil&gas problems. For this reason the thesis deals with two challenging problems: on one hand, a reservoir scale problem, that of hydraulic fracture; and on the other hand, a material scale problem, that of sand production. To achieve this objective, some specific objectives have been defined:

1. Enhancing numerical tools. In order to be able to solve challenging problems, the objective of the work has been the improvement of the computational capacities to

accelerate the calculations. Improvements in the constitutive law of the elements (in 2D) and the introduction in parallel computing have been the main objectives.

2. Mesomechanical analysis of rock samples. An objective of this thesis has been the analysis of rock behavior throughout samples described at the mesoscopic level. The mesoscopic scale takes into account the heterogeneity at grain level, which, together with the use of zero-thickness interface elements and fracture-based laws, leads to a model that has intrinsic size effect and other convenient features for rock sanding simulations.

3. Extension of the hydro-mechanical formulation with zero-thickness interfaces, to 3D analysis. Departing from the hydro-mechanical formulation proposed by Segura and Carol (2008a) for double-node interfaces, that formulation has been extended to 3D analysis.

4. Application studies.

1.3 Methodology

The development of this thesis has combined ingredients of different areas of knowledge (geomechanics, petroleum engineering, numerical methods and fracture mechanics) that are related in the following way. The study includes two problems of petroleum engineering with a strong mechanical behavior for which concepts of geomechanics have to be applied, hydraulic fracture and sand production. For both problems, fracture propagation is a fundamental ingredient for an adequate modeling. The treatment of fracture initiation and propagation requires the use of concepts of fracture mechanics, which in this case are incorporated into the zero-thickness interface constitutive law. In addition, the need to solve the fluid interaction, especially for hydraulic fracture simulations, forces the introduction of a coupled hydro-mechanical formulation ("u-p") (Geomechanics). Numerical methods are then naturally introduced to solve the differential equations by means of Finite Element Method (FEM), with special emphasis in the use of the zero-thickness interface elements. Finally a mention has to be made to mesh generation regarding microstructural examples (sand production) and to parallelization, both related to numerical methods. The map of concepts, including its main relationships is presented in Fig. 1.1.

This thesis has been carried out in the MECMAT group (Mechanics and Nanotechnology of Engineering Materials). The beginning of the doctoral thesis has started from previous work developed by former members of the group. Additional to the initial version of the computer code DRAC , actively developed by the former members of the group, in particular by I. Carol and P. Prat, this work is born from the following contributions: a) the hydro-mechanical formulation proposed by Segura (2007).

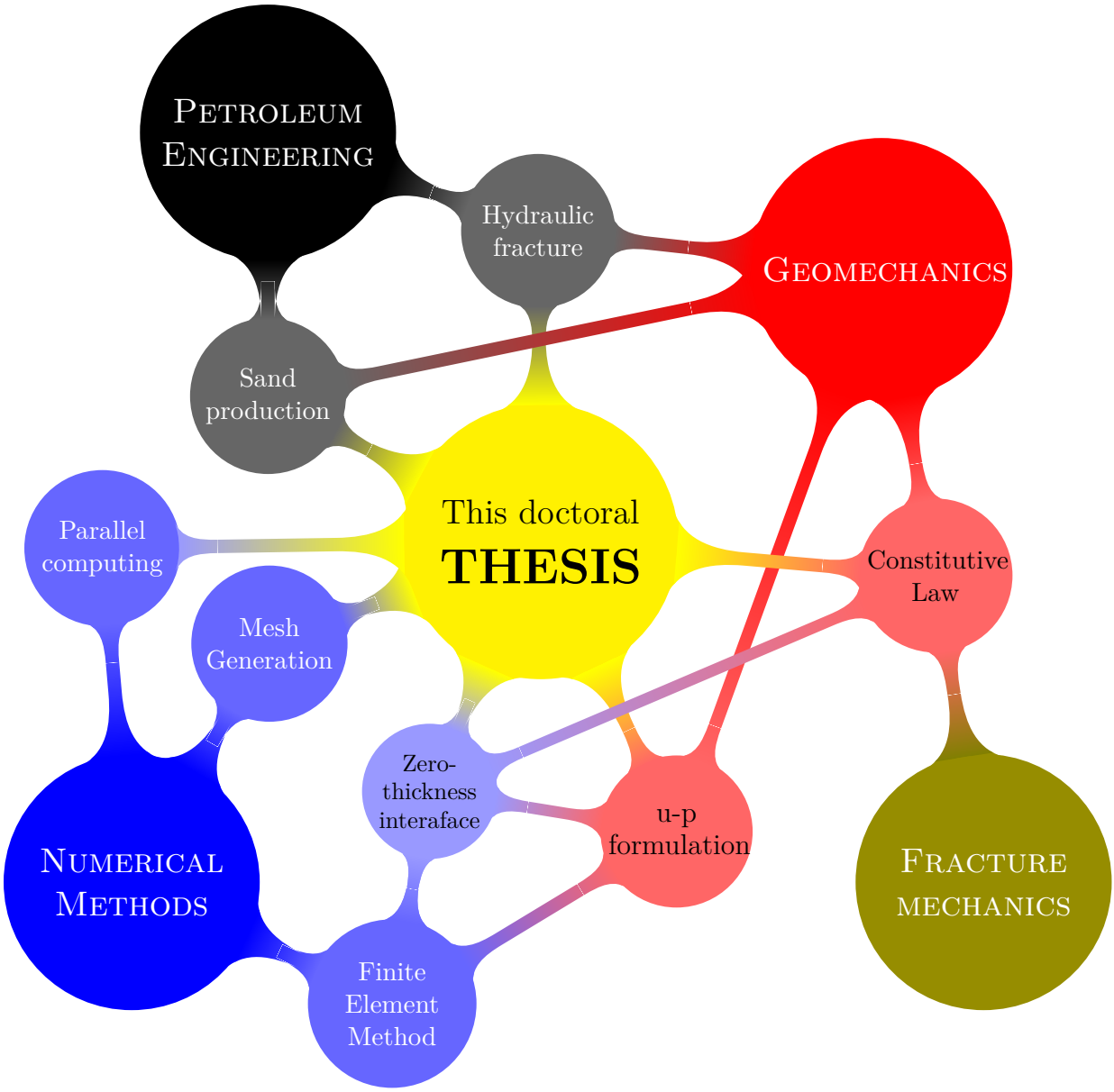

Figure 1.1: Thesis mindmap. An overview of main concepts developed in this thesis

b) code optimization (iterative solvers, GiD post-processing) done by Caballero (2005); and c) The initial version of micromechanical mesh generator departed from a version developed by Roa (2004).;

The following paragraphs show the specific lines of work of this thesis, which can be classified into four sections: 1) literature review; 2) geometry generation; 3) FEM code developing; and 4) simulations

Literature review The literature review has been focused on three aspects of the thesis: 1) numerical methods for the solution of linear systems, with a particular interest in all aspects related to parallel computing; 2) the state of the art of hydraulic fracture, with special interest in validation procedures; and 3) the state of the art of sand production.

Model generation The improvement and the development of mesh generation tools can be divided in two parts:.

- Microstructal generation (emphVoronoi-based geometries)
  - On one hand the existing discrete mesh generator has been improved to allow a large number of grains. This task mainly consisted of implementing, into the existing generation code, a *convex-hull* algorithm for *Delaunay*'s triangulation.
  - On the other hand a new code was developed that manages mesh operations: cut initial discrete mesh (rectangular) in order to obtain a ring-shaped mesh; creation of the continuum element mesh to extend the domain to both the inner and outer boundaries; and assemble the different meshes and produce input files for code DRAC .
- Discontinuous geometries (arbitrary geometries)
  - Generation of automatic algorithms to introduce zero-thickness interface elements in general continuum meshes.

FEM code development This part has consumed much of the effort of this thesis. The purpose of this section has been to provide the necessary tools for the numerical simulation. For this reason attention has been mainly focused on four specific aspects of the model:

- The beginning of this work started with the implementation of backward-Euler algorithm with sub-incrementation (Pérez-Foguet et al., 2001) in the constitutive law for interfaces in 2D. The purpose of this implementation was the improvement of return mapping algorithm to increase the speed of the finite element calculation.

- Due to the strong coupling effects between flow and stresses, a hydro-mechanical FEM code has been developed. The original mechanical code DRAC has evolved into a new code (DRAC4) by implementing Segura's formulation (Segura, 2007, Segura and Carol, 2008a). Although Segura's work had provided a coupled code (dracflow_coupled), it was decided to generate a new code to take the advantage of full features of DRAC system which included 3D analysis capabilities. Additionally the DRAC system provides us the possibility of evolutive geometry (construction/excavation), necessary in sand production analysis, and full access to numerical library, especially the use of iterative solvers.

- Parallel implementation. Based on DRAC4, a new version of code has been implemented in order to introduce parallel computing. Changes, made in collaboration with other members of the group, focused on the implementation of the parallel library PETSc, including the modification of the code structure to take advantage of the parallel procedure, the minimization of memory use, and the optimal distribution of tasks between processors.

- Grain detection and excavation. The production of sand has been modeled thanks to the implementation of an automatic algorithm, that after identifying the cracked interface elements, detects whether a part of the domain has become detached from the rest of the mesh and therefore it can be excavated. This procedure has been started from the beginning using concepts of hierarchical geometry models in order to identify potential failure paths.

Simulations A number of calculations have been performed in order to verify the code developed and the models implemented. The simulations included in this thesis are the following: in 2D, simulations were performed on the one hand to establish the constitutive behavior of homogeneous material, Uniaxial Compression Tests (UCT) and Triaxial compression Tests (TCT); and on the other hand to analyze sand production simulations itself. In 3D, calculation have been oriented to represent hydraulic fracture problems

1.4 Structure of the thesis

This thesis document consists of six chapters, the Introduction, two chapters dedicated to the description of the theoretical concepts (fundamentals), two chapters related to the application studies, and finally one chapter of Conclusions and Perspectives.

The first part is devoted to fundamentals explains the theoretical formulations implemented and describes the numerical tools used for the simulations, and is divided into two chapters (2 to 3).

- **Chapter 2 Hydro-Mechanical formulation in 3D**. This chapter deals with the formulation of Hydro-mechanical coupling in 3D for both continuum and interface elements, including "u-p" formulation, time integration, fully coupled resolution and a detailed description of the energy-based mechanical constitutive law.
- **Chapter 3 Parallelization**. This chapter is divided in two sections. First, some theoretical aspects of parallel implementation are presented, focusing on the particular aspects of the DRAC code. Second, a performance analysis is presented in order to determine the degree of parallelization achieved.

The applications part consists of two chapters, 4 and 5, where hydraulic fracture and sand production applications are presented.

- **Chapter 4 Hydraulic fracture**. The application of the model to hydraulic fracturing is presented in this chapter. This includes a state of the art, with special interest in the analytical formulations used for the validation. Then the analysis of a single fracture is presented for both 2D and 3D in Section 4.2. The main objective of this section is to validate the model developed against analytical expressions or against existing numerical solutions. Then Section 4.3 shows the results for 2D multistage analysis with non-prestablish path. Finally, Section 4.4 presents a realistic 3D analysis of multistage hydraulic fracture.
- **Chapter 5 Sand production modeling**. The chapter is divided in two sections. After a brief introduction, the suggested methodology is presented. Also in this chapter the aspects related to the mesomechanical model are presented, including geometry generation for both constitutive samples and sand production cross-sections. This section includes a description of the removal algorithm that will be crucial for the excavation procedure. Afterwards, the analysis of a sandstone material is presented which allows to show the sensitivity to the main variables of the proposed model. This section includes micromechanical characterization analysis and the simulation of the hollow cylinder test. The last section shows the results of real case, including parameter characterization and hollow cylinder formulation.

Finally, the last part of the thesis document consists of **Chapter 6 Summary, conclusions and future work**. The main conclusions of this work are presented in this section as well as some considerations for future research.

Chapter 2

Hydro-Mechanical formulation in 3D

Contents

This chapter describes the mathematical framework of the numerical model. The hydro-mechanical (HM) formulation follows the work of Lewis and Schrefler (1998) for the continuum and Segura and Carol (2008a) for the interfaces.

The sign criterion for the continuum and the interfaces follows the classical mechanics criterion: compressive stresses are negative and tensile stresses are positive. Consequently, the relative displacements on the interface are positive in opening. Fluid pressures in continuum and interfaces are positive and suctions are negative.

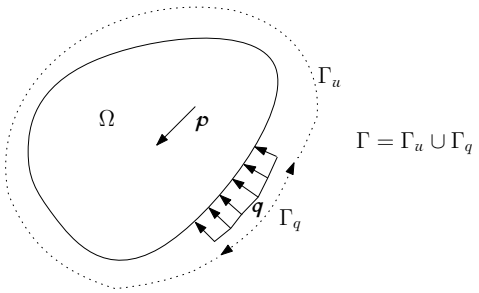

Figure 2.1: Scheme of a boundary value problem (BVP): Ω represents the full domain, Γ is the boundary, p and q independent terms of domain and boundary solutions respectively.

2.1 Formulation of continuum elements

The continuum formulation is developed as a Boundary Value Problem (BVP). The general form describes the problem with the following two equations:

$$\mathcal{A}(\boldsymbol{u}) = \mathcal{C}(\boldsymbol{u}) + \boldsymbol{p} = 0 \qquad in\ \Omega \tag{2.1}$$

$$\mathcal{B}(\boldsymbol{u}) = \mathcal{M}(\boldsymbol{u}) + \boldsymbol{q} = 0 \qquad on\ \Gamma \tag{2.2}$$

where $\mathcal{A}$ describes the behavior in the domain (Ω); $\mathcal{B}$ on the boundary (Γ); $\mathcal{C}$ and $\mathcal{M}$ represent the differential operators; and $\boldsymbol{p}$ and $\boldsymbol{q}$ are the independent terms. The boundary is composed into two parts, a part where the values of the solution are prescribed (Γ_u) and a part where the flow (stress or specific discharge) is imposed (Γ_q) (see Fig. 2.1).

Equations (2.1) and (2.2) represent the strong form of the governing differential equations of the problem. They will be exactly satisfied if applied to the exact solution of the problem. However, if they are applied to an approximate solution they will not be satisfied exactly at all points. In that case, the optimal approximation can be found with the following equation:

$$\int_\Omega \mathbf{w}^\mathsf{T}\, \mathcal{A}(\boldsymbol{u})\, d\Omega + \int_\Gamma \overline{\mathbf{w}}^\mathsf{T}\, \mathcal{B}(\boldsymbol{u})\, d\Gamma = \mathbf{0} \tag{2.3}$$

which involve the weight functions vectors $\mathbf{w}$ and $\overline{\mathbf{w}}$ and constitute a weak form of the governing equations. Equation (2.3) defines the weighted residual method and it will be used for the mechanical problem where the unknowns ($\boldsymbol{u}$) are the displacements ($\mathbf{u}$), f and for the hydraulic problem where the unknowns ($\boldsymbol{u}$) are the fluid pressures ($\mathbf{p}^f$).

2.1.1 The linear momentum balance equation

The first governing equation of the mechanical problem is the balance of linear momentum (Eq. (2.4)), in which the inertial term is neglected (no accelerations are considered):

$$\mathscr{A}\left(\mathbf{u}\right) = \mathbf{L}_{\mathrm{C}}^{u\mathsf{T}}\,\boldsymbol{\sigma} + \rho\,\mathbf{g} = \mathbf{0} \tag{2.4}$$

where the differential operator $\mathbf{L}_{\mathrm{C}}^{u}$ is given by Eq. (2.5); the total stress tensor ($\boldsymbol{\sigma}$) is represented following the *Voigt* notation (Eq. (2.6)); the gravity vector is represented with $\mathbf{g}$, in which g_i are de components of gravity in "xyz" system; and the average density ρ is a function of the porosity n, the skeleton density ρ_s and the fluid density ρ_f (Eq. (2.7)).

$$\mathbf{L}_{\mathrm{C}}^{u\mathsf{T}} = \begin{pmatrix} \dfrac{\partial}{\partial x} & 0 & 0 & \dfrac{\partial}{\partial y} & 0 & \dfrac{\partial}{\partial z} \\ 0 & \dfrac{\partial}{\partial y} & 0 & \dfrac{\partial}{\partial x} & \dfrac{\partial}{\partial z} & 0 \\ 0 & 0 & \dfrac{\partial}{\partial z} & 0 & \dfrac{\partial}{\partial y} & \dfrac{\partial}{\partial x} \end{pmatrix} \tag{2.5}$$

$$\boldsymbol{\sigma} = \begin{pmatrix} \sigma_x & \sigma_y & \sigma_z & \tau_{xy} & \tau_{yz} & \tau_{zx} \end{pmatrix}^{\mathsf{T}} \tag{2.6}$$

$$\mathbf{g} = \begin{pmatrix} g_x & g_y & g_z & 0 & 0 & 0 \end{pmatrix}^{\mathsf{T}} \tag{2.7}$$

$$\rho = (1-n)\rho_s + n\rho_f \tag{2.8}$$

The boundary conditions associated with the linear momentum equation are defined by the following equation for $\mathscr{B}$:

$$\mathscr{B}\left(\mathbf{u}\right) = \mathbf{l}^{\mathsf{T}}\,\boldsymbol{\sigma} - \tilde{\mathbf{t}} = \mathbf{0} \tag{2.9}$$

where $\tilde{\mathbf{t}}$ are the stress tractions over the part of the boundary Γ_q with prescribed stress tractions $\tilde{\mathbf{t}}$, and $\mathbf{l}$ is the operator defined as:

$$\mathbf{l}^{\mathsf{T}} = \begin{pmatrix} n_x & 0 & 0 & n_y & 0 & n_z \\ 0 & n_y & 0 & n_x & n_z & 0 \\ 0 & 0 & n_z & 0 & n_y & n_x \end{pmatrix} \tag{2.10}$$

where n_i are the components of the unit vector $\hat{\mathbf{n}}$ normal to the boundary surface in xyz system.

The integral form or weak form of the differential equations plus boundary conditions is obtained by applying the weighted residuals Eq. (2.3) to Eqs. (2.4) and (2.9):

$$\int_{\Omega} \mathbf{w}^{\mathsf{T}}\,\mathbf{L}_{\mathrm{C}}^{u\mathsf{T}}\,\boldsymbol{\sigma}\,d\Omega + \int_{\Omega} \mathbf{w}^{\mathsf{T}}\,\rho\,\mathbf{g}\,d\Omega + \int_{\Gamma_q} \overline{\mathbf{w}}^{\mathsf{T}}\left(\mathbf{l}^{\mathsf{T}}\,\boldsymbol{\sigma} - \tilde{t}\right)d\Gamma = \mathbf{0} \tag{2.11}$$

where $\mathbf{w}$ and $\overline{\mathbf{w}}$ are three-component vectors containing the weight functions.

After applying the divergence theorem [1] to the first term of Eq. (2.11),

$$-\int_{\Omega}\left(\mathbf{L}_{\mathrm{C}}^{u}\,\mathbf{w}\right)^{\mathsf{T}}\boldsymbol{\sigma}\,d\Omega+\int_{\Gamma}\mathbf{w}^{\mathsf{T}}\,\mathbf{l}^{\mathsf{T}}\,\boldsymbol{\sigma}\,d\Gamma+\int_{\Omega}\mathbf{w}^{\mathsf{T}}\,\rho\,\mathbf{g}\,d\Omega+\int_{\Gamma}\overline{\mathbf{w}}^{\mathsf{T}}\left(\mathbf{l}^{\mathsf{T}}\,\boldsymbol{\sigma}-\tilde{\boldsymbol{t}}\right)d\Gamma=\mathbf{0}\tag{2.12}$$

and considering that the weight function is selected such that $\mathbf{w}=0$ on the mechanical boundary Γ_u and that $\overline{\mathbf{w}}=-\mathbf{w}$ on the boundary Γ_q , the following is obtained:

$$\begin{aligned}&-\int_{\Omega}\left(\mathbf{L}_{\mathrm{C}}^{u}\,\mathbf{w}\right)^{\mathsf{T}}\boldsymbol{\sigma}\,d\Omega+\int_{\Gamma}\mathbf{w}^{\mathsf{T}}\,\mathbf{l}^{\mathsf{T}}\,\boldsymbol{\sigma}\,d\Gamma+\int_{\Omega}\mathbf{w}^{\mathsf{T}}\,\rho\,\mathbf{g}\,d\Omega\\&\qquad-\int_{\Gamma}\mathbf{w}^{\mathsf{T}}\left(\mathbf{l}^{\mathsf{T}}\,\boldsymbol{\sigma}-\tilde{\boldsymbol{t}}\right)d\Gamma=\mathbf{0}\Rightarrow\\\Rightarrow\qquad&-\int_{\Omega}\left(\mathbf{L}_{\mathrm{C}}^{u}\,\mathbf{w}\right)^{\mathsf{T}}\boldsymbol{\sigma}\,d\Omega+\int_{\Omega}\mathbf{w}^{\mathsf{T}}\,\rho\,\mathbf{g}\,d\Omega+\int_{\Gamma_q}\mathbf{w}^{\mathsf{T}}\,\tilde{\boldsymbol{t}}\,d\Gamma=\mathbf{0}\end{aligned}\tag{2.13}$$

For the spatial discretization, the Finite Element Method is applied. The displacements are approximated by Eq. (2.14), considering that the coefficients a_i correspond in this case to the values of the nodal displacements $\left(\mathbf{u}_e\right)$.

$$\mathbf{u}\simeq\hat{\mathbf{u}}=\sum_{i=1}^{n}N_i^u a_i=\mathbf{N}^u\,\mathbf{u}_e\tag{2.14}$$

where n is the number of nodes used for the interpolation. Then the Galerkin method is applied, which consists in applying the weighted residual Eq. (2.13) repeatedly, taking the weight functions equal to each of the nodal interpolation functions, ($\mathbf{w}=\begin{pmatrix}N_i^u & N_i^u & N_i^u\end{pmatrix}$). With this the integral form is transformed into:

$$-\int_{\Omega}\left(\mathbf{L}_{\mathrm{C}}^{u}\,\mathbf{N}^u\right)^{\mathsf{T}}\boldsymbol{\sigma}\,d\Omega+\int_{\Omega}\mathbf{N}^{u\mathsf{T}}\,\rho\,\mathbf{g}\,d\Omega+\int_{\Gamma_q}\mathbf{N}^{u\mathsf{T}}\,\tilde{\mathbf{t}}\,d\Gamma=\mathbf{0}\tag{2.15}$$

The effective stresses ($\boldsymbol{\sigma}'$) are:

$$\boldsymbol{\sigma}=\boldsymbol{\sigma}'-\alpha\,p^f\,{\mathbf{m}_{\mathrm{C}}}^{\mathsf{T}}\tag{2.16}$$

where α is the Biot's coefficient, p^f is the fluid pressure and ${\mathbf{m}_{\mathrm{C}}}^{\mathsf{T}}$ the identity matrix. Following the discretization made for the displacements field, the fluid pressure is approximated by:

$$\mathbf{p}\simeq\hat{\mathbf{p}}=\sum_{i=1}^{n}N_i^p a_i=\mathbf{N}^p\,{\mathbf{p}^f}_e\tag{2.17}$$

Substituting now Eqs. (2.16) and (2.17) into Eq. (2.15), and defining the deformation

[1] $\left(\int_{\Omega}\phi\,(\nabla\psi)\;d\Omega=-\int_{\Omega}(\nabla\phi)\,\psi\,d\Omega+\int_{\Gamma}\phi\psi n\,d\Gamma\right)$

matrix ($\mathbf{B}_{\mathrm{C}} = \mathbf{L}\ \mathbf{N}^{u}$), the following equation results:

$$\begin{aligned} &\int_{\Omega} \mathbf{B}_{\mathrm{C}}{}^{\mathsf{T}}\, \boldsymbol{\sigma}'\, d\Omega - \int_{\Omega} \mathbf{B}_{\mathrm{C}}{}^{\mathsf{T}}\, \alpha\, \mathbf{N}^{p}\, \mathbf{p}^{f}{}_{e} \mathbf{m}_{\mathrm{C}}{}^{\mathsf{T}}\, d\Omega = \\ &= \int_{\Omega} \mathbf{N}^{u\mathsf{T}}\, \rho\, \mathbf{g}\, d\Omega + \int_{\Gamma_q} \mathbf{N}^{u\mathsf{T}}\, \tilde{\boldsymbol{t}}\, d\Gamma \end{aligned} \tag{2.18}$$

which is further transformed into the mechanic continuum equation:

Summary 1 – Mechanical continuum equation.

$$\int_{\Omega} \mathbf{B}_{\mathrm{C}}{}^{\mathsf{T}}\, \boldsymbol{\sigma}'\, d\Omega - \mathbf{Q}_{\mathrm{C}}\, \mathbf{p}^{f}{}_{e} = \mathbf{f}^{u}_{\mathrm{C}} \tag{2.19}$$

where $\mathbf{Q}_{\mathrm{C}}$ is the coupling matrix and $\mathbf{f}^{u}_{\mathrm{C}}$ the vector of external forces.

$$\mathbf{Q}_{\mathrm{C}} = \int_{\Omega} \mathbf{B}_{\mathrm{C}}{}^{\mathsf{T}}\, \alpha\, \mathbf{N}^{p} \mathbf{m}_{\mathrm{C}}{}^{\mathsf{T}}\, d\Omega \tag{2.20}$$

$$\mathbf{f}^{u}_{\mathrm{C}} = \int_{\Omega} \mathbf{N}^{u\mathsf{T}}\, \rho\, \mathbf{g}\, d\Omega + \int_{\Gamma_q} \mathbf{N}^{u\mathsf{T}}\, \tilde{\boldsymbol{t}}\, d\Gamma \tag{2.21}$$

2.1.2 Fluid mass balance equation

The fluid mass balance equation in a continuum porous medium may be expressed in the following form:

$$\mathscr{A}\left(p^{f}\right) = \frac{1}{M^{sf}} \frac{\partial p^{f}}{\partial t} + \alpha \boldsymbol{\nabla}^{\mathsf{T}}\ \mathbf{v}^{s} + \boldsymbol{\nabla}^{\mathsf{T}}\ \left[\frac{\mathbf{k}^{f}}{\mu^{f}} \left(-\boldsymbol{\nabla}\, p^{f} + \rho^{f}\, \mathbf{g}\right)\right] = 0 \tag{2.22}$$

where, M^{sf} is the Biot's modulus Eq. (2.23); α the Biot's coefficient; $\boldsymbol{\nabla} = \left(\frac{\partial}{\partial x} \quad \frac{\partial}{\partial y} \quad \frac{\partial}{\partial z}\right)^{\mathsf{T}}$; $\mathbf{v}^{s}$ is the solid velocity, which is the rate of solid deformation, described in Eq. (2.24); $\mathbf{k}^{f}$ is the hydraulic conductivity; μ^{f} is the dynamic viscosity; ρ^{f} is the fluid density; and $\mathbf{g}$ is the gravity vector.

$$\frac{1}{M^{sf}} = \left(\frac{\alpha - n}{K^{s}} + \frac{n}{K^{f}}\right) \tag{2.23}$$

$$\boldsymbol{\nabla}^{\mathsf{T}}\ \mathbf{v}^{s} = \mathbf{m}_{\mathrm{C}}{}^{\mathsf{T}} \frac{\partial \boldsymbol{\epsilon}}{\partial t} = \mathbf{m}_{\mathrm{C}}{}^{\mathsf{T}}\ \mathbf{L}^{u}_{\mathrm{C}} \frac{\partial\, \mathbf{u}}{\partial t} \tag{2.24}$$

The Dirichlet ($\tilde{p}^{f}$ prescribed values of fluid pressure on Γ^{f}_{p}) and Neumann ($\tilde{q}^{f}$ prescribed flow, or specific discharge, on Γ^{f}_{q}) boundary conditions are, respectively:

$$p^{f} = \tilde{p}^{f} \tag{2.25}$$

$$\mathcal{B}(p^f) = \frac{\mathbf{k}^f}{\mu^f}\Big(-\boldsymbol{\nabla} p^f + \rho^f \mathbf{g}\Big)^{\mathsf{T}} \boldsymbol{n} - \tilde{q}^f \qquad = 0 \tag{2.26}$$

The integral form is obtained by applying the weighted residual method (2.3) to Eqs. (2.22) and (2.26), where in this case the weight functions w are scalar:

$$\begin{aligned}
&\int_\Omega w \frac{1}{M^{sf}} \frac{\partial p^f}{\partial t} d\Omega + \int_\Omega w \alpha \mathbf{m}_{\mathrm{C}}{}^{\mathsf{T}}\, \mathbf{L}_{\mathrm{C}}^u \frac{\partial\, \mathbf{u}}{\partial t} d\Omega \\
&+ \int_\Omega w \boldsymbol{\nabla}^{\mathsf{T}} \left[\frac{\mathbf{k}^f}{\mu^f}\Big(-\boldsymbol{\nabla} p^f + \rho^f \mathbf{g}\Big)\right] d\Omega \\
&+ \int_{\Gamma_q^f} \overline{w} \left(\frac{\mathbf{k}^f}{\mu^f}\Big(-\boldsymbol{\nabla} p^f + \rho^f \mathbf{g}\Big)^{\mathsf{T}}\, \mathbf{n} - \tilde{q}^f\right) d\Gamma = 0
\end{aligned} \tag{2.27}$$

Developing the Darcy term in the preceding Eq. (2.27), and applying the divergence theorem, the following is obtained:

$$\begin{aligned}
&\int_\Omega w \boldsymbol{\nabla}^{\mathsf{T}} \left[\frac{\mathbf{k}^f}{\mu^f}\Big(-\boldsymbol{\nabla} p^f + \rho^f \mathbf{g}\Big)\right] d\Omega = \\
&= -\int_\Omega \boldsymbol{\nabla} w \left[\frac{\mathbf{k}^f}{\mu^f}\Big(-\boldsymbol{\nabla} p^f + \rho^f \mathbf{g}\Big)\right] d\Omega + \int_\Gamma w \left[\frac{\mathbf{k}^f}{\mu^f}\Big(-\boldsymbol{\nabla} p^f + \rho^f \mathbf{g}\Big)\right] \boldsymbol{n}\, d\Gamma
\end{aligned} \tag{2.28}$$

º Then Eq. (2.27) is further modified into:

$$\begin{aligned}
&\int_\Omega w \frac{1}{M^{sf}} \frac{\partial p^f}{\partial t}\, d\Omega + \int_\Omega w \alpha \mathbf{m}_{\mathrm{C}}{}^{\mathsf{T}}\, \mathbf{L}_{\mathrm{C}}^u \frac{\partial\, \mathbf{u}}{\partial t}\, d\Omega \\
&- \int_\Omega \boldsymbol{\nabla} w \left[\frac{\mathbf{k}^f}{\mu^f}\Big(-\boldsymbol{\nabla} p^f + \rho^f \mathbf{g}\Big)\right] d\Omega \\
&+ \int_\Gamma w \left[\frac{\mathbf{k}^f}{\mu^f}\Big(-\boldsymbol{\nabla} p^f + \rho^f \mathbf{g}\Big)\right] \boldsymbol{n}\, d\Gamma \\
&+ \int_{\Gamma_q^f} \overline{w} \frac{\mathbf{k}^f}{\mu^f}\Big(-\boldsymbol{\nabla} p^f + \rho^f \mathbf{g}\Big)^{\mathsf{T}} \boldsymbol{n}\, d\Gamma - \int_{\Gamma_q^f} \overline{w} \tilde{q}^f\, d\Gamma = 0
\end{aligned} \tag{2.29}$$

Considering that the weight function is such that $w = 0$ on Γ_p^f and $\overline{w} = -w$ on Γ_q^f,

$$\begin{aligned}
&\int_\Omega w \frac{1}{M^{sf}} \frac{\partial p^f}{\partial t}\, d\Omega + \int_\Omega w \alpha \mathbf{m}_{\mathrm{C}}{}^{\mathsf{T}}\, \mathbf{L}_{\mathrm{C}}^u \frac{\partial\, \mathbf{u}}{\partial t}\, d\Omega - \\
&- \int_\Omega \boldsymbol{\nabla} w \left[\frac{\mathbf{k}^f}{\mu^f}\Big(-\boldsymbol{\nabla} p^f + \rho^f \mathbf{g}\Big)\right] d\Omega + \int_{\Gamma_q^f} w \tilde{q}^f\, d\Gamma = 0
\end{aligned} \tag{2.30}$$

Once more, the spatial discretization is made using the FEM. The fluid pressure is approximated with Eq. (2.17), with the coefficients a_i corresponding to the values of the nodal fluid pressure $\mathbf{p}^f{}_e$, and the Galerkin approach is applied, which consists in repeating Eq. (2.30) as many times as nodes in the element, each time using $w = N_i^p$.

Arranging the resulting equations in matrix form, the following equation is obtained:

$$\begin{aligned}
&\int_{\Omega} \mathbf{N}^{p\mathsf{T}} \frac{1}{M^{sf}} \mathbf{N}^{p} \frac{\partial \mathbf{p}^{f}{}_{e}}{\partial t} \, d\Omega + \int_{\Omega} \mathbf{N}^{p\mathsf{T}} \, \alpha \mathbf{m}_{\mathrm{C}}{}^{\mathsf{T}} \, \mathbf{L}_{\mathrm{C}}^{u} \, \mathbf{N}^{u} \frac{\partial \mathbf{u}_{e}}{\partial t} \, d\Omega \\
&- \int_{\Omega} \boldsymbol{\nabla} \, \mathbf{N}^{p\mathsf{T}} \left[\frac{\mathbf{k}^{f}}{\mu^{f}} \left(- \boldsymbol{\nabla} \, \mathbf{N}^{p} \, \mathbf{p}^{f}{}_{e} + \rho^{f} \, \mathbf{g} \right) \right] d\Omega \\
&+ \int_{\Gamma_{q}^{f}} \mathbf{N}^{p\mathsf{T}} \, \tilde{q}^{f} \, d\Gamma = 0
\end{aligned} \tag{2.31}$$

which eventually becoming

$$\begin{aligned}
&\int_{\Omega} \left(\boldsymbol{\nabla} \, \mathbf{N}^{p} \right)^{\mathsf{T}} \left(\frac{\mathbf{k}^{f}}{\mu^{f}} \right) \boldsymbol{\nabla} \, \mathbf{N}^{p} \, \mathbf{p}^{f}{}_{e} \, d\Omega \\
&+ \int_{\Omega} \mathbf{N}^{p\mathsf{T}} \, \alpha \mathbf{m}_{\mathrm{C}}{}^{\mathsf{T}} \, \mathbf{L}_{\mathrm{C}}^{u} \, \mathbf{N}^{u} \frac{\partial \mathbf{u}_{e}}{\partial t} \, d\Omega + \int_{\Omega} \mathbf{N}^{p\mathsf{T}} \frac{1}{M^{sf}} \mathbf{N}^{p} \frac{\partial \mathbf{p}^{f}{}_{e}}{\partial t} \, d\Omega = \\
&= \int_{\Omega} \left(\boldsymbol{\nabla} \, \mathbf{N}^{p} \right)^{\mathsf{T}} \frac{\mathbf{k}^{f}}{\mu^{f}} \rho^{f} \, \mathbf{g} \, d\Omega - \int_{\Gamma_{q}^{f}} \mathbf{N}^{p\mathsf{T}} \, \tilde{q}^{f} \, d\Gamma
\end{aligned} \tag{2.32}$$

Because the nodal fluid pressure and the nodal displacements are independent of the integration, Eq. (2.32) if further transformed into the following Eq. (2.33):

Summary 2 – Hydraulic continuum equation.

$$\mathbf{H}_{\mathrm{C}} \, \mathbf{p}^{f}{}_{e} + \mathbf{Q}_{\mathrm{C}}{}^{\mathsf{T}} \frac{\partial \mathbf{u}_{e}}{\partial t} + \mathbf{S}_{\mathrm{C}} \frac{\partial \mathbf{p}^{f}{}_{e}}{\partial t} = \mathbf{f}_{\mathrm{C}}^{p} \tag{2.33}$$

where, $\mathbf{H}_{\mathrm{C}}$ is the diffusion matrix; $\mathbf{Q}_{\mathrm{C}}$ the coupling matrix between the mechanical and hydraulic problems; $\mathbf{S}_{\mathrm{C}}$ the storage matrix and $\mathbf{f}_{\mathrm{C}}^{p}$ the right-hand side term, in this case the term including the external flow.

$$\mathbf{H}_{\mathrm{C}} = \int_{\Omega} \left(\boldsymbol{\nabla} \, \mathbf{N}^{p} \right)^{\mathsf{T}} \left(\frac{\mathbf{k}^{f}}{\mu^{f}} \right) \boldsymbol{\nabla} \, \mathbf{N}^{p} \, d\Omega \tag{2.34}$$

$$\mathbf{Q}_{\mathrm{C}}{}^{\mathsf{T}} = \int_{\Omega} \mathbf{N}^{p\mathsf{T}} \, \alpha \mathbf{m}_{\mathrm{C}}{}^{\mathsf{T}} \, \mathbf{B}_{\mathrm{C}} \, d\Omega \tag{2.35}$$

$$\mathbf{S}_{\mathrm{C}} = \int \mathbf{N}^{p\mathsf{T}} \frac{1}{M^{sf}} \mathbf{N}^{p} \, d\Omega \tag{2.36}$$

$$\mathbf{f}_{\mathrm{C}}^{p} = \int_{\Omega} \left(\boldsymbol{\nabla} \, \mathbf{N}^{p} \right)^{\mathsf{T}} \left(\frac{\mathbf{k}^{f}}{\mu^{f}} \right) \rho^{f} \, \mathbf{g} \, d\Omega - \int_{\Gamma_{q}^{f}} \mathbf{N}^{p\mathsf{T}} \, \tilde{q}^{f} \, d\Gamma \tag{2.37}$$

2.2 Formulation of zero-thickness interface elements

The present work follows the definition of the zero-thickness interface element proposed by Goodman et al. (1968). The main characteristic of this type of elements is that one of its dimensions has collapsed (see Fig. 2.2). Therefore, the integration is reduced in one order, line integration for 2D and surface integration for 3D (Fig. 2.3). The mid-plane surface is defined via isoparametric interpolation on the basis of the coordinates of the mid-points, or points at mid-distance between each pair of nodes. This interpolation is based on a set of local coordinates ξ, η for the mid-plane surface in 3D, or ξ for the mid-plane line in 2D. Nodal unknowns are transformed into mid-plane variables which represent variations (jumps or drops) of field variables (§2.2.1). Mid-plane variables are expressed in terms of the local orthogonal coordinate system, presented in §2.2.2.

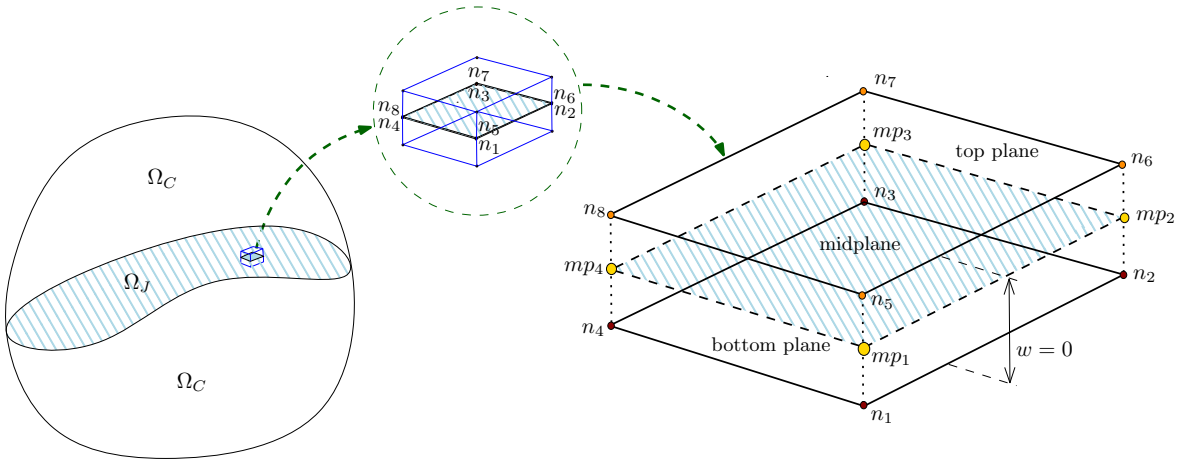

Figure 2.2: Zero-thickness interface element description. Example of a quadrilateral interface embedded between two hexahedral continuum finite elements, where n_i are the element nodes and mp_i the mid-plane points.

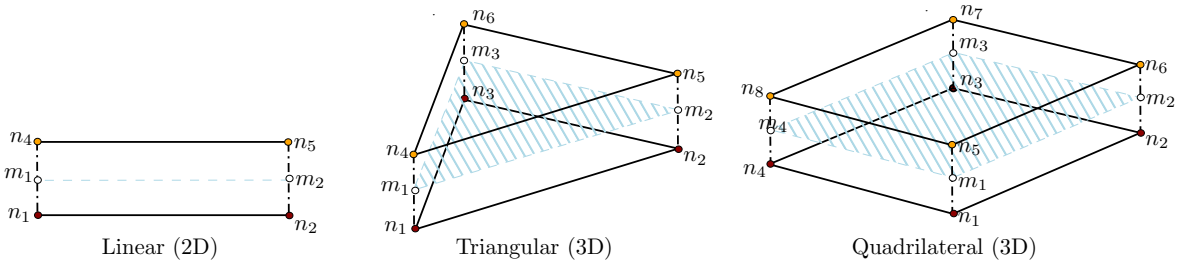

Figure 2.3: Zero-thickness interface element types.

2.2.1 Zero-thickness variables

For compatibility with the continuum elements in the same mesh, the nodal variables in a hydro-mechanical problem include the nodal displacements ($\mathbf{u}_e$) and the nodal fluid pressures ($\mathbf{p}_e^f$). In the case of zero-thickness interfaces, the nodal (absolute) displacements are transformed into normal (r_n) and shear (r_{l_1}, r_{l_2}) relative displacements,

which have the meaning of displacements jumps across the discontinuity surface. The other variable, fluid pressure, is transformed into two components, the average pressure ($\bar{p}^f_{\text{J}}$) and the pressure drop ($\check{p}^f_{\text{J}}$), across the discontinuity. A description of these variables and their conjugates is provided in the following paragraphs.

The relative displacement at a mid-plane point with local coordinates (ξ, η) of the discontinuity is represented by:

$$\mathbf{r} = \begin{pmatrix} r_n & r_{l_1} & r_{l_2} \end{pmatrix}^{\mathsf{T}} \tag{2.38}$$

where r_n is the normal component and the $r_{l_{(*)}}$ are the tangential components. These relative displacements are shown in Fig. 2.4.

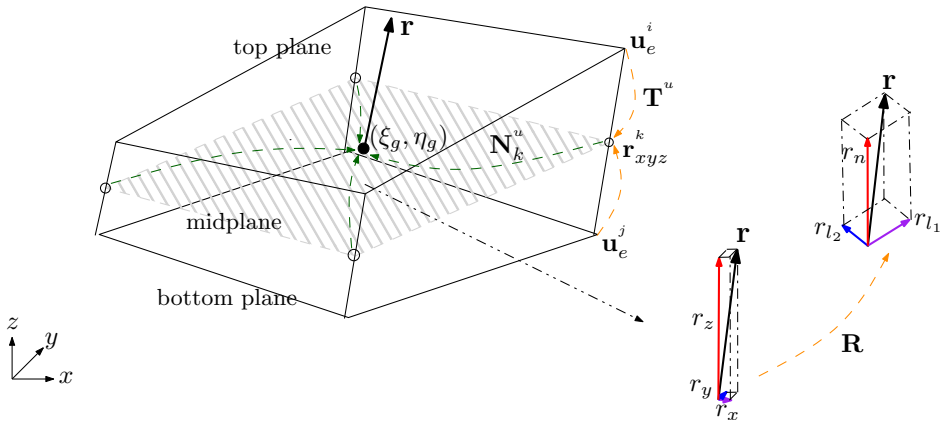

Figure 2.4: Relative displacements of zero-thickness interface element.

The relation between relative displacements at the local point (ξ, η) and the absolute nodal displacements of the interface element is given by the following expressions:

$$\mathbf{r} = \mathbf{R}\, \mathbf{N}^u_{\text{J}}\, \mathbb{T}^u\, \mathbf{u}_e = \mathbf{B}_{\text{J}}\, \mathbf{u}_e \tag{2.39}$$

In this equation $\mathbf{R}$ is the rotation matrix that transforms vector components into components in local orthogonal axes (n, l_1, l_2) defined in Section 2.2.2, $\mathbf{N}^u_{\text{J}}$ is the matrix of nodal shape functions evaluated at the integration position (ξ_g, η_g), and $\mathbb{T}^u$ is the "transport" matrix, which converts absolute nodal variables into "jumps" at the mid-plane points.

Then, matrix $\mathbf{B}_{\text{J}}$ is defined in analogy to the continuum description as.

$$\mathbf{B}_{\text{J}} = \mathbf{R}\, \mathbf{N}^u_{\text{J}}\, \mathbb{T}^u \tag{2.40}$$

The matrix of nodal shape functions is defined in Eq. (2.41), where index m represents the number of nodes at midplane, which is equivalent to half of the number of nodes of the element (n). Index d represents the number of mechanical degrees of freedom per node, for instance in 3D $d = 3$ and 2D $d = 2$. The Kronecker product is

used in their definition[2]

$$\mathbf{N}^u_{\text{J}} = \begin{pmatrix} N_1 & N_2 & \cdots & N_m \end{pmatrix} \otimes \mathbf{I}_d \tag{2.41}$$

The mechanical transport matrix for the mechanical problem is defined as:

$$\mathbb{T}^u = \begin{pmatrix} -\mathbf{I}_m & \mathbf{I}_m \end{pmatrix} \otimes \mathbf{I}_d \tag{2.42}$$

The conjugate variables to the relative displacements are the tractions (or stress traction vector) at the discontinuity mid-plane ($\boldsymbol{\sigma}_{\text{J}}$), which at a given point (ξ, η) of that surface, may be expressed as:

$$\boldsymbol{\sigma}_{\text{J}} = \begin{pmatrix} \sigma_n & \tau_{l_1} & \tau_{l_2} \end{pmatrix}^{\mathsf{T}} \tag{2.43}$$

where σ_n is the normal stress and τ_{l_1} and τ_{l_2} are the tangential components.

The average fluid pressure ($\bar{p}^f_{\text{J}}$) at a given point "(ξ, η)" of the discontinuity is obtained as the average between bottom and top fluid pressures and it can be expressed as:

$$\bar{p}^f_{\text{J}} = \mathbf{N}^p_{\text{J}}\, \mathbb{T}^p_L\, \mathbf{p}_e \tag{2.44}$$

$$\mathbf{N}^p_{\text{J}} = \begin{pmatrix} N_1 & N_2 & \cdots & N_m \end{pmatrix} \otimes \mathbf{I}_1 \tag{2.45}$$

$$\mathbb{T}^p_L = \frac{1}{2} \begin{pmatrix} \mathbf{I}_m & \mathbf{I}_m \end{pmatrix} \otimes \mathbf{I}_1 \tag{2.46}$$

The fluid pressure drop at the same point is given by the difference between top and bottom fluid pressures at element nodes:

$$\check{p}^f_{\text{J}} = \mathbf{N}^p_{\text{J}}\, \mathbb{T}^p_T\, \mathbf{p}_e \tag{2.47}$$

$$\mathbb{T}^p_T = \begin{pmatrix} -\mathbf{I}_m & \mathbf{I}_m \end{pmatrix} \otimes \mathbf{I}_1 \tag{2.48}$$

The conjugate variable of the fluid pressure drop is the transversal flow (q_t), and for the fluid average is the longitudinal flow (q_l), see Fig. 2.5.

2.2.2 Geometric aspects

2.2.2.a Local orthonormal basis

An important aspect in 3D analysis with zero-thickness interfaces is the definition of the local orthonormal basis of at each point within the element. Initially two system of coordinates are available: (i) Global system, denoted with "xyz", based on the

[2]The Kronecker product "$\otimes$" of two matrices is defined as: $\mathbf{A} \otimes \mathbf{B} = \begin{pmatrix} a_{11}\,\mathbf{B} & \cdots & a_{1n}\,\mathbf{B} \\ \vdots & \ddots & \vdots \\ a_{m1}\,\mathbf{B} & \cdots & a_{mn}\,\mathbf{B} \end{pmatrix}$

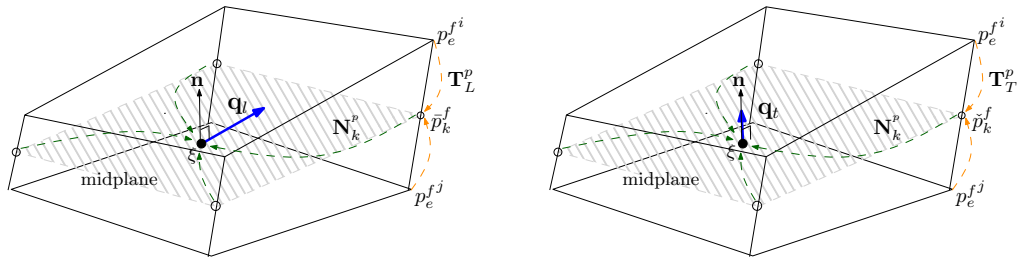

(a) (b)

Figure 2.5: Longitudinal and transversal flow of zero-thickness interface element: (a)) longitudinal and (b)) transversal flow.

canonical basis $\{\hat{\mathbf{e}}_x, \hat{\mathbf{e}}_y, \hat{\mathbf{e}}_z\}$;.and (ii) Local element system, denoted with "$\xi\eta$"", which corresponds to the one defined within the isoparametric element. The local basis will be generated with the following requirements: (i) **Local definition**. The basis has to be defined in terms of local axes, with normal and tangential components. (ii) **Orthonormality**. The vector basis will be composed of orthonormal vectors. The new system, inherent to interfaces, will be denoted with "nl_1l_2" or "l_1l_2" if referring only to "in-plane" components.

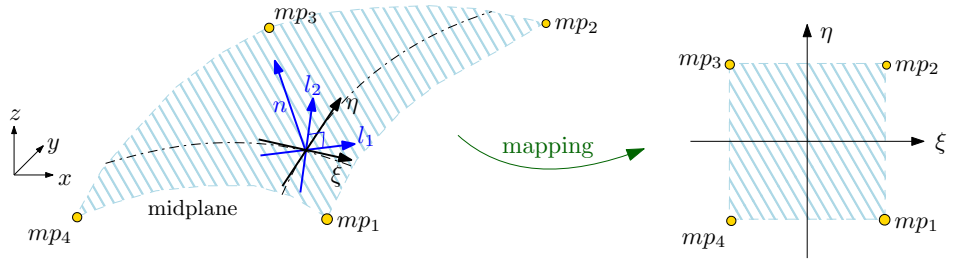

Physical element (mid-plane) isoparametric element

Figure 2.6: Zero-thickness coordinate systems. Global system (x, y, z), local element system $(\xi\eta)$ and local orthogonal system (n, l_1, l_2)

Due to the fact that the local system "$\xi\eta$" is not orthogonal, it is necessary to define a new orthonormal basis at each point of the interface mid-plane.

The unit normal vector to the interface plane is obtained as the cross product of the partial derivatives of the global coordinates with respect to the local coordinates (Fig. 2.7a):

$$\hat{\mathbf{n}} = \frac{1}{J}\left(\frac{\partial \mathbf{x}}{\partial \xi} \times \frac{\partial \mathbf{x}}{\partial \eta}\right) \tag{2.49}$$

where J is the modulus of such product, i.e.:

$$J = \left|\frac{\partial \mathbf{x}}{\partial \xi} \times \frac{\partial \mathbf{x}}{\partial \eta}\right| \tag{2.50}$$

Because of the isoparametric representation of the mid-plane geometry, the derivatives of the global coordinates with respect to the local coordinates may be obtained as the

product of the derivatives of the shape functions with respect to the local base and the vector of mid-point coordinates $\mathbf{x}_{mp}$:

$$\begin{pmatrix} \frac{\partial \mathbf{x}}{\partial \xi} \\ \frac{\partial \mathbf{x}}{\partial \eta} \end{pmatrix} = \begin{pmatrix} \frac{\partial \mathbf{N}_{\mathrm{J}}}{\partial \xi} \\ \frac{\partial \mathbf{N}_{\mathrm{J}}}{\partial \eta} \end{pmatrix} \mathbf{x}_{\mathrm{mp}} \tag{2.51}$$

$$\mathbf{x}_{\mathrm{mp}} = \begin{pmatrix} x_{mp_1} & y_{mp_1} & z_{mp_1} \\ \vdots & \vdots & \vdots \\ x_{mp_m} & y_{mp_m} & z_{mp_m} \end{pmatrix} \tag{2.52}$$

$$\begin{pmatrix} \frac{\partial \mathbf{N}_{\mathrm{J}}}{\partial \xi} \\ \frac{\partial \mathbf{N}_{\mathrm{J}}}{\partial \eta} \end{pmatrix} = \begin{pmatrix} \frac{\partial N_1}{\partial \xi} & \frac{\partial N_2}{\partial \xi} & \cdots & \frac{\partial N_m}{\partial \xi} \\ \frac{\partial N_1}{\partial \eta} & \frac{\partial N_2}{\partial \eta} & \cdots & \frac{\partial N_m}{\partial \eta} \end{pmatrix} \tag{2.53}$$

The second vector of this base ($\hat{\mathbf{l}}_1$) is defined as the cross product of the unit normal vector $\hat{\mathbf{n}}$ and the canonical base vector $\hat{\mathbf{e}}_z$ and, in case that $\hat{\mathbf{n}}$ is parallel to $\hat{\mathbf{e}}_z$, then $\hat{\mathbf{e}}_y$ is used instead of $\hat{\mathbf{e}}_z$. The last term ($\hat{\mathbf{l}}_2$) is obtained as the cross product of $\hat{\mathbf{n}}$ and $\hat{\mathbf{l}}_1$, therefore being orthogonal to both. (see Fig. 2.7b-c)

$$\hat{\mathbf{l}}_1 = \hat{\mathbf{n}} \times \hat{\mathbf{e}}_z \tag{2.54}$$

$$\hat{\mathbf{l}}_2 = \hat{\mathbf{n}} \times \hat{\mathbf{l}}_1 \tag{2.55}$$

Other authors (e.g.Cerfontaine et al. (2015)) generate the local orthogonal basis using the first vector of the "$\xi\eta$" basis and the vector product of that vector with the normal vector. Although both procedures are equivalent, in this case the present method has been selected due to physical meaning of generated basis. In a case of a non-horizontal plane, vector $\hat{\mathbf{l}}_1$ corresponds to the direction of maximum slope (dip direction) and the vector $\hat{\mathbf{l}}_2$ is to the direction of the plane (azimuth direction). In the case of a horizontal plane, vectors $\hat{\mathbf{n}}$, $\hat{\mathbf{l}}_1$, and $\hat{\mathbf{l}}_2$ correspond directly to the unit vectors in the x, y and z directions.

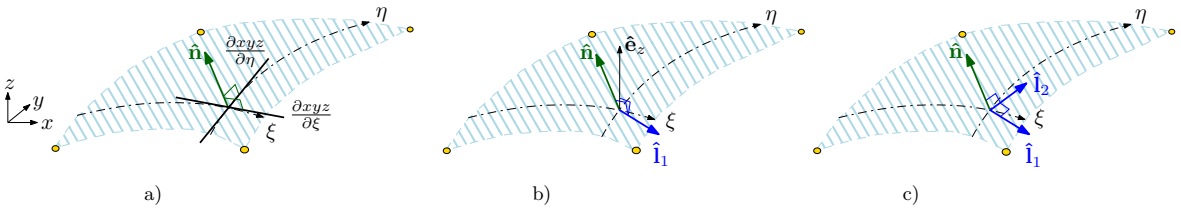

Figure 2.7: Local orthogonal system generation. a) Generation of normal vector base, b) and c) tangential vector base.

Once the orthogonal system has been set, the rotation matrix ($\mathbf{R}_{\mathrm{J}}$) that relates the "xyz" system with the local orthogonal system "nl_1l_2" has to be defined. Note that

due to the orthonormality of the vectors, the determinant of $\mathbf{R}_{\text{J}}$ matrix is equal to one, and the inverse matrix is equal to the transpose, that is, $\mathbf{R}_{\text{J}}$ is an "orthogonal matrix".

$$\mathbf{R}_{\text{J}} = \mathbf{P}^{xyz}_{\text{nl}_1\text{l}_2} = \left(\mathbf{P}^{nl_1l_2}_{\text{xyz}}\right)^{-1} = \left(\mathbf{P}^{nl_1l_2}_{\text{xyz}}\right)^{\mathsf{T}} \tag{2.56}$$

where (see Fig. 2.8):

$$\mathbf{P}^{nl_1l_2}_{\text{xyz}} = \begin{pmatrix} n_x & l_{1x} & l_{2x} \\ n_y & l_{1y} & l_{2y} \\ n_z & l_{1z} & l_{2z} \end{pmatrix}; \qquad \mathbf{P}^{xyz}_{\text{nl}_1\text{l}_2} = \begin{pmatrix} x_n & y_n & z_n \\ x_{l_1} & y_{l_1} & z_{l_1} \\ x_{l_2} & y_{l_2} & z_{l_2} \end{pmatrix} \tag{2.57}$$

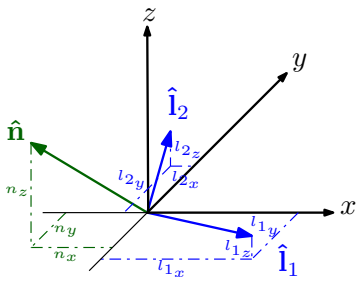

Figure 2.8: Zero-thickness coordinate systems. Global system (x, y, z), local element system (n, s, t) and local orthogonal system (n, l_1, l_2)

The rotation matrix can also be interpreted as the partial derivative of the "nl_1l_2" system with respect to the "xyz" system. Neglecting the normal component (vector $\hat{\mathbf{n}}$), the components of the in-plane vector $(\hat{\mathbf{l}}_1, \hat{\mathbf{l}}_2)$ in the "xyz" system are:

$$\frac{\partial l_1 l_2}{\partial xyz} = \begin{pmatrix} l_{1_x} & l_{1_y} & l_{1_z} \\ l_{2_x} & l_{2_y} & l_{2_z} \end{pmatrix} \tag{2.58}$$

2.2.2.b Local gradient

The gradient of the shape functions in terms of the local orthogonal system is obtained by applying the chain rule with intermediate variables $\xi\eta$:

$$\boldsymbol{\nabla}_{\text{J}}\, \mathbf{N}_{\text{J}} = \frac{\partial\, \mathbf{N}_{\text{J}}}{\partial l_1 l_2} = \frac{\partial\, \mathbf{N}_{\text{J}}}{\partial \xi\eta} \frac{\partial \xi\eta}{\partial l_1 l_2} = \frac{\partial\, \mathbf{N}_{\text{J}}}{\partial \xi\eta} \left(\frac{\partial l_1 l_2}{\partial \xi\eta}\right)^{-1} \tag{2.59}$$

where the auxiliary relationship between both in-plane bases, "$l_1 l_2$" and "$\xi\eta$" is obtained as:

$$\frac{\partial l_1 l_2}{\partial \xi\eta} = \frac{\partial l_1 l_2}{\partial xyz}\frac{\partial xyz}{\partial \xi\eta} \qquad \Rightarrow$$
$$\Rightarrow \begin{pmatrix} \frac{\partial l_1}{\partial \xi} & \frac{\partial l_1}{\partial \eta} \\ \frac{\partial l_2}{\partial \xi} & \frac{\partial l_2}{\partial \eta} \end{pmatrix} = \begin{pmatrix} l_{1_x} & l_{1_y} & l_{1_z} \\ l_{2_x} & l_{2_y} & l_{2_z} \end{pmatrix} \begin{pmatrix} \frac{\partial x}{\partial \xi} & \frac{\partial x}{\partial \eta} \\ \frac{\partial y}{\partial \xi} & \frac{\partial y}{\partial \eta} \\ \frac{\partial z}{\partial \xi} & \frac{\partial z}{\partial \eta} \end{pmatrix} \tag{2.60}$$

2.2.3 Mechanical formulation

2.2.3.a Governing equations

In the presence of fluid in the pores, the formulation of stress follows Terzaghi's effective principle. In the particular case of interfaces, as the fluid pressure only affects the volumetric component, only the normal term is affected as shown in eq. (2.61). Biot's formulation is introduced for this reason,

$$\boldsymbol{\sigma}'_{\text{J}} = \boldsymbol{\sigma}_{\text{J}} + \alpha_j \, \mathbf{m}_{\text{J}} \, \bar{p}^f_{\text{J}} \tag{2.61}$$

where $\mathbf{m}_{\text{J}} = \begin{pmatrix} 1 & 0 & 0 \end{pmatrix}^{\mathsf{T}}$, α_j is the Biot's coefficient and $\bar{p}^f_{\text{J}}$ is the average fluid pressure at the mid-plane Eq. (2.44)

The mechanical constitutive law in this kind of elements relates the effective stress ($\boldsymbol{\sigma}'_{\text{J}}$) and the relative displacements ($\mathbf{r}$) through the stiffness matrix $\mathbf{D}$. Due to the material non-linearity, this relationship is expressed in incremental form.

$$d\,\boldsymbol{\sigma}'_{\text{J}} = \mathbf{D}_{\text{J}} \; d\mathbf{r} \tag{2.62}$$

$$d\mathbf{r} = \mathbf{R}\; \mathbf{N}^u_{\text{J}}\, \mathbb{T}^u \; d\,\mathbf{u}_e = \mathbf{B}_{\text{J}} \; d\,\mathbf{u}_e \tag{2.63}$$

where $d\,\mathbf{u}_e$ are the variation of nodal displacements of the interface element and the matrix $\mathbf{B}_{\text{J}}$ is the relation between relative displacements and nodal displacements given in Eq. (2.40).

2.2.3.b Finite element discretization

The weak form of equilibrium equation is obtained by means of the Principle of Virtual Work (PVW) (2.64). According to this principle, the work produced by the external forces with virtual displacements is equivalent to the internal work produced by virtual relative displacements:

The weak form of the equilibrium equation is obtained by means of the PVW Eq. (2.64). According to this principle, the work produced by the external forces with

the virtual nodal displacements $\delta\,\mathbf{u}_e$ must be equivalent to the internal work produced by the virtual relative displacements $\delta\mathbf{r}$ over the mid-plane surface:

$$\delta\,\mathbf{u}_e\,\mathbf{f}^u{}_e = \int_{\Omega_j} \delta\mathbf{r}^{\mathsf{T}}\ \boldsymbol{\sigma}_{\mathrm{J}}\,d\Omega_j \tag{2.64}$$

In this equation, $\delta\mathbf{r}$ may be replaced in terms of $(\delta\,\mathbf{u}_e)$, Eq. (2.64), and since the equation has to be satisfied for any value of the virtual displacements $(\delta\,\mathbf{u}_e)$, this leads to:

$$\begin{aligned}\delta\,\mathbf{u}_e\,\mathbf{f}^u{}_e &= \int_{\Omega_j} \delta\,\mathbf{u}_e{}^{\mathsf{T}}\,\mathbb{T}^{u\mathsf{T}}\,\mathbf{N}_{\mathrm{J}}^{u\mathsf{T}}\,\mathbf{R}^{\mathsf{T}}\ \boldsymbol{\sigma}_{\mathrm{J}}\,d\Omega_j \Rightarrow \\ \Rightarrow \mathbf{f}^u{}_e &= \mathbb{T}^{u\mathsf{T}} \int_{\Omega_j} \mathbf{N}_{\mathrm{J}}^{u\mathsf{T}}\,\mathbf{R}^{\mathsf{T}}\ \boldsymbol{\sigma}_{\mathrm{J}}\,d\Omega_j\end{aligned} \tag{2.65}$$

Substituting the effective stresses from Eq. (2.65) into Eq. (2.65) results in:

$$\mathbf{f}^u{}_e = \mathbb{T}^{u\mathsf{T}} \int_{\Omega_j} \mathbf{N}_{\mathrm{J}}^{u\mathsf{T}}\,\mathbf{R}^{\mathsf{T}}\ \boldsymbol{\sigma}'_{\mathrm{J}}\,d\Omega_j + \mathbb{T}^{u\mathsf{T}} \int_{\Omega_j} \mathbf{N}_{\mathrm{J}}^{u\mathsf{T}}\,\mathbf{R}^{\mathsf{T}}\ \alpha_j\,\mathbf{m}_{\mathrm{J}}\,\bar{p}^f_{\mathrm{J}}\,d\Omega_j \tag{2.66}$$

And adding the fluid average pressure $(\bar{p}^f_{\mathrm{J}})$ from Eq. (2.44) one obtains:

$$\begin{aligned}\mathbf{f}^u{}_e = {}& \mathbb{T}^{u\mathsf{T}} \int_{\Omega_j} \mathbf{N}_{\mathrm{J}}^{u\mathsf{T}}\,\mathbf{R}^{\mathsf{T}}\ \boldsymbol{\sigma}'_{\mathrm{J}}\,d\Omega_j \\ & + \mathbb{T}^{u\mathsf{T}} \left(\int_{\Omega_j} \mathbf{N}_{\mathrm{J}}^{u\mathsf{T}}\,\mathbf{R}^{\mathsf{T}}\ \alpha_j\,\mathbf{m}_{\mathrm{J}}\,\mathbf{N}_{\mathrm{J}}^{p\mathsf{T}}\,d\Omega_j \right) \mathbb{T}^p_L\,\mathbf{p}_e\end{aligned} \tag{2.67}$$

The nodal values of the fluid pressure and the transformation matrices are constant over the integration domain. This leads to the definition of the coupling matrix for interfaces $(\mathbf{Q}_{\mathrm{J}})$ and the final expression of the weak form of the mechanical equation for interfaces which has identical structure as its counterpart for the continuum, Eq. (2.19):

Summary 3 – Mechanical equation. In which the $\mathbf{Q}_{\mathrm{J}}$ matrix contains the hydro-mechanical coupling terms.

$$\int_{\Omega_j} \mathbf{B}_{\mathrm{J}}^{u\mathsf{T}}\ \boldsymbol{\sigma}'_{\mathrm{J}}\,d\Omega_j + \mathbf{Q}_{\mathrm{J}}\,\mathbf{p}^f{}_e = \mathbf{f}^u_{\mathrm{J}} \tag{2.68}$$

$$\mathbf{Q}_{\mathrm{J}} = \mathbb{T}^{u\mathsf{T}} \int_{\Omega_j} \mathbf{N}_{\mathrm{J}}^{u\mathsf{T}}\,\mathbf{R}^{\mathsf{T}}\ \alpha_j\,\mathbf{m}_{\mathrm{J}}\,\mathbf{N}_{\mathrm{J}}^{p\mathsf{T}}\,d\Omega_j\ \mathbb{T}^p_L \tag{2.69}$$

2.2.4 Hydraulic formulation

2.2.4.a Governing equations

The definition of the hydraulic behavior of the interfaces follows the work of Segura (2007) in which the flow for double node interfaces was proposed. The formulation of this kind of elements is composed of two terms: the flow along the interface or longitudinal flow and the transversal flow across the interface Segura and Carol (2004, 2007, 2008a, 2008b).

Longitudinal flow

The longitudinal flow, formulated in the mid-plane, is defined with the mass balance Eq. (2.70) and the constitutive relationship, Darcy's equation Eq. (2.71). The fluid mass balance is related to the fluid mass divergence along the mid-plane, plus a term considering the compression of the fluid, adding a term considering the mass variation due to the evolution of the volume caused by opening/closing of the interface:

$$\boldsymbol{\nabla}_{\mathrm{J}}^{\mathsf{T}}\ \mathbf{Q'}_{l} + \frac{1}{M_J^f}\frac{\partial\, \bar{p}_{\mathrm{J}}^f}{\partial t} + \alpha\frac{\partial r_n}{\partial t} + S = 0 \tag{2.70}$$

The relationship between the longitudinal fluid flow (q_l) and the average fluid pressure ($\bar{p}_{\mathrm{J}}^f$) is derived from an adaptation of the generalised Darcy's law to flow in interfaces, consisting in introducing an equivalent thickness term (w) on both sides of the equation that leads to a substitution of the conductivity ($\mathbf{K}^f$) by the transmissivity ($\mathbf{T}^f = \mathbf{K}^f w$), and the specific discharge (Darcy's velocity, ($\mathbf{q}_l$)) by a discharge per unit width ($\mathbf{Q'}_l$) :

$$\mathbf{Q'}_{l} = \mathbf{q}_l w = -\,\mathbf{T}^f\ \boldsymbol{\nabla}_{\mathrm{J}}\left(\frac{\bar{p}_{\mathrm{J}}^f}{\gamma_f} + z\right) \tag{2.71}$$

where $\mathbf{T}^f$ is the transmissivity matrix in terms of the local in-plane axis is:

$$\mathbf{T}^f = \begin{pmatrix} T_{l_{1,1}} & T_{l_{1,2}} \\ T_{l_{2,1}} & T_{l_{2,2}} \end{pmatrix} \tag{2.72}$$

and $\boldsymbol{\nabla}_{\mathrm{J}}$ is the partial differential operator for local in-plane axis:

$$\boldsymbol{\nabla}_{\mathrm{J}} = \begin{pmatrix} \dfrac{\partial}{\partial l_1} & \dfrac{\partial}{\partial l_2} \end{pmatrix}^{\mathsf{T}} \tag{2.73}$$

Cubic law Although Eq. (2.72) is the general expression of the transmissivity matrix, in the implemented formulation the expression has been simplified. First, it has been assumed equal value of the diagonal terms (T_l), therefore there is no preferential flow direction along the plane. Second, the cross terms are neglected. Eq. (2.72) has

been transformed into:

$$\mathbf{T}^f = T_l \begin{pmatrix} 1 & 0 \\ 0 & 1 \end{pmatrix} \tag{2.74}$$

Additionally, the definition of the value of T_l can be realized by means of a non-linear relation depending on the opening (r_n) (normal relative displacement) of the interface element. In this case, due to the inherent hypothesis of the model, laminar flow, and assuming that the flow is parallel, low roughness, the use of the cubic law (Poiseuille law) has been adopted (Witherspoon et al., 1980, Oron and Berkowitz, 1998):

$$T_l = \frac{\gamma_f}{12\mu} r_n^3 \tag{2.75}$$

where γ_f is the fluid specific weight and μ is the dynamic viscosity.

Transversal flow

The transversal flow is defined in terms of an equation similar to Darcy's law but in discrete terms: a constant parameter, the transverse hydraulic coefficient $\check{K}_t$, relates f the transverse fluid flow (q_t) to the transversal pressure drop ($\check{p}^f_{\text{J}}$):

$$q_t = \check{K}_t \, \check{p}^f_{\text{J}} \tag{2.76}$$

2.2.4.b Finite element discretization

Longitudinal flow For the longitudinal flow, the fluid mass continuity equation combined with Darcy's law leads to the governing equation of the longitudinal flow:

$$\mathcal{A}(\bar{p}^f_{\text{J}}) = \boldsymbol{\nabla}_{\text{J}}{}^{\mathsf{T}} \left(- \mathbf{T}^f \, \boldsymbol{\nabla}_{\text{J}} \left(\frac{\bar{p}^f_{\text{J}}}{\gamma_f} + z \right) \right) + \frac{1}{M^f_J} \frac{\partial \, \bar{p}^f_{\text{J}}}{\partial t} + \alpha \frac{\partial r_n}{\partial t} = 0 \tag{2.77}$$

where, M^f_J is the Biot's modulus; α the Biot's coefficient; $\boldsymbol{\nabla}_{\text{J}} = \left(\frac{\partial}{\partial l_1} \quad \frac{\partial}{\partial l_2} \right)^{\mathsf{T}}$ is the nabla operator for the local orthogonal in-plane system; $\mathbf{k}^f$ the hydraulic conductivity; μ^f the dynamic viscosity; ρ^f the fluid density; $\mathbf{g}$ the gravity vector; and r_n is the normal relative displacement and the rate of normal displacements may be easily related to the rate of relative displacement in xyz coordinates:

$$\frac{\partial r_n}{\partial t} = \mathbf{m}_{\text{J}}{}^{\mathsf{T}} \frac{\partial \, \mathbf{r}}{\partial t} \tag{2.78}$$

The Dirichlet and Neumann boundary conditions are, respectively:

$$\bar{p}^f_{\text{J}} = \tilde{p}^f \tag{2.79}$$

$$\mathcal{B}(p^f) = \left(- \mathbf{T}^f \, \boldsymbol{\nabla}_{\text{J}} \left(\frac{\bar{p}^f_{\text{J}}}{\gamma_f} + z \right) \right)^{\mathsf{T}} \cdot \boldsymbol{n} - \tilde{Q}'^f = 0 \tag{2.80}$$

where $\tilde{Q}^f$ is the prescribed value of the fluid pressure on the Γ_p^f boundary, and $\tilde{q}^f$ is the prescribed value of the discharge on the Γ_q^f boundary.

The integral form is obtained by applying the weighted residual method Eq. (2.3) to Eqs. (2.77) and (2.80) leading to

$$\begin{aligned}&\int_{\Omega_j} w \left(\boldsymbol{\nabla}_{\mathrm{J}}^{\mathsf{T}} \left(- \mathbf{T}^f \, \boldsymbol{\nabla}_{\mathrm{J}} \left(\frac{\bar{p}_{\mathrm{J}}^f}{\gamma_f} + z \right) \right) + \frac{1}{M_J^f} \frac{\partial \bar{p}_{\mathrm{J}}^f}{\partial t} + \alpha \frac{\partial r_n}{\partial t} \right) d\Omega_j \\ &+ \int_{\Gamma_q^f} \overline{w} \left(\left(- \mathbf{T}^f \, \boldsymbol{\nabla}_{\mathrm{J}} \left(\frac{\bar{p}_{\mathrm{J}}^f}{\gamma_f} + z \right) \right)^{\mathsf{T}} \cdot \boldsymbol{n} - \tilde{Q}'^f \right) d\Gamma = 0 \end{aligned} \tag{2.81}$$

Developing the Darcy term in this equation, and applying the divergence theorem, results in:

$$\begin{aligned}&\int_{\Omega_j} w \boldsymbol{\nabla}_{\mathrm{J}}^{\mathsf{T}} \left(- \mathbf{T}^f \, \boldsymbol{\nabla}_{\mathrm{J}} \left(\frac{\bar{p}_{\mathrm{J}}^f}{\gamma_f} + z \right) \right) d\Omega_j = \\ = \; &- \int_{\Omega_j} \boldsymbol{\nabla}_{\mathrm{J}} w \left(- \mathbf{T}^f \, \boldsymbol{\nabla}_{\mathrm{J}} \left(\frac{\bar{p}_{\mathrm{J}}^f}{\gamma_f} + z \right) \right) d\Omega_j + \\ &+ \int_{\Gamma} w \left(- \mathbf{T}^f \, \boldsymbol{\nabla}_{\mathrm{J}} \left(\frac{\bar{p}_{\mathrm{J}}^f}{\gamma_f} + z \right) \right) \boldsymbol{n} \, d\Gamma \end{aligned} \tag{2.82}$$

Substituting Section 2.2.4.b into Eq. (2.81):

$$\begin{aligned}&- \int_{\Omega_j} (\boldsymbol{\nabla}_{\mathrm{J}} w)^{\mathsf{T}} \left(- \mathbf{T}^f \, \boldsymbol{\nabla}_{\mathrm{J}} \left(\frac{\bar{p}_{\mathrm{J}}^f}{\gamma_f} + z \right) \right) d\Omega_j + \\ &+ \int_{\Gamma} w \left(- \mathbf{T}^f \, \boldsymbol{\nabla}_{\mathrm{J}} \left(\frac{\bar{p}_{\mathrm{J}}^f}{\gamma_f} + z \right) \right) \boldsymbol{n} \, d\Gamma + \\ &+ \int_{\Omega_j} w \frac{1}{M_J^f} \frac{\partial \bar{p}_{\mathrm{J}}^f}{\partial t} \, d\Omega_j + \int_{\Omega_j} w \alpha \frac{\partial r_n}{\partial t} \, d\Omega_j + \\ &+ \int_{\Gamma_q^f} \overline{w} \left(- \mathbf{T}^f \, \boldsymbol{\nabla}_{\mathrm{J}} \left(\frac{\bar{p}_{\mathrm{J}}^f}{\gamma_f} + z \right) \right)^{\mathsf{T}} \boldsymbol{n} \, d\Gamma - \\ &- \int_{\Gamma_q^f} \overline{w} \tilde{Q}'^f \, d\Gamma = 0 \end{aligned} \tag{2.83}$$

Assuming that $w = 0$ in Γ_p^f and $\overline{w} = -w$ in Γ_q^f:

$$\begin{aligned}&- \int_{\Omega_j} (\boldsymbol{\nabla}_{\mathrm{J}} w)^{\mathsf{T}} \left(- \mathbf{T}^f \, \boldsymbol{\nabla}_{\mathrm{J}} \left(\frac{\bar{p}_{\mathrm{J}}^f}{\gamma_f} + z \right) \right) d\Omega_j + \\ &+ \int_{\Omega_j} w \frac{1}{M_J^f} \frac{\partial \bar{p}_{\mathrm{J}}^f}{\partial t} \, d\Omega_j + \int_{\Omega_j} w \alpha \frac{\partial r_n}{\partial t} \, d\Omega_j + \\ &+ \int_{\Gamma_q^f} w \tilde{Q}'^f \, d\Gamma = 0 \end{aligned} \tag{2.84}$$

The spatial discretization is made using the Finite Element Method. The fluid pressure is approximated with the following equation (2.85), where the Galerkin approach

is applied, which consists in applying the weighted residual equation several times, each time taking one of the shape functions as the weight function ($w = N_{J_i}$):

$$p^f_{mp} \simeq \hat{p}^f_{mp} = \sum_i^m N^p_{J_i} a_i = \mathbf{N}^p_{\mathrm{J}} \mathbf{p}^f_{\mathrm{mp}} \tag{2.85}$$

where the coefficients a_i correspond to the values of the nodal fluid pressure $\mathbf{p}^f_{\mathrm{mp}}$. Then the Eq. (2.84) may be collected into the following matrix equation:

$$\begin{aligned}
&- \int_{\Omega_j} (\boldsymbol{\nabla}_{\mathrm{J}}\, \mathbf{N}^p_{\mathrm{J}})^{\mathsf{T}} \left(- \mathbf{T}^f\, \boldsymbol{\nabla}_{\mathrm{J}} \left(\frac{1}{\gamma_f}\, \mathbf{N}^p_{\mathrm{J}} \mathbf{p}^f_{\mathrm{mp}} + z \right) \right) d\Omega_j + \\
&+ \int_{\Omega_j} \mathbf{N}^{p\mathsf{T}}_{\mathrm{J}} \frac{1}{M^f_J}\, \mathbf{N}^p_{\mathrm{J}} \frac{\partial \mathbf{p}^f_{\mathrm{mp}}}{\partial t}\, d\Omega_j + \\
&+ \int_{\Omega_j} \mathbf{N}^{p\mathsf{T}}_{\mathrm{J}}\, \alpha \mathbf{m}^{\mathsf{T}}\, \mathbf{R}_{\mathrm{J}}\, \mathbf{N}^u_{\mathrm{J}} \frac{\partial\, \mathbf{r}_{\mathrm{xyz}}}{\partial t}\, d\Omega_j + \int_{\Gamma^f_q} \mathbf{N}^{p\mathsf{T}}_{\mathrm{J}}\, \tilde{Q}'^f\, d\Gamma = 0
\end{aligned} \tag{2.86}$$

Physically, each of the terms in the integral Eq. (2.86) may be reinterpreted as a contribution to a nodal flow continuity equation (total flow in minus total flow out equals to total flow accumulation:

$$\mathbf{Q}^1_{\mathrm{Lmp}} + \mathbf{Q}^2_{\mathrm{Lmp}} + \mathbf{Q}^0_{\mathrm{Lmp}} = 0 \tag{2.87}$$

where

$$\begin{aligned}
\mathbf{Q}^1_{\mathrm{Lmp}} &= - \left(\int_{\Omega_j} \boldsymbol{\nabla}_{\mathrm{J}}\, \mathbf{N}^{p\mathsf{T}}_{\mathrm{J}} \left(\frac{-\,\mathbf{T}^f}{\gamma_f} \right) \boldsymbol{\nabla}_{\mathrm{J}}\, \mathbf{N}^p_{\mathrm{J}}\, d\Omega_j \right) \mathbf{p}^f_{\mathrm{mp}} \\
\mathbf{Q}^2_{\mathrm{Lmp}} &= \left(\int_{\Omega_j} \mathbf{N}^{p\mathsf{T}}_{\mathrm{J}} \frac{1}{M^f_J}\, \mathbf{N}^p_{\mathrm{J}}\, d\Omega_j \right) \frac{\partial\, \mathbf{p}^f_{\mathrm{mp}}}{\partial t} = \\
\mathbf{Q}^0_{\mathrm{Lmp}} &= \left(\int_{\Omega_j} \mathbf{N}^{p\mathsf{T}}_{\mathrm{J}}\, \alpha \mathbf{m}^{\mathsf{T}}\, \mathbf{R}\, \mathbf{N}^u_{\mathrm{J}}\, d\Omega_j \right) \frac{\partial \mathbf{r}}{\partial t} \\
&\quad + \int_{\Omega_j} \boldsymbol{\nabla}_{\mathrm{J}}\, \mathbf{N}^{p\mathsf{T}}_{\mathrm{J}} \left(- \mathbf{T}^f \right) \boldsymbol{\nabla}_{\mathrm{J}}\, z\, d\Omega_j \\
&\quad + \int_{\Gamma^f_q} \mathbf{N}^{p\mathsf{T}}_{\mathrm{J}}\, \tilde{Q}'^f\, d\Gamma
\end{aligned} \tag{2.88}$$

All these flows are evaluated at the mid-plane, therefore, a relationship between mid-plane flow and element flow is needed. To obtain this relation, first a similar relation is recovered between mid-plane fluid pressures $\mathbf{p}^f_{\mathrm{mp}}$ and the full vector of nodal interface element pressures $\mathbf{p}^f_{\mathrm{e}}$. This relationship was already included in Eqs. (2.44) and (2.47):

$$\mathbf{p}^f_{\mathrm{mp}} = \mathbb{T}^p_L\, \mathbf{p}^f_{\mathrm{e}} \tag{2.89}$$

Now the PVW is applied between pressures $\mathbf{p}$ and flows $\mathbf{Q}$, and the two systems of

nodal variables (full nodes, or mid-points), leading to:

$$\delta\,\mathbf{p}_{\mathrm{e}}^{f\mathsf{T}}\,\mathbf{Q}_{L_e} = \delta\,\mathbf{p}_{\mathrm{mp}}^{f\ \mathsf{T}}\,\mathbf{Q}_{L_{mp}} \qquad (\forall\delta\,\mathbf{p}_{\mathrm{e}}^{f}) \tag{2.90}$$

Then, after replacing Eq. (2.89) and because the equation has to be satisfied for any virtual variation $\delta\,\mathbf{p}_{\mathrm{e}}^{f}$, the following relation is obtained:

$$\mathbf{Q}_{L_e} = \mathbb{T}_{L}^{p\mathsf{T}}\,\mathbf{Q}_{L_{mp}} \tag{2.91}$$

Note that this relation between nodal flow vectors is dual (with the same matrix transposed) than the one for pressures (Eq. (2.89)).

Finally, substitution of Eqs. (2.89) and (2.91) into Eq. (2.86) results in:

$$\begin{aligned}
&\mathbb{T}_{L}^{p\mathsf{T}} \int_{\Omega_j} \boldsymbol{\nabla}_{\mathrm{J}}\,\mathbf{N}_{\mathrm{J}}^{p\mathsf{T}} \left(\frac{-\,\mathbf{T}^{f}}{\gamma_f}\right) \boldsymbol{\nabla}_{\mathrm{J}}\,\mathbf{N}_{\mathrm{J}}^{p}\,\mathbb{T}_{L}^{p}\,\mathbf{p}_{e}\,d\Omega_j \\
&+\,\mathbb{T}_{L}^{p\mathsf{T}} \int_{\Omega_j} \mathbf{N}_{\mathrm{J}}^{p\mathsf{T}}\,\alpha\mathbf{m}^{\mathsf{T}}\,\mathbf{B}_{\mathrm{J}}\,\frac{\partial\overline{\mathbf{u}}}{\partial t}\,d\Omega_j \\
&+\,\mathbb{T}_{L}^{p\mathsf{T}} \int_{\Omega_j} \mathbf{N}_{\mathrm{J}}^{p\mathsf{T}}\,\frac{1}{M_J^f}\,\mathbf{N}_{\mathrm{J}}^{p}\,\mathbb{T}_{L}^{p}\frac{\partial\,\mathbf{p}^{f}{}_{e}}{\partial t}\,d\Omega_j = \\
&+\,\mathbb{T}_{L}^{p\mathsf{T}} \int_{\Omega_j} \boldsymbol{\nabla}_{\mathrm{J}}\,\mathbf{N}_{\mathrm{J}}^{p\mathsf{T}} \left(-\,\mathbf{T}^{f}\right) \boldsymbol{\nabla}_{\mathrm{J}}\,z\,d\Omega_j \\
&+\,\mathbb{T}_{L}^{p\mathsf{T}} \int_{\Gamma_q^f} \mathbf{N}_{\mathrm{J}}^{p\mathsf{T}}\,\tilde{Q}'^{f}\,d\Gamma
\end{aligned} \tag{2.92}$$

Because the nodal fluid pressure and the nodal displacements are constant over the integration domain, Eq. (2.92) may be rewritten as:

$$\mathbf{H}_{\mathrm{J}_L}^{p}\,\mathbf{p}^{f}{}_{e} + \mathbf{Q}_{\mathrm{J}}^{\ \mathsf{T}}\,\frac{\partial\,\mathbf{u}_e}{\partial t} + \mathbf{S}_{\mathrm{J}}\,\frac{\partial\,\mathbf{p}^{f}{}_{e}}{\partial t} = \mathbf{f}_{\mathrm{J}}^{p} \tag{2.93}$$

where, $\mathbf{H}_{\mathrm{J}_L}^{p}$ is the longitudinal diffusion matrix; $\mathbf{Q}_{\mathrm{J}}$ is the hydro-mechanical coupling matrix; $\mathbf{S}_{\mathrm{J}}$ is the storage matrix and $\mathbf{f}_{\mathrm{J}}^{p}$ the right-hand-side term, in this case including the external flow.

$$\mathbf{H}_{\mathrm{J}_L}^{p} = \mathbb{T}_{L}^{p\mathsf{T}} \left(\int_{\Omega_j} (\boldsymbol{\nabla}_{\mathrm{J}}\,\mathbf{N}_{\mathrm{J}}^{p})^{\mathsf{T}} \left(\frac{-\,\mathbf{T}^{f}}{\gamma_f}\right) \boldsymbol{\nabla}_{\mathrm{J}}\,\mathbf{N}_{\mathrm{J}}^{p}\,d\Omega_j\right) \mathbb{T}_{L}^{p} \tag{2.94}$$

$$\mathbf{Q}_{\mathrm{J}}^{\ \mathsf{T}} = \mathbb{T}_{L}^{p\mathsf{T}} \left(\int_{\Omega_j} \mathbf{N}_{\mathrm{J}}^{p\mathsf{T}}\,\alpha\mathbf{m}^{\mathsf{T}}\,\mathbf{R}\,\mathbf{N}_{\mathrm{J}}^{u}\,d\Omega_j\right) \mathbb{T}^{u} \tag{2.95}$$

$$\mathbf{S}_{\mathrm{J}} = \mathbb{T}_{L}^{p\mathsf{T}} \left(\int \mathbf{N}_{\mathrm{J}}^{p\mathsf{T}}\,\frac{1}{M_J^f}\,\mathbf{N}_{\mathrm{J}}^{p}\,d\Omega_j\right) \mathbb{T}_{L}^{p} \tag{2.96}$$

$$\begin{aligned}
\mathbf{f}_{\mathrm{J}}^{p} = \mathbb{T}_{L}^{p\mathsf{T}} &\int_{\Omega_j} \left(\boldsymbol{\nabla}_{\mathrm{J}}\,\mathbf{N}_{\mathrm{J}}^{p}\right)^{\mathsf{T}} \left(-\,\mathbf{T}^{f}\right) \boldsymbol{\nabla}_{\mathrm{J}}\,z\,d\Omega_j \\
+\,\mathbb{T}_{L}^{p\mathsf{T}} &\int_{\Gamma_q^f} \mathbf{N}_{\mathrm{J}}^{p\mathsf{T}}\,\tilde{Q}'^{f}\,d\Gamma
\end{aligned} \tag{2.97}$$

Transversal flow The transversal flow can be expressed in the following form by using the analogy with the mechanical problem and applying the PVW:

$$\delta\,\mathbf{p}_e{}^{\mathsf{T}}\;\mathbf{f}^p{}_e = \int_{\Omega_j} \delta\,\check{p}^f_{\mathrm{J}}\;q_t\,d\Omega_j \tag{2.98}$$

Substituting the transversal flow (q_t) and the drop pressure ($\check{p}^f_{\mathrm{J}}$) from Eqs. (2.47) and (2.76), respectively:

$$\delta\,\mathbf{p}_e{}^{\mathsf{T}}\;\mathbf{f}^p{}_e = \delta\,\mathbf{p}_e{}^{\mathsf{T}}\int_{\Omega_j} \mathbb{T}^{p\mathsf{T}}_T\,\mathbf{N}^{p\mathsf{T}}_{\mathrm{J}}\,\check{K}_t\mathbf{N}^p_{\mathrm{J}}\,\mathbb{T}^p_T\,\mathbf{p}_e\,d\Omega_j \tag{2.99}$$

And because the equation has to be satisfied for any virtual variation $\delta\,\mathbf{p}_e$, this leads to:

$$\mathbf{H}^p_{\mathrm{J}_T}\;\mathbf{p}^f{}_e = \mathbf{f}^p_{\mathrm{J}} \tag{2.100}$$

where $\mathbf{H}^p_{\mathrm{J}_T}$ is the transversal diffusion matrix and $\mathbf{f}^p_{\mathrm{J}}$ the right-hand-side term including the external flow.

$$\mathbf{H}^p_{\mathrm{J}_T} = \mathbb{T}^{p\mathsf{T}}_T\left(\int_{\Omega_j}\mathbf{N}^{p\mathsf{T}}_{\mathrm{J}}\,\check{K}_t\mathbf{N}^p_{\mathrm{J}}\,d\Omega_j\right)\mathbb{T}^p_T \tag{2.101}$$

Summary

Summary 4 – Hydraulic interface equation. Combining the longitudinal and transversal flow that share the same nodal variables $\mathbf{p}^f{}_e$ from Eqs. (2.93) and (2.100), the hydraulic interface equation is obtained:

$$\mathbf{H}_{\mathrm{J}}\;\mathbf{p}^f{}_e + \mathbf{Q}_{\mathrm{J}}{}^{\mathsf{T}}\frac{\partial\,\mathbf{u}_e}{\partial t} + \mathbf{S}_{\mathrm{J}}\frac{\partial\,\mathbf{p}^f{}_e}{\partial t} = \mathbf{f}^p_{\mathrm{J}} \tag{2.102}$$

where, $\mathbf{H}_{\mathrm{J}} = \mathbf{H}^p_{\mathrm{J}_L} + \mathbf{H}^p_{\mathrm{J}_T}$ is the combined diffusion matrix from Eqs. (2.94) and (2.101); $\mathbf{Q}_{\mathrm{J}}$ is the coupling matrix between the mechanical and hydraulic problems; $\mathbf{S}_{\mathrm{J}}$ is the

storage matrix and $\mathbf{f}_{\mathrm{J}}^{p}$ the is right-hand-side term including the external flow.

$$\begin{aligned}
\mathbf{H}_{\mathrm{J}} &= \mathbf{H}_{\mathrm{J}_L}^{p} + \mathbf{H}_{\mathrm{J}_T}^{p} = \\
&= \mathbb{T}_{L}^{p\mathsf{T}} \left(\int_{\Omega_j} \boldsymbol{\nabla}_{\mathrm{J}} \mathbf{N}_{\mathrm{J}}^{p\mathsf{T}} \left(\frac{T_l}{\gamma^f} \right) \boldsymbol{\nabla}_{\mathrm{J}} \mathbf{N}_{\mathrm{J}}^{p} \, d\Omega_j \right) \mathbb{T}_{L}^{p} \\
&+ \mathbb{T}_{T}^{p\mathsf{T}} \left(\int_{\Omega_j} \mathbf{N}_{\mathrm{J}}^{p\mathsf{T}} \check{K}_t \mathbf{N}_{\mathrm{J}}^{p} \, d\Omega_j \right) \mathbb{T}_{T}^{p} \qquad (2.103) \\
\mathbf{Q}_{\mathrm{J}}{}^{\mathsf{T}} &= \mathbb{T}_{L}^{p\mathsf{T}} \left(\int_{\Omega_j} \mathbf{N}_{\mathrm{J}}^{p\mathsf{T}} \, \alpha \mathbf{m}^{\mathsf{T}} \, \mathbf{R} \, \mathbf{N}_{\mathrm{J}}^{u} \, d\Omega_j \right) \mathbb{T}^{u} \qquad (2.104) \\
\mathbf{S}_{\mathrm{J}} &= \mathbb{T}_{L}^{p\mathsf{T}} \left(\int \mathbf{N}_{\mathrm{J}}^{p\mathsf{T}} \frac{1}{M_J^f} \mathbf{N}_{\mathrm{J}}^{p} \, d\Omega_j \right) \mathbb{T}_{L}^{p} \qquad (2.105) \\
\mathbf{f}_{\mathrm{J}}^{p} &= \mathbb{T}_{L}^{p\mathsf{T}} \int_{\Omega_j} \left(\boldsymbol{\nabla}_{\mathrm{J}} \mathbf{N}_{\mathrm{J}}^{p} \right)^{\mathsf{T}} \left(- \mathbf{T}^{f} \right) \boldsymbol{\nabla}_{\mathrm{J}} z \, d\Omega_j \\
&+ \mathbb{T}_{L}^{p\mathsf{T}} \int_{\Gamma_q^f} \mathbf{N}_{\mathrm{J}}^{p\mathsf{T}} \tilde{Q}'^{f} \, d\Gamma \qquad (2.106)
\end{aligned}$$

2.3 Time discretization

For the time discretization, the unknowns (x) are evaluated at time ($n+\theta$) and the time derivatives are replaced by increments ($\Delta x_{n+\theta}$), following a finite differences scheme. This approach assumes a linear variation of the unknown within a time increment. The parameter θ indicates the time at which the variable is evaluated with a range from 0 (explicit forward scheme) to 1 (implicit scheme).

$$\begin{aligned}
x_{n+\theta} &= x_n + \theta \Delta x_n \\
\dot{x}_n &= \frac{\Delta x_n}{\Delta t_{n+1}} \\
\Delta x_n &= x_{n+1} - x_n
\end{aligned} \qquad (2.107)$$

Because both continuum and interface formulations lead to similar expressions for the mechanical (Eqs. (2.19) and (2.68)) and hydraulic problem (Eqs. (2.33) and (2.102)), the subscript "C" and "J" will be dropped in further developments. Considering the mechanical equilibrium and the fluid mass balance, the time discretization shown in Eq. (2.107) is introduced. A manipulation of algebraic expressions is performed in order to obtain a symmetric fully coupled system. The mechanical equation is multiplied by -1 and the hydraulic one is multiplied by Δt_{n+1}.

$$\begin{pmatrix}
- \int_{\Omega} \mathbf{B}^{u\mathsf{T}} \, \boldsymbol{\sigma}'_{n+\theta} \, d\Omega + \mathbf{Q} \, \mathbf{p}_{\mathrm{e}}^{f}{}_{n+\theta} & = & - \mathbf{f}^{u}{}_{n+\theta} \\
\Delta t_{n+1} \, \mathbf{H}_{n+\theta} \, \mathbf{p}_{\mathrm{e}}^{f}{}_{n+\theta} + \mathbf{Q}^{\mathsf{T}} \, \Delta \, \mathbf{u}_{\mathrm{e}}{}_{n+1} + \mathbf{S}_{n+\theta} \Delta \, \mathbf{p}_{\mathrm{e}}^{f}{}_{n+1} & = & \Delta t_{n+1} \, \mathbf{f}^{p}{}_{n+\theta}
\end{pmatrix} \qquad (2.108)$$

Finally, because a system of equations in terms of the increments $\Delta \mathbf{u}^{e}{}_{n+1}$ and $\Delta \mathbf{p}^{f}{}_{n+1}$ are needed, Eq. (2.108) is converted into the following hydro-mechanical formulation after time discretization by using. Eq. (2.107):

Summary 5 – HM formulation after time discretization.

$$\begin{pmatrix} -\int_{\Omega} \mathbf{B}^{u\mathsf{T}} \boldsymbol{\sigma}'_{n+\theta}\, d\Omega + \theta\, \mathbf{Q}\, \Delta\, \mathbf{p}^{f}_{\mathrm{e}\, n+1} + \mathbf{Q}\, \mathbf{p}^{f}_{\mathrm{e}\, n} + \mathbf{f}^{u}{}_{n+\theta} & = & \mathbf{0} \\ \left(\mathbf{S}_{n+\theta} + \theta \Delta t_{n+1}\, \mathbf{H}_{n+\theta}\right) \Delta\, \mathbf{p}^{f}_{\mathrm{e}\, n+1} + \mathbf{Q}^{\mathsf{T}}\, \Delta\, \mathbf{u}_{\mathrm{e}\, n} + & & \\ + \Delta t_{n+1}\, \mathbf{H}_{n+\theta}\, \mathbf{p}^{f}_{\mathrm{e}\, n} - \Delta t_{n+1}\, \mathbf{f}^{p}{}_{n+\theta} & = & 0 \end{pmatrix} \tag{2.109}$$

2.4 Fully coupled resolution

Due to the non-linear nature of the fully H-M coupled system proposed in Eq. (2.109) an iterative procedure based on the Newton-Raphson method (NR) has been implemented. Zienkiewicz and Taylor (2000a,b), Potts and Zdravković (1999), Segura (2007), Smith and Giffiths (2004), Mira and Pastor (2002a,b) For that purpose, first the variables $\mathbf{u}_{\mathrm{e}}$ and $\mathbf{p}^{f}_{\mathrm{e}}$ are grouped into the single vector of nodal variables ($\boldsymbol{x}$), for both knowns $\boldsymbol{x}_n$ and unknowns $\Delta \boldsymbol{x}_{n+1}$. The system of equation to be solved is represents the residual of the coupled system and it will denoted as $\boldsymbol{\Psi}$.

$$\boldsymbol{\Psi}_{n+\theta}\left(\boldsymbol{x}_n, \Delta \boldsymbol{x}_{n+1}\right) = \begin{pmatrix} \boldsymbol{\Psi}^{u}_{n+\theta} \\ \boldsymbol{\Psi}^{p}_{n+\theta} \end{pmatrix} \tag{2.110}$$

$$\boldsymbol{x}_n = \begin{pmatrix} \mathbf{u}_{\mathrm{e}\, n} \\ \mathbf{p}^{f}_{\mathrm{e}\, n} \end{pmatrix} \tag{2.111}$$

$$\Delta \boldsymbol{x}_{n+1} = \begin{pmatrix} \Delta\, \mathbf{u}_{\mathrm{e}\, n+1} \\ \Delta\, \mathbf{p}^{f}_{\mathrm{e}\, n+1} \end{pmatrix} \tag{2.112}$$

For the Newtown-Raphson method, the first order Taylor expansion of the residual operator $\boldsymbol{\Psi}_{n+\theta}$ is calculated first:

$$\begin{aligned} \boldsymbol{\Psi}_{n+\theta}(\boldsymbol{x}_n, {}^{i+1}\Delta \boldsymbol{x}_{n+1}) \simeq\ & \boldsymbol{\Psi}_{n+\theta}(\boldsymbol{x}_n, {}^{i}\Delta \boldsymbol{x}_{n+1}) \\ & + \boldsymbol{J}_{n+\theta}\left(\boldsymbol{x}_n, {}^{i}\Delta \boldsymbol{x}_{n+1}\right)\ {}^{i}\delta \Delta \boldsymbol{x}_{n+1} \end{aligned} \tag{2.113}$$

Because the objective is to obtain a value of the unknowns such that the residual at the next iteration is zero, the condition $\boldsymbol{\Psi}_{n+\theta}\left(\boldsymbol{x}_n, {}^{i+1}\Delta \boldsymbol{x}_{n+1}\right) = \mathbf{0}$ is imposed, from

which the following linear system to be solved is obtained:

$$\boldsymbol{J}_{n+\theta}\left(\boldsymbol{x}_n, {}^{i}\Delta\boldsymbol{x}_{n+1}\right) {}^{i}\delta\Delta\boldsymbol{x}_{n+1} = -\boldsymbol{\Psi}_{n+\theta}(\boldsymbol{x}_n, {}^{i}\Delta\boldsymbol{x}_{n+1}) \tag{2.114}$$

Finally,

$$\boldsymbol{\Psi}_{n+\theta} = \begin{pmatrix} -\frac{1}{\theta}\int_\Omega \mathbf{B}^{u\mathsf{T}} \, {}^{i}\boldsymbol{\sigma}'_{n+\theta}\, d\Omega + \mathbf{Q}\,{}^{i}\Delta\,\mathbf{p}^{f}_{\mathrm{e}\,n} + \frac{1}{\theta}\,\mathbf{Q}\,\mathbf{p}^{f}_{\mathrm{e}\,n} + \frac{1}{\theta}\boldsymbol{f}^{u}_{n+\theta} \\ (\boldsymbol{S}_{n+\theta} + \theta\Delta t_{n+1}\boldsymbol{H}_{n+\theta})\;{}^{i}\Delta\,\mathbf{p}^{f}_{\mathrm{e}\,n} + \mathbf{Q}^{T}\,{}^{i}\Delta\,\mathbf{u}_{\mathrm{e}\,n} \\ +\Delta t_{n+1}\boldsymbol{H}_{n+\theta}\,\mathbf{p}^{f}_{\mathrm{e}\,n} - \Delta t_{n+1} f^{p}_{n+\theta} \end{pmatrix} = \mathbf{0} \tag{2.115}$$

The jacobian matrix is obtained after dropping the second order derivatives terms:

$$\begin{aligned} \boldsymbol{J}_{n+\theta}\left(\,\boldsymbol{x}_n, {}^{i}\Delta\boldsymbol{x}_{n+1}\right) &= \left.\frac{\partial\boldsymbol{\Psi}_{n+\theta}}{\partial\Delta\boldsymbol{x}}\right|_{\boldsymbol{x}_n, {}^{i}\Delta\boldsymbol{x}_{n+1}} = \\ &= \left.\begin{pmatrix} \frac{\partial\boldsymbol{\Psi}^{u}_{n+\theta}}{\partial\Delta\boldsymbol{u}} & \frac{\partial\boldsymbol{\Psi}^{u}_{n+\theta}}{\partial\Delta\boldsymbol{p}} \\ \frac{\partial\boldsymbol{\Psi}^{p}_{n+\theta}}{\partial\Delta\boldsymbol{u}} & \frac{\partial\boldsymbol{\Psi}^{p}_{n+\theta}}{\partial\Delta\boldsymbol{p}} \end{pmatrix}\right|_{\boldsymbol{x}_n, {}^{i}\Delta\boldsymbol{x}_{n+1}} \end{aligned} \tag{2.116}$$

The components of the Jacobian matrix in Eq. (2.116) can be calculated as follows:

- Partial derivative of the mechanical equation with respect to the displacement increment.

$$\frac{\partial\boldsymbol{\Psi}^{u}_{n+\theta}}{\partial\Delta\boldsymbol{u}} = \frac{\partial}{\partial\Delta\boldsymbol{u}}\left\{-\frac{1}{\theta}\int_\Omega \mathbf{B}^{u\mathsf{T}} \, {}^{i}\boldsymbol{\sigma}'_{n+\theta}\, d\Omega\right\} \tag{2.117}$$

  Assuming that the stresses can be decomposed in incremental form such as

$${}^{i}\boldsymbol{\sigma}'_{n+\theta} = \boldsymbol{\sigma}'_{n} + \theta\;{}^{i}\Delta\boldsymbol{\sigma}'_{n+1} \tag{2.118}$$

  and if $\boldsymbol{D}_{n+1}$ is the tangent stiffness matrix of the constitutive law, then

$${}^{i}\Delta\boldsymbol{\sigma}'_{n+1} = {}^{i}\boldsymbol{D}_{n+1}\,{}^{i}\Delta\boldsymbol{\epsilon}_{n+1} = {}^{i}\boldsymbol{D}_{n+1}\boldsymbol{B}_u\,{}^{i}\Delta\boldsymbol{u}_{n+1} \tag{2.119}$$

  with this, Eq. (2.117) can be transformed into

$$\frac{\partial\boldsymbol{\Psi}^{u}_{n+\theta}}{\partial\Delta\boldsymbol{u}} = \frac{\partial}{\partial\Delta\boldsymbol{u}}\left\{\left(-\int_\Omega \mathbf{B}^{u\mathsf{T}} \, {}^{i}\boldsymbol{D}_{n+1}\,\mathbf{B}^{u}\, d\Omega\right){}^{i}\Delta\boldsymbol{u}_{n+1}\right\} = -{}^{i}\boldsymbol{K}_{n+\theta} \tag{2.120}$$

  where

$${}^{i}\boldsymbol{K}_{n+\theta} = \int_\Omega \mathbf{B}^{u\mathsf{T}} \, {}^{i}\boldsymbol{D}_{n+1}\boldsymbol{B}_u\; d\Omega \tag{2.121}$$

- Partial derivative of the mechanical equation with respect to the fluid pressure

increment.

$$\frac{\partial \boldsymbol{\Psi}^{u}_{n+\theta}}{\partial \Delta \boldsymbol{p}} = \mathbf{Q} \tag{2.122}$$

- Partial derivative of the hydraulic equation with respect to the displacement increment.

$$\frac{\partial \boldsymbol{\Psi}^{p}_{n+\theta}}{\partial \Delta \boldsymbol{u}} = \Delta t_{n+1} \frac{\partial \boldsymbol{H}_{n+\theta}}{\partial \Delta \boldsymbol{u}} \;\; \mathbf{p}^{f}_{\mathrm{e}\, n+\theta} + \mathbf{Q}^{T} \tag{2.123}$$

  This derivative is only considered non-zero for interface elements, and in that case the equations may be further specified as follows:

$$\begin{aligned} \frac{\partial \boldsymbol{\Psi}^{p}_{n+\theta}}{\partial \Delta \boldsymbol{u}} &= \Delta t_{n+1} \frac{\partial}{\partial \Delta \boldsymbol{u}} \left(\mathbf{H}^{p}_{\mathrm{J}_L} \right) \;\; \mathbf{p}^{f}_{\mathrm{e}\, n+\theta} + \mathbf{Q}^{T} = \\ &= \frac{\Delta t_{n+1}}{\gamma_f} \left(\mathbb{T}^{p\mathsf{T}}_{L} \left(\int_{\Omega_j} \left(\boldsymbol{\nabla}_{\mathrm{J}}\, \mathbf{N}_{\mathrm{J}} \right)^{\mathsf{T}} \frac{\partial T_l}{\partial \Delta \boldsymbol{u}} \boldsymbol{\nabla}_{\mathrm{J}}\, \mathbf{N}_{\mathrm{J}}\, d\Omega_j \right) \mathbb{T}^{p}_{L} \right) \;\; \mathbf{p}^{f}_{\mathrm{e}\, n+\theta} \\ &+ \mathbf{Q}^{T} \end{aligned} \tag{2.124}$$

  where

$$\begin{aligned} \frac{\partial T_l}{\partial \Delta \boldsymbol{u}} &= \frac{\partial}{\partial \Delta \boldsymbol{u}} \left(\frac{\gamma_f}{12\mu} r_n^3 \right) = \frac{\partial}{\partial \Delta \boldsymbol{u}} \left(\frac{\gamma_f}{12\mu} \left(\boldsymbol{m}^{\mathsf{T}}\, \boldsymbol{B} \boldsymbol{u}^{e} \right)^3 \right) = \\ &= \theta \frac{\gamma_f}{4\mu} \left(\boldsymbol{m}^{\mathsf{T}}\, \boldsymbol{B} \boldsymbol{u}^{e}_{n+\theta} \right)^2 \boldsymbol{m}^{\mathsf{T}}\, \boldsymbol{B} \end{aligned} \tag{2.125}$$

- Partial derivative of the hydraulic equation with respect to the fluid pressure increment.

$$\frac{\partial \boldsymbol{\Psi}^{p}_{n+\theta}}{\partial \Delta \boldsymbol{p}} = \; {}^{i}\boldsymbol{S}_{n+\theta} + \theta \Delta t_{n+1} \; {}^{i}\boldsymbol{H}_{n+\theta} \tag{2.126}$$

2.5 Mechanical constitutive law for interfaces

The constitutive law used in this work is presented in this section.

One of the fundamental points of any mechanical modeling is the constitutive law, the relationship between deformations and stress. In the particular case of zero-thickness interface elements this relationship is established between the relative displacements ($\mathbf{r}$), which take a role analogous to strain in continuum elements, and the conjugate magnitude, the stress tractions on the interface plane ($\boldsymbol{\sigma}_{\text{J}}$). Both variables are evaluated on the mid-plane of the interface and using a local reference system

In this thesis two constitutive laws for interfaces are used, the basic elastic relationship and a fractured-based law. The elastic law is defined by means of two parameters, the normal (K_n) and tangential (K_t) stiffness coefficients. The stiffness matrix becomes:

$$\boldsymbol{\sigma}_{\text{J}} = \mathbf{D}_{\text{J}}^{el}\mathbf{r} \Rightarrow \begin{pmatrix} \sigma_n \\ \tau_1 \\ \tau_2 \end{pmatrix} = \begin{pmatrix} K_n & 0 & 0 \\ 0 & K_t & 0 \\ 0 & 0 & K_t \end{pmatrix} \begin{pmatrix} r_n \\ r_1 \\ r_2 \end{pmatrix} \tag{2.127}$$

The fractured-based constitutive equation is an elasto-plastic law in which the state variable is formulated in terms of energy (Carol et al., 1997, López, 1999, Caballero et al., 2008). The energy allows us to introduce concepts of fracture mechanics.

2.5.1 Constitutive law definition

The constitutive model used in this work was originally proposed by Carol and Prat (1990, 1995) and subsequently modified by Carol et al. (1997, 2001), López (1999) and Caballero et al. (2008). The model, based on the theory of elasto-plasticity, includes concepts of fracture mechanics and fracture energy parameters. The material behavior is formulated in terms of one normal and two tangential components of stress and relative displacements on the interface plane (Fig. 2.9).

$$\boldsymbol{\sigma}_{\text{J}} = \begin{pmatrix} \sigma & \tau_1 & \tau_2 \end{pmatrix} \tag{2.128}$$

$$\mathbf{r} = \begin{pmatrix} r_n & r_{l_1} & r_{l_2} \end{pmatrix} \tag{2.129}$$

2.5.2 Failure surface

Cracking begins when the stress on the interface plane reaches the condition F = 0, where F is the fracture or cracking surface defined in the space of normal and shear stresses. As in the classical theory of plasticity, the yield surface or plastic loading surface is defined in terms of the stress components, and some strength parameters:

$$F = F(\boldsymbol{\sigma}, \kappa) \tag{2.130}$$

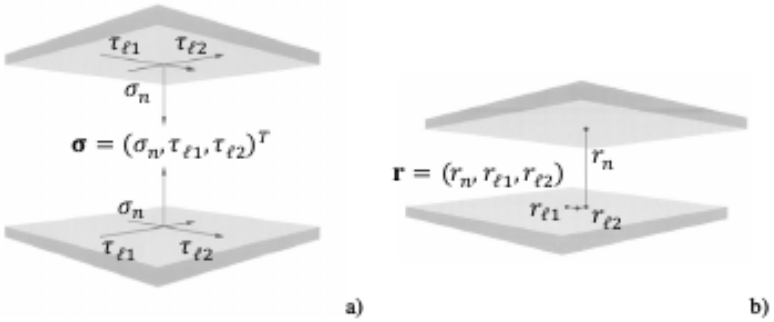

Figure 2.9: Stress and relative displacement variables for interface elements: a) shows a perspective view of the two sides of the fracture facing each other, and the stress traction components based on the local reference system., and b) shows a similar scheme with the components of the relative displacement vector ($\mathbf{r}$)

For this model, a three-parameter hyperbolic fracture surface Carol and Prat (1990) has been adopted:

$$F\left(\boldsymbol{\sigma}, \mathbf{p}\left(W^{cr}\right)\right) = |\tau|^2 - (c - \sigma \tan\phi)^2 + (c - \chi \tan\phi)^2 \tag{2.131}$$

Present work follows the suggestion proposed by Caballero (2005), in which the initial hyperbola was modified in order to avoid double solution inherent to hyperbola's equation. The In order to avoid numerical problems caused by the two solutions of the original hyperbolic expression above, a modified version (Caballero et al., 2008) given by Eq. (2.132) is adopted:

$$F\left(\boldsymbol{\sigma}, \mathbf{p}\left(W^{cr}\right)\right) = \tan\phi\,\sigma + \sqrt{\tau^2 + (c - \chi \tan\phi)^2} - c \tag{2.132}$$

where τ is the modulus of the shear stresses $\left(\tau = \boldsymbol{\tau} = \sqrt{\tau_1^2 + \tau_2^2}\right)$; σ is the normal stress; χ is the vertex of the hyperbola representing the tensile strength, and c and $\tan\phi$ are the cohesion and the tangent of friction angle parameters of the asymptote to the hyperbola (as shown in Fig. 2.10)

Once the crack has started opening, the fracture surface starts contracting and the stresses starts decreasing, so that the updated stress point always remains on the cracking surface. For a given initial fracture surface, represented by curve "0" in Fig. 2.10c, its final configuration will depend on the specific mode of fracture taking place. For pure tension (Mode I) a fully developed crack requires, as the only kinematic condition, that normal separation of the two sides of the interface be allowed (Fig. 2.10b). Because of the material's heterogeneity the cracking surface is rough and the final fracture surface is a hyperbola with vertex at the origin, given by curve "1" in Fig. 2.10c.

The other limit situation corresponds to cracking under shear and very high compression with no dilatancy, which is called "asymptotic mixed mode" or "Mode IIa"

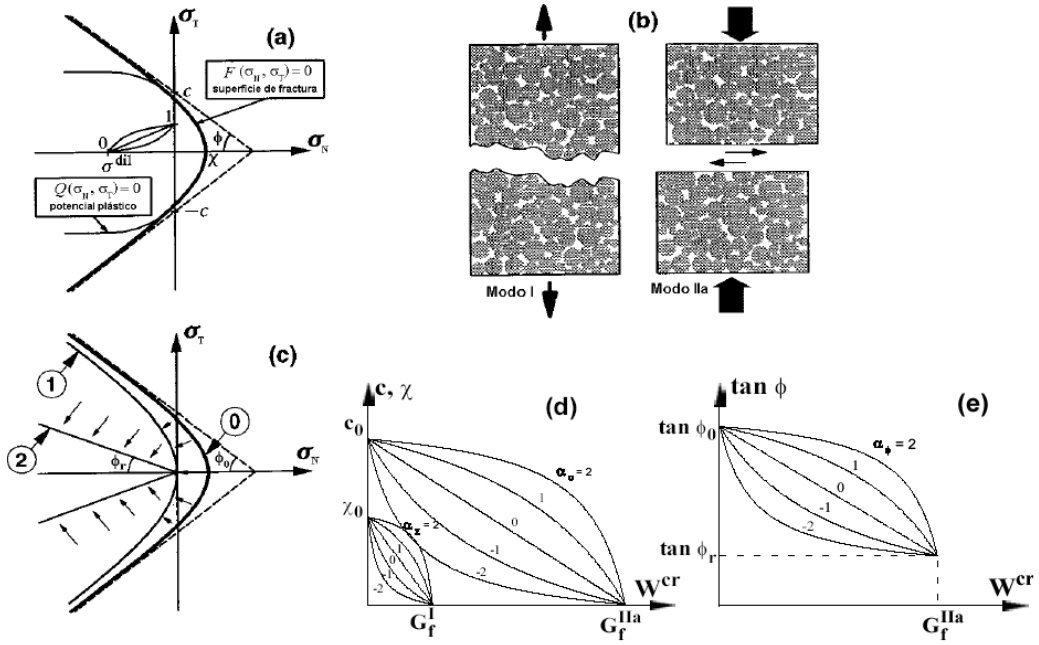

Figure 2.10: Constitutive model of the interface: (a) fracture surface and plastic potential; (b) basic modes of fracture; (c) development of the fracture surface; (d) and (e) softening laws (Carol and Prat, 1990).

(Carol and Prat, 1990). In this second fracture mode, slip occurs in the tangential direction with no normal dilatancy allowed (Fig. 2.10b), and the final fracture surface is defined by a pair of straight lines representing pure frictional behavior (curve "2" in Fig. 2.10c).

The parameters that control the two fracture modes described above are the classical fracture energy in Mode I, G_f^I (pure tension), and the additional Mode IIa fracture energy, G_f^{IIa}

2.5.3 Flow rule (dilatancy)

The definition of the flow rule in this model is similar to the flow rule in classical continuum plasticity. The plastic potential is called here fracture potential Q and it is formulated in terms of the relative displacements and stresses on the interface plane. The relative displacement vector, $\mathbf{r}$, contains an elastic part ($d\mathbf{r}^e$), and a non-recoverable part, the fracture ("crack") component ($d\mathbf{r}^{cr}$):

$$d\mathbf{r} = d\mathbf{r}^e + d\mathbf{r}^{cr} \tag{2.133}$$

The fracture component is given by:

$$d\mathbf{r}^{cr} = d\lambda \, \frac{\partial Q}{\partial \boldsymbol{\sigma}_J} = d\lambda \, \boldsymbol{m}_Q \tag{2.134}$$

where, $d\lambda$ is the fracture multiplier and $\boldsymbol{m}_Q$ is the gradient of Q.

The work of fracture is defined in the following incremental form: Then, if we are in tensile conditions ($\sigma_N \geq 0$):

$$dW^{cr} = \begin{cases} \boldsymbol{\sigma}_{\text{J}} \cdot d\mathbf{r}^{cr} = d\lambda \;\; \boldsymbol{\sigma}_{\text{J}} \cdot \boldsymbol{m}_Q & \text{if } \sigma \geq 0 \\ \left(|\tau| + \sigma \tan\phi\right) |d\mathbf{r}_l^{cr}| & \text{if } \sigma < 0 \end{cases} \tag{2.135}$$

where $d\mathbf{r}_l^{cr}$ represents the increment of relative crack opening displacements in the tangential direction and $d\mathbf{r}_l^{cr} = \sqrt{dr_{l_1}^{cr\,2} + dr_{l_2}^{cr\,2}}$.

The preceding equations imply that for pure tension all the dissipated work is used for crack formation. However, in compression, the work dissipated includes also some frictional work (heat) and therefore the work spent fracture processes (crack formation) is only the remaining part of the dissipated work (Eq. (2.135)).

In heterogeneous materials, fracture planes exhibit some roughness due to the tendency of the cracks to propagate along the weakest areas (particle contacts, particle-matrix boundary, etc.). In this context, shear slip will in general produce also dilatancy (crack opening) due to the "saw tooth effect". To determine the direction of dilatancy the methods of the theory of plasticity can be used, in which the direction of the fracture deformation vector at each point is perpendicular to the fracture (or cracking) potential (flow rule). The dilatancy angle can be interpreted as the angle between the gradient of Q and the shear axis. Therefore, a direction parallel to the shear axis indicates no dilatancy, while a direction parallel to the normal stress axis indicates a fracture opening without tangential displacement, such as in a pure tension case. The fracture potential can be defined depending on the fracture surface by a transformation matrix $\mathbf{A}$, so that this relationship can be expressed as follows:

$$\boldsymbol{m}_Q = \frac{\partial Q}{\partial\, \boldsymbol{\sigma}_{\text{J}}} = \mathbf{A}\;\mathbf{n} \tag{2.136}$$

$$\boldsymbol{n} = \frac{\partial F}{\partial\, \boldsymbol{\sigma}_{\text{J}}} = \begin{pmatrix} \frac{\partial F}{\partial \sigma} \\ \frac{\partial F}{\partial \tau_1} \\ \frac{\partial F}{\partial \tau_2} \end{pmatrix} = \begin{pmatrix} \tan\phi \\ \dfrac{\tau_1}{\sqrt{|\tau|^2 + (c + \chi\tan\phi)^2}} \\ \dfrac{\tau_2}{\sqrt{|\tau|^2 + (c + \chi\tan\phi)^2}} \end{pmatrix} \tag{2.137}$$

$$\mathbf{A} = \begin{pmatrix} f_c^{dil} f_\sigma^{dil} & 0 & 0 \\ 0 & 1 & 0 \\ 0 & 0 & 1 \end{pmatrix} \tag{2.138}$$

If $\mathbf{A}$ is equal to the identity tensor ($\mathbf{A} = \mathbf{I}$), then the flow rule is associated. In the present model, however, in order to obtain a more realistic dilatancy for shear-

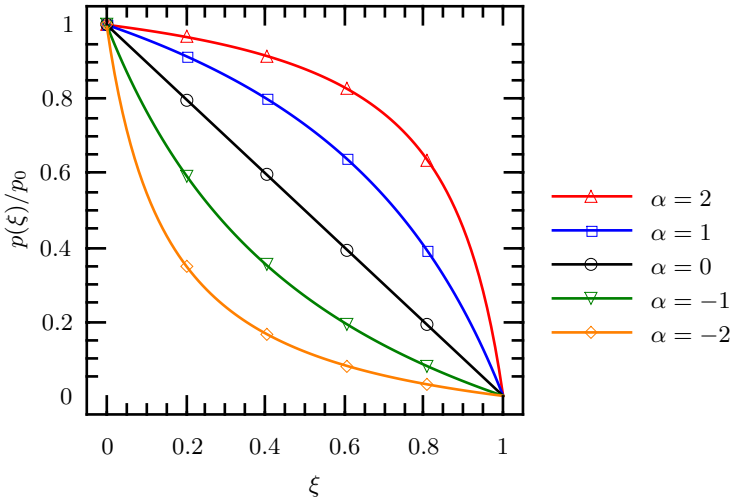

Figure 2.11: Evolution law

compression state, a non-associated formulation has been adopted.

In order to generalize the constitutive response, an intermediate linear scaling is used to define the evolution of some properties. For this purpose, a family of curves S (Eq. (2.139)) with different evolution according to a scaling factor is adopted (see Fig. 2.11 or Fig. 2.10d for its use in the evolution of χ and), whose expression is given as follows (Carol and Prat, 1990):

$$S(\xi, \alpha) = \left(\frac{e^{-\alpha}\xi}{1 + (e^{-\alpha} - 1)\xi} \right) \tag{2.139}$$

where ξ is the generic property to be scaled and α the scaling factor. Note that for $\alpha = 0$ the particular case $S(\xi, 0) = \xi$ is obtained.

Experimental results for quasi-brittle materials with dilatant behavior (Amadei et al., 1989), show that the higher the value of the compressive stress the smaller the effect of dilatancy. Furthermore, the variation of dilatancy decreases with the increase of joint degradation. For example, in a constant compression shear test, the dilatancy angle decreases with the increase of total tangential relative displacement (Pande et al., 1990).

The effects of dilatancy mentioned in the preceding paragraphs are taken into account by reducing the normal component of the $\mathbf{A}$ matrix using the f_c^{dil} and f_σ^{dil} factors:

(a) Reduction with stress level. To account for the effect of stress level, the dilatancy varies with the intensity of the compressive stress. This effect is canceled when the compression reaches a pre-defined value . The function decreases from 1 to

0, as shown in Fig. 2.10a.

$$f_{\sigma}^{dil} = 1 - S\left(\frac{\sigma}{\sigma_{dil}}, \alpha_{\sigma_{dil}}\right) \tag{2.140}$$

(b) Reduction with degradation. Dilatancy decreases as the fracture surface is degraded, and it is canceled when the surface F reaches its state of residual friction, (curve "2" in Fig. 2.10b):

$$f_{c}^{dil} = 1 - S\left(\frac{W^{cr}}{G_F^{IIa}}, \alpha_{c_{dil}}\right) \tag{2.141}$$

2.5.4 Evolution law

The evolution of the fracture surface follows a reduction of the hyperbola's parameters, Eq. (2.131): tensile strength (χ), cohesion (c) and friction angle ($\tan\phi$) as a function of the work of dissipation (W^{cr}) during crack formation, Eq. (2.135).

The evolution of the three parameters is described in the following sections.

Tensile strength (χ)

The tensile strength (χ) decreases from its initial value χ_0 as W^{cr} increases, becoming zero when $W^{cr} = G_I^F$. The scaling function $S(\xi_\chi, \alpha_\chi)$ is applied considering $\xi_\chi = W^{cr}/G_I^F$ and $\alpha = \alpha_\chi$ (Fig. 2.10d). The evolution is given by the expression:

$$\chi = \begin{cases} \chi_0 \left(1 - S\left(\xi_\chi, \alpha_\chi\right)\right) & \text{if } W^{cr} < G_I^F \\ 0 & \text{if } W^{cr} \geq G_I^F \end{cases} \tag{2.142}$$

Cohesion (c)

The reduction of the variable c can be defined through χ, $\tan\phi$ and a new parameter "a" representing the horizontal distance between the vertex of the hyperbola and its asymptotes (shown in Fig. 2.12), and is given by:

$$c = (\chi + a)\tan\phi \tag{2.143}$$

Assuming that this new parameter a changes from its initial value a 0 (obtained from Eq. (2.143) with the initial values of χ, c and $\tan\phi$) becoming zero when $W^{cr} = G_{IIa}^F$, the parameters of the scaling function $S(\xi_a, \alpha_a)$ are given by $\xi_a = W^{cr}/G_{IIa}^F$ and $\alpha = \alpha_a$.

The reduction of c can be expressed then as follows:

$$c = \begin{cases} c_0 \left[1 - S(\xi_a, \alpha_a) - \dfrac{\chi_0}{c_0}\tan\phi\left(S\left(\xi_\chi, \alpha_\chi\right) - S\left(\xi_a, \alpha_a\right)\right)\right] & \text{if } W^{cr} < G_{IIa}^F \\ 0 & \text{if } W^{cr} \geq G_{IIa}^F \end{cases} \tag{2.144}$$

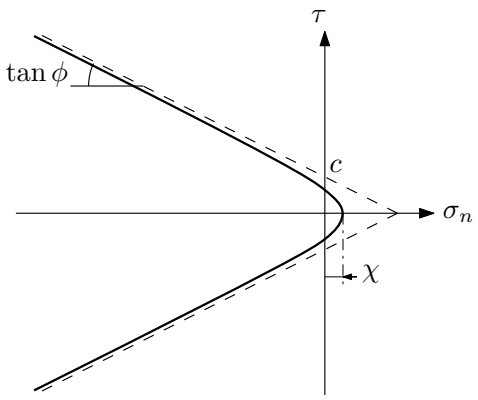

Figure 2.12: Failure surface parameters

This equation allows splitting the evolution of the fracture surface, F, into a translation plus a contraction, which in the context of the theory of plasticity can be interpreted as a combined kinematic plus isotropic softening (López, 1999).

2.5.4.a Friction angle ($\tan\phi$)

The variation of the internal friction angle is given by:

$$\tan\phi = \begin{cases} \tan\phi_0 - (\tan\phi_0 - \tan\phi_{res})\, S(\xi_\phi, \alpha_\phi) & \text{if } W^{cr} < G^F_{IIa} \\ \tan\phi_{res} & \text{if } W^{cr} \geq G^F_{IIa} \end{cases} \tag{2.145}$$

where ϕ_0 is the initial friction angle and ϕ_{res} is the residual friction angle. Thus $\tan\phi$ varies from its initial value to its residual value when the final fracture surface (Fig. 2.10e) is reached.

2.5.5 Constitutive integration

Integration is performed using an implicit integration algorithm (backward Euler) with substepping (López, 1999), wherein the system is solved taking into account the stresses as well as the history variables and the plastic multiplier (Caballero, 2005), based on the work of Pérez-Foguet et al. (2001).

A more detailed and extensive description of the interface constitutive law can be found in the literature (Carol et al., 1997, 2001, López, 1999, López et al., 2008). Details of the numerical implementation of the model can be found in the work of Caballero (Caballero et al., 2008).

In order to reduce the number of iterations of the nonlinear procedure, the stresses $\begin{pmatrix}\sigma & \tau_1 & \tau_2\end{pmatrix}$ and the fracture energy (W^{cr}) in addition to the plastic multiplier (λ) are considered as independent variables in the iterative process. Therefore the vector of

unknowns is $\boldsymbol{x}$:

$$\boldsymbol{x} = \begin{pmatrix} \boldsymbol{\sigma}_{\mathrm{J}} \\ W^{cr} \\ \lambda \end{pmatrix} \tag{2.146}$$

The equations are solved using the *backward-Euler* scheme (Ortiz and Popov, 1985). For a given sub-increment k of m the system of equations to be solved is defined by the residual $\boldsymbol{f}$:

$$\mathbf{f}\left({}^{k}\mathbf{x}\right) = \mathbf{0} \Rightarrow \begin{cases} {}^{n+\left(\frac{k}{m}\right)}\boldsymbol{\sigma} + \lambda \mathbf{E} : \mathbf{m}\left({}^{n+\left(\frac{k}{m}\right)}\boldsymbol{\sigma}, {}^{n+\left(\frac{k}{m}\right)}W^{cr}\right) - {}^{n+\left(k-\frac{1}{m}\right)}\boldsymbol{\sigma} - \mathbf{E} : \Delta\boldsymbol{\epsilon} = \mathbf{0} \\ {}^{n+\left(\frac{k}{m}\right)}W^{cr} - \lambda h\left({}^{n+\left(\frac{k}{m}\right)}\boldsymbol{\sigma}, {}^{n+\left(\frac{k}{m}\right)}W^{cr}\right) - {}^{n+\left(k-\frac{1}{m}\right)}W^{cr} = 0 \\ F\left({}^{n+\left(\frac{k}{m}\right)}\boldsymbol{\sigma}, \mathbf{p}\left({}^{n+\left(\frac{k}{m}\right)}W^{cr}\right)\right) = 0 \end{cases} \tag{2.147}$$

where $\mathbf{x} = (\boldsymbol{\sigma},\ W^{cr},\ \lambda)$, is the solution; λ, el plastic multiplier; $\mathbf{m} = \frac{\partial Q}{\partial \boldsymbol{\sigma}}$, la regla de flujo; y $h = \frac{\partial W^{cr}}{\partial \lambda}$, the plastic modulus.

The nonlinear system presented in Eq. (2.147) is solved with a Newton-Raphson procedure which requires the evaluation of the Jacobian matrix $\mathbf{J}$ expressed below:

$${}^{n+\left(\frac{k}{m}\right)}\mathbf{J} = \frac{d\mathbf{f}}{d\left({}^{n+\left(\frac{k}{m}\right)}\boldsymbol{\sigma}, {}^{n+\left(\frac{k}{m}\right)}W^{cr}, \lambda_k\right)} = \begin{pmatrix} \left(\mathbf{I} + \lambda\mathbf{E} : \frac{\partial \mathbf{m}}{\partial \boldsymbol{\sigma}}\right) & \lambda\mathbf{E} : \frac{\partial \mathbf{m}}{\partial W^{cr}} & \mathbf{E} : \mathbf{m} \\ -\lambda\frac{\partial h}{\partial \boldsymbol{\sigma}} & \left(1 - \lambda\frac{\partial h}{\partial W^{cr}}\right) & -h \\ \mathbf{n}^T & \xi & 0 \end{pmatrix}_{t={}^{n+\left(\frac{k}{m}\right)}t} \tag{2.148}$$

where $\mathbf{m}$ is the normal to the yield surface and ξ is the derivative of the yield surface with respect to the energy:

$$\xi = \frac{\partial F}{\partial W^{cr}} = \frac{\partial F}{\partial \chi}\frac{\partial \chi}{\partial W^{cr}} + \frac{\partial F}{\partial c}\frac{\partial c}{\partial W^{cr}} + \frac{\partial F}{\partial \tan\phi}\frac{\partial \tan\phi}{\partial W^{cr}} \tag{2.149}$$

Then, assuming that α_k is the displacement factor associated to each increment

$$\Delta\boldsymbol{\epsilon} = \sum_{k=1}^{m} \Delta\boldsymbol{\epsilon}_k = \sum_{k=1}^{m} \alpha_k \Delta\boldsymbol{\epsilon} \tag{2.150}$$

A recursive expression for calculating the consistent tangent operator is defined as:

$$\frac{d^{n+1}\boldsymbol{\sigma}}{d\Delta\epsilon} = \mathbf{P}^T \left[\sum_{i=1}^{m}\left(\alpha_i \prod_{j=m}^{i} {}^{\mathrm{n}+\left(\frac{\mathrm{j}}{\mathrm{m}}\right)}\mathbf{A}\right)\right]\mathbf{P}\mathbf{E} \tag{2.151}$$

where

$$\mathbf{P}^T = \begin{pmatrix} \mathbf{I}_{l\times l} & 0 & 0 \end{pmatrix} \tag{2.152}$$

$$\mathbf{A} = {}^{n+\left(\frac{k}{m}\right)}\mathbf{J}^{-1}\begin{pmatrix} \mathbf{I}_{l\times l} & \mathbf{0} \\ \mathbf{0} & 0 \end{pmatrix} \tag{2.153}$$

Where l is the number of stress components ($l = 2$ for 2D and $l = 3$ for 3D analysis)

Chapter 3

Parallelization

Contents

The increase in the complexity of numerical simulations has gone hand in hand with the improvement of computational capacities. Limits of CPU miniaturization, heat dissipation problems, and excessive power consumption have pushed current hardware enhancements to multiprocessor architectures. Current operating systems allow the execution of sequential codes in multiprocessor environments, however the maximum capacity of the computer calculation can only be achieved with parallel codes. Parallel programming models can be divided into two basic types according to the computer architecture:

Shared memory Shared memory machines are commonly single motherboard computers with multiple CPUs sharing the same memory bank. The programming model focuses on the parallelization of the instructions, in which *OpenMP* being the most used programming interface. The main advantages of this type of programming are the simplicity of implementation and the optimal use of shared resources. In contrast, the main limitation of this technique is that it is restricted to shared memory environments, normally involving a low number of processors, typically up to 8 or 16.

Distributed memory Parallel programming with distributed memory involves carrying out simultaneous calculations in all type of different processors or computers. Therefore computers with shared memory may be also a particular case of distributed memory group. Through network communications, this type of programming allows interaction between all processors or computers. The most

commonly used communication interface is the *MPI* (*Message Passing Interface*). The main advantage of this programming model is the scalability and portability in all types of machines. The main disadvantage is the increase of the complexity in the implementation, since it is necessary to control explicitly the communications between the different processors.

In order to facilitate parallel programming, some libraries have become popular in recent years. They collect basic functionalities for the manipulation of matrices and vectors in parallel environments. Among them some of the most popular are PETSc (Balay et al., 2016), Trilinos (Heroux et al., 2005) and Hips (Jérémie Gaidamour and Pascal Hénon and Yousef Saad, 2010).

This chapter is dedicated to describe the most important points for the parallelization of the research code DRAC (Prat et al., 1993). Among the available options, due to code robustness and simplicity of implementation, the PETSc library has been chosen for the purpose. The description is divided into two parts: the first part includes the main aspects of the numerical implementation, and the second part presents a performance analysis to determine the degree of parallelization, including a scalability test and a memory assessment study.

3.1 Parallel implementation

The PETSc library (Portable, Extensible Toolkit for Scientific Computation) is "*a suite of data structures and routines for the scalable (parallel) solution of scientific applications modeled by partial differential equations, providing the building blocks for the implementation of large-scale application codes on parallel (and serial) computers*" (Balay et al., 2016)

The philosophy of the PETSc library is not to provide a parallel solver *per se*, but rather to provide a parallel environment, in which the data is distributed over processors and the solution is performed at the same time across the network. Due to the change of paradigm (sequential-parallel), a gradual modification of the code structure has been achieved in order to adapt it to a multiprocessors environment. The transformation was carried out progressively in four implementation stages:

1. Solver parallelization. The first stage of the implementation was focused on the main matrix system solution operations. This implementation has consisted of generating the system matrix ($\mathbf{K}$) with the original sequential procedure and then distributing it through PETSc objects for a parallel solution procedure. As a first attempt, the distribution of system matrix to the processors is achieved by assigning a similar number of rows per processor.

2. Domain decomposition (phase I): direct matrix assembly. The objective of this implementation stage has been the assembly of the matrices and vectors of the

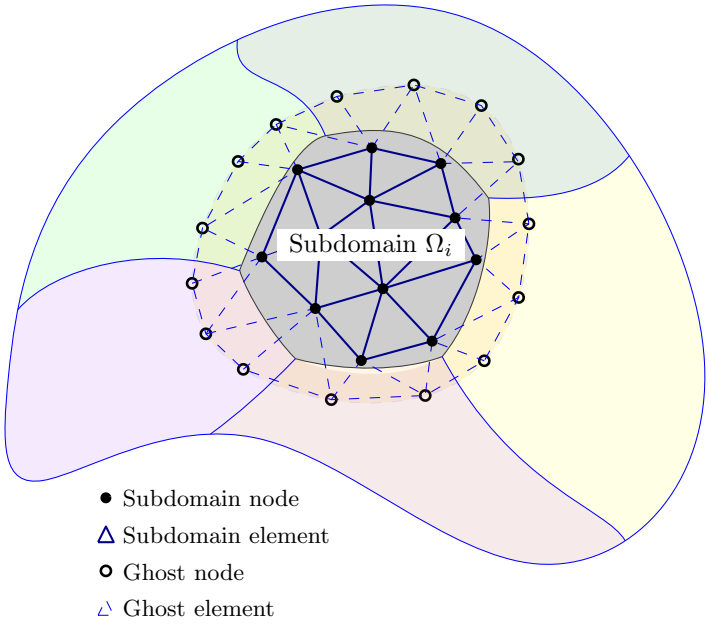

Figure 3.1: Nodal decomposition scheme selected in the parallel implementation of DRAC .

system directly in to a PETSc object. This modification has involved subdivision of the model into subdomains. In this phase the subdomains have been generated from a pre-established distribution of degrees of freedom according to the stage numeration.

3. Domain decomposition (phase II): mesh partitioning. The domain decomposition implementation has been completed with the inclusion of optimal methods of partitioning domains for general meshes.

4. Parallel input/output. Modification of the reading and writing routines in order to take advantage of the peculiarities of the HDF5 files and their adaptation to the format of visualization of *Paraview* (Ayachit, 2015)

3.1.1 Domain decomposition implementation

In order to optimize the parallel capabilities of PETSc, the structure of DRAC has been modified with a direct distribution of the mesh nodes to each processor or rank. This has allowed that each rank only performs integrations of elements with nodes belonging to this rank. Additionally, this scheme introduces the use of ghost nodes and ghost elements (see Fig. 3.1). The ghost nodes are nodes that belong to another rank, but they are needed for rank element integrations. The ghost elements are elements in which at least one node belongs to another rank and, therefore, are border elements. In the implementation developed it has been chosen to duplicate ghost element integrations, rather than calculation only once but then requiring communications between ranks with shared elements.

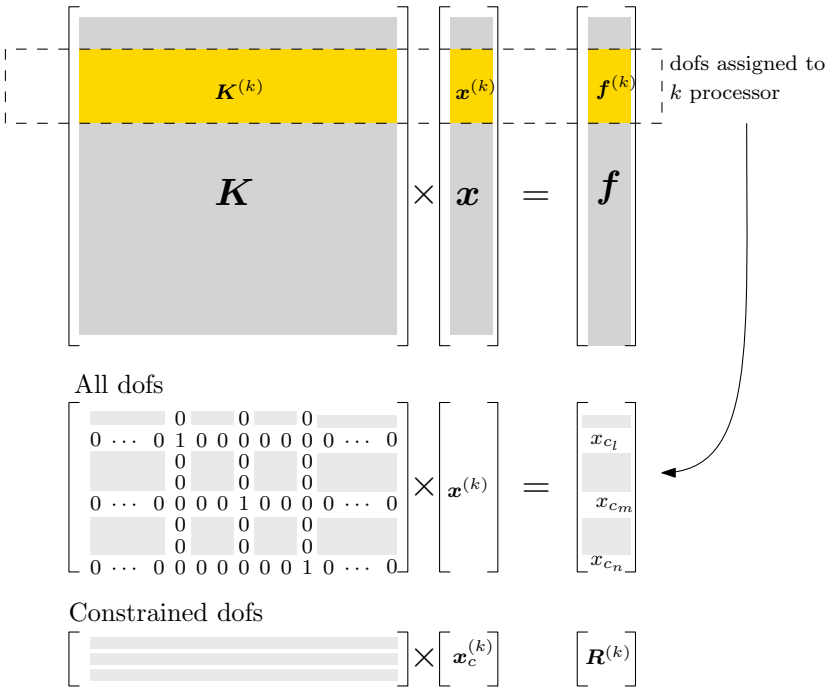

Figure 3.2: New matrix structure in the parallel implementation of DRAC

Each rank stores only its own data and the ghost nodes data in order to calculate stresses of the border elements (ghost elements).

3.1.1.a Matrix assembly

An essential part of the implementation is the global matrix structure using distributed PETSc objects, and the direct assembly of the element matrices into those PETSc objects. In the current implementation the global stiffness matrix and force vectors are PETSc objects divided in horizontal stripes that correspond to each processor. In this global matrix, rows and columns that correspond to prescribed dofs are set to zero (except diagonal terms to 1) and the corresponding values needed for calculation of reactions are stored locally in separate reaction calculation matrices for each processor (see Fig. 3.2).

3.1.1.b Mesh partitioning

For an optimal implementation of the domain decomposition technique, an efficient division of the model into subdomains is required. In the literature there are several methods and computational libraries devoted to this task, among them *METIS*, *ParMETIS* and Scotch. In this case, the *METIS* library was selected due to robustness and implementation convenience.

The implementation of this library uses the *k-way* method proposed by Karypis and Kumar (1998), method which as implemented, can be used in two ways:

- Using DRAC first as pre-processor in order to generate a file with partition infor-

mation. This option will run the code in sequential mode and it will call *METIS* and will generate an h5 file with the domain decomposition information. This needs to be done only the first time a given problem and number of processors is chosen. Then, for any subsequent calculations of the same problem and same n. or processors, the code can be run in parallel (w/o calling *METIS*), because the subdomain information, when needed, will be read from the said file.

- Using DRAC directly in parallel with mode "run". This option will call *METIS* from the "master" processor, and the subdomain information will be distributed to each processor during the same run.

3.1.2 Data storage: HDF5 file system

As the number of processors increases, an essential aspect for the efficiency of parallel calculations becomes the reading and writing ("input/ouput") scheme adopted. There are different types of scheme: independent, collective, only master etc. (Prabhat and Koziol, 2014, Thakur et al., 1999, Hadri, 2011). This implementation uses a collective scheme of reading/writing through the hdf5 library la Cruz et al. (2011). "*HDF5 is a completely new Hierarchical Data Format product consisting of a data format specification and a supporting library implementation*" (The HDF Group, 2017)

The adaptation of this type of storage in DRAC includes (see 3.3):

Write operations In order to minimize the calls to HDF5 writing subroutine, the writings to H5 files are done in a single block for each (vector or matrix) variable and subdomain. The variables are sorted according to the rank numbering. Then an additional record containing the reference numbering is added, in order to eventually being able to identify the record. Since the partition is made by nodes, all nodes belong to some rank. This does not occur in a similar way with the elements, in particular the frontier elements ("ghost") are repeated in all the subdomains that share them. To avoid writing duplicities, these "ghost" elements are assigned arbitrarily to the rank that owns the first node of the element.

Read operations The variables are read by a loop that makes block calls according to a pre-set buffer size, until all the registers are read. For each buffer reading, the reference identifier (ID Ref) is read and if that value belongs to the subdomain, the value is stored in a local subdomain vector. Similar to the case of write operations, the motivation of this procedure is to minimize the number of HDF5 accesses. The size of the buffer depends on the computer architecture, for the architectures tested the optimum value was 1 MB.

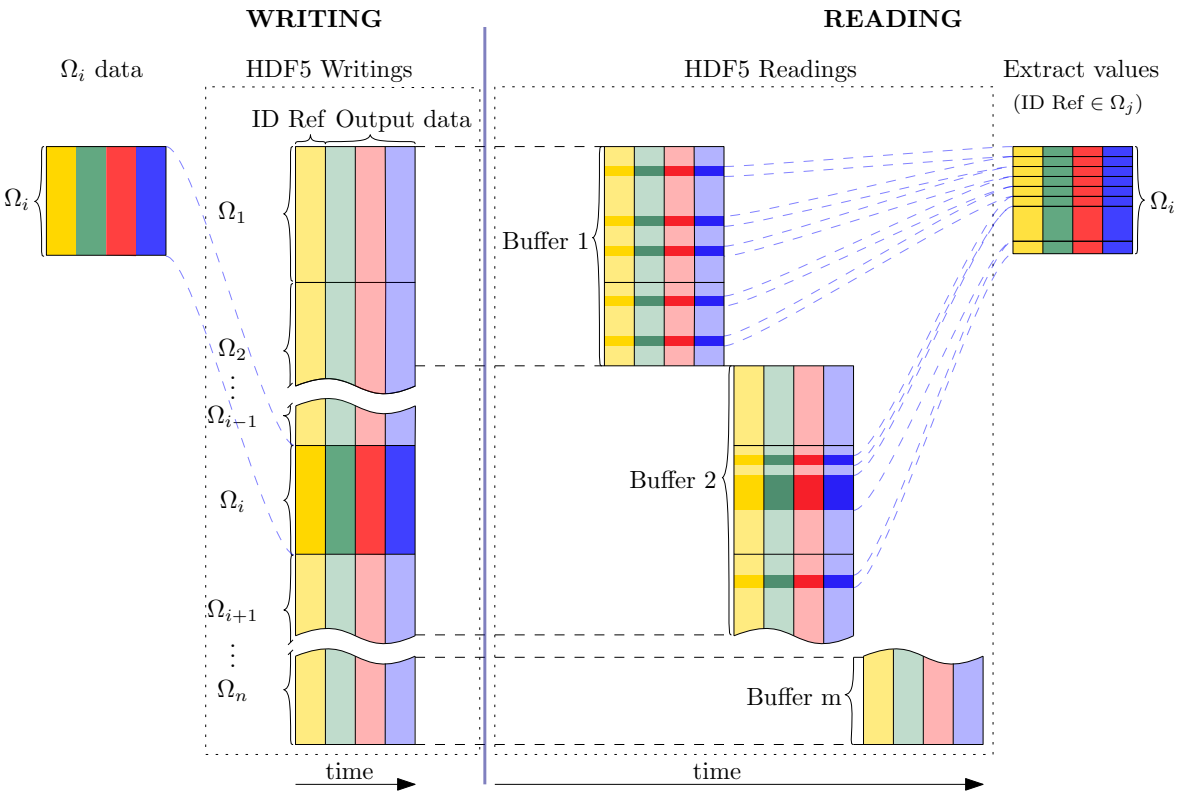

Figure 3.3: Schematic diagram of reading and writing data files in HDF5 format used in the DRAC implementation.

3.1.3 Code workflow

The DRAC code is structured in four main loops:

1. **Stage loop** This loop goes through different geometries of the problem (associated with construction and excavation events).
2. **Step loop** The second nesting level is related to different loading states and prescribed boundary conditions.
3. **Increment loop** In a non-linear case, the third loop is used in order subdivide (or exceptionally reduce/increase) the load step.
4. **Iteration loop** The last loop is related to iterative solver technique.

The main flow diagram of the code is presented below, focusing on the modifications for the parallel work. As a general comment, thanks to domain decomposition technique, the loops on elements and nodes of the subroutines are made over rank range (Ω_i). All PETSc objects are distributed over all processors, while FORTRAN data contains data from a given subdomain, with some exceptions pending of revision. The writing process is performed as described in Section 3.1.2, except for standard ASCII files which is only done by the processor with rank zero (the master processor). In the rest of the calculations, all processors perform all FORTRAN operations of the code, including the calculation of the reactions and stresses.

Additionally, an algorithm with the workflow is shown in Algorithm 1.

1. First the general data (*GenIn*) is read by all processors.

2. After entering the first loop (loop stage), data related to the stage is read in *StagIng* by all processors. If a partition file exists, some heavy data related to the geometry will be avoided at this point.

3. Then, if partition file exists, each processor reads its associated geometry. This task is performed in parallel by means of collective read of HDF5 file (h5). On the contrary, if partition file does not exist, the master process reads full model and performs a mesh partitioning (preferably with *METIS*). Once the task is concluded, master processor distributes the results, assigning each domain to a single processor.

   An important point is the sparse structure of stiffness matrix which is obtained from element connectivityy. In particular, the number of non-zero components per each row is computed, in order to assign the memory through a pre-allocation routine from PETSc. This operation is essential for a good computational efficiency. The pre-allocation of the PETSc sub-matrix is performed in parallel, where each processor only allocates values in the rows associated with it.

4. Initialization of the variables: the nodal and element (*ElmIni*) variables are initialized or read from a restart file (h5).

5. The simulation enters the loop of steps. Loads and prescribed conditions are read in *LoadIn*.

6. After loop of increments, the evaluation of stiffness matrix (${}^0\mathbb{K}_{n+\theta}$), the internal forces (${}^0\boldsymbol{F}^{int}_{n+\theta}$) and the external forces ($\boldsymbol{F}^{ext}_{n}$) is performed in *ElmIncr0*. These values are used in *Residual0* to evaluate the residual vector (${}^0\boldsymbol{F}^{int}_{n+\theta}$). The updated values are then shared in parallel by a PETSc assembly subroutine. This operation requires the necessary communications to indicate to all the processors the situation of each value.

7. After the evaluation of the residual and the stiffness matrix, the Newton-Raphson procedure is started.

8. Solve the system. Solution of the system involves the following steps:

   a) First, the force terms from prescribed degrees are extracted from the RHS vector

   b) Second, the iterative solver is run in parallel.

   c) Finally, the solution (displacement vector) is transformed into a sequential vector. Using PETSc functions the distributed array is copied into a sequential FORTRAN vector, which contains the “own” degrees of freedom plus

the ghost values. The reactions are computed using the reaction calculation matrix available for each processor (Fig. 3.2).

9. Update of the stiffness matrix (*ElmIncr1*) and residual (*Residual1*), back to step 8 until the convergence is reached.

10. Finally, once the convergence is achieved, the results are stored in *NodalOut* and *ElmOut*.

Algorithm 1 shows a the structure of the code, with special emphasis on the parallel communications.

3.2 Scalability analysis

In order to evaluate the performance of the parallel implementation, a cubic mesh with different level of discretization (from 500k to 32M elements) have been tested. The geometric and material description as well as the the main results obtained are given in the following subsections.

3.2.1 Model

A performance study of the current parallel implementation has been run on a simple cube of 1 m of side (Fig. 3.4) with elastic properties ($E = 5000$ MPa and $\nu = 0.0$). The model was discretized with a regular mesh of linear hexahedral elements of different sizes, getting models from 500 000 elements up to a largest model of approximately 32 million elements (see Table 3.1).

The boundary conditions selected were in terms of nodal restrictions, one node of the bottom (corner $x = y = z = 0$) was prescribed in x, y and z; a second corner of the base ($x = 1, y = z = 0$) was prescribed in y and z; and the rest of the base with $z = 0$. The top boundary, a vertical negative displacement was imposed in order to compress the sample, while x and z displacements were left free on the top face.

The models are subdivided into as many subdomains as the processors can be used in each simulation, so each processor will have to handle the nodes of only one subdomain.

The simulations have been performed using the GMRES solver and BJACOBI preconditioner. All test were performed in a large parallel computer system with access to up to 1024 processors organized in nodes of 16 processors each. The main features of the system are:

- Standard node:
  - 2×CPU E5-2670 SandyBridge-EP 2.6GHz cache 20MB and 8 cores
  - 8×4GB DDR3-1600 DIMMs (32 GB/node)

Algorithm 1 Parallel code structure of DRAC

Table 3.1: Cube test element/node sizes.

Case	Nº divisions ($n_x \times n_y \times n_z$)	Nº elements	Nº nodes
500k	79×79×79	493 039	512 000
1M	100×100×100	1 000 000	1 030 301
2M	126×126×126	2 000 376	2 048 383
4M	159×159×159	4 019 679	4 096 000
8M	200×200×200	8 000 000	8 120 601
16M	250×253×253	16 002 250	16 193 516
32M	316×318×319	32 055 672	32 359 360

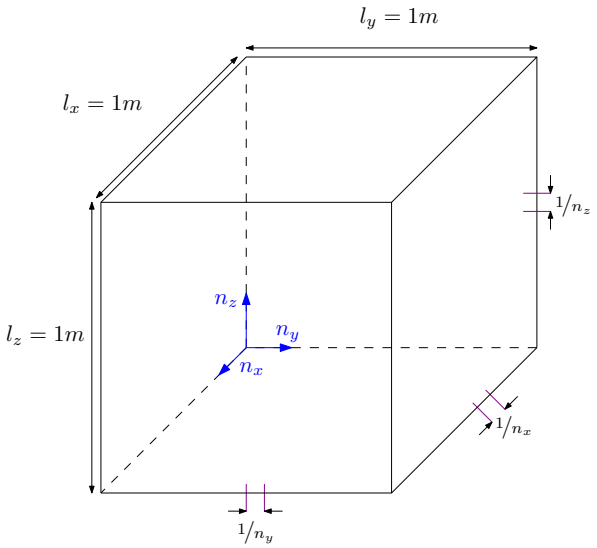

Figure 3.4: Geometry of cubical test

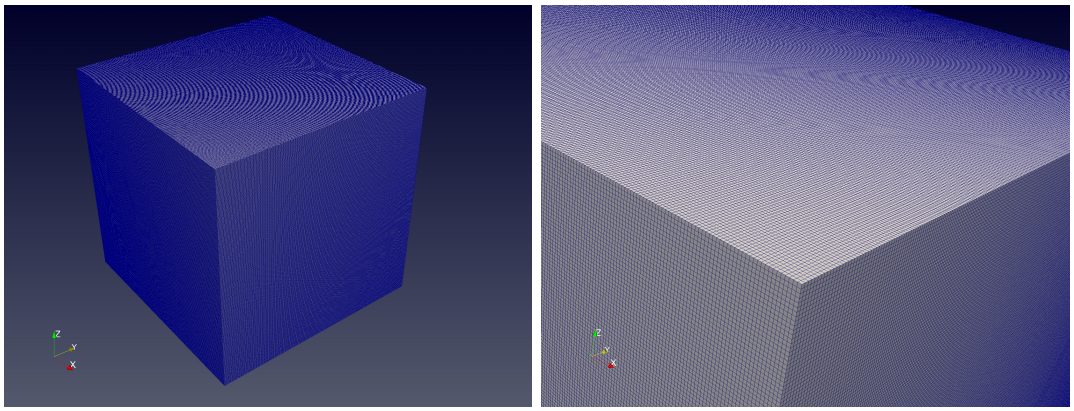

(a) Complete view (b) Detail view

Figure 3.5: Mesh discretization of 32M case; left) full model; right) detail of corner

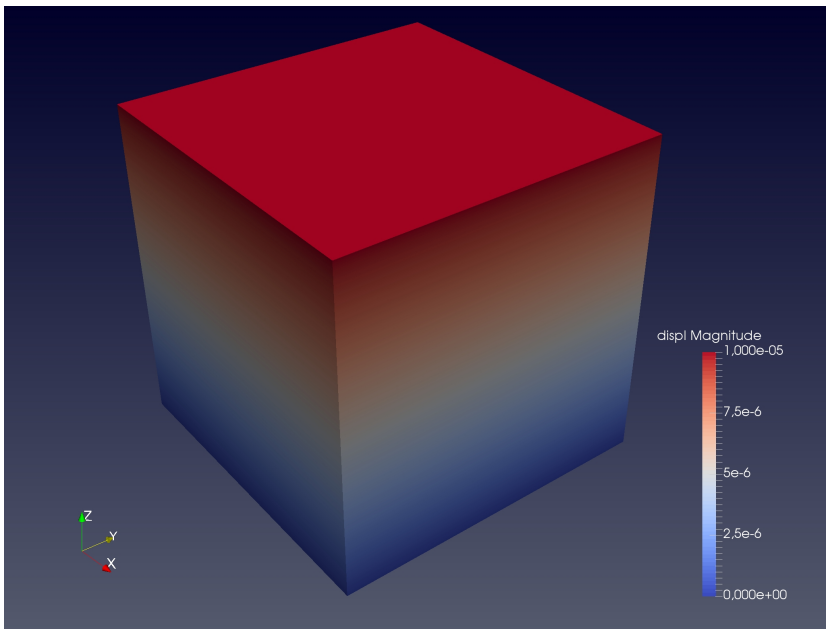

Figure 3.6: Magnitude (module) of displacement for 32M case.

- GPFS storage system
- Operation system: Linux – SuSe distribution 11 SP 3

The results returned by all discretizations show the same correct physical solution. As an example, Fig. 3.6 shows the magnitude of displacements for case 32M.

The analysis has focused, first, on the determination of the degree of scalability. For this purpose, the evolution of the computation time is analyzed with respect to the number of processors used in each computation. Second, the study has also focused on the use of RAM memory as the number of processors is increased.

During preliminary evaluation tests, the main bottle neck points have been eliminated in order to avoid excessive losses of performance and RAM increase with the number of processors. The results shown in the following subsections correspond to the most recent stage of development including all improvements.

Finally, some additional implementation work has been necessary for the output to the *ParaView* post-processor. The use of this visualization tool has been necessary in order to be able to represent large meshes in order to overcome limitations of the alternative post-processor which is normally used for smaller meshes. The main changes have been focused on the adaptation of the "restart" files of the code to be compatible with the formats required by *Paraview*, and therefore be used also as output files.

Summarizing, the work described in this section 2.1 includes the following parts:

1. Debugging of parallel implementation
2. Parallelization performance analysis (scalability)
3. Memory requirements analysis

4. The use of new graphical tools (*Paraview*)

Some of the items in the list are described in the following subsections.

3.2.2 Parallelization performance analysis

The number of processors used for analysis depend on the problem size. Small cases have been computed using up to 256 processors, and the largest up to 1024. Calculations have been limited to 1024 because of administrative access limitations to the system.

3.2.2.a Total time

The results presented in Figs. 3.7 and 3.8 show comparisons on the basis of the total time of the simulation. This time includes the following steps:

1. Input and pre-solver operations:
   a) Read model data from files
   b) Generation of global vectors.
   c) Element integration for getting stiffness matrix and right-hand side vector.
2. Solver calculation
3. Post-solver operations:
   a) Integration of elements in order to obtain stress evaluation
   b) Output writing to files

Figure 3.7 shows the evolution of the total time used against the number of processors for the different meshes analyzed. Note that the optimal number of processors (identified as the minimum point of the curves), varies with the size of the problem. This fact can be related to the increase of the relative importance of time spent in communications with respect to the calculation time of each subdomain.

Figure 3.8 shows the speed-up curves for the cases of 0.5M, 1M and 2M. These curves give an idea of the degree of parallelization achieved. The horizontal axis shows the number of processors used for the calculation and the vertical axis represents the time of calculation normalized with respect to the time of the same calculation spent using a single processor. Therefore an "x" value on the vertical axis would mean that the calculation is "x" times faster than the same calculation performed with a single processor (sequential calculation).

Due to peculiarities of the PETSc library (related to the stiffness matrix assembly), the reference time that would correspond to a sequential calculation is in fact obtained from a calculation with two processors, which is then multiplied by two (this time is

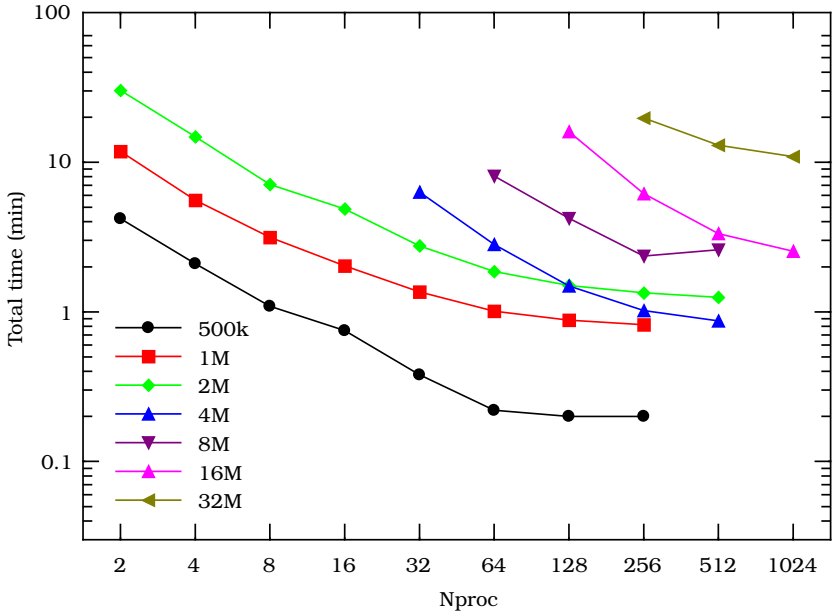

Figure 3.7: Evolution of required time with respect to the number of processors (nproc).

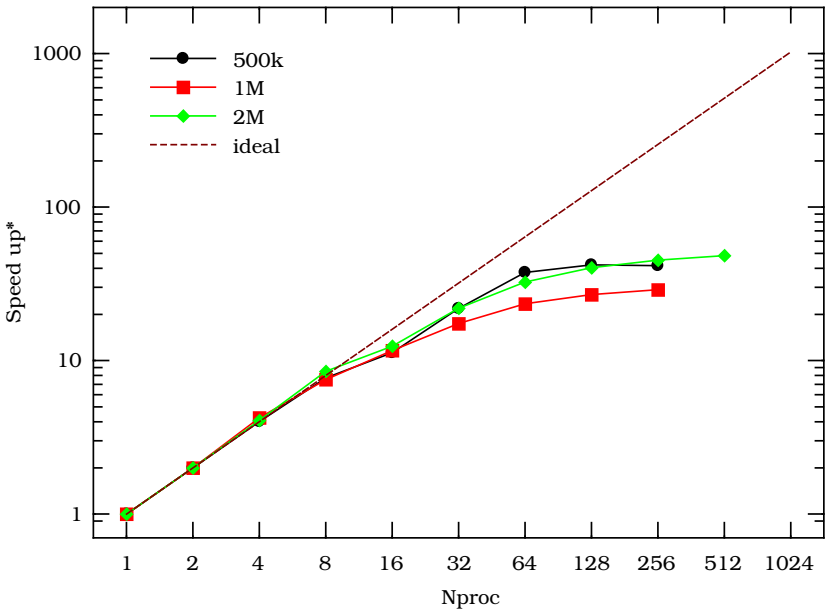

Figure 3.8: Speed up* observed for different discretizations.

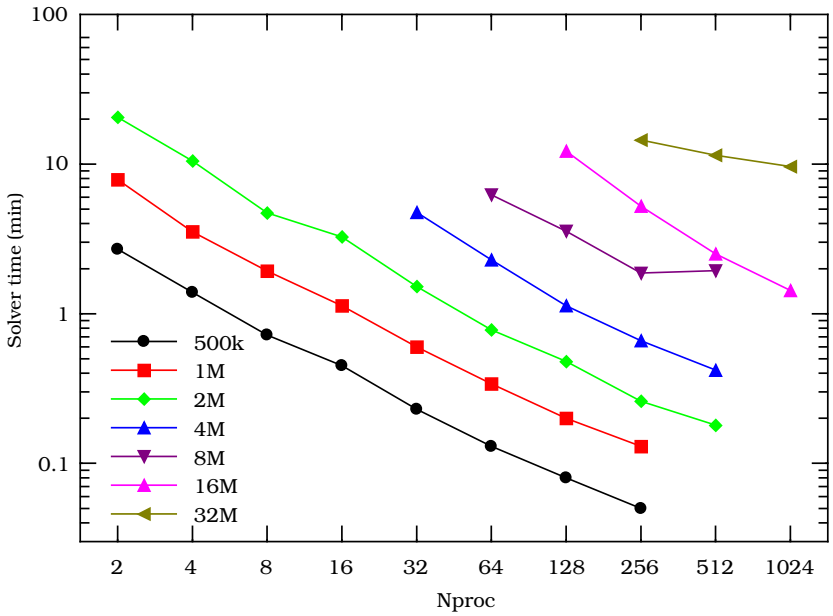

Figure 3.9: Solver wall clock time evolution.

considered to be two times faster than what would correspond to one simple processor). Symbol (*) in the figure heading refers to that way to calculate the reference time.

In Fig. 3.8, the results depicted are all compared with respect to the dashed straight line, which represents the theoretical optimum of perfect scalability. Some comments to the curves in the figure are given below:

1. Between 4 and 8 processors (Depending on the size) super-convergence is observed, the simulation scales better than the ideal ratio.

2. Beyond 64 processors there seems to be a loss of scalability (curves more and more distant from the theoretical straight dotted line), and some eventually exhibit a maximum depending on the size of the model. The smaller model shows a maximum near 128 processors. In general, the deviation from ideal scalability can be related to the greater relative weight of the communications between processors as compared to the internal calculations of each processor.

3.2.2.b Solver time

In order to isolate the part of the code responsible for the loss of scalability, the previous figures have been repeated considering only the solver time (instead the total time of the calculation). Both, Figs. 3.9 and 3.10, exhibit a better performance in terms of scalability.

The results presented in this section seem to suggest that the part of the code still to be improved must be related to the loading of the model, and to the post-processing of the solution.

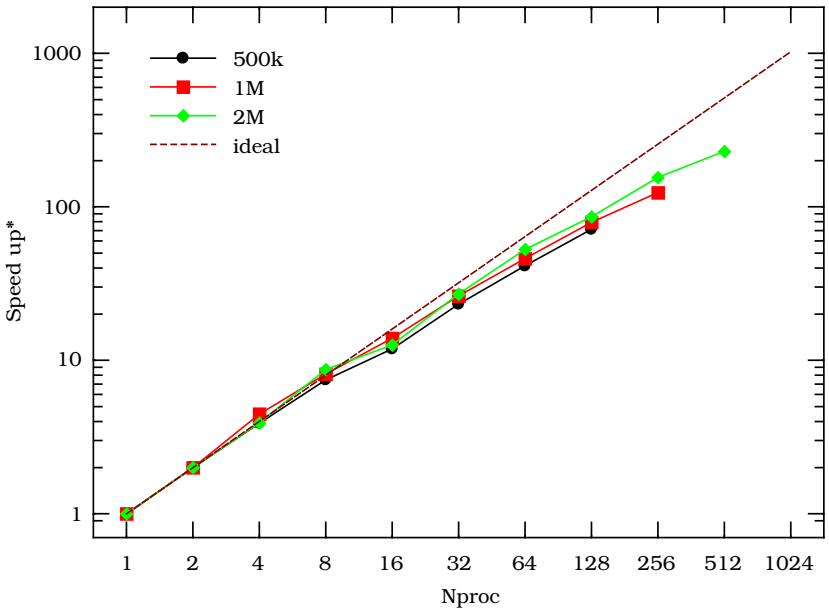

Figure 3.10: Speed-up computed over solver wall clock time.

3.2.3 Memory requirements analysis

In HPC calculations, a relevant aspect to study is the use of RAM memory. The analysis has focused on the study of memory used by a typical processor in a node (a node usually has a number of processors sharing a common amount of RAM, in this case 16 processors sharing 32 GB of RAM). Although as a first approach the maximum memory available to a processor may be taken as the maximum memory in the node divided by the number of processors, in practice one single processor in the node can use all the RAM available, that is, it can use more than its share of RAM, provided the other processors use less than their share. Therefore, a more detailed analysis of the usage of RAM by each processor in the node can help us to optimize the code performance.

Looking in the literature, one can find several types of memory usage indicators. In this case the so called vmHWM has been selected, which seems to be the closest to the intuitive RAM concept. After analyzing the results, it would also seem that this indicator is the closest to the information provided by the system logs.

Similarly to the previous section, the results presented here correspond to the latest simulations after a few rounds of code improvement. It should be mentioned that the initial excessive use of memory has motivated the modification of the code in two directions:

1. Replacement of all possible global vectors/matrices (ie. with dimensions equal to total number of mesh nodes, elements, etc.) by vectors/matrices with size equal to the number of nodes, elements, etc. of a single subdomain.

2. Use of temporary disk storage. This option consists storing a certain types of variables, in this case those associated with elements history, in the local disk of each node rather than in RAM memory. This option is referred to as using "SCRATCH" discs. In principle, this option could decrease the performance of the calculation due to the mechanical access to the disc (instead of faster RAM access). However, in the cases analyzed computation time has not changed significantly by using this option.

Figures 3.11 and 3.12 show the minimum and maximum memory values associated to any single processor, for the various meshes of increasing size. The differences in RAM usage between processors is due to one single processor acting as the node master, while all the rest are doing similar tasks. This also explains why (although not shown in the figures), the mean value or RAM usage per processor turns out close to the minimum value. Therefore, the results represented in the figure can be interpreted as the average RAM per processor as well. Note that although the cases with 1 M and 2 M nodes exceed the limit of 2 GB per processor, since the real limitation is the total amount of 32 GB per node, the calculations have been completed successfully.

The results show the expected general trend of a reduction of the RAM used with the number of processors. This reduction is linear with few processors and for small cases. With the increase of processors and/or increase of the size of the problem, RAM reduction becomes lower (less effective) than what would correspond to the linear relation. The reason for this change may be due to two simultaneous effects:

1. When the size of the model is increased, some few vectors with global indices, which still remain in the code, increase their relative weight.

2. When the number of subdomains is increased, we increase the size of boundary region between subdomains. In the way the code has been developed, the operations on the elements on the boundary regions are duplicated in neighboring subdomains. This a counterpart to the higher benefit of reducing inter-processor communications (that would be required if one element is only computed in one processor, but the results are needed in the processor handling the neighbor element); however the counterpart is a slight increase of computation time with excessive mesh partitioning.

Figure 3.12 shows the maximum memory per cpu. The results with few processors coincide with the previous figure, but as the number of processors is increased, a minimum is observed. This behavior, aside from including the effects described above, also reflects the effect of HDF5 storage. The use of this library implies that one of the processors, usually the master ("0"), has a memory overhead because it contains the addresses of the file structure. This effect that in small cases is negligible, in large cases

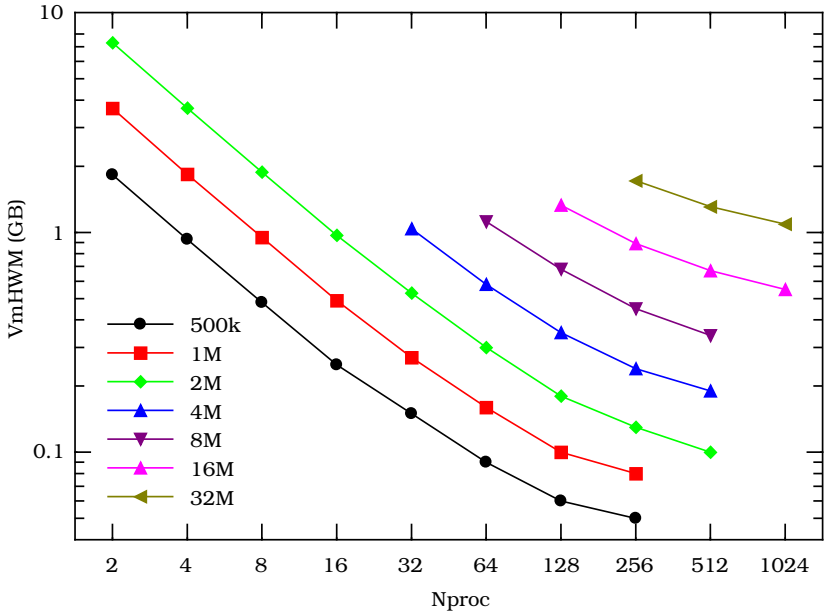

Figure 3.11: Minimum required RAM for a single processor of a node.

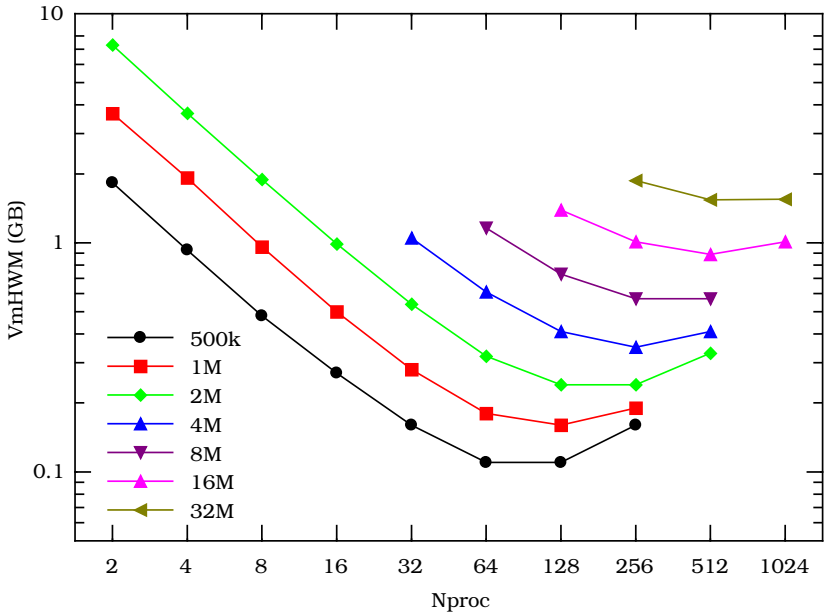

Figure 3.12: Maximum required RAM for a single processor of a node.

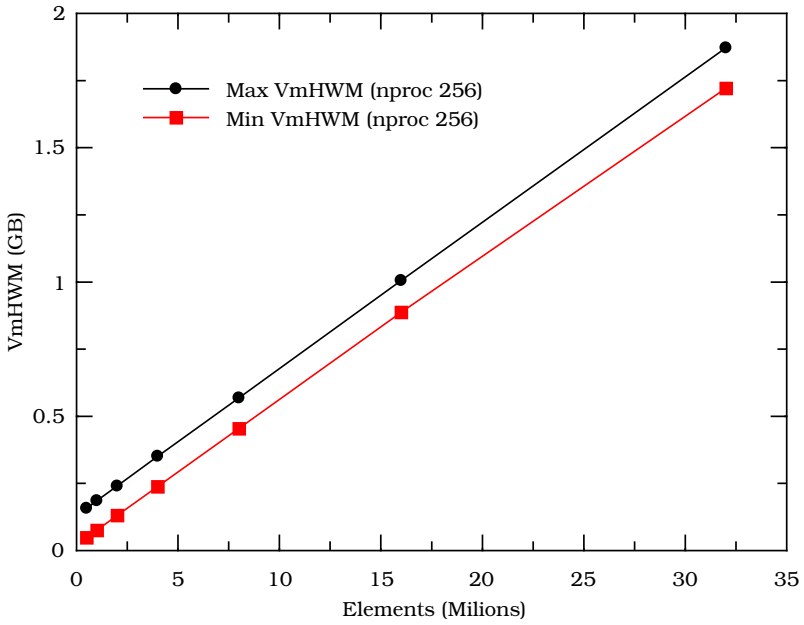

Figure 3.13: Maximum and minimum required RAM for a single processor of a node, using 256 processors.

may mean a non-negligible additional overload of RAM usage for the master processor in the node.

Figure 3.13 reconfirms this interpretation, which shows how, for the same number of processors, the difference between maximum and minimum remains constant regardless of the size of the problem.

Finally, Fig. 3.14 shows the evolution over time of the maximum memory peak per processor for the case of 32M elements with 512 processors. This figure allows us to determine the points of maximum interest in order to reduce the use of RAM. In this case the *StagIn* subroutine ("Stage Input") is identified as the main source of memory increase. This subroutine will be the main focus in future optimization studies.

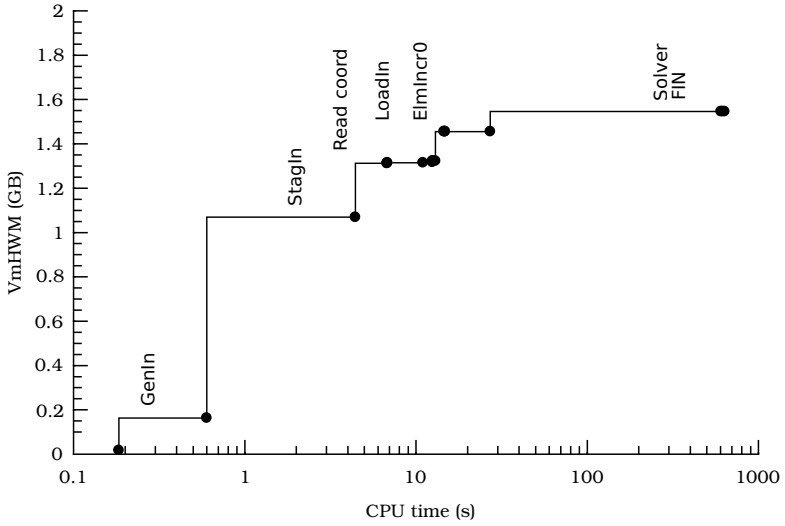

Figure 3.14: Max memory for 32M case using 512 proc.

Chapter 4

Hydraulic fracture

Contents

This chapter describes the application of zero-thickness interface elements to hydraulic fracturing modeling. First, a brief state of the art about hydraulic fracture propagation is presented, with special interest in analytical formulations. That is followed by a section devoted to the analysis of a single fracture in both 2D and 3D. In this section, the numerical simulations are compared with analytical formulations in order to understand and validate the aspects of the numerical approach method. The last two sections deal with multi-stage analysis. In particular, the third section shows some results regarding 2D analysis with multiple propagation paths, and the fourth section includes the application to a real case of multi-stage analysis in 3D.

4.1 State of the art of hydraulic fracture modeling

Hydraulic fracturing is a phenomenon, that can occur naturally, i.e. dike intrusion into a geologic formation, or it can be artificially induced (hydro-fracking), consisting in pumping a viscous fluid at a certain rate and pressure into the geological formation to induce fractures.

In the context of Petroleum Engineering, hydraulic fracturing was first used as a stimulation technique in the *Hugoton* field in 1947. Since then, the number of applications of this procedure has increased. The following list describes the main usages of hydraulic fracturing (Fjaer et al., 2008).

- **Well stimulation**. Hydraulic fracturing is used to enhance the production of hydrocarbons especially in low permeability reservoirs (i.e. tight gas sands; gas shale). Induced fractures increase the reservoir conductivity and consequently this method increases oil recovery. An important aspect of hydraulic fracture is the treatment after pumping stops. Naturally, the fractures would tend to close when fluid pressure decreases. Therefore, additional treatments must be applied to avoid fracture closing and to ensure certain conductivity after fracturing. At present, two solutions are the most widely used: acid attack over the fracture surface to avoid a perfect closing; and the introduction of solid elements (proppant) inside fractures to avoid closure and allow preferential flow paths.
- ***Frac and pack***. This application is a particular case of hydraulic fracture (HF) well stimulation for poorly consolidated or highly permeable formations. A preventive HF treatment is performed near the well to eliminate damage from the formation and replace it with proppant.
- **Fracturing during water injection**. Thermally induced fracturing is used to overcome plugging problems around the injector. Due to the different thermal gradient between the formation and the injected fluid a shrinkage phenomenon occurs. As a result, fractures are developed into the formation and they help to extend the life of the well.
- **Waste storage**. The re-injection of contaminated drill cuttings from hydraulic fracturing is used to reduce the environmental impact of hydrocarbons production.
- **Well design and stress determination**. For well design the *leak-off* test is used to determine the maximum well pressure allowed, that will be necessary to assess the mud weight window for stable drilling. The stress determination will be provided by the *extended leak-off* test that may lead to an estimate of the minimum confining stress.

Although hydraulic fracture is a technique that has been extensively used for over 60 years, its modeling is still posing serious challenges. It is a complex non-linear

mathematical problem that involves the mechanical interaction of the propagating fracture with the fluid dynamics of the injected fluid. Moreover, thermal effects can add additional difficulties to the model.

At the beginning of hydraulic fracturing, no model was used to estimate or control the method. Then, due to the increase of reservoir's complexity, analytical formulation or numerical tools started to be used. The first models were those so-called planar 2D models, in particular the Perkins Kern Nordgren (PKN) and Geertsma De-Klerk Khristianovich (GDK) models. Afterwards the *Pseudo3D* models appeared which could be understood as an extension of the previous ones. Almost at the same time appeared the planar3D model which has been widely used in industrial companies up to the present. Nowadays, a new family of methods has arisen based in a real 3D analysis carried out with the FEM o DEM analysis.

The importance of numerical models in fracture jobs could be summarized in the following points (Mack and Warpinski, 2000).

- **Economic optimization**. Providing an estimate of the cost to produce a fracture job. HF can be especially expensive in deep formations, so it becomes crucial to determine its utility and efficiency in order to correctly plan the treatment.
- Design of a **pump schedule**. Determining the fluid pressure necessary to fracture the rock.
- Simulation of **fracture geometry** and **proppant placement**. Once the pump schedule is fixed, models can give an estimate of fracture geometry and proppant concentration, which will be fundamental to maintain drainage after shut-in.
- Fracture **treatment evaluation**. Back analysis of the fracture treatment in order to adjust the model and optimize it for forthcoming jobs.

4.1.1 Physics of hydraulic fracture

Hydraulic fracturing is a complex phenomenon due to the strong coupling between several mechanisms. The main disciplines involved in that problem are: fluid mechanics, solid mechanics, fracture mechanics and thermal mechanics.

- **Fluid mechanics** or hydrodynamics are required to describe the viscous fluid flow that is pumped into the fracture. This flow pushes the wall of the fracture and it allows the fracture to propagate. An important concept related to fluid mechanics is the evaluation of leak-off from the fracture into the formation.
- **Fracture mechanics**. Due to the stress concentration (tensile) at the tip of the fracture, the rock resistance is exceeded and the fracture propagates. Crack opening is controlled by fracture mechanics, which relates the crack extension to the amount of work (energy) dissipated in the process.

- **Solid mechanics**. Due to fracture propagation, the solid that is surrounding the crack is also deformed and stresses are modified.
- **Thermal mechanics**. The fluid pumped into the reservoir may have a different temperature from the formation temperature. This difference can affect the mechanical problem related to dilatations or contractions. Moreover it can affect the fluid problem by modifying some of the fluid properties (dynamic viscosity).

4.1.2 Fracture initiation (vertical well)

Fracture occurs perpendicular to the direction of the minor principal stress. Therefore, except for tectonized or shallow reservoirs, the fractures usually grow vertically because the overburden stress is larger than the horizontal stress. Moreover, fracture growth tends to be from the bottom to the top.

Due to the complexity and variability of the problem, the following working assumptions are made in this section: a) the hydraulic fracture develops in a vertical borehole; b) in general, the initial stress distribution is supposed to follow the normal consolidation state ($\sigma_v > \sigma_H > \sigma_h$); c) the material is considered homogeneous; and d) fracture occurs in mode I (tensile failure).

For hydraulic fracturing, a large net pressure is necessary for driving the fluid out from the fracture into the porous medium. The net pressure is defined as the difference between the fluid pressure in the fracture (P_{frac}) and the far-field pore pressure (P_0).

In the typical evolution of bottom-hole pressure during hydraulic fracture job, four phases may be identified (see Fig. 4.1).

1. The first phase corresponds to the active injection process; in this step, a fracture is created by continuous fluid injection at a pressure higher than $P_w^{frac} = \sigma_\theta + T_0 - P_0$, where σ_θ is the *in situ* stress, T_0 the tensile strength and P_0 the far-field pore pressure.
   Generalizing to anisotropic horizontal stress conditions, the expression of P_w^{frac} becomes Eq. (4.1), which is considered an upper limit due to the implicit consideration of impermeable wall (also known as fast pressurization) (Detournay and Carbonell, 1997, Fjaer et al., 2008).

$$P_w^{frac} = 3\sigma_h - \sigma_H - P_0 + T_0 \tag{4.1}$$

   where σ_h and σ_H are the maximum and minimum horizontal stresses.
   An alternative expression may be obtained if fully permeable wall and steady conditions are assumed. In this case, the equation is considered a lower limit

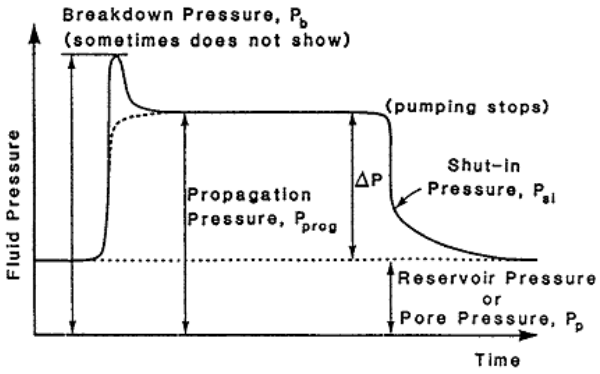

Figure 4.1: Bottom-hole pressures for one injection cycle (Yew, 1997).

(slow pressurization) Detournay and Carbonell (1997), Fjaer et al. (2008).

$$P_w^{frac} = \frac{3\sigma_h - \sigma_H + T_0 - \alpha\left(\frac{1-2\nu}{1-\nu}\right)P_0}{2 - \alpha\left(\frac{1-2\nu}{1-\nu}\right)} \tag{4.2}$$

Here, α is the Biot's coefficient $\left(\alpha = 1 - \frac{K_{rock}}{K_{skeleton}}\right)$.

2. Once the fracture is opened, the fluid is continuously injected with solids (proppant) that are carried by the fracturing fluid moving along the fracture. During this process solids can deposit on the fracture face (solid cake), which implies a fluid pressure increase due to the reduction of infiltration between the flowing fracture and the formation.
3. When the injection process ceases, the pressure in the fracture drops instantaneously to a level which is referred to as the instantaneous shut-in pressure (P_{si}). This point is usually used to retrieve information about minimum horizontal far-field stress.
4. Next, the pressure in the fractured region is still higher than the formation pressure, because the remnant slurry sustained a certain amount of energy required to maintain the fracture open. As the remaining fluid is expelled from the fracture, the higher energy is finally dissipated and the fracture closes. The pressure in the fracture domain then slowly returns to the initial pressure of the formation (P_0).

$$P_w = \sigma_h \tag{4.3}$$

4.1.3 Geometry modeling (fracture geometry)

The main objective of HF modeling is to characterize the geometry of the fracture, in particular the height, length, width and direction of the fracture. Furthermore, with the addition of the equations of proppant transport/reaction, the evaluation of proppant concentration after treatment is also of interest.

Another important question is the available information. Due to the high cost of wellbore data, only few measurements are available: from logs, the Young's modulus (E) and porosity; and from *mini-frac* jobs, *in situ* stresses, pore pressure and tensile strength. In some cases, due to the possibility of extracting cores, additional parameters may be obtained from laboratory tests (cohesion, friction angle, permeability, etc.)

As it is pointed out in the previous section, HF modeling is a complex task. Due to the difficulty, some simplifications have been adopted by most of the models proposed so far. The most common simplifying assumptions are the following (Warpinski et al., 1994):

1. **Plane fractures** with symmetry with respect to the wellbore.
2. **Elastic formation**. The medium surrounding the fracture is assumed to be perfectly elastic.
3. **Linear Elastic Fracture Mechanics (LEFM)** for fracture propagation. Fracture toughness is commonly used for tip resistance.
4. **Power law** behavior of fracturing **fluids** and **slurries**.

Current fracture geometry models could be divided into four types (Adachi et al., 2007):

1. **Planar-2D** analytical models. This kind of models were developed in the 1970's and solve the problem in a homogeneous formation. These models assume plane strain conditions and they only consider flow along the horizontal axis. The fracture shape is fixed and it depends on the model. The classical PKN and GDK are examples of this kind of models.
2. **Pseudo-3D** models. Due to the increasing complexity of the reservoirs, starting in the 1980's, a new family of methods was developed. In addition to planar 2D methods, this new family adds the possibility of lithological variation on the vertical axis. Depending on the model, the variation was restricted to 3 to 5 horizontal layers.
3. **Planar-3D**. This new family assumes that the fracture footprint and the coupled fluid flow equation are described by a 2D mesh. This procedure returns a more approximate solution but it requires more computation time. The FEM and Finite Difference Method (FDM) are used for the numerical solution.
4. **Full-3D**. In this group several methods are inscribed, for instance methods based on the FEM. Two are the common approaches for crack modeling: smeared crack models (considering the fracture as a zone of finite thickness with damaged properties), and discrete crack models (describing the fracture with zero thickness in an explicit way).

Finally, the selection of the right model is important. As indicated previously, there are several numerical models for hydraulic fracturing. However, depending on the

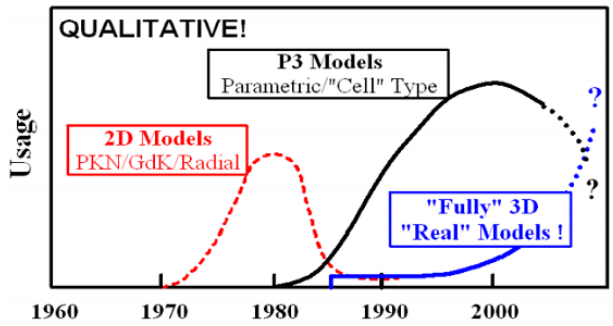

Figure 4.2: Historical qualitative usage of models in hydraulic fracturing (Smith et al., 2012).

situation one or the other will be preferred. For instance, Barree suggests a draft criterion for its choice (Barree, 2009).

- The **simplest models** are characterized primarily by their simplicity, use of few parameters, and low computational cost. These methods can be useful to get a first estimate in the completion design. Another interesting application is in the production phase in order to get quick results for verification purposes.
- The **sophisticated models** usually require more information for reservoir description. However they describe more accurately the fracture geometry and allow for making informed decisions. For that reason this kind of models are more suitable to determine final well completion during design phase.

4.1.3.a Planar 2D analytical models

This family of methods starts from the fluid motion inside the fracture equation (mass conservation). The average flow is assumed to be proportional to the pressure gradient (*Poiseuille* equation), which incorporates the effect of fracture aperture. Some models are enriched with a sink term corresponding to the leak-off effect.

Advantages: fast, few parameters, allow parametric studies.

Disadvantages: simple cases, homogeneous material and uniform stress conditions.

PKN (Perkins-Kern-Nordgren) The basic underlying assumption is that every vertical cross-section can be analyzed independently from the rest. The PKN model neglects the effect of fracture tip and fracture mechanics, and focuses on fluid flow and pressure gradients (Perkins and Kern, 1961). Other assumptions of PKN model are that the height of the vertical fracture is constant and does not exceed the pay zone (Perkins and Kern, 1961). The cross-section of the fracture is assumed to be elliptical. At any cross-section, the maximum width is proportional to the net pressure at that point and independent of the width at the pay point. The *in situ* stresses are assumed to be homogeneous and the PKN model utilizes the Sneddon width equation (Sneddon, 1946).

The original work from Perkins and Kern neglected the effects of fluid leak-off and storage resulting from width increase. For this reason Nordgren (Nordgren, 1972) added the leak-off effect and storage width in what is known as the standard PKN model:

1. Case of Storage dominated or high-efficiency (no leak-off). In this case the fluid efficiency, the rate between fracture contained in the fracture and the injected fluid, approaches one ($\eta \rightarrow 1$) and the fracture length $L(t)$, opening width at injection point $w_o(t)$ and net wellbore pressure $P_w(t)$ of the fracture for a given time t, are given by:

$$L\left(t\right) = 0.68\left(\frac{GQ^3}{\left(1-\nu\right)\mu H^4}\right)^{\frac{1}{5}} t^{\frac{4}{5}} \tag{4.4}$$

$$w_o\left(t\right) = 2.5\left(\frac{\left(1-\nu\right)\mu Q^2}{G\ H}\right)^{\frac{1}{5}} t^{\frac{1}{5}} \tag{4.5}$$

$$P_w\left(t\right) = 2.5\left(\frac{G^4\mu Q^2}{\left(1-\nu\right)^4 H^6}\right)^{\frac{1}{5}} t^{\frac{1}{5}} \tag{4.6}$$

   where G is the shear modulus; Q the volumetric flow rate; ν the poisson ratio; μ the dynamic viscosity; and H the hight of the fracture

2. High leak-off. In this case fluid efficiency approaches zero ($\eta \rightarrow 0$) and the length $L(t)$, opening width $w_o(t)$, and net wellbore pressure $P_w(t)$ of the fracture are given by:

$$L\left(t\right) = \left(\frac{Q}{\pi c_l H}\right) t^{\frac{1}{2}} \tag{4.7}$$

$$w_o\left(t\right) = 4\left(\frac{2\left(1-\nu\right)\mu Q^2}{\pi^3 G c_l H}\right)^{\frac{1}{4}} t^{\frac{1}{8}} \tag{4.8}$$

$$P_w\left(t\right) = 4\left(\frac{2G^3\mu Q^2}{\pi^3\left(1-\nu\right)^3 c_l H^5}\right)^{\frac{1}{4}} t^{\frac{1}{8}} \tag{4.9}$$

   where c_l is the leak-off coefficient.

For any point at distance x from the wellbore the following are the approximations for the PKN model: the aperture along propagation axis is given by:

$$w\left(x\right) = w_{\max}\left(1-\frac{x}{L}\right)^{\frac{1}{4}} \tag{4.10}$$

and the average aperture is given by:

$$\bar{w} = \frac{\pi}{2} w_{\max} \tag{4.11}$$

where w_{max} is the maximum aperture given by Eqs. (4.5) and (4.8); L the length (Eqs. (4.4) and (4.7)).

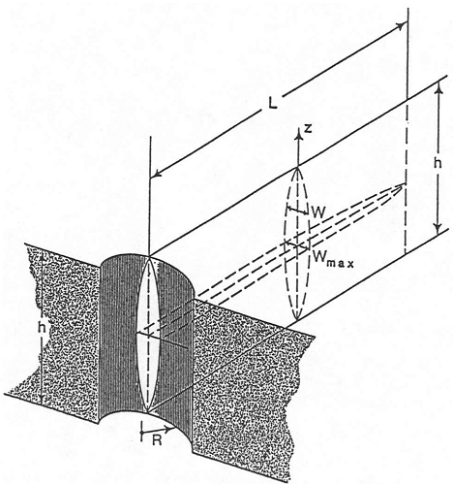

Figure 4.3: The PKN constant height fracture model (Yew, 1997).

GDK (Geertsma-De Klerk-Khristianovich) The GDK model is based on the following assumptions:

- The fracture width is proportional to its fracture length ($W \propto L$).
- The fracture height is constant ($H = \text{cons}$).
- The fracture has an elliptical cross-section in the horizontal plane.
- There is slippage between layers.
- Fluid does not act on the entire fracture length.
- The cross-section in the vertical plane is rectangular (fracture width is constant along its height).

Then, the length of the fracture $L(t)$, fluid pressure P_w and maximum opening at injection point w_o are given by the following expressions:

$$L(t) = 0.48\left(\frac{8\ G\ Q^3}{(1-\nu)\mu}\right)^{\frac{1}{6}} t^{\frac{2}{3}} \tag{4.12}$$

$$P_{\mathrm{w}} = \sigma_{min} + 0.96\left(\frac{2G^3 Q\mu}{(1-\nu)^3 L^2}\right)^{\frac{1}{4}} \tag{4.13}$$

$$w_{\mathrm{o}} = 1.32\left(\frac{8\,(1-\nu)\,Q^3\mu}{G}\right)^{\frac{1}{6}} t^{\frac{1}{3}} \tag{4.14}$$

For any point at distance x from the wellbore, the following are the approximations for the GDK model:

$$w\,(x) = w_{\max}\left(1 - \frac{x}{L}\right)^{\frac{1}{2}} \tag{4.15}$$

$$\acute{w} = \frac{\pi}{2} w_{\max} \tag{4.16}$$

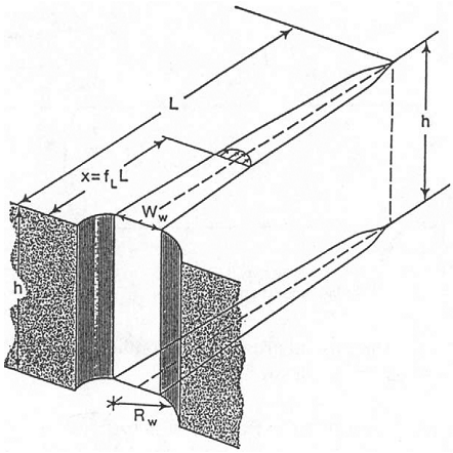

Figure 4.4: The GDK constant height fracture model (Yew, 1997).

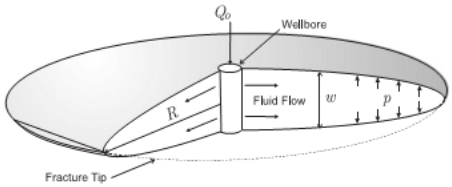

Figure 4.5: Schematic showing radial fracture geometry (Adachi et al., 2007).

Radial (Penny shaped) crack This model is applicable in case that the well axis coincides with the minimum principal stresses direction and therefore the crack develops along a plane perpendicular to the well axis. This model assumes that the fracture propagates in a uniform stress medium without any vertical restriction, the shape of the fracture is circular and the maximum width is at its center. Other assumptions made in this fracture model are that the fracture propagates radially by the same distance, pressure drop at the same distance from the wellbore in all directions is equal, no boundary restriction or interface slippage, and that the width decreases in all directions. Geertsma and de Klerk developed the equations for a radial fracture. The expressions for the width $w_0(t)$ and radius $R(t)$ are summarized below:

$$R\left(t\right) = 0.548\left(\frac{GQ^3}{\mu}\right)^{\frac{1}{9}} t^{\frac{4}{9}} \tag{4.17}$$

$$w_o\left(t\right) = 21\left(\frac{\mu^2 Q^3}{G^2}\right)^{\frac{1}{9}} t^{\frac{1}{9}} \tag{4.18}$$

4.1.3.b Pseudo-3D models (P3D)

These models were developed from the PKN model by removing the requirement of constant fracture height. They use equations based on simple geometries (radial, two dimensional, elliptical) to calculate fracture width as a function of position and pressure, and to apply a fracture propagation criterion to both length and height. Furthermore,

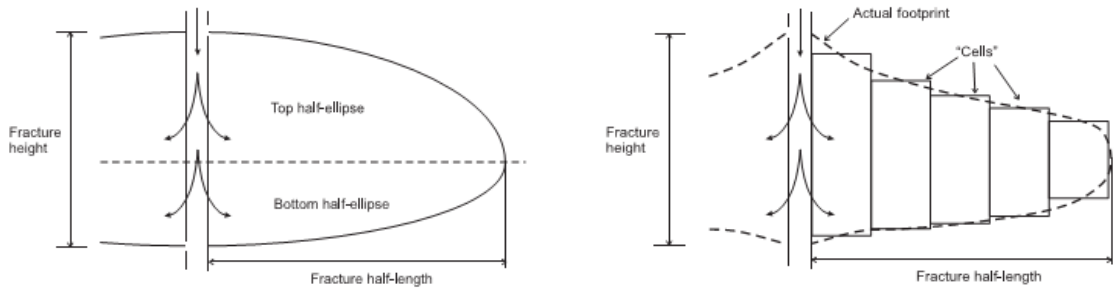

Figure 4.6: Pseudo-3D models: a) Schematic showing fracture geometry based on pseudo 3D lumped elliptical mode; b) Schematic showing cell-based pseudo-3D fracture geometry. (Adachi et al., 2007).

they assume one-dimensional flow along the length of the fracture.

These models can be divided into two categories:

1. Models that use a parametric representation of the total fracture geometry, such as the lumped method. This method represents the final footprint of the fracture as an approximation of two half-ellipses (see Fig. 4.6(a)).
2. In the cell-based models, the fracture is composed by a series of PKN-like cells, where each cell has its own width.

As the result of these assumptions, it is expected that in general each cell will have a different fracture geometry, even for the simple case of confined fracture.

The pseudo-3D simulators are extensively used for fracture design because of their efficiency and their availability on PC. However, they are directly applicable only for the geometries that are not significantly different from the basic assumptions of the model.

Advantages: fast (low computational cost), few parameters.

Disadvantages: not suitable when hour-glass shaped fracture footprint is expected.

4.1.3.c Planar 3D Models

Planar 3D models (PL3D) assume that the fracture footprint and the coupled fluid flow equation are described by a 2D mesh. This kind of models formulates the physics more rigorously and the main assumptions are:

- Planar fractures of arbitrary shape in linearly elastic formations.
- Two-dimensional flow in the fracture.
- Power law fluids.
- Linear elastic fracture mechanics for fracture propagation.

Within this family of models there exist two subgroups depending on how the numerical solution is calculated. Their difference is in the numerical technique to calculate fracture opening:

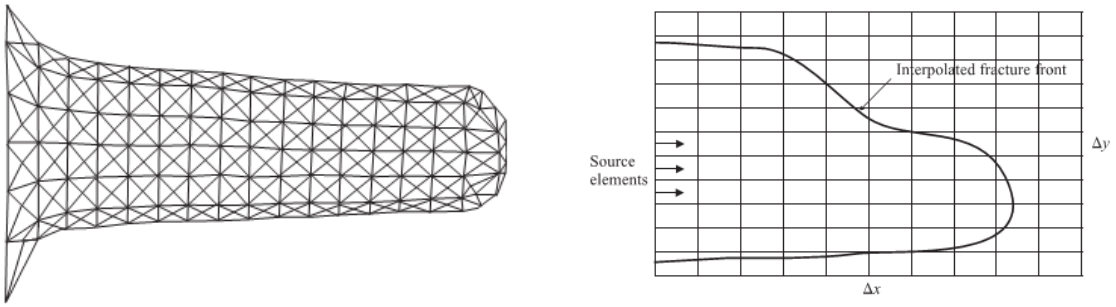

(a) (b)

Figure 4.7: Schematics showing planar 3D fracture geometry based: a) on a moving mesh system of triangular elements; b) on a regular (fixed) system of quadrangular elements (Adachi et al., 2007).

1. **Moving mesh**: this group belongs to those methods in which the mesh is evolving with the footprint evolution (see Fig. 4.7(a)).
2. Fixed rectangular mesh: the equations are solved in the full domain, the footprint is obtained after interpolation (see Fig. 4.7(b)).

This kind of models are more accurate and computationally far more expensive than Pseudo 3D. The need of PL3D models arose because there are specific treatments that P3D are not suited to model, for instance when the confining stress varies with depth or unconfined height growth occurs. In general when an hour-glass-shaped fracture footprint occurs.

Advantages: more realistic representation than previous approaches-

Disadvantages: higher computational cost, planar fractures.

4.1.3.d Full 3D models

This group is composed by a miscellaneous collection of methods that model the real 3D domain (fluid and mechanical equations are solved in three dimensions).

The number of methods in the existing literature that follows this approach is very limited, and practically all are based on the FEM for the mechanical behavior (Li et al., 2012, Secchi and Schrefler, 2012), sometimes combined with FDM for fluid. Basically, this group of models is still under development.

From a solid mechanics viewpoint, both 3D and 2D models simulating hydraulic fracture can be grouped into two general families:

1. **Smeared crack** models: this family of models simulates the fracture with standard elements equipped with special constitutive law. Therefore continuum material behavior controls the fracture process. As an example the code RFPA3D (Li et al., 2012), where continuum elements are equipped with a damage-based material law. A tracking algorithm is needed; only one or two independent cracks can be followed at a time.

2. **Discrete crack** models: in this kind of models the behavior of fractures is differentiated from the continuous medium. Several methods have been proposed, among them:
    a) **Remeshing method**: this is the traditional implementation of Fracture Mechanics in Finite Elements, originally with LEFM and stress singularity (Ingraffea & Heuze, 1980). Later it has been implemented with the cohesive crack. Still, it requires determination of crack propagation direction, remeshing, etc. All this complicates extremely the implementation and increases the computational cost. Only one or two independent cracks may be followed at a time.
    b) Introduction of **special elements** (interfaces/contacts) between continuum elements, without remeshing. This method is robust, and it allows multiple crack paths and all kinds of interactions between them. Limitations are that cracks are only allowed along the pre-inserted special elements, and that in 3D analysis potential cracks must be limited in order to avoid unnecessary computational cost.
    c) Use of **enriched continuum elements** to allow jumps/drops (Extended Finite Element Method (XFEM)). The main benefit of this method is that it allows the growth of a fracture without spatial limitation. However, only a reduced number of simultaneous cracks are allowed in the analysis, and interaction between intersecting cracks is still subject of research in this method.

The main challenges for 3D fracture methods are mentioned in the following list:

- **Full coupling**: Due to the strong coupling between the mechanical and the fluid problem, a monolithic implementation (fully coupled) may be considered a requirement. The use of a staggered approach is in most cases inefficient because it does not lead to convergence between both mechanical and fluid solutions.
- **Tracking or remeshing algorithms**: the methods that determine the crack at each time step need a special algorithm to determine the growth direction. In a 3D case this may pose a very serious challenge.

Advantages: the most realistic modeling

Disadvantages: still under development, computational cost, time for generating a case, number of parameters.

4.1.4 Current Challenges

As mentioned above, hydraulic fracture modeling still offers difficulties, and thus it opens the door to interesting lines of investigation. The following items are some

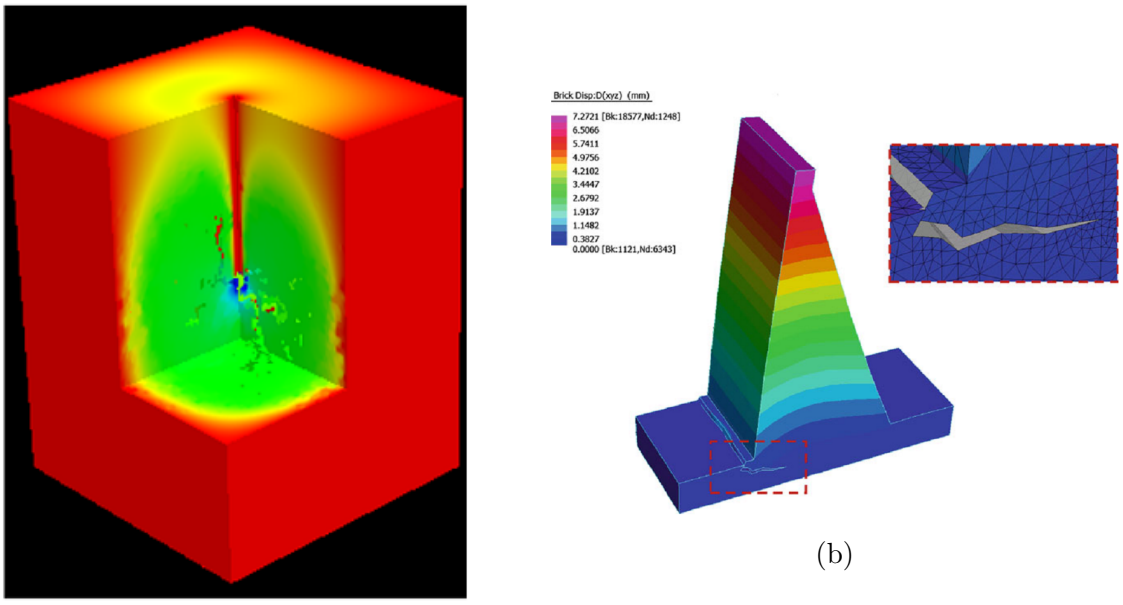

(a) (b)

Figure 4.8: a) smeared crack model: spatial distribution of fractures using RFPA3D-Parallel (Li et al., 2012); b) discrete crack analysis: fracture at the base of the dam (Secchi and Schrefler, 2012).

examples of aspects of industrial interest that are not well solved with current numerical tools.

- **Non planar fractures**. Except full 3D computations, the rest of methods assume that fractures are planar. This assumption could be right (or acceptable) for uniform far-field stresses. However this assumption is in general not correct, for instance in the case of stress distribution around a salt dome.
- **Deviated boreholes** As the fractures grow perpendicular to the minor effective stress and they tend to open from the bottom to the top, the fracture in deviated boreholes tends to twist toward the minimum energy configuration.

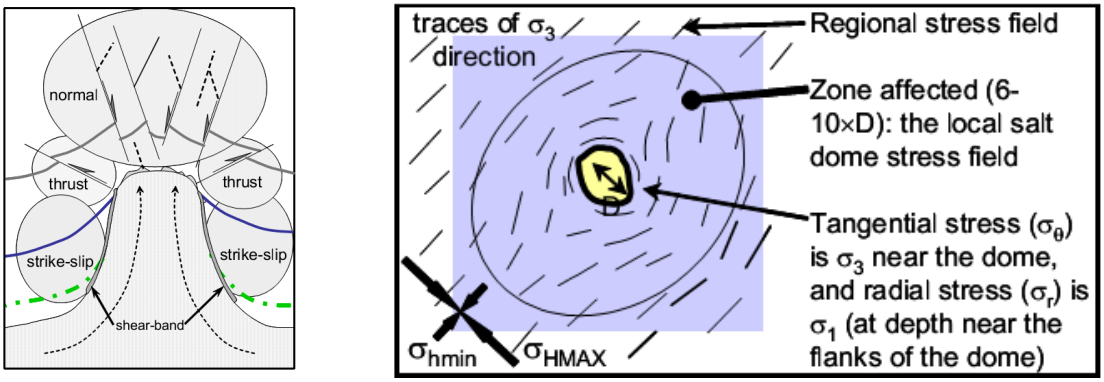

(a) (b)

Figure 4.9: a) Generalized stress regimes around a dome; b) Stress field perturbation by salt diapirism. (Dusseault et al., 2004)

- **Hydraulic fracturing in faults/natural discontinuities**. The traditional methods only assume the generation of fractures around the wellbores. However in real cases natural fractures can be mobilized during well injection.
- **Multiphase fluid flow and THM**. The composition of an oil reservoir is a mixture of oil, water and gas. Therefore it will be optimal to simulate the real composition of pores in the numerical models. For this purpose the introduction of a thermal variable (thermo-hydro-mechanical problem) may be necessary to take into account the effects of phase transitions. Moreover, this procedure could provide a tool to study related scenarios such as the injection of water or CO_2 into a reservoir.

In general, further development and improvement is needed in full 3D models, reducing cost, improving reliability and robustness, etc., so that those models can become useful tools to solve the problems listed above, and also they can offer better, more efficient and more accurate solutions to the more standard situations.

4.2 Single fracture analysis

Modeling hydraulic fracture is a challenging problem due to the strong coupling between the equation that governs the solid deformations (momentum balance) and the equation that controls the fluid pressure (fluid mass continuity). The coupling is produced in two ways: on one hand, the fluid pressure is causing solid deformations, and on the other hand, the fluid transmissivity along the fractures is controlled by their apertures. Additionally, due to the strong localization of deformations (along fractures), it is necessary to introduce numerical techniques to treat numerical singularities.

The aim of this study is to develop the study of hydraulic fracturing with zero-thickness interface elements which was initiated by Segura (2007), Segura and Carol (2008b). In that preliminary study, a fully coupled hydro-mechanic formulation with interfaces was used to simulate a 2D fracture, although the interface behavior was assumed as linear elastic with very low moduli. The new results obtained in 2D will be shown to be in good agreement with the analytical models (GDK, Section 4.1.3.a; and PKN, Section 4.1.3.a) and with the numerical solution given by Boone and Ingraffea (1990) in 2D. In a subsequent section the results of the 3-D analysis of a single fracture are presented. The calculations performed include two different cases, and whenever possible, the results are compared with previous existent 2D analytical and numerical solutions.

Objectives The fundamental objective of this section is to explore 2D and 3D capabilities of zero-thickness interface elements equipped with realistic non-linear material laws, for the hydraulic fracturing modeling. In particular, this work focuses on the following points:

1. **Validation of 2D and 3D models** with simple analytical methods. In 2D, due to the analytical model assumptions, the comparison is only available with GDK method. The results are presented in Section 4.2.1. The 3D analysis is compared with both GDK and PKN methods. The results will be included in Section 4.2.3 and Section 4.2.4.
2. Analysis of the **parameter sensitivity**. For instance sensitivity to initial stress and to changes of energy parameters for energy-based constitutive law (Section 4.2.2).

4.2.1 Constant fracture aperture in height in 2D

The numerical study of hydraulic fracture starts with the analysis of a single fracture in 2D. A semicircular domain of radius 80 m representing a transversal cross-section of the borehole, as depicted in Fig. 4.11(a), is discretized with a standard linear triangular finite element mesh (Fig. 4.11(b)). The fracture is inserted along the abscissa axis with

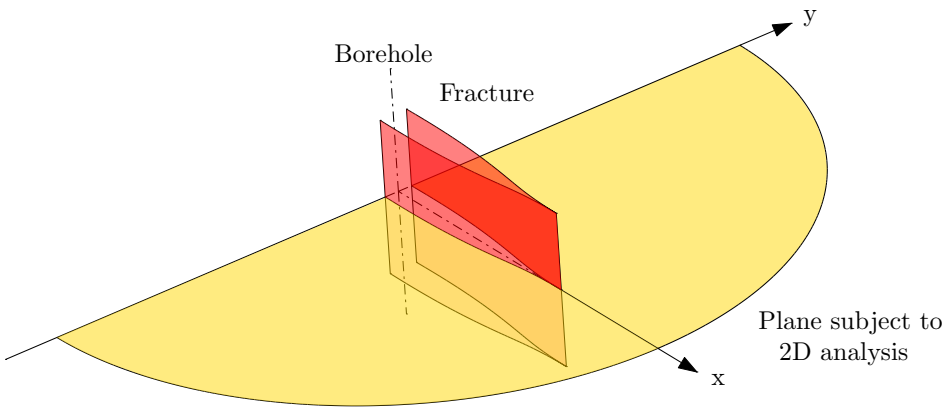

Figure 4.10: Scheme of the hydraulic fracture test.

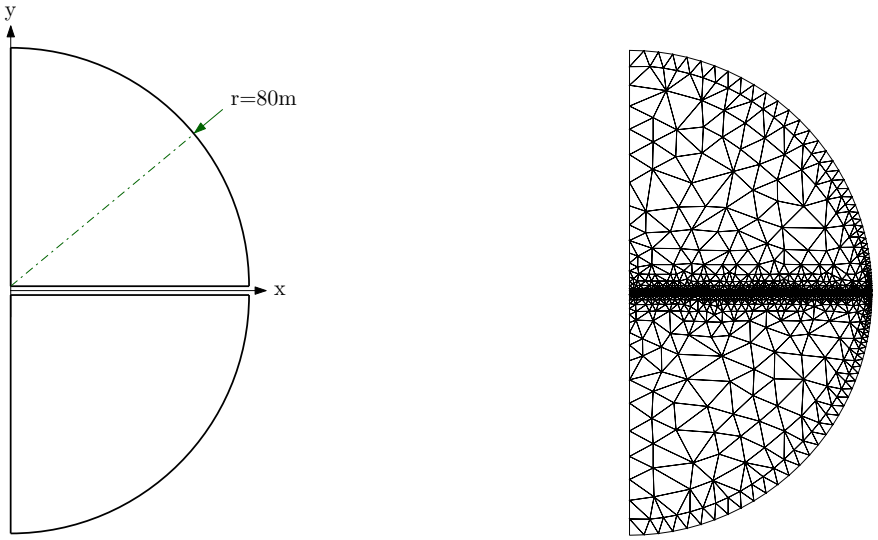

(a) (b)

Figure 4.11: 2D model for single fracture. (a) the sketch of the geometry, and (b) current FE refined mesh.

double-node linear interface elements. This example is taken from Boone and Ingraffea (1990).

Regarding the boundary conditions, the simulation is divided in two steps (see Fig. 4.12):

1. A distributed load of 1.0 MPa is applied over the outer boundary in order to simulate the *in situ* initial stress. Initial pore pressure is assumed to be zero in the entire domain.
2. A fluid is injected at the fracture mouth with constant Q=0.0001 m^3/s. The remaining boundary conditions defined in step 1 are maintained. This step is run under transient conditions with increasing time steps until a total duration of 25 s.

The continuum elements are assumed to be linear elastic and isotropic, with parameters extracted from Boone and Ingraffea (1990). For the hydraulic setup, two

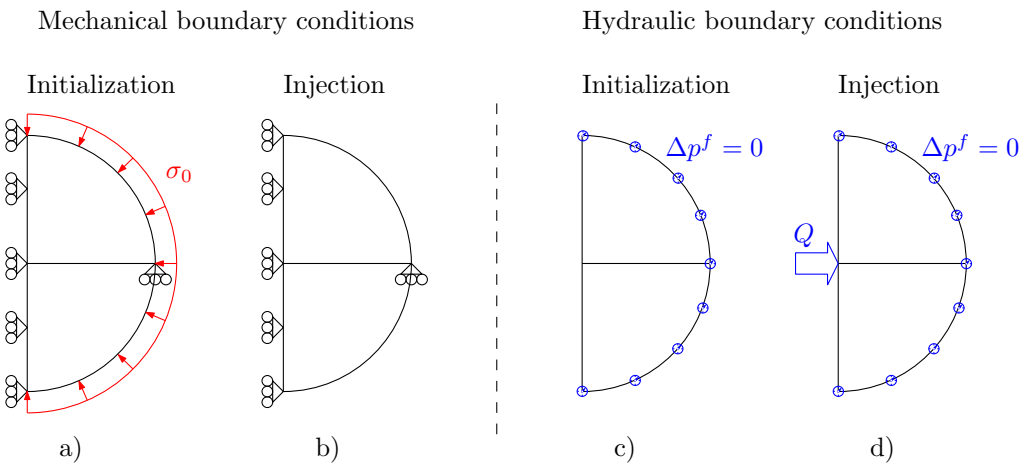

Figure 4.12: Boundary conditions for mechanical (a-b diagrams) and flow (c-d diagrams), for each of the initialization and injection steps of the analysis.

Table 4.1: Material properties of continuum

Parameter	*Value*		*Units*
E (Young modulus)	14400		MPa
ν (Poisson ratio)	0.2		
	Impervious	*Pervious*	
K (Hydraulic conductivity)	$1.0 \cdot 10^{-15}$	$1.0 \cdot 10^{-7}$	$\mathrm{m} \cdot \mathrm{s}^{-1}$
K_s (skeleton compressibility)	36 000.0	36 000.0	MPa
α_{Biot}	1.0	1.0	

scenarios are analyzed, one without leak-off (which corresponds to a case with a fracture embedded in an impervious continuum medium) and another one with low leak-off (corresponding to a case with pervious medium). In current analysis, the first scenario is defined with a fictitious hydraulic conductivity of $1.0 \cdot 10^{-15}\,\mathrm{m} \cdot \mathrm{s}^{-1}$, and the second with a value of $1.0 \cdot 10^{-7}\,\mathrm{m} \cdot \mathrm{s}^{-1}$. All parameters are displayed in Table 4.1.

For the mechanical behavior of the interface elements, high values of normal and shear stiffness modules are selected. These parameters are understood as penalty coefficients in order to avoid elastic deformations at the interfaces. Therefore, the deformation can be assumed inelastic due to the use of an elastoplastic constitutive law. The energy-based constitutive law presented in Section 2.5 is used for the interfaces, with fictitious strength parameters (low values) in order to compare with analytical methods which consider existent fractures of zero tensile strength. In particular, cohesion (c_0) and tensile strength (χ_0) are defined with residual very small values. To avoid numerical instabilities and due to the low confinement, a low friction angle ($\tan\phi$) was selected. The definition of fracture energies (G_f^I and G_f^{IIa}) is not relevant due to the use of residual strength parameters. Table 4.2 shows the parameters used for this study.

Regarding the hydraulic problem, since hydraulic transitivity is controlled by open-

Table 4.2: Mechanical properties of interfaces

Parameter	*Value*	*Units*
K_n	$1.0 \cdot 10^6$	$\mathrm{MPa} \cdot \mathrm{m}^{-1}$
K_t	$1.0 \cdot 10^6$	$\mathrm{MPa} \cdot \mathrm{m}^{-1}$
$\tan\phi$ (friction angle)	0.20	
χ_0 (tensile strength)	0.002	MPa
c_0 (cohesion)	0.01	MPa

Table 4.3: Hydraulic properties of interfaces

Parameter	*value*	*units*
Tl_0	0.0	m^2/s
K_t	1.0	s^{-1}
M_J	$1.0 \cdot 10^{10}$	
μ	$1.0 \cdot 10^{-9}$	$\mathrm{MPa} \cdot \mathrm{s}$

ing, the so-called *cubic law* (Eq. (2.75)) and a nearly zero initial value (T_l) have been assumed. Water is assumed to be the injection fluid ($\mu = \mu_{water}$), and the Biot modulus (M_J) has been defined with a very high value to avoid effects of compressibility. Finally, the value of transversal conductivity of the interfaces (K_t) is considered irrelevant because of the symmetry which causes no flow to cross the interface transversally. Table 4.3 shows the summary of hydraulic parameters selected for current analysis.

4.2.1.a Propagation without leak-off (impervious case)

The modeling of hydraulic fracture without leak-off theoretically corresponds to an impervious continuum. However in practice a very low permeability is assumed equal to $1.0 \cdot 10^{-15}\,\mathrm{m} \cdot \mathrm{s}^{-1}$ has been considered to be sufficiently low.

The simulation of hydraulic fracture in 2D with plane strain conditions without leak-off coincides with the assumptions of the GDK analytical method (Geertsma J. and De Klerk F., 1969). Then, it allows us to use this example as a validation test. The results from the simulations performed are compared with the results obtained with GDK formulas Eqs. (4.12) to (4.14).

Additionally, numerical results from Boone and Ingraffea (1990) available for the first 24 s of injection, are also included in the comparison. For this reason, the analysis is performed for the same duration of 24 s of injection. Moreover, an initial *in situ* stress (σ_0) equal to 1.0 MPa is applied in the initialization step.

In general the results obtained in the present study using zero-thickness interfaces (DRAC) and those obtained by Boone and Ingraffea (1990) show a good agreement. Both numerical solutions tend to give larger openings (Crack Mouth Opening Displacement (CMOD)) than the analytical solution (Fig. 4.14) and larger values of the

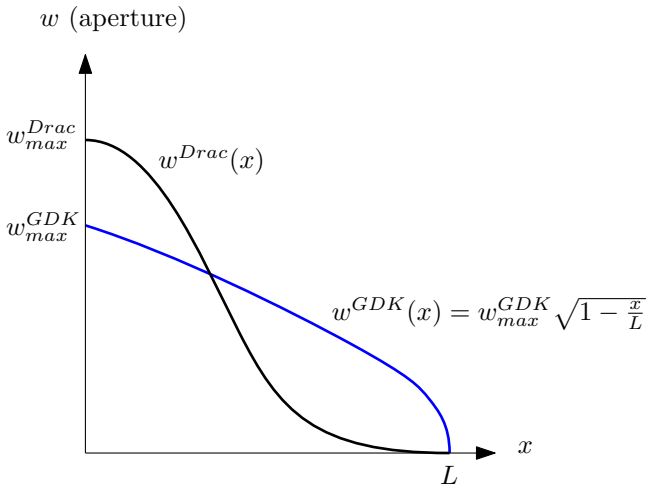

Figure 4.13: Aperture (w) profiles along fracture propagation axis for analytical formula (GDK) and numerical model (DRAC).

Crack Mouth fluid Pressure (CMP) (Fig. 4.15). The final fracture length, presented in Fig. 4.16, also shows a slightly larger prediction for the numerical models as compared to the analytical solution. Note the sawtooth shape observed in the numerical solution provided by DRAC caused by the model discretization; each step corresponds to the crack extending to the next interface element along the fracture.

The systematic difference between numerical and analytical solutions could be explained with the shape of fracture along the propagation axis. The analytical model assumes an elliptic shape given by Eq. (4.15). However, the numerical solution can not give that shape due to the geometric restriction intrinsically imposed at the crack tip, the derivative of aperture respect to fracture propagation must be 0 $\left(\frac{dw}{dx} = 0\right)$, which necessarily produces a sharp crack tip (probably more realistic than the round-shape tip used in the formulas). Figure 4.13 illustrates the shape of the aperture profiles along propagation axis (x).

Figure 4.17 shows the fluid pressure profiles at time 24 s for the current model and Boone and Ingraffea's model. The match is quite good except near the crack tip, probably because of the different approaches for the modeling of flow continuity (Boone and Ingraffea used finite differences for fluid flow). Note in this figure, the negative pressure near the crack tip known as "fluid lag", which has been obtained in the proposed model as the result of the delay between opening of the crack and filling with fluid, which in an impermeable medium can only reach the crack tip along the fracture itself.

4.2.1.b Propagation with low leak-off (pervious case)

The present section shows the 2D analysis of a single fracture allowing certain amount of leak-off. The only changes with regard to the previous section are the consideration of permeable rock. The *in situ* stress has been increased slightly to be similar to the

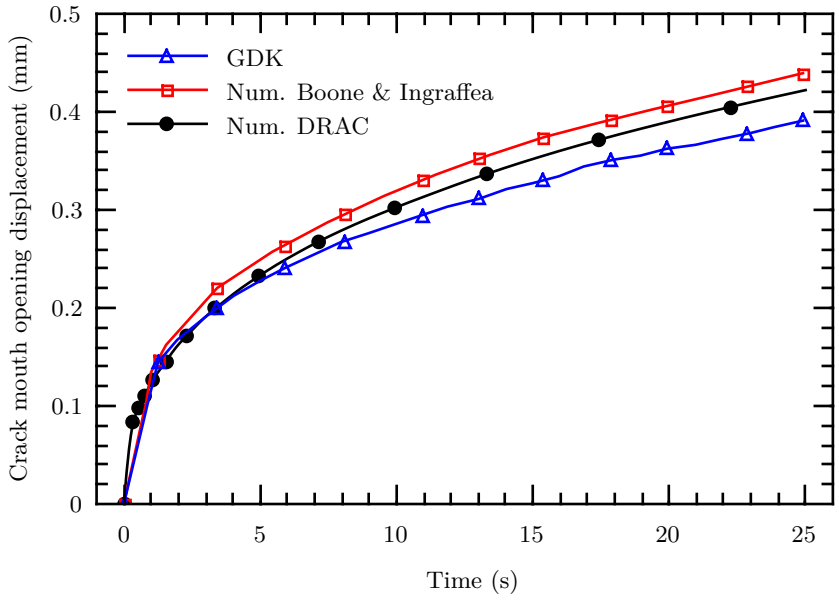

Figure 4.14: Crack mouth opening displacement (CMOD) evolution for the case without leak-off. Comparison to analytical GDK formulas and to numerical results by Boone and Ingraffea (1990).

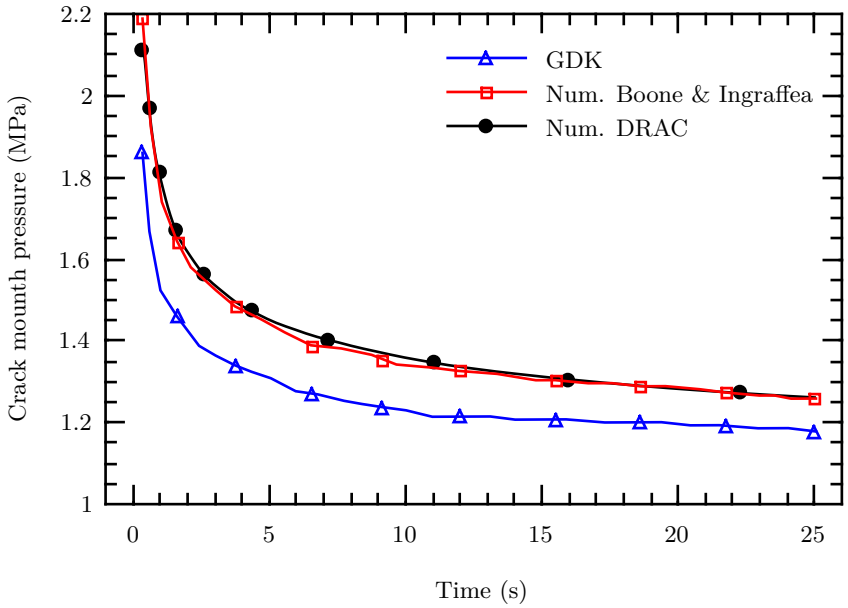

Figure 4.15: Crack mouth pressure (CMP) evolution for the case without leak-off. Comparison to analytical GDK formulas and to numerical results by Boone and Ingraffea (1990).

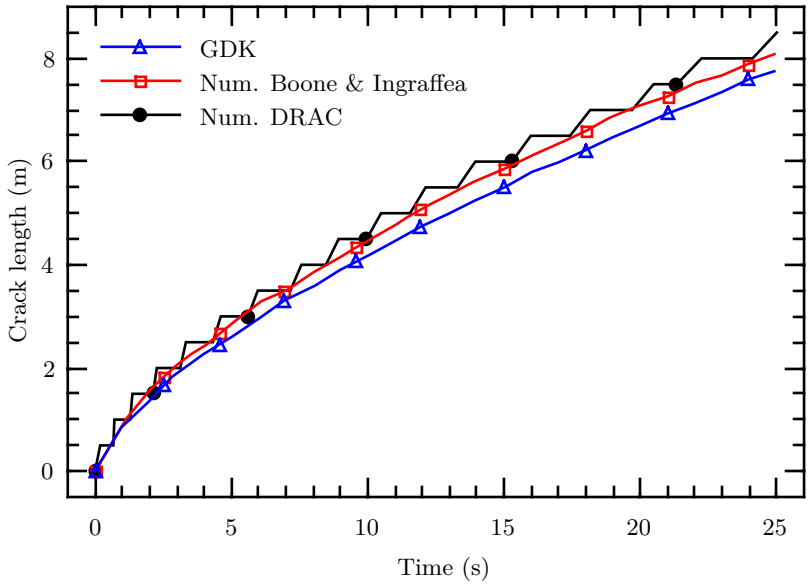

Figure 4.16: Crack length evolution for the case without leak-off. Comparison to analytical GDK formulas and to numerical results by Boone and Ingraffea (1990).

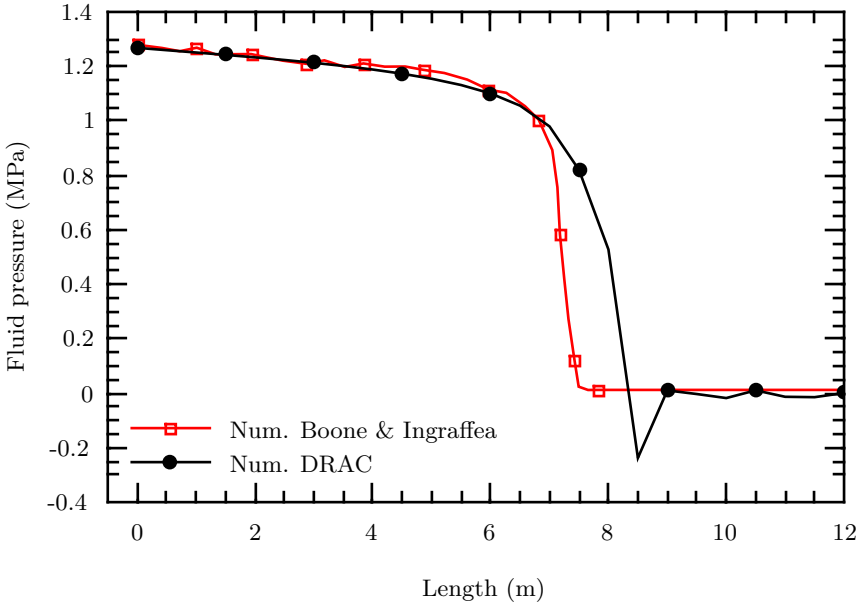

Figure 4.17: Fluid pressure profile at 24 s for the case without leak-off. Comparison to analytical GDK formulas and to numerical results by Boone and Ingraffea (1990).

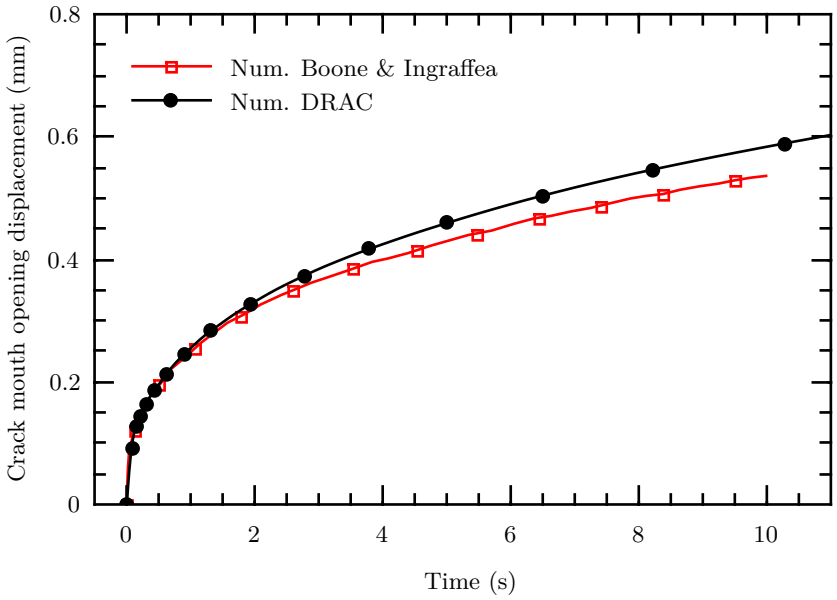

Figure 4.18: Crack mouth opening displacement (CMOD) evolution for the case with leak-off. Comparison to numerical results by Boone and Ingraffea (1990).

value used in Boone and Ingraffea (1990):

- Continuum permeability $\mathrm{K} = 2 \cdot 10^{-7}\,\mathrm{m} \cdot \mathrm{s}^{-1}$
- Initial *in situ* stress 1.2 MPa (total = effective in this case)

Note that, no analytical formula exists for this case and the only comparison can be done with other numerical results such as the ones published in that reference. The original reference only provides results for the first 10 s and, therefore, comparisons are made in this range of time.

The results depicted in Figs. 4.18 and 4.19 show a good agreement between both models. Figure 4.18 shows a slightly larger aperture of the DRAC model with respect to Boone and Ingraffea (1990). However, Fig. 4.19 shows a good agreement, in spite of some initial difference that might be related to mesh discretization and/or initialization parameters such as initial transmissivity.

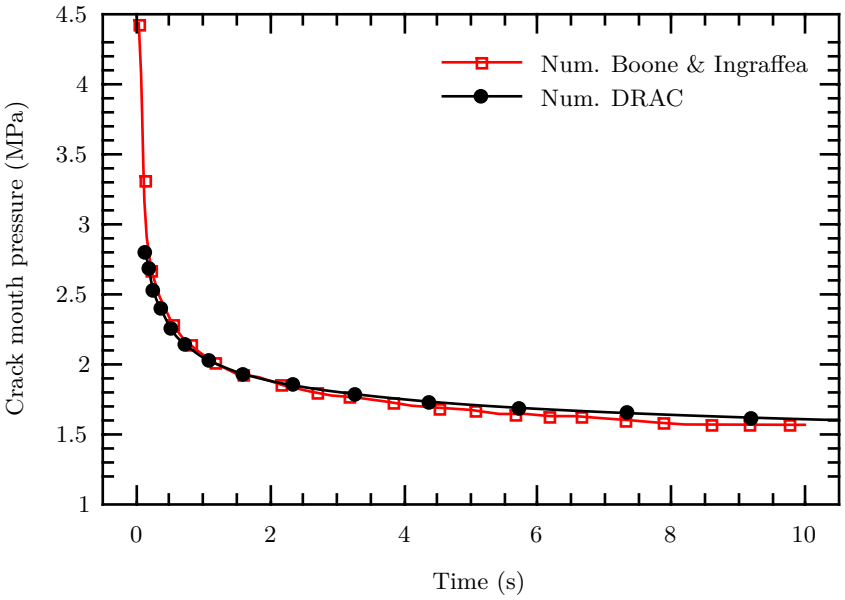

Figure 4.19: Crack mouth pressure (CMP) evolution for the case with leak-off. Comparison to numerical results by Boone and Ingraffea (1990).

4.2.2 Sensitivity to fracture energy in 2D

After the validation carried out in previous sections, this section explores the effect of changing the values of the fracture parameters of the fracture-based interface constitutive law. The main parameters of that law are tensile strength (χ_0), cohesion (c_0), friction angle ($\tan\phi$) and fracture energies in mode I (G_f^I) and mode IIa (G_f^{IIa}) (Carol et al., 1997).

In order to explore different scenarios, two types of parameter variations respect fracture propagations are proposed:

- Changing fracture energy (G_f^I) with fixed tensile strength ($\chi_0 = 0.5MPa$).
- Changing tensile strength (χ_0) and fracture energy (G_f^I) with a constant ratio $\chi_0/\sqrt{G_I^f}$.

The case with the lowest values of χ_0 and G_f^I (practically zero), corresponds to the case already considered in Section 4.2.1 and, also to the results obtained by Boone and Ingraffea (1990). Reference material properties for energy-based constitutive law are taken from Sarris and Papanastasiou (2012). Those are $\chi_0 = 0.5\,\text{MPa}$ and $G_f^I = 1.12 \cdot 10^{-4}\,\text{MPa} \cdot \text{m}$. Table 4.4 contains all parameters related to the mechanical law.

4.2.2.a Changing fracture energy (G_f^I) with fixed tensile strength (χ).

This section describes the study of the changes in propagation of the fracture due the variation of the fracture energy. In particular, the range considered is from 0.1

Table 4.4: Material properties for fracture energy-based constitutive law.

Parameter	*Value*	*Units*
$\tan\phi$	0.2 (11.3°)	
χ_0	0.5	MPa
c_0	1.515	MPa
G_f^I	$1.12 \cdot 10^{-4}$	MPa · m
G_f^{IIa}	$10 \times G_f^I$	MPa · m
σ_{dil}	1.0	MPa

to 10 times the fracture energy in mode I with respect to the reference value G_I^{f*} (see Table 4.5). In this analysis, due to the crack opening mode in pure tension, the value of the future energy parameter in mode IIa is not relevant, however the common assumption of $G_f^{IIa} = 10 \times G_f^I$ is maintained. As observed in Fig. 4.20, the shape of the descending branch of the stress-relative displacements of the interface curve is indeed changed drastically with G_f^I , being clearly more ductile as G_f^I increases, or more brittle as G_f^I decreases.

Table 4.5: Values of fracture energy in mode I.

G_I^f/G_I^{f*}	G_f^I (MPa · m)
×0.1	$1.12 \cdot 10^{-5}$
×0.5	$0.65 \cdot 10^{-4}$
×1	$1.12 \cdot 10^{-4}$
×2	$2.24 \cdot 10^{-4}$
×10	$1.12 \cdot 10^{-3}$

The results obtained by changing fracture energy while keeping constant tensile strength, are shown in Figs. 4.21 to 4.23. The results are not showing remarkable effect due to energy variation, although the general trend is clearly observed that higher G_f^I brings higher crack mouth pressures and smaller propagations Figs. 4.22 and 4.23.

However the effect on CMOD is less trivial (see Fig. 4.21). On the one hand, at short injection times, cases of low fracture energy exhibit larger apertures than cases with higher energies. This phenomenon could be explained taking into account that as the energy is reduced, the tensile strength decreases more rapidly. Therefore larger apertures might appear earlier. On the other hand, there is a tendency to increase the aperture when the energy is increased. The explanation of this effect might be related to the difficulty to propagate the fracture along the crack path and the kind of boundary condition selected for the example. This combination produces an increase of fluid pressure at the crack mouth, as observed in Fig. 4.22, in order to accommodate the imposed injected volume. Larger values of fluid pressure imply larger deformations at the crack mouth.

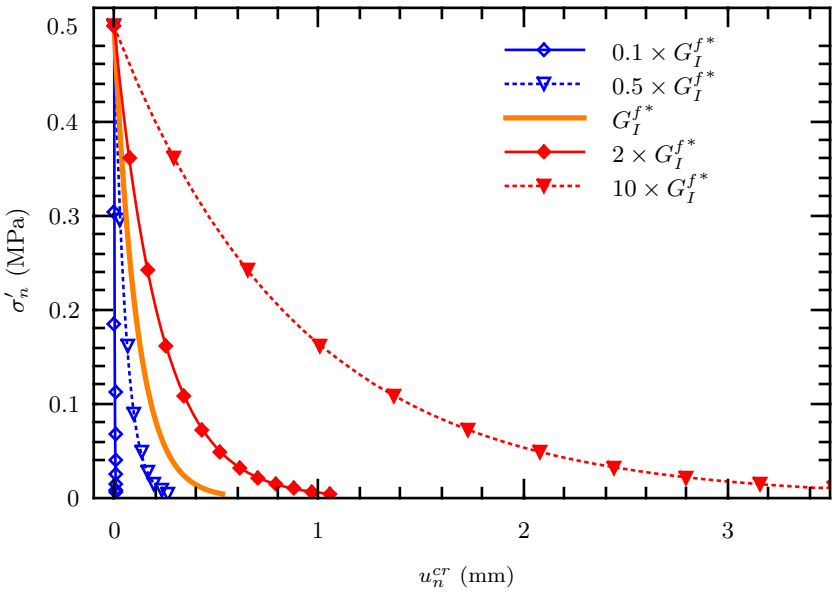

Figure 4.20: Stress-relative displacement of the interface for various values of G_f^I ($G_{I_0}^f = 1.12 \cdot 10^{-4}\,\mathrm{MPa} \cdot \mathrm{m}$) and fixed χ_0.

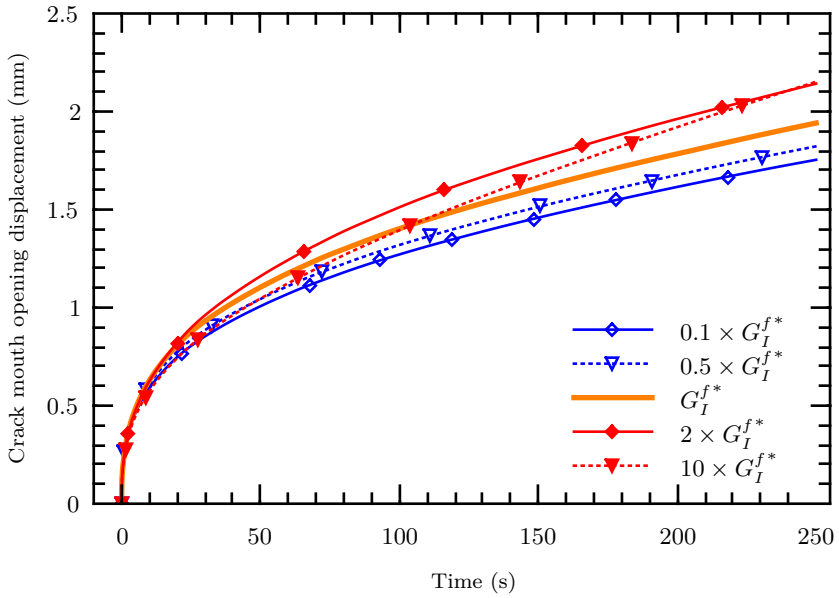

Figure 4.21: CMOD evolution for different values of G_f^I and fixed χ_0.

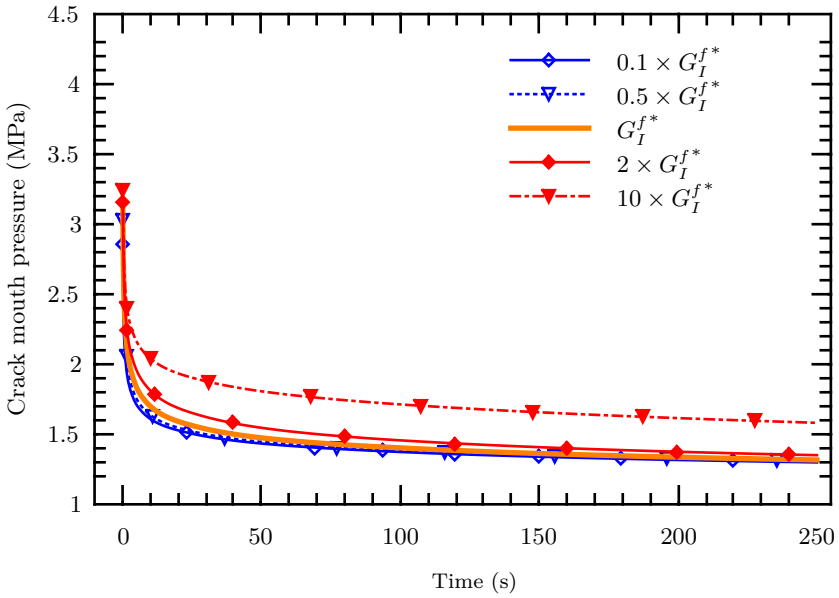

Figure 4.22: CMP evolution for different values of G_f^I and fixed χ_0.

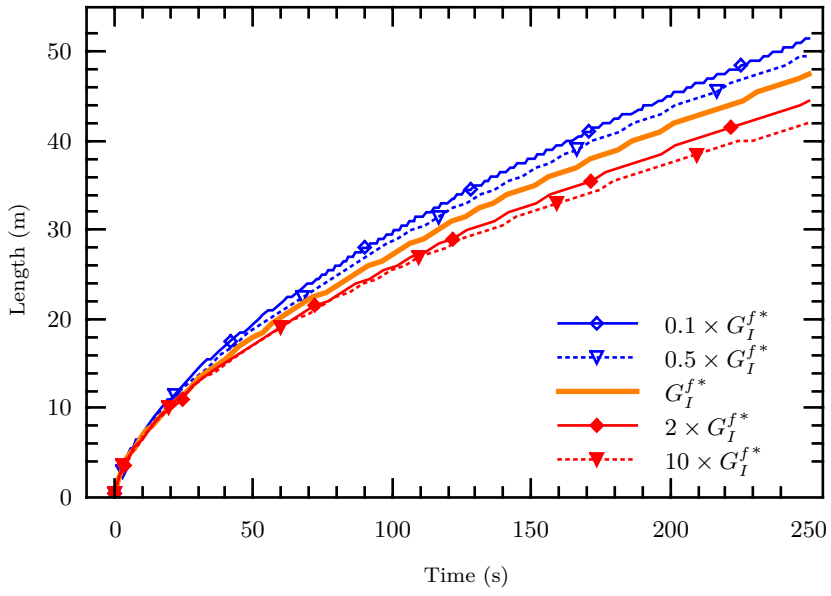

Figure 4.23: Length evolution for different values of G_f^I and fixed χ_0.

Table 4.6: Values of fracture energy in mode I.

	χ_0 (MPa)	G_f^I (MPa · m)
×0.5	0.25	$2.797 \cdot 10^{-5}$
×1	0.5	$1.119 \cdot 10^{-4}$
×2	1.0	$4.475 \cdot 10^{-4}$
×4	2.0	$1.179 \cdot 10^{-3}$
×10	5.0	$1.119 \cdot 10^{-2}$

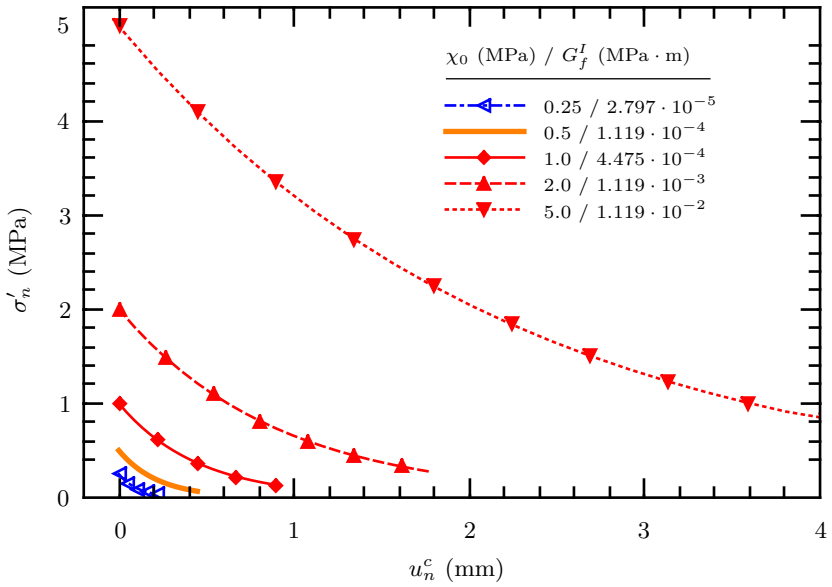

Figure 4.24: Tensile diagram for each pair of values of χ and G_f^I used in this analysis.

4.2.2.b Changing tensile strength χ and fracture energy (G_f^I) at the same time.

Because the fracture energy (G_f^I) corresponds to the area under the stress-opening curve of the interface or crack, it is reasonable to assume that both may vary at the same time to keep the shape of the diagram. For this reason, in this section it is assumed that G_f^I varies with the square of the change in tensile strength χ (see Table 4.6 and Fig. 4.24).

The most significant results obtained by changing tensile strength and fracture energy at the same time, in a way that preserves the shape of the stress-opening diagram of the fracture, are shown in the following three figures (Figs. 4.25 to 4.27)

Figure 4.26 shows that when the tensile strength and G_f^I are increased, the effect on the crack mouth pressure is clear and intuitive: since the crack is harder to propagate, the pressure of the fluid is higher. Figure 4.27, similarly, shows that for larger values of χ_0 and G_f^I , length decreases.

The effect on the CMOD evolution is not so obvious (Fig. 4.25).

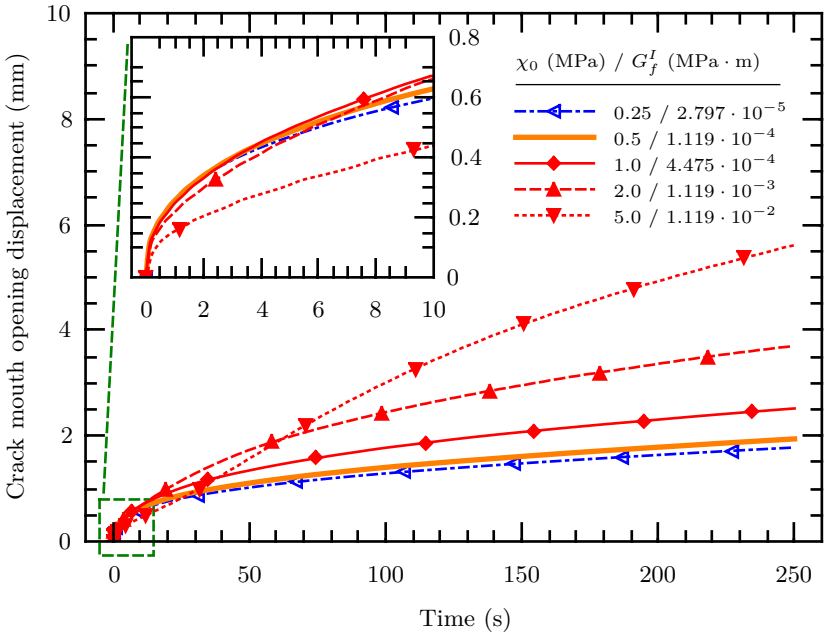

Figure 4.25: CMOD evolution for various pairs of values of χ and G_f^I , maintaining a similar shape of tensile diagram.

Table 4.7: Material properties of continuum

Parameter	*Value*	*Units*
E (Young modulus)	14 400.0	MPa
ν (Poisson ratio)	0.2	
K (Hydraulic conductivity)	$1.0 \cdot 10^{-15}$	$m \cdot s^{-1}$
K_s (skeleton compressibility)	36 000.0	MPa
α_{Biot}	1.0	MPa

4.2.3 Constant fracture aperture in height in 3D, GDK validation

This section describes the study of the 3D analysis of a single fracture embedded into horizontal layer of 1 m of thickness with a line-like distributed flow injection, with the purpose of simulating as close as possible the conditions of the standard GDK formula Yew (1997).

4.2.3.a Material properties

The material properties that have been used in the simulations are given below. For the continuum elements, the material is assumed to be elastic isotropic. Regarding the hydraulic behavior, the material is taken as practically impervious as it corresponds to the assumptions of the GDK solution. All parameters are displayed in Table 4.7.

For the mechanical behavior of the interface elements, the model used for the fractures is the elastoplastic constitutive formulation with fracture energy-based evolution laws described in detail in Carol et al. (1997). Normal and shear stiffness are assigned

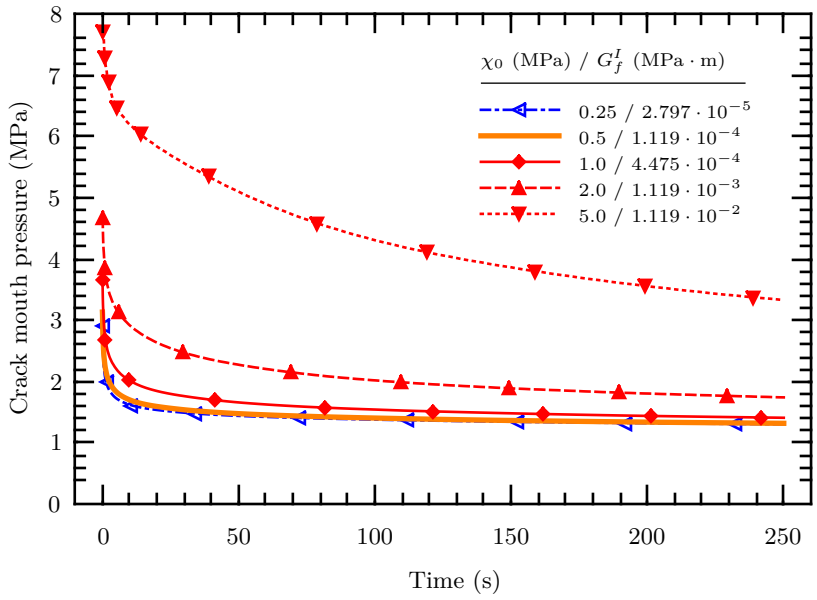

Figure 4.26: CMP evolution for various pairs of values of χ and G_f^I , maintaining a similar shape of tensile diagram.

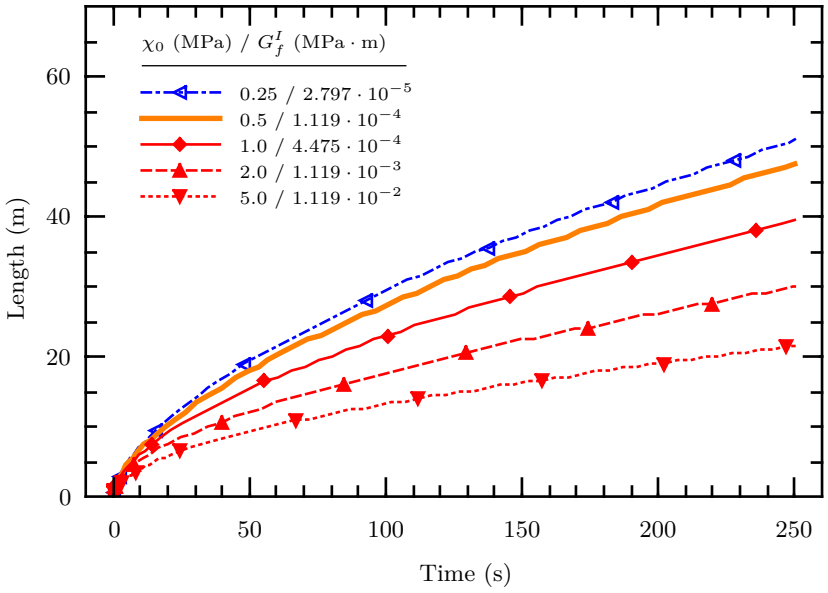

Figure 4.27

Figure 4.28: Crack length evolution for various pairs of values of χ and G_f^I , maintaining a similar shape of tensile diagram.

Table 4.8: Material properties of interfaces

Parameter		*Value*	*Units*
K_n		$1.0 \cdot 10^6$	$\text{MPa} \cdot \text{m}^{-1}$
K_{t_1}, K_{t_2}		$1.0 \cdot 10^6$	$\text{MPa} \cdot \text{m}^{-1}$
$\tan \phi$	Friction angle	0.2 (11.3°)	
χ	Tensile strength	$2.0 \cdot 10^{-3}$	MPa
c	Cohesion	$1.0 \cdot 10^{-2}$	MPa
G_f^I	Fracture energy mode I	0.001	$\text{MPa} \cdot \text{m}$
G_f^{IIa}	Fracture energy mode IIa	0.01	$\text{MPa} \cdot \text{m}$
Tl_0	Longitudinal transmissivity	0.0	m^2/s
K_t	Transversal conductivity	1.0	s^{-1}
α_{Biot}	Biot's coef.	1.0	s^{-1}
M_{Biot}	Biot's modulus	$1.0 \cdot 10^{10}$	

to high values. These parameters may be understood as penalty coefficients with high values in order to avoid excessive unrealistic elastic deformations at the interfaces. Therefore, in practice the resulting deformation of the fractures can be assumed to represent almost exclusively the inelastic behavior, that is, crack opening and shear slip. Low values of strength (tensile strength and cohesion) are selected in order to simulate existent fractures with very low or practically null cohesion (Boone and Ingraffea, 1990). The hydraulic behavior of the interface is controlled by the so-called *cubic law*. The summary of interface parameters is shown in Table 4.8.

4.2.3.b Model description

The objective of this Section is to reproduce in 3D one case already run with 2D analysis Garolera et al. (2013, 2014), in order to compare the results for validation. For this purpose, a 3D layer of 1m thickness, as depicted in Fig. 4.29, is analyzed. A fracture plane is placed vertically in the middle of the model. Figure 4.30 shows the linear mesh used for the simulations (8165 nodes), with diagram (a) showing the continuum mesh (30 545 tetrahedrons) and diagram (b) the fracture plane, which is composed of planar interface elements (1331 triangular zero-thickness interface elements). Due to the high gradients at the injection line, a finer discretization is used along this line.

The boundary conditions are applied in two steps (see Figure 4.31):

1. **Initial stress step**. A distributed compressive load of 1.0 MPa is applied over the entire outer boundary in order to simulate the *in situ* initial stress. Hydraulic pressure is assumed to be zero.

2. **Injection stress step**. During the injection step, the fluid flow is injected at the fracture mouth. Given the purpose of simulating conditions as close as possible to the 2D model, the flow rate is imposed all along the fracture mouth line, at the

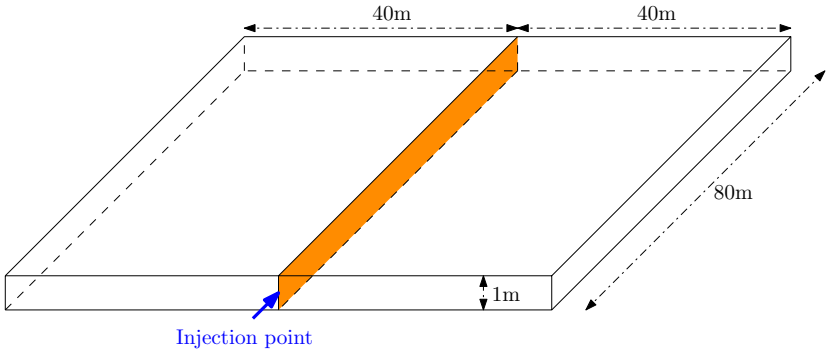

Figure 4.29: Scheme of the 3D model simulating plane strain conditions.

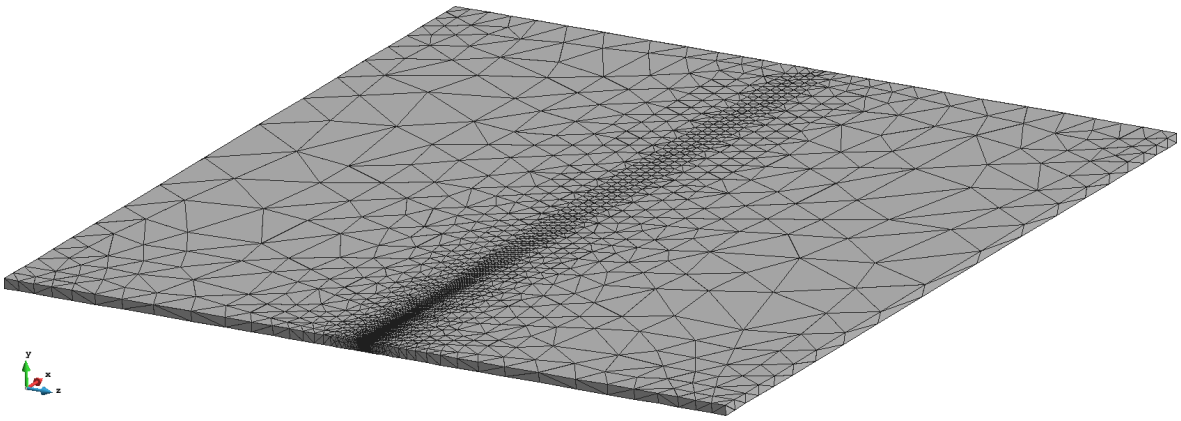

(a)

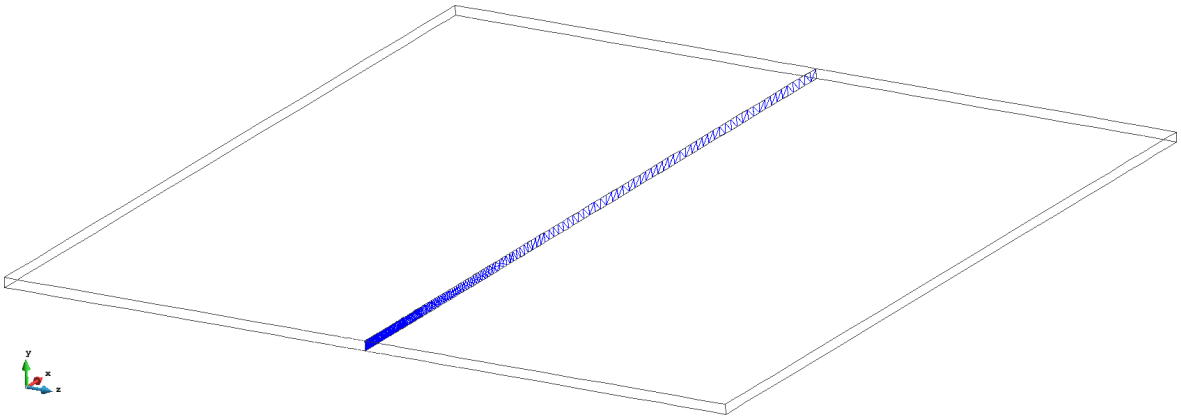

(b)

Figure 4.30: Model mesh; a) entire domain (continuum elements); and b) detail of the pre-establish fracture surface (interfaces).

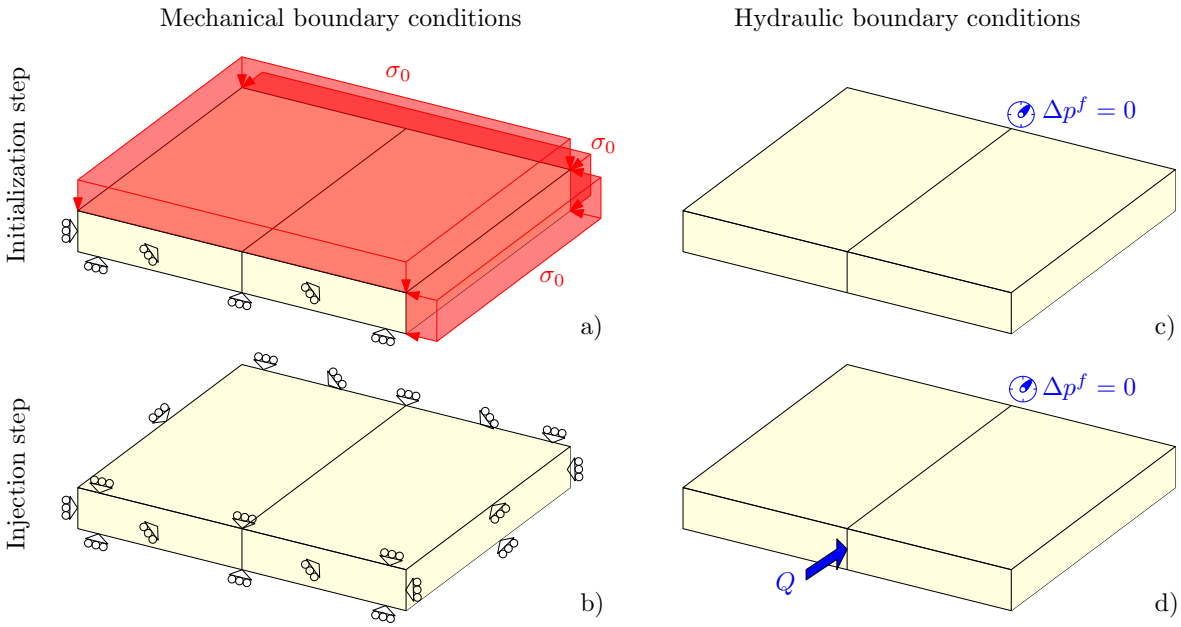

Figure 4.31: Boundary conditions for mechanical (left column) and flow (right columns), for each of the steps of the analysis (rows).

constant value of 0.0001 $m^3/s/m$ and during a time step of 25 s. The boundary conditions on the face at the opposite side of the injection correspond to a zero fluid pressure increment, while zero flow is assumed for the rest of the domain boundaries.

4.2.3.c Numerical Results and discussion

Figures 4.32 and 4.33 show the evolution of the crack mouth opening displacement (CMOD) and the evolution of the crack mouth pressure, for the first 25 s of injection. The results obtained with the 3D analysis assuming plane strain conditions are in good agreement with those results obtained with both analytical (GDK) and numerical solutions (Boone and Ingraffea and DRAC 2D). Therefore, the 3D model seems to be consistent with those results and can be considered preliminarily validated.

The final deformation of the fracture plane after the 25 s injection is depicted in Fig. 4.34. The left column shows a 3D image of the deformed fracture, and the right column shows a comparison between 2D and 3D, very similar in both cases, 7.90 m for 2D and 7.73 m in length for the 3D numerical results. It can be observed that the final length is also well captured by the analysis.

Figures 4.35 to 4.37 represent the fluid pressure distribution and the minimum and maximum effective stress after injection, respectively.

Figure 4.38 shows the evolution of the fracture opening profile over time.

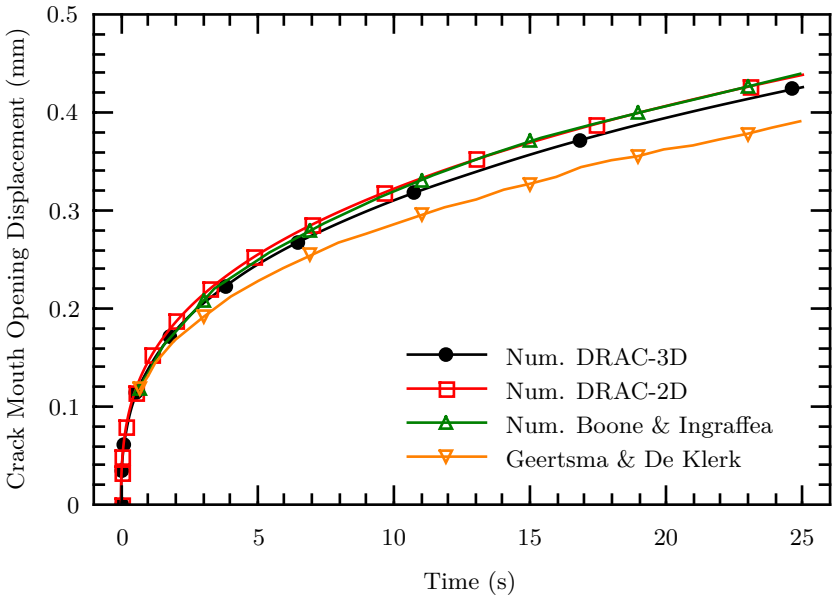

Figure 4.32: Crack Mouth Opening Displacement (CMOD) evolution. 3D results compared with analytical and 2D numerical solutions. Time expressed in log scale.

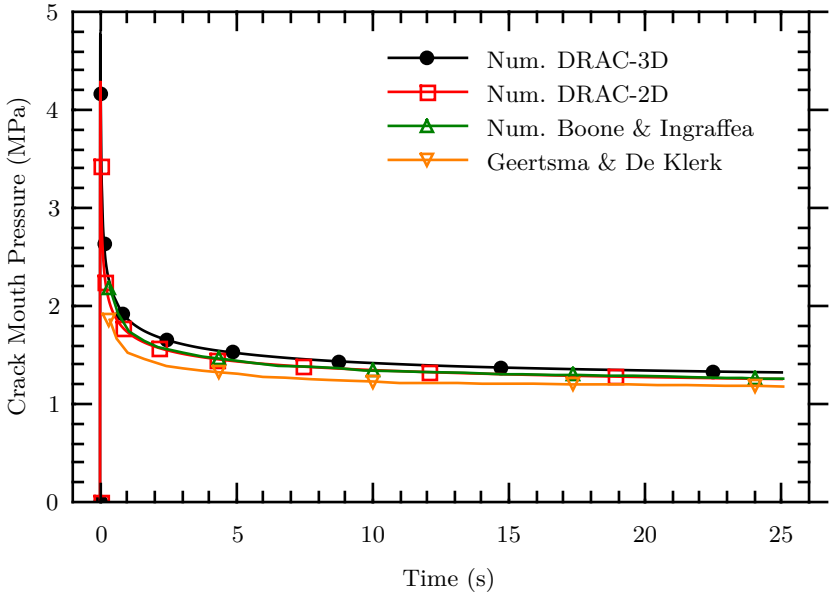

Figure 4.33: Crack Mouth Pressure (CMP) evolution. 3D results compared with analytical and 2D numerical solutions. Time expressed in log scale.

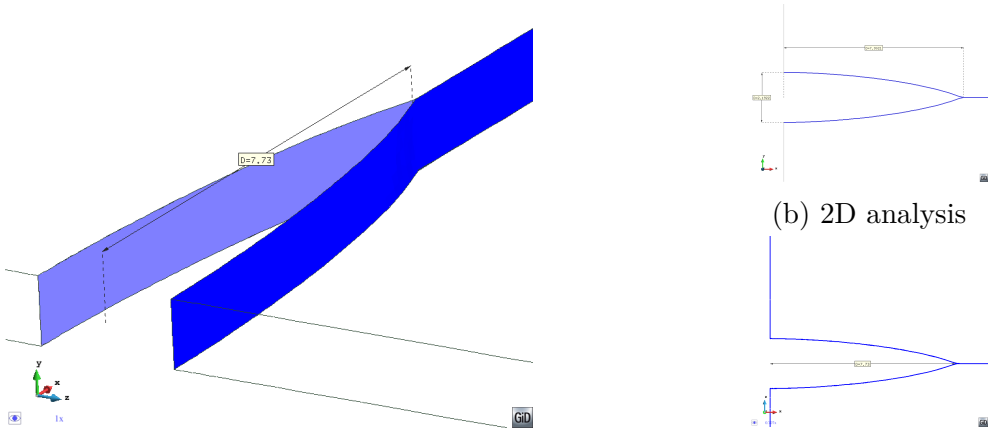

(a)

(b) 2D analysis

(c) 3D analysis

Figure 4.34: Deformation of fractured plane after 25 s. Left 3D deformation; and right comparison between 2D and 3D footprints (×5000 magnification).

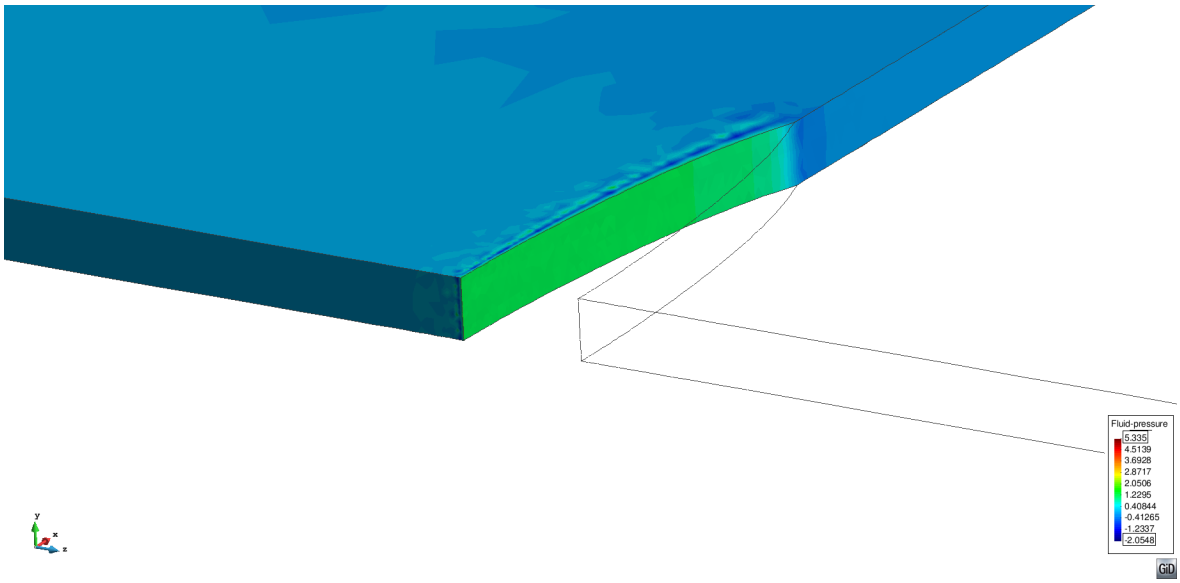

Figure 4.35: Fluid pressure distribution after stopping injection represented the over deformed mesh (×5000).

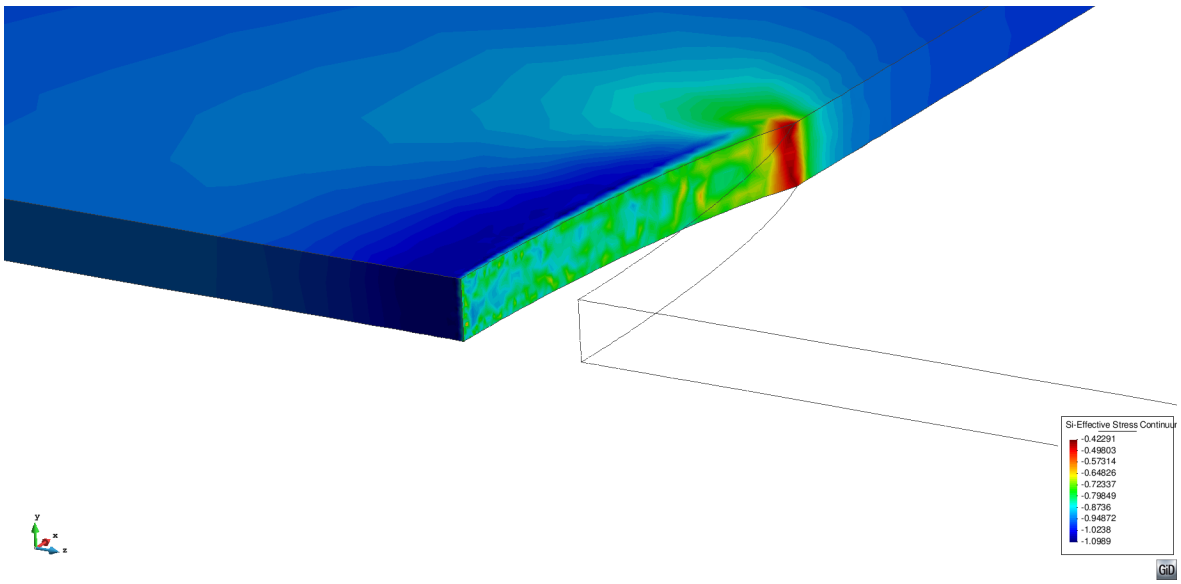

Figure 4.36: Minimum effective stress ($\sigma_1^{'}$) after stopping injection (time = 25 s) represented the over deformed mesh (×5000).

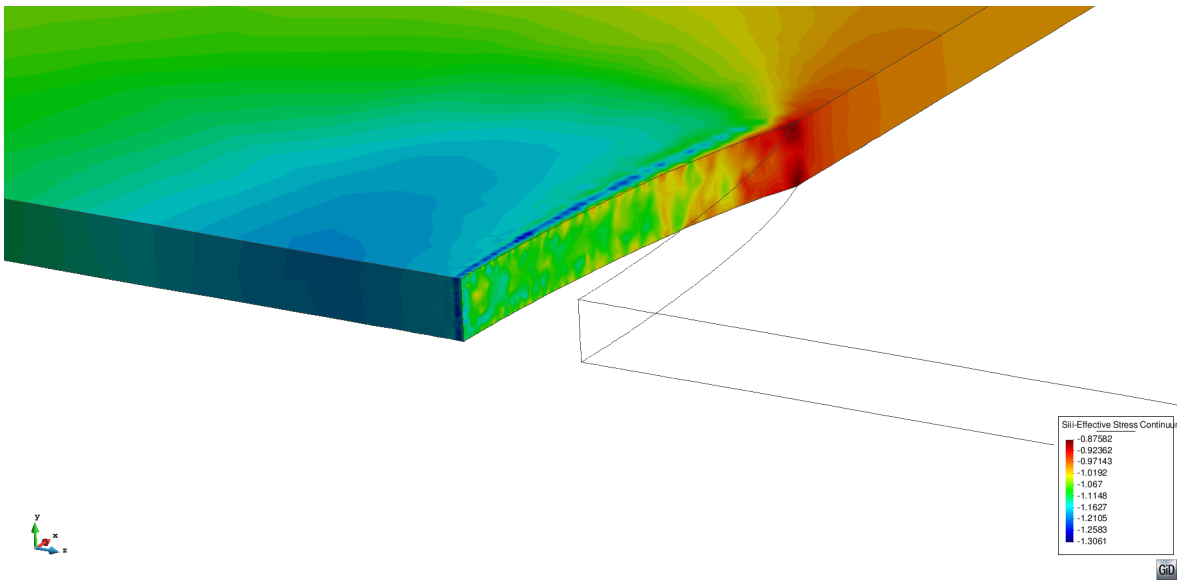

Figure 4.37: Maximum effective stress ($\sigma_3^{'}$) after stopping injection (time = 25 s) represented the over deformed mesh (×5000).

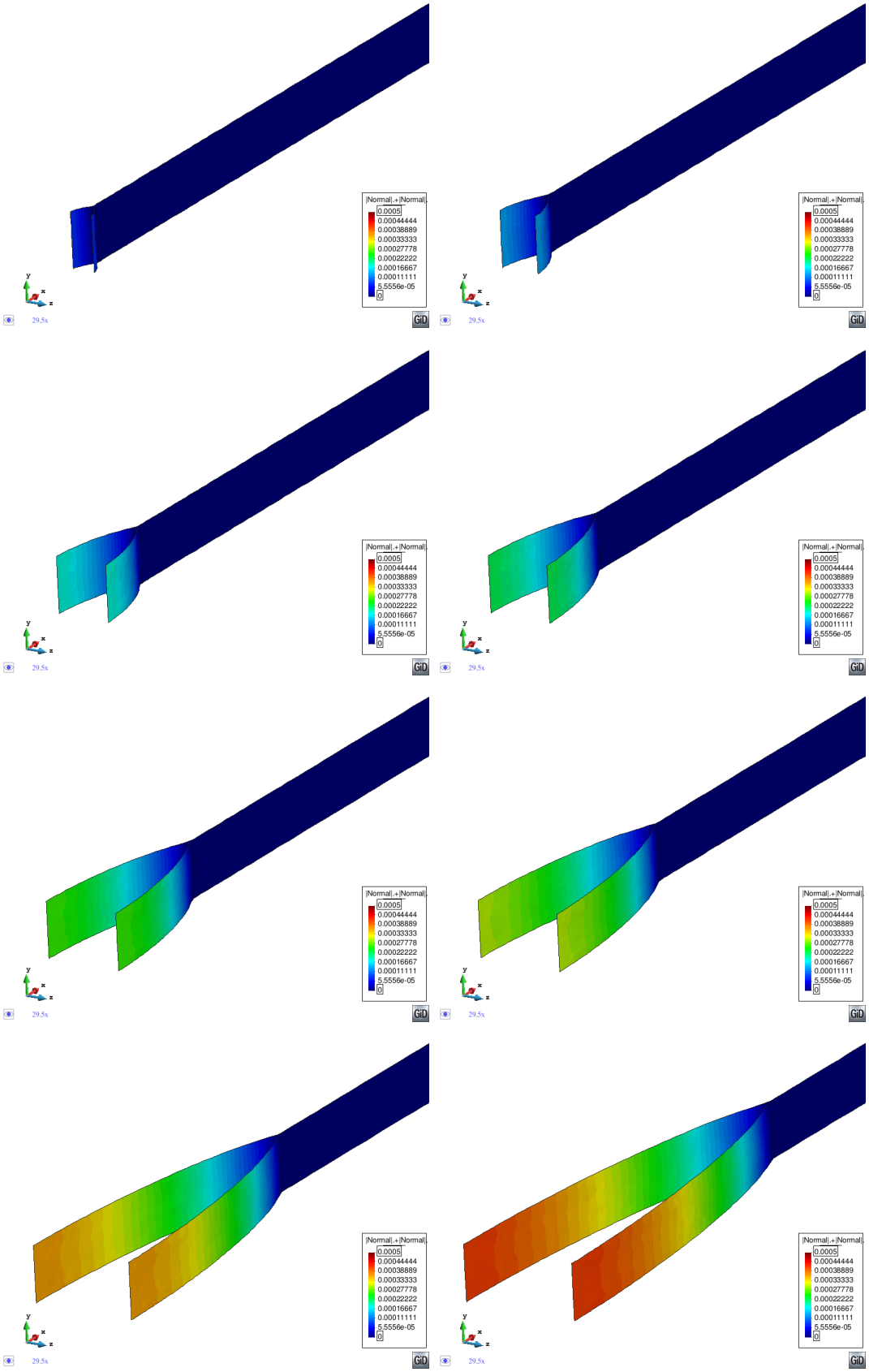

Figure 4.38: Evolution of fracture aperture (interface normal displacements). From left to right and top to bottom: 0.22 s, 0.94 s, 1.95 s, 3.97 s, 6.51 s, 10.50 s, 16.22 s and 25 s.

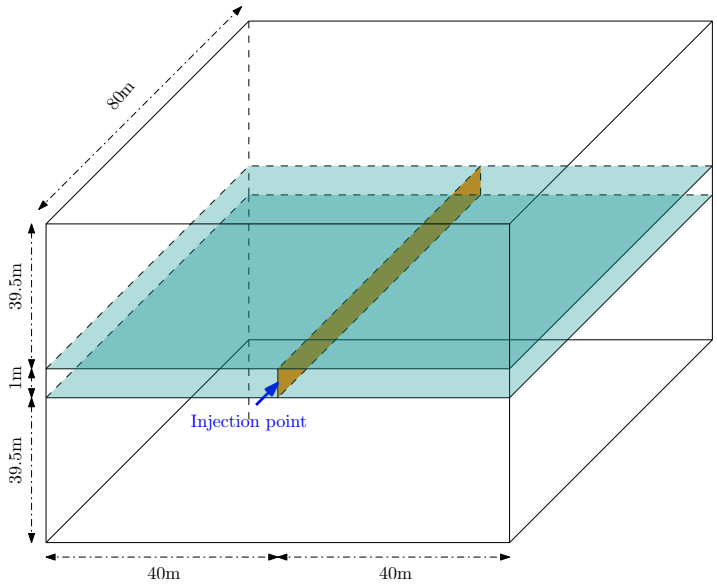

Figure 4.39: Scheme of the 3D model simulating triaxial boundary conditions.

4.2.4 Variable fracture aperture in height in 3D, PKN validation

4.2.4.a Model description

The second 3D simulation involves a cubic block of 80 m side. Zero-thickness interface elements are pre-inserted over the vertical mid-plane belonging to the middle layer including the potential fracture path. A second set of interface elements are located at each contact between the horizontal layers. The geometry of the model is illustrated in Fig. 4.39. Figure 4.40 shows the mesh of lienar elements used for the simulations (24 198 nodes). Figure 4.40(a) shows the continuum mesh (109 033 tetrahedrons) and Figs. 4.40(b) and 4.40(c) show the fracture planes and the layer discontinuities, which are composed of planar interface elements (9015 triangular zero-thickness interface elements). Due to the high gradients at the injection point, a finer discretization is used near the injection point.

In this analysis, the horizontal interface plane is assumed to be elastic with $K_n = 1000\,\mathrm{GPa}\cdot\mathrm{m}^{-1}$ and $K_t = 25\,\mathrm{GPa}\cdot\mathrm{m}^{-1}$.

The boundary conditions are applied in a single step (see figure 4.41), with a prescribed constant flow rate of $0.0001\,\mathrm{m}^3/\mathrm{s}$, during a time step of 25 s, at the mid-point of the fracture mouth. On the opposite side of the injection point, zero fluid-pressure conditions are imposed, while no flow is assumed for the rest of the boundary.

4.2.4.b Numerical Results and discussion

The results provided by the three-layer analysis give a general good agreement with PKN equations (Eqs. (4.4) to (4.6)). Figures 4.42 to 4.44 show the results obtained, evolution of CMOD, CMP and fracture length, toghether with the results obtained with the PKN equations. Figure 4.42 shows the crack mouth opening displacement

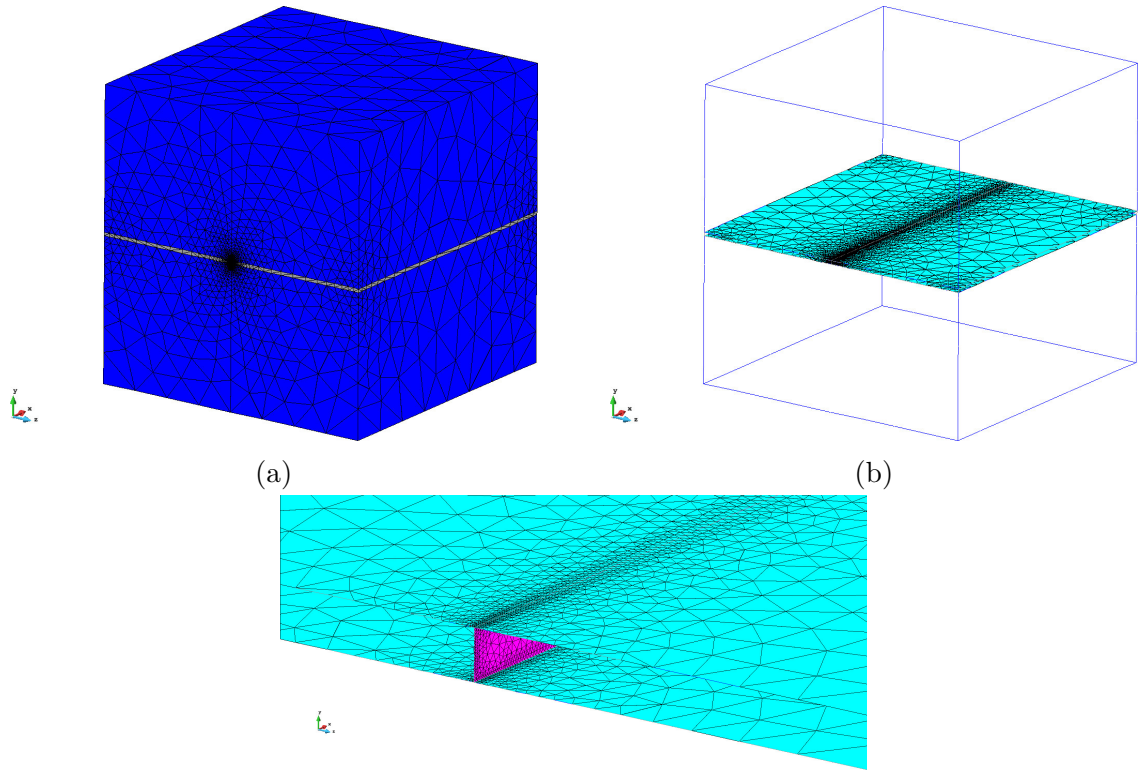

Figure 4.40: Model mesh; a) entire domain (continuum elements); b) fracture planes; and c) detail of the pre-established fracture surfaces at the crack mouth (interfaces).

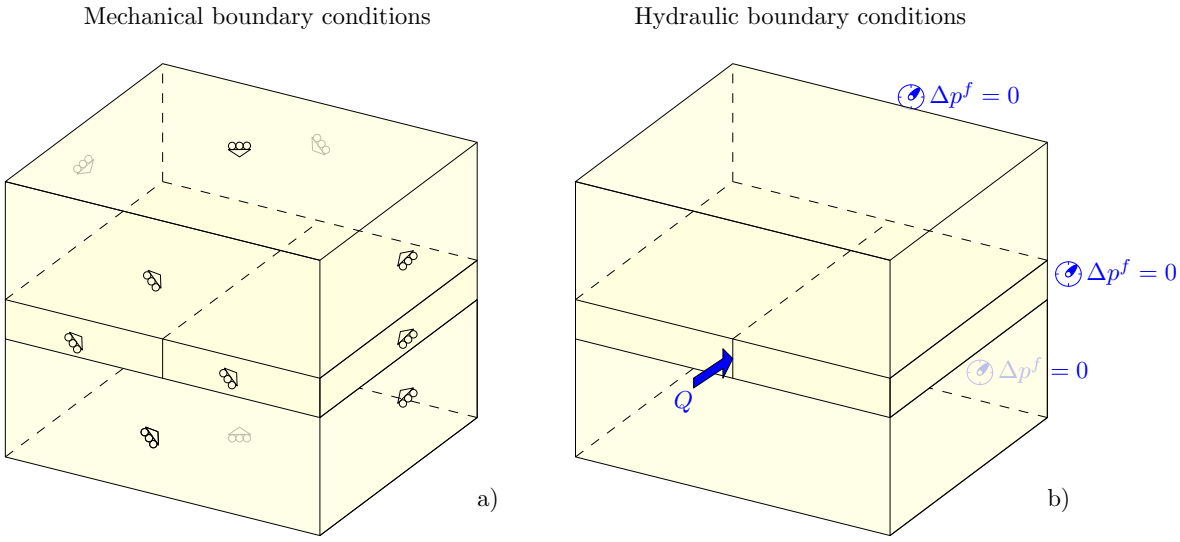

Figure 4.41: Boundary conditions for mechanical (left column) and flow (right columns).

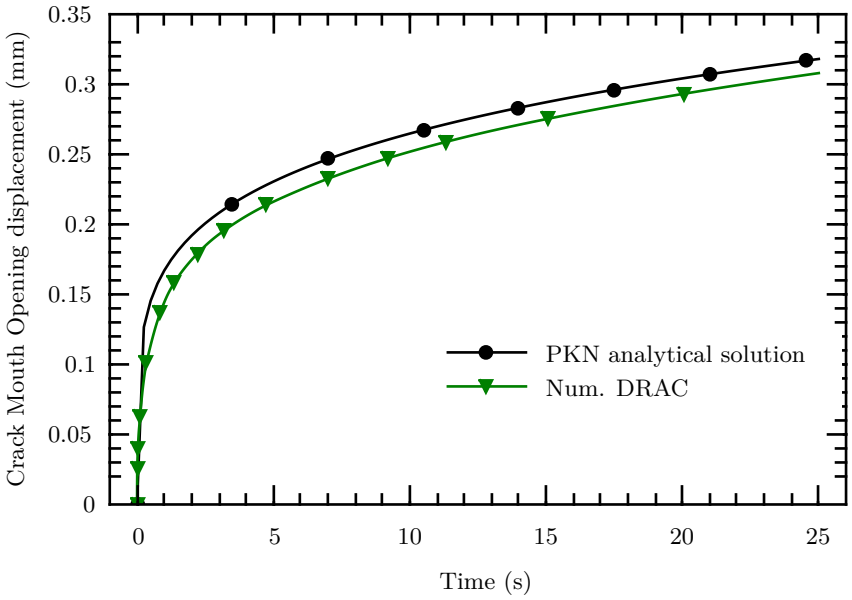

Figure 4.42: Evolution of crack mouth opening displacement (CMOD) compared to the analytical solution and to the single plane numerical solutions.

evolution (CMOD), which is slightly lower than the values obtained with the original PKN expressions. Figure 4.43 shows the crack-mouth pressure evolution (CMP), in which the analytical solution is slightly higher. Figure 4.44 shows the fracture-length evolution, which shows a little more discrepancy in comparison to the analytical Eq. (4.6).

Same as in the comparison to the GDK formulas (Section 4.1.3.a), the minor discrepancies observed with respect to the GDK model may be attributed to the differences in shape of the fracture opening near the fracture limits, which in the GDK has a predeterminated shape given by the assumed formula, while in the numerical analysis has no predeterminated shape and is simply part of the outcomes of the computations.

The distributions of normal interface aperture and fluid pressure, both for 25 s of injection, are presented in Figs. 4.45 and 4.46, respectively.

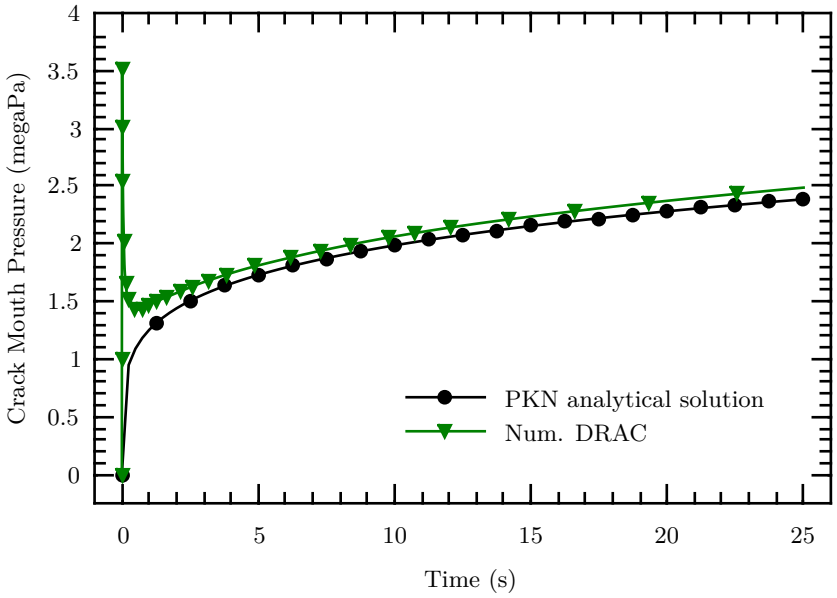

Figure 4.43: Evolution of crack mouth pressure (CMP) compared to the analytical solution and to the single plane numerical solutions.

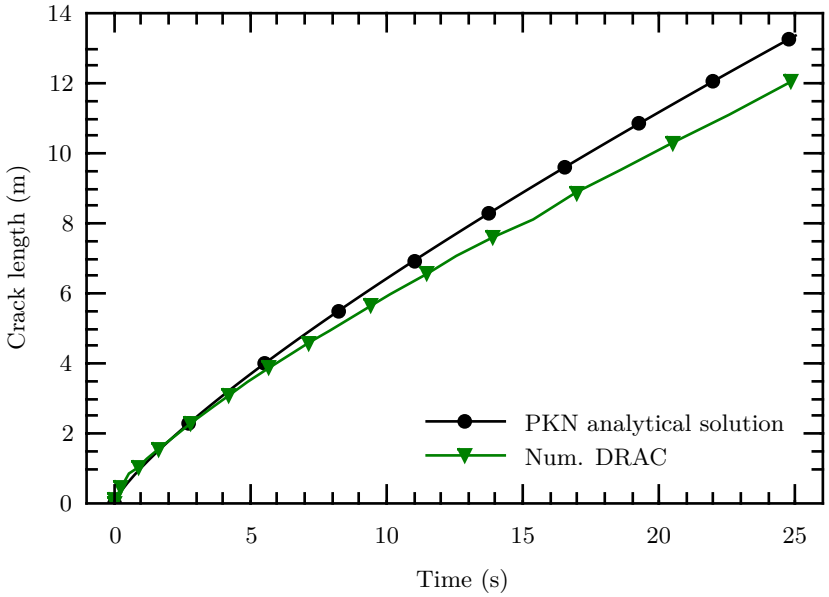

Figure 4.44: Evolution of the fracture length compared with the analytical solution and to the single plane numerical solutions.

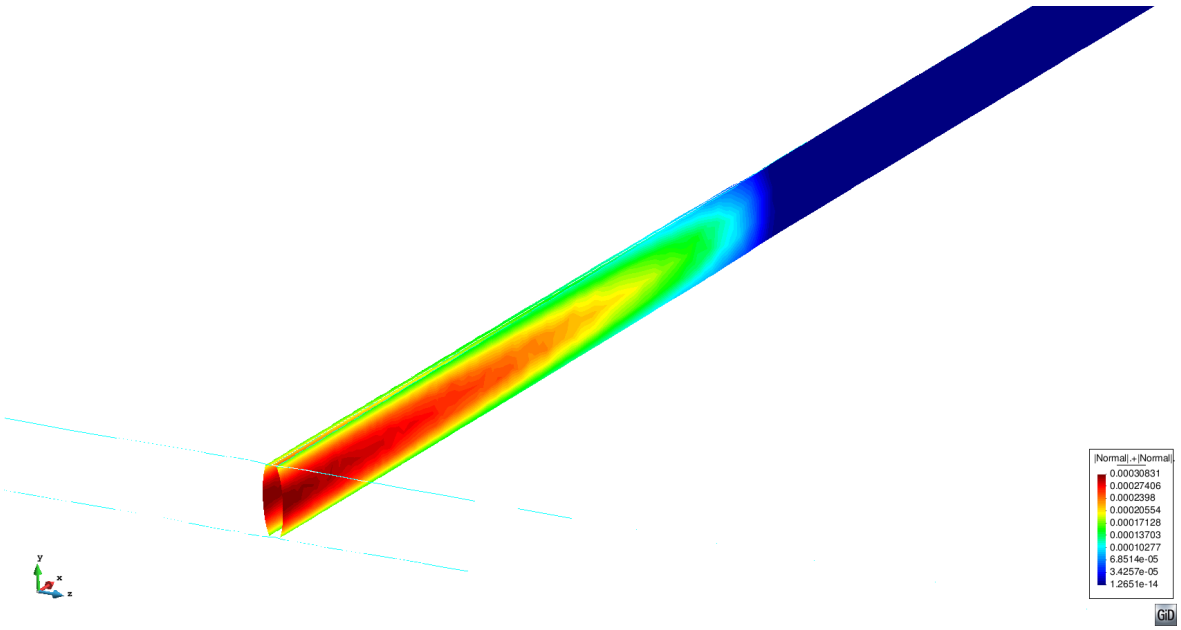

Figure 4.45: Normal aperture distribution at 25 s for each boundary condition plotted on the deformed mesh (×1000).

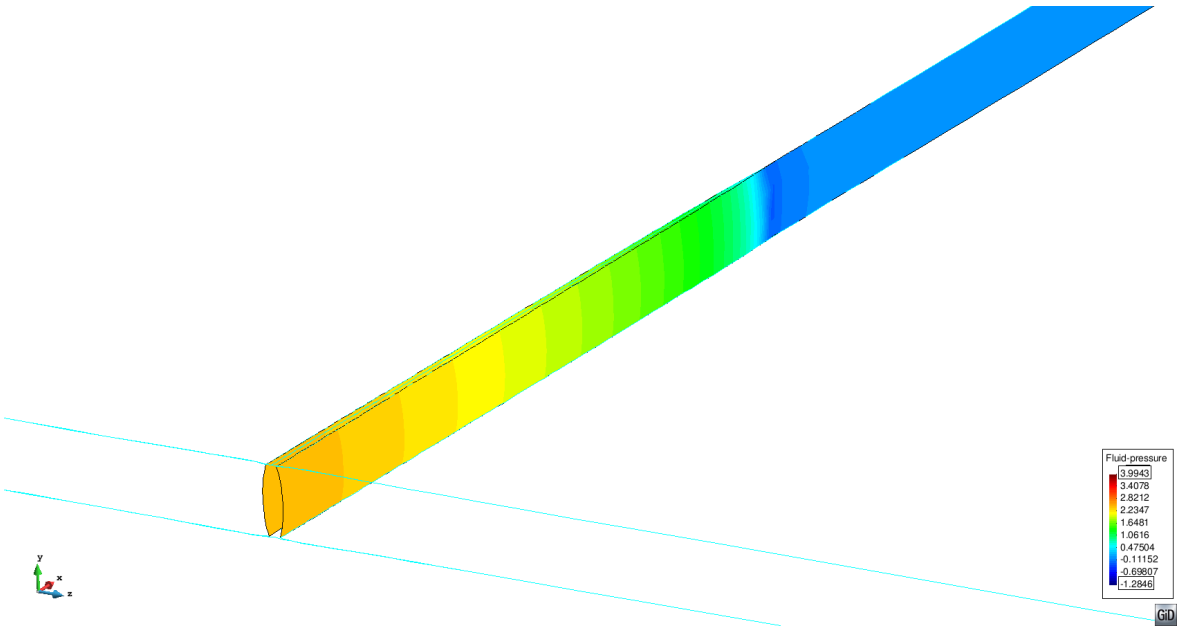

Figure 4.46: Fluid pressure distribution after stopping injection, plotted on the deformed mesh (×1000).

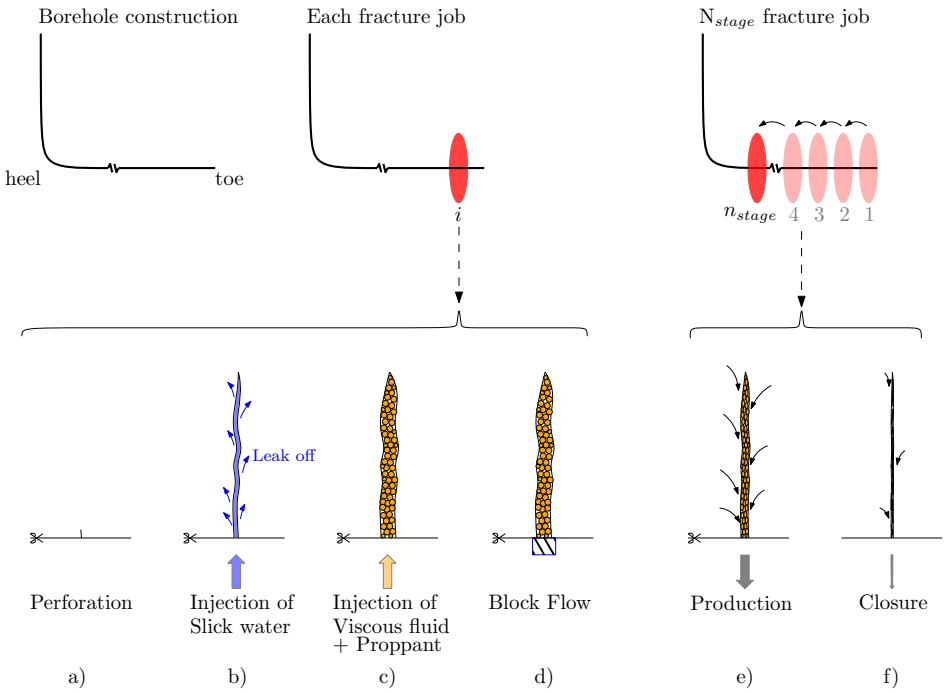

Figure 4.47: Schema of a working and multi-stage procedure

4.3 Multi-stage analysis in 2D with multiple fracture paths

Hydraulic fracture, as explained in Section 4.1, is a technique that may be used for several applications, among them the stimulation of large reservoir areas in order to mobilize the oil&gas occluded in the porosity. The recovery is carried out by extensive hydraulic fracturing treatments, that consist of parallel fractures usually originated from a horizontal well. After the construction of the borehole, several hydraulic fracture stages (or jobs) are made from toe to heel (see 4.47, top). Each job is divided in several steps (see Fig. 4.47, a)-d)). In low permeability formations, a low viscosity fluid ("slick water") is usually used at the beginning of the injection to facilitate the propagation of the fracture. Once the fracture has been created, the fluid viscosity is changed in order to facilitate solid transport and then injection of the proppant is started. Proppant is used to avoid premature closure of the fracture. Additionally in carbonate formations, acid may be injected to increase the roughness and therefore avoid perfect closure. Once the injection is stopped, the pressure is blocked with packers and new fracture job is started. Finally, when all fracture jobs have finished the packers are removed, and with the backflow, the injection fluids are recovered partially, and the production of hydrocarbon is started (Fig. 4.47e-f).

Most methods used for the numerical simulation of hydraulic fracture consider each fracture individually, discretizing only the fractured area and assuming continuum elastic material. This assumption is acceptable as a first approach, due to its low computational cost, and usually it is the method employed for common horizontal

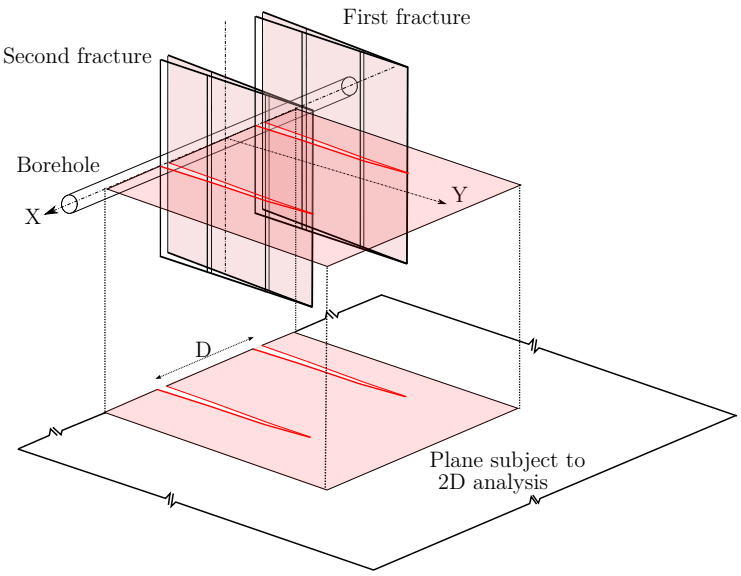

Figure 4.48: Scheme of the example of the interaction between two fractures out of a horizontal perforation.

completion simulations. However this procedure has an important drawback due to not considering the fracture interaction.

In this section, the capability of the proposed formulation to account for fracture interaction is illustrated. Several examples with increasing complexity are proposed in order to clarify the main contributing factors regarding fracture interaction. The first example is a two-stage case, which is focused on the study of the effect of spacing between stages. The second example is a five-stage simulation in which the fracture/trajectory is not pre-established. This example is focused mainly on analysis of the effect of *in situ* stress variation and the effect of interface strength.

4.3.1 Study of two-stage hydraulic fracture in 2D

4.3.1.a Model description

The main purpose of this example is to study the effects of fracture interaction. This effect takes place because any fracture modifies the local stress field around its neighborhood. In the case analyzed focus is made on the effect of spacing (D, see Fig. 4.48) between the subsequent injections (jobs) on the geometry of the resulting fractures.

The geometry considered is represented in Fig. 4.48. The first fracture is similar to those generated in Section 4.2, therefore the fracture is assumed to develop on a single vertical plane. The second fracture is given the possibility of different trajectories. To that end, a field of potential paths is pre-inserted in the mesh to allow fracture to chose its own path according to local stress conditions and a minimum energy criterion. As a first approach, the analysis is performed in 2D and assuming plane strain conditions.

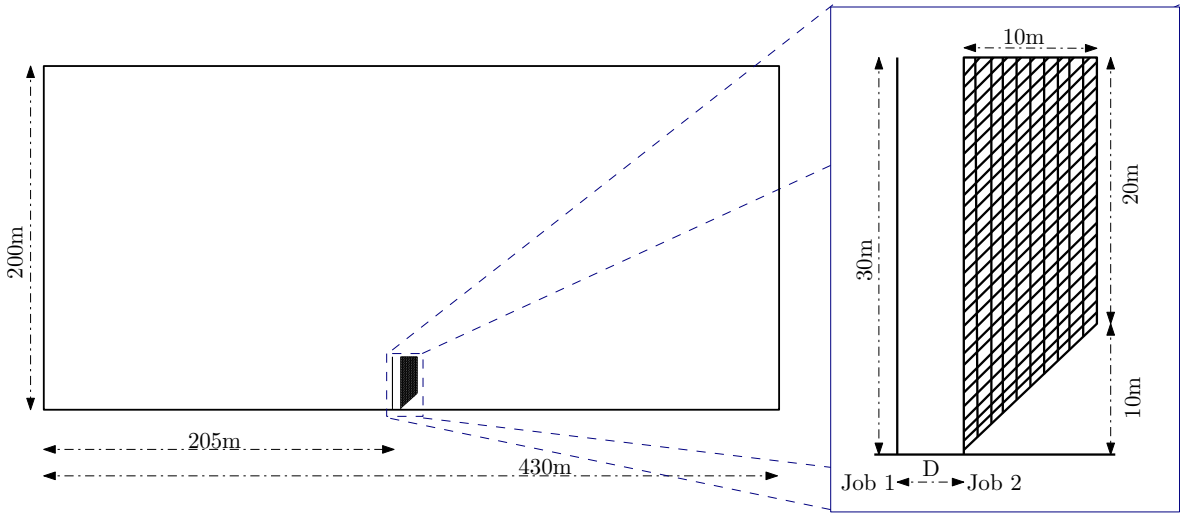

Figure 4.49: Geometry of the two-stage fracture case: left) domain geometry with the two fractures, and right) detail of geometry at injection points (only domain perimeter and interface elements represented).

The model geometry considered is sketched in Fig. 4.49. In order to avoid boundary effects, the domain is extended to around 200 m away from the fracture area. In this academic example, three spacing distances (D) are considered: a) 5 m, b) 10 m and c) 20 m.

The boundary conditions are applied in a sequence of three steps (see Fig. 4.50). The values of the injection rates and times are taken from those employed in examples from Section 4.2, which were based on Boone and Ingraffea (1990):

1. *Stress initialization.* In this step, a distributed load is applied over the external boundary: 1 MPa and 0.9 MPa are imposed on the Y- and X-axis, respectively. The slight difference of principal stresses ensures that the preferential fracture direction is the vertical direction.
2. *First fracture job.* A volumetric flow rate of $0.001\,\mathrm{m}^3/\mathrm{s}$ is injected at the first injection point for a period of 25 s.
3. *Second fracture job.* The flow rate in the first point is stopped and then the injection at the second point is started. Injection conditions are equal to the previous step: a flow rate of $0.001\,\mathrm{m}^3/\mathrm{s}$ during 25 s.

At constitutive level, the behavior and material properties used in this analysis elastic behavior for the continuum elements and fracture energy-based law for interface elements with parameters equal to those used in Section 4.2.2.

4.3.1.b Numerical Results and discussion

Low permeable scenario ($K = 10 \cdot 10^{-10}\,\mathrm{m}^2/\mathrm{s}$)

The numerical results, depicted in Table 4.9 and summarized Fig. 4.51, show a clear interaction between both fracture jobs. For the smallest separation, the second fracture

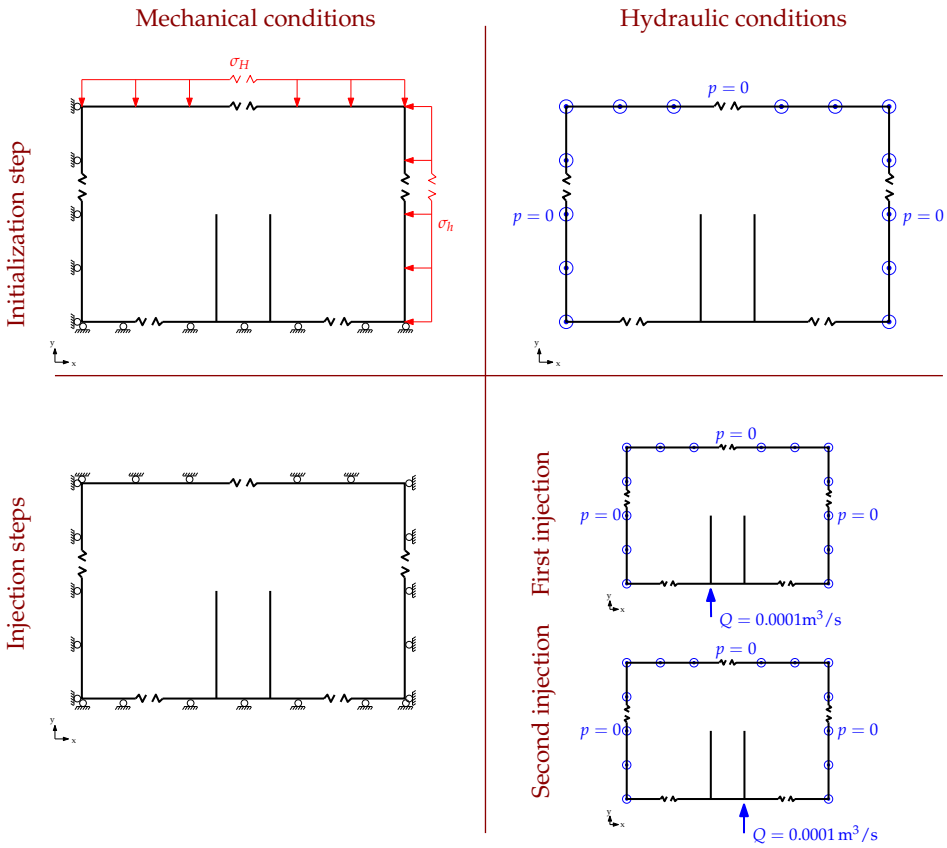

Figure 4.50: Boundary conditions for mechanical (upper diagrams) and flow (lower diagrams), for each of the two steps of the analysis (vertical columns).

clearly deviates from the vertical trajectory, that would not have been predicted by any model that considers each new fracture as if it were an isolated fracture (no interaction). For the other two cases with larger separation (D), there is a clear reduction of deviation (angle between the axis of the first fracture (y-axis) and the axis of the second fracture) as the spacing is increased, with very little interaction for largest separation case of $D = 20\,\mathrm{m}$.

Table 4.9: Trajectory of the second second fracture job for low continuum permeability ($K = 10 \cdot 10^{-10}\,\mathrm{m}^2/\mathrm{s}$).

	Spacing between fracture jobs (m)		
	a) 5	b) 10	c) 20
Total length (m)	8.11	7.77	7.78
Deviation [1]	37.08°	22.66°	7.12°

[1] Angle respect to Y axis.

Figure 4.52 shows the fluid pressure contours for the three cases analyzed. Note the limited penetration of fluid pressures into the continuum is due to the low permeability considered, and some minor oscillations in the solution due to the ill-conditioning associated to low permeability combined with the element size (more stable results

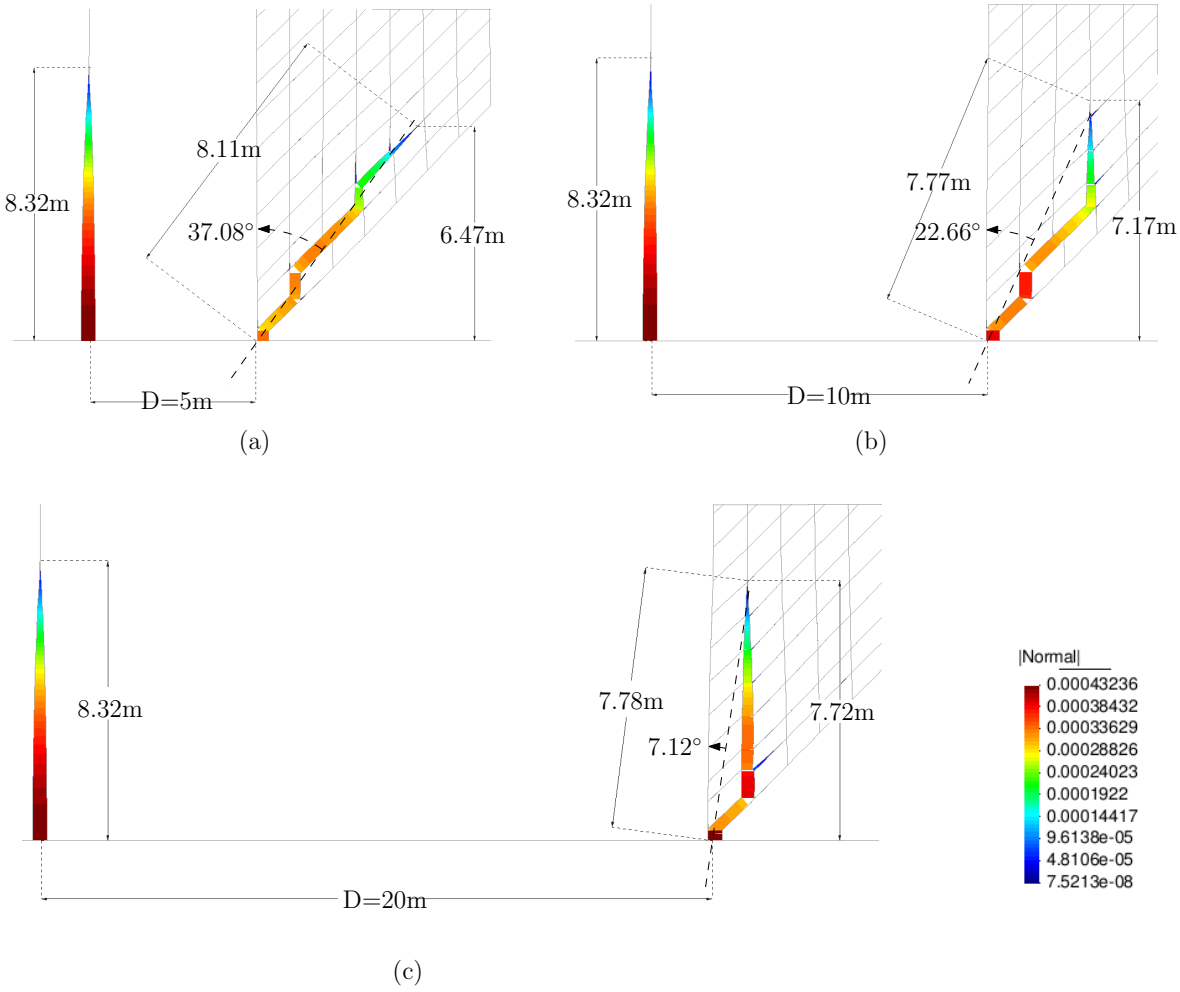

Figure 4.51: Fracture aperture (normal displacement) of low continuum permeability analysis ($K = 1.0 \cdot 10^{-10}\,\mathrm{m}^2/\mathrm{s}$), for spacing D equal to: a) 5 m, b) 10 m and c) 20 m.

would require finer meshes with higher computation times).

Figure 4.53 shows the contours of the intensity of maximum compressive principal stress, after the first fracture (a), and after the second fracture (b). In the first one, the stress is increased with respect to the original initial stress near the fracture mouth, but decreases ahead of the fracture tip. In Fig. 4.53(b), note also the higher compression generated around the crack mouth of the second fracture, since the opening occurs in a zone affected by the compression created by the first fracture.

Higher permeability scenario ($K = 10 \cdot 10^{-8}\,\mathrm{m}^2/\mathrm{s}$)

A sensitivity analysis of the results with respect to the continuum permeability has also been carried out. For this purpose, the same geometric configuration was run considering a higher value of the rock permeability ($K = 1.0 \cdot 10^{-8}\,\mathrm{m}^2/\mathrm{s}$).

According to the results summarized in Table 4.10, and comparing them with those presented in Table 4.9, the change of permeability has a non-negligible effect over the final geometry of the open fractures: note an average reduction of around 15% in total length and a slight difference in the fracture direction for the intermediate separation of 10 m (see Fig. 4.54).

Table 4.10: Trajectory of the second fracture job, for intermediate value of continuum permeability ($K = 10 \cdot 10^{-8}\,\mathrm{m}^2/\mathrm{s}$).

	Spacing between fracture jobs (m)		
	a)	b)	c)
Total length (m)	6.77	6.85	6.97
Deviation [1]	26.28°	25.93°	8.13°

[1] Angle respect to Y axis.

In Fig. 4.55 the pressure contours are depicted for the cases with fracture separation 5 m and 10 m. Note the wider zone affected by pressure changes and the absence of instabilities in the results, as compared to the lower permeability case (Fig. 4.52a, b)

In Fig. 4.56, the maximum compressive principal effective stress, after the first and second injection, is represented for the entire mesh in the form of arrows for each Gauss point of the continuum elements. At the remote locations the maximum horizontal stresses are oriented with the y-axis. Note the perturbation of the field induced by the first fracture injection; the main principal stress near the fracture mouth become horizontal. However, upon second injection, the max effective compression near the second fracture becomes approximately perpendicular to it, which given the zig-zagging fracture leads to a more intricate stress state in that area.

As a summary, this basic example demonstrates the interaction between fracture jobs. The modification of the spacing between injections (jobs) shows a clear effect.

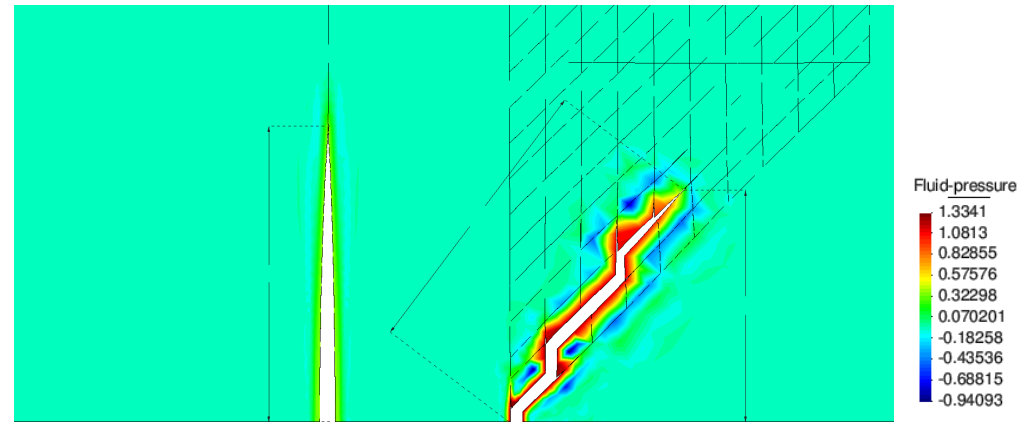

(a)

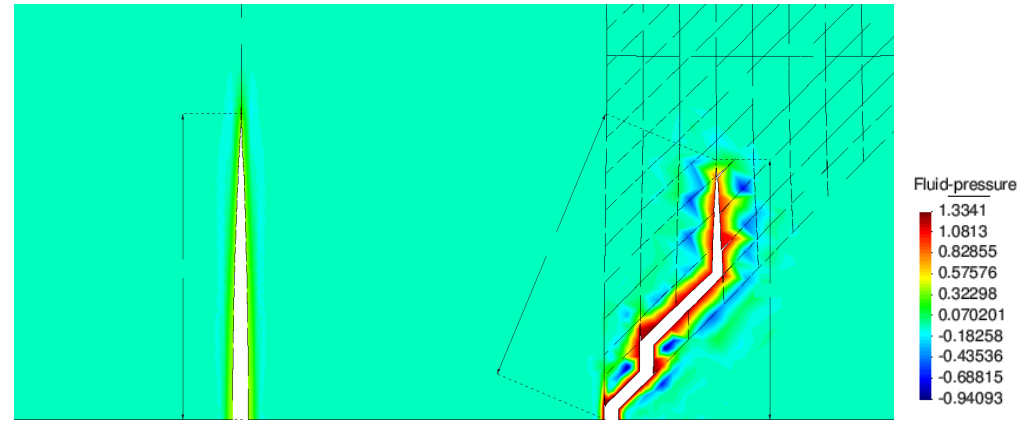

(b)

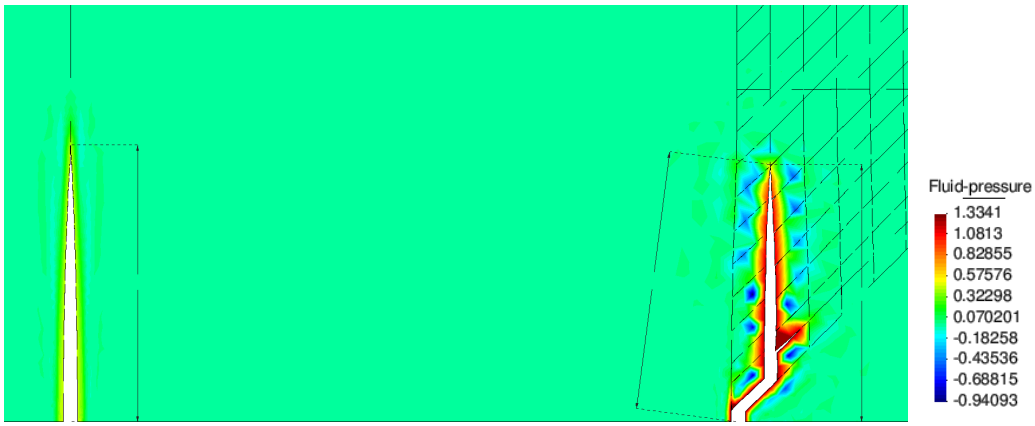

(c)

Figure 4.52: Fluid pressure distribution at the end of the second fracture job. Analysis considering low continuum permeability ($K = 1.0 \cdot 10^{-10}\,\mathrm{m}^2/\mathrm{s}$). Spacing configurations: a) 5 m , b) 10 m and c) 20 m.

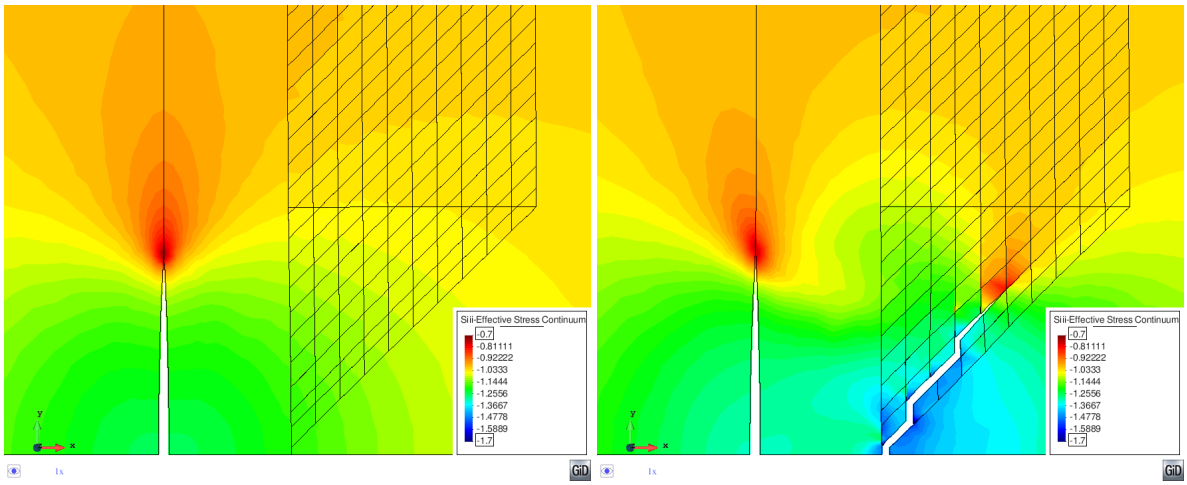

(a) First injection. (b) Second injection.

Figure 4.53: Maximum compressive stress contours σ_3, for case $D = 5\,\mathrm{m}$; with low continuum permeability ($K = 1.0 \cdot 10^{-10}\,\mathrm{m}^2/\mathrm{s}$).

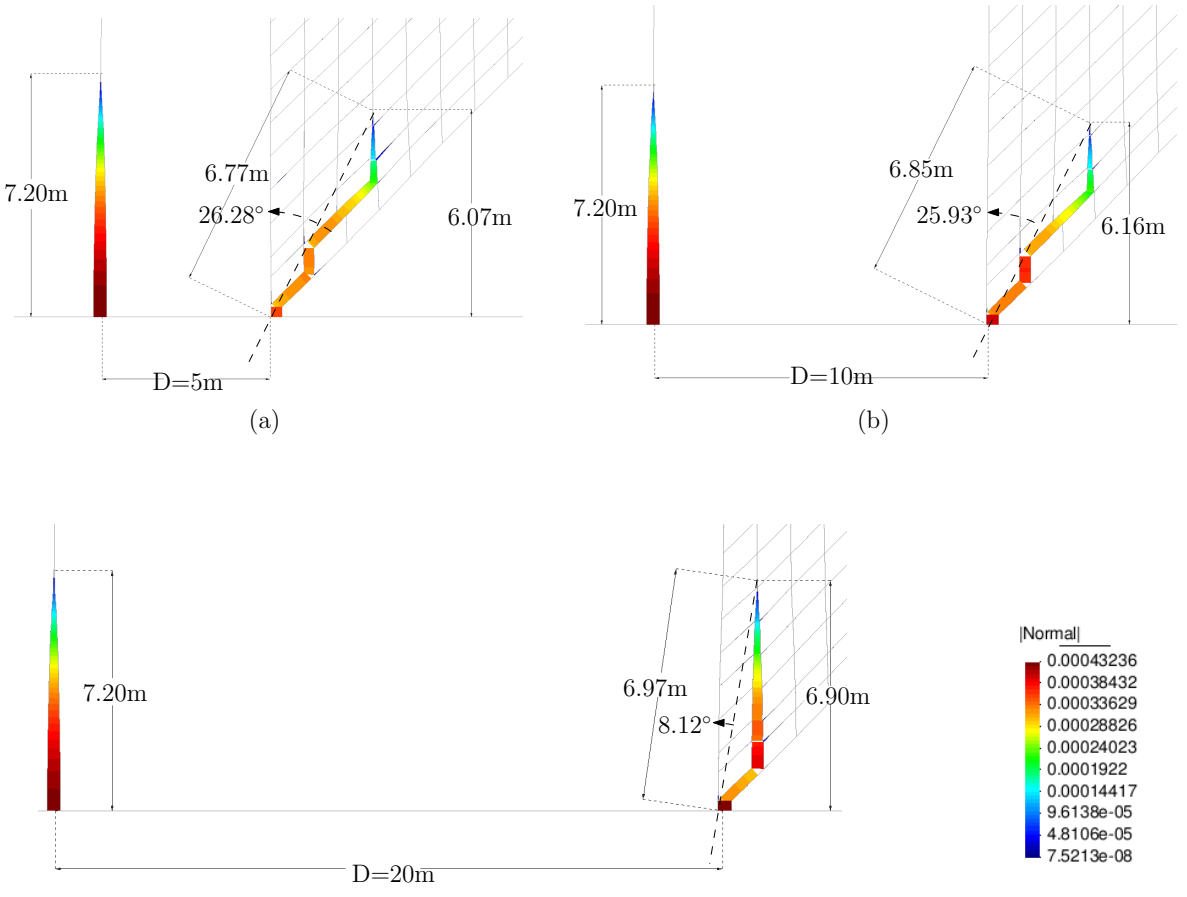

Figure 4.54: Fracture aperture (normal displacement) for the analysis with an intermediate value of continuum permeability ($K = 1.0 \cdot 10^{-8}\,\mathrm{m}^2/\mathrm{s}$). Spacing configurations: a) 5 m, b) 10 m and c) 20 m.

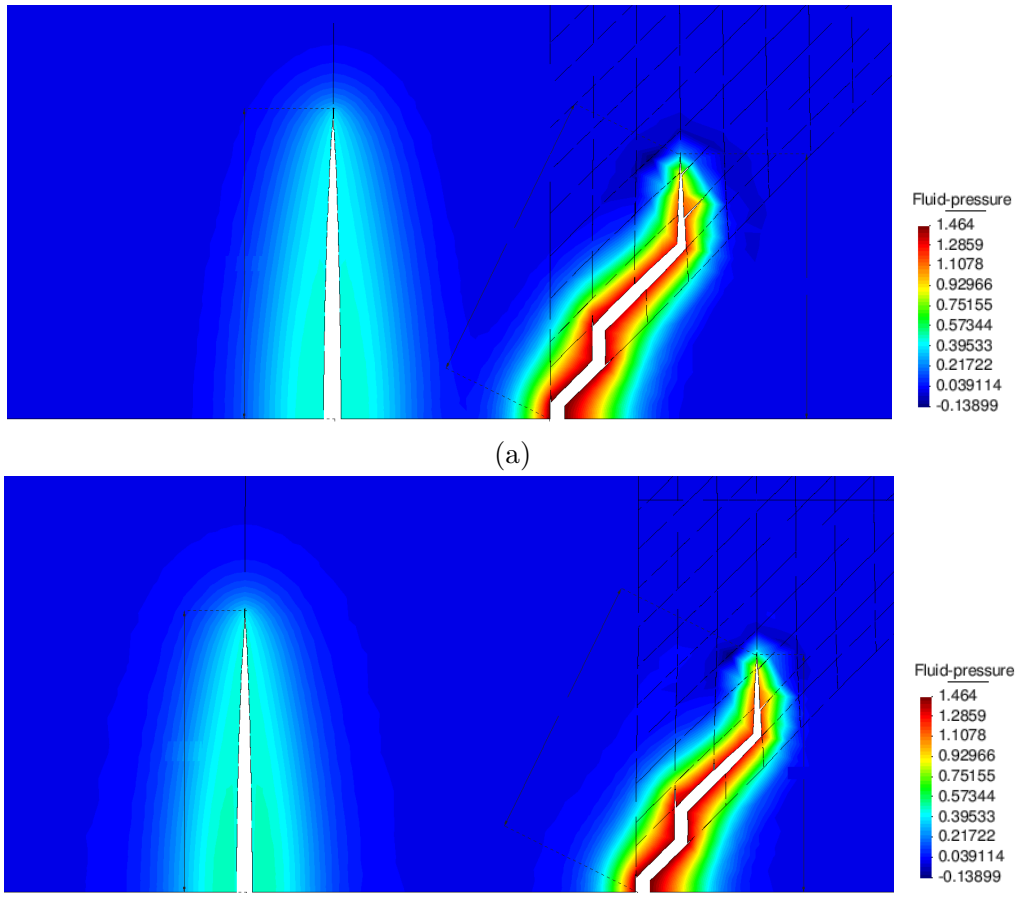

Figure 4.55: Fluid pressure distribution at the end of the second fracture job. Analysis considering intermediate value of the continuum permeability ($K = 10 \cdot 10^{-8}\,\mathrm{m}^2/\mathrm{s}$). Spacing configurations: a) 5 m and b) 10 m

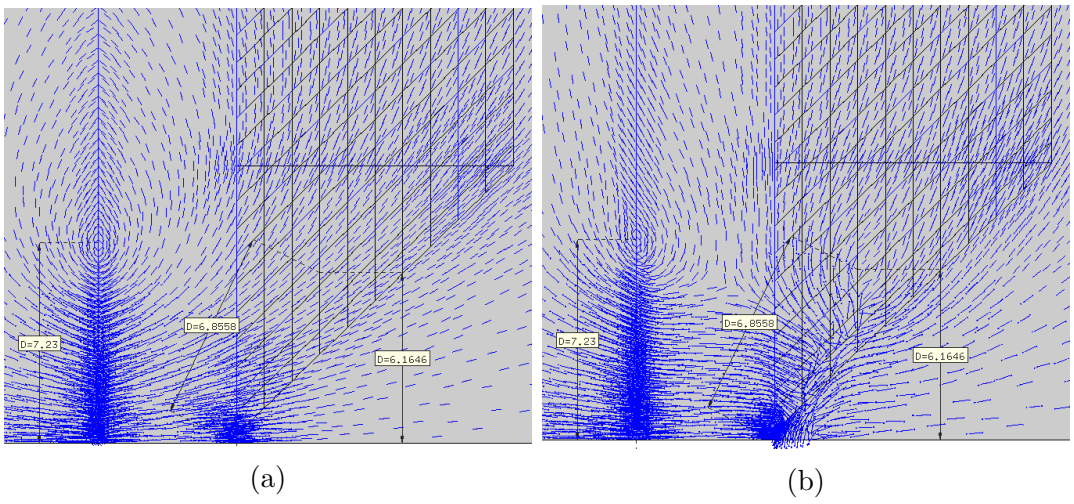

Figure 4.56: Principal stresses after: a) the first fracture job, and b) the second fracture job, both considering the intermediate value of the continuum permeability ($K = 1.0 \cdot 10^{-8}\,\mathrm{m}^2/\mathrm{s}$) and the smallest separation ($D = 5\,\mathrm{m}$).

Additionally, the effect of change of continuum hydraulic conductivity has been analyzed, an increase of this parameter seems to decrease the fracture interaction. This effect must be related to the reduction of fracture propagation due to the increase of leak-off effect.

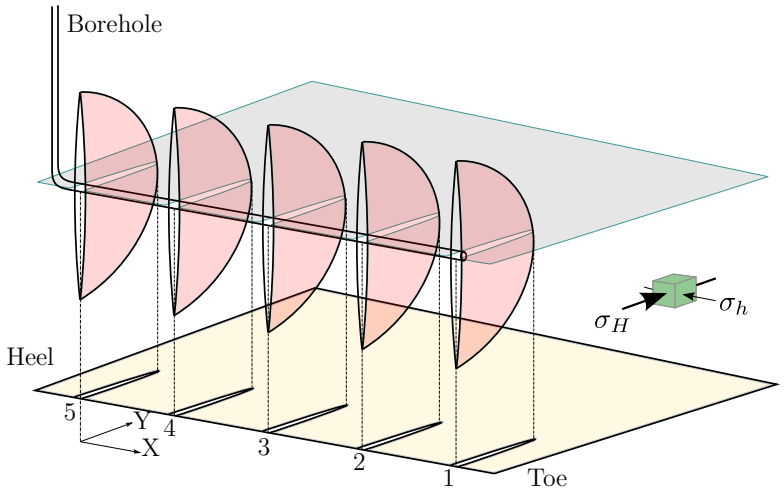

Figure 4.57: Scheme of five-stage fracture test.

4.3.2 Study of five-stage hydraulic fracturing in 2D

The study presented in this section is the analysis of multiple interacting hydraulic fractures using an academic example of 5 fracture jobs in a horizontal perforation (Fig. 4.57). The main purpose of this study is to show the influence of previous hydraulic fractures on a subsequent fracture.

4.3.2.a Model description

The main changes with respect to previous case (Section 4.3.1), are the more refined mesh discretization and the increase of the number of fracture jobs considered.

Geometry

The physical configuration of five fracture jobs in a horizontal perforation together with its 2D representation for the analysis, are depicted in Fig. 4.57. The domain considered for the numerical analysis is decomposed of two subdomains (see Fig. 4.58):

- A *Fractured subdomain*, which includes the zone in which the fractures can propagate (Fig. 4.58b), is discretized with a relatively dense FE mesh in which a netwok of interfaces is pre-inserted in between most continuum elements (Fig. 4.58c), with the purpose of allowing for sufficient freedom in the propagation of the fractures without predefined trajectories.

- A *Continuum subdomain*, which corresponds to the surrounding domain farer from the fractures themselves, and consists standard or continuum elements with-

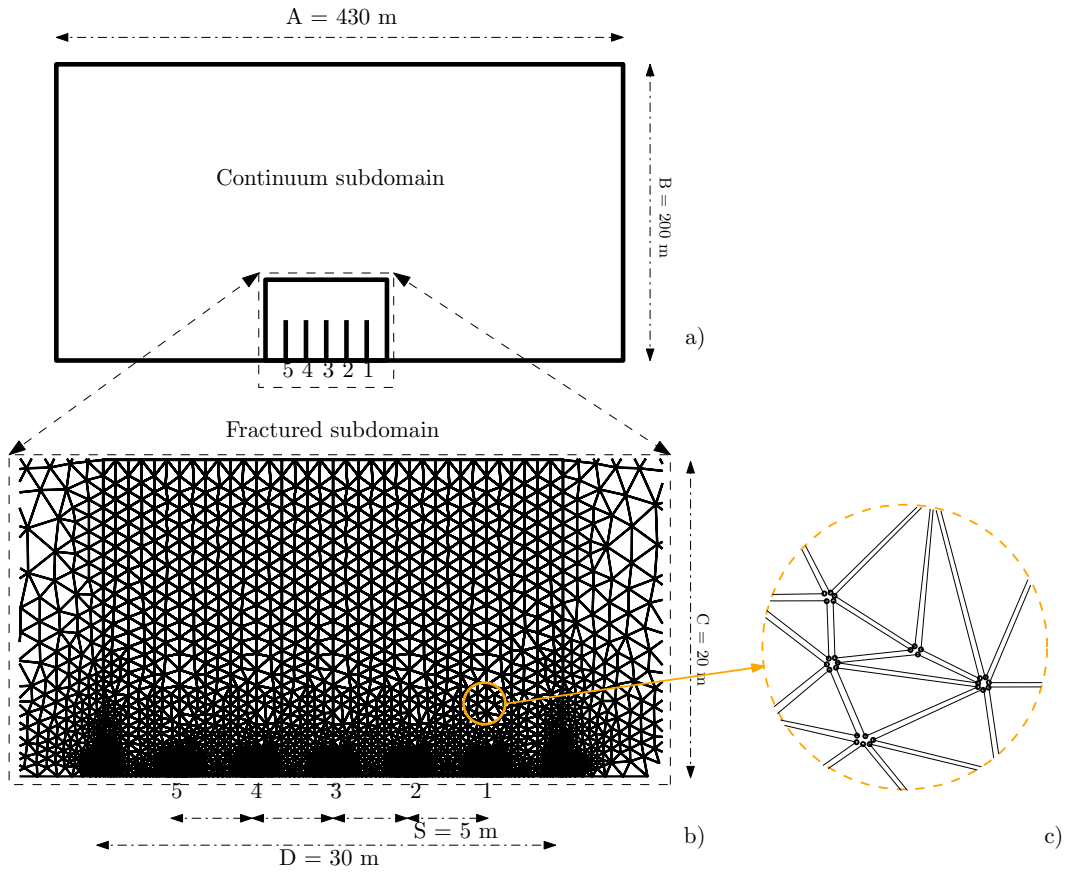

Figure 4.58: 2D model geometry for five-stage fracture test; a) full domain with lines along subdomain limits and along straight crack paths, no interaction were considered; b) potential fracture lines within inner subdomain, with position of injection points; and c) detail of network of interface elements inserted between continuum element. All dimensions are in meters.

out interfaces (Fig. 4.58a). This outer subdomain extends sufficiently far from the fractures to avoid boundary effects.

In this model the injection points are distributed along the x-axis (horizontal well) with fixed spacing of 5 m. Finally, as a first (2D) approach, the analysis is performed assuming plane strain conditions. Note that in order to avoid perturbations due to boundary conditions, the external boundary is taken around 200 m away from the interest area. In the fractured subdomain (Fig. 4.58b) zero-thickness interface elements are introduced between each pair of continuum elements. To ensure compatibility between the two subdomains, elastic interface elements are introduced all along the perimeter between the (outer) continuous and the (inner) fracture subdomains.

Material properties

The material properties used in the simulations are given below. For the continuum elements, an elastic isotropic material is assumed. Regarding the hydraulic behavior, a practically impervious material is selected. All parameters are displayed in Table 4.11.

Table 4.11: Material properties of continuum.

Parameter		*Value*	*Units*
E	Young's modulus	14 400	MPa
ν	Poisson's ratio	0.2	-
K	Hydraulic conductivity	$1 \cdot 10^{-15}$	$m \cdot s^{-1}$
Ks	Solid compressibility	36 000	MPa
α	Biot coef.	1.0	-

Table 4.12: Material properties of interfaces.

Parameter		*Value*	*Units*
K_n	Normal stiffness	$1 \cdot 10^{-6}$	$MPa \cdot m^{-1}$
K_t	Tangential stiffness	$1 \cdot 10^{-6}$	$MPa \cdot m^{-1}$
χ_0	Tensile strength	0.05	MPa
$\tan(\phi)$	Friction angle	0.2 (11.3°)	
c_0	Cohesion	0.5	MPa
G_f^I	Energy mode I	0.001	$MPa \cdot m$
G_f^{IIa}	Energy mode IIa	0.01	$MPa \cdot m$
T_{l_0}	Ini. Long. transmi.	0.0	m^2/s
K_t^p	Trans. conduc.	1.0	s^{-1}

For the mechanical behavior of the interface elements, normal and shear stiffness are assigned high values. These parameters may be understood as penalty coefficients with high values in order to avoid excessive unrealistic elastic deformations at the interfaces. Therefore, in practice the resulting deformation of the fractures can be assumed to represent almost exclusively the inelastic behavior, that is, crack opening and shear slip.

The constitutive model used for the fractures is the elastoplastic constitutive formulation with fracture energy-based evolution laws described in detail in Carol et al. (1997). Low values of strength (tensile strength and cohesion) are selected in order to simulate existing fractures with very low or practically null cohesion Boone and Ingraffea (1990). The hydraulic behavior of the interface is controlled by the so-called "cubic law" Eq. (2.75) (§2.2.4.a). The summary of interface parameters is given in Table 4.12.

Boundary conditions The boundary conditions are applied in a sequence of six steps (see Fig. 4.59):

Step 1: Stress initialization. In this step, a distributed load is applied over the external boundary: 1.0 MPa is imposed in the y-direction (σ_H). For the x-axis three cases are considered: 0.5 MPa, 0.7 MPa and 0.9 MPa (values of σ_h). The difference of principal stresses ensures that the preferential fracture direction will be the y-direction (see Fig. 4.58, first row).

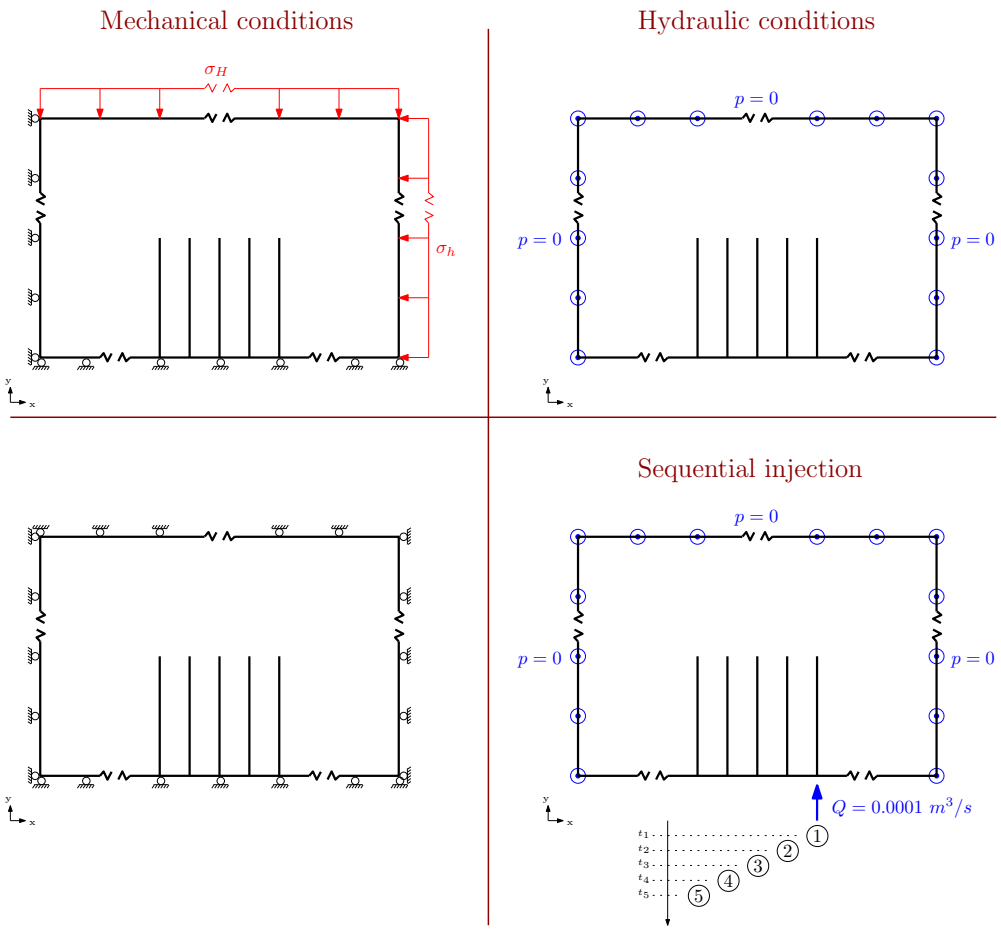

Figure 4.59: Boundary conditions for mechanical (left column) and flow (right column), for each of all the steps of the analysis (rows) in the two injection sequences considered.

Steps 2-6: Single fracture jobs. A flow rate of $Q = 0.001\,\mathrm{m}^3/\mathrm{s}$ is injected at the corresponding injection point during 25 s. This step is repeated starting from job 1 and finishing at job 5 (see Fig. 4.58, second row)

4.3.2.b Numerical Results and discussion

As already said, the objective of this study case was to learn about the interaction between subsequent fracturing jobs. The interaction is caused by the modification of the effective stress field during fracture propagation. For this purpose, several computations were performed focusing on the effect of the *in situ* stress anisotropy. In particular, three scenarios with different ratio between maximum (σ_H) and minimum (σ_h) horizontal stress were run. All calculations assume the same maximum compression applied along the y-axis (on top and bottom limits of the domain), and different levels of minimum compression applied over x-axis.

Additionally, the effect of interface properties and the mesh objectivity is also evaluated and presented in following subsections.

The results with stress anisotropy of 0.7 in the horizontal plane[1] ($\sigma_h = 0.7\sigma_H$) are presented below. This case is used as a base case for further comparisons. Figure 4.60 shows the evolution of fluid pressure and Fig. 4.61 shows the effective stress distribution. In both cases, the results represented correspond to the end of each injection stage (just before the following job is started for injections 1-4, or the very final stage of the analysis after injection 5 is completed).

A slight interaction between fractures may seem to start appearing already from the second injection, although a clear interaction is not observed until the fifth and last injection, when the fracture clearly deviates from the initial vertical trajectory. It is possible that these results may be slightly affected by the mesh layout, although after various tentative calculations these effects seem not to be very significant, and a more detailed analysis of this influence is left for a later study.

[1] It is considered that σ_H is oriented along the y-axis.

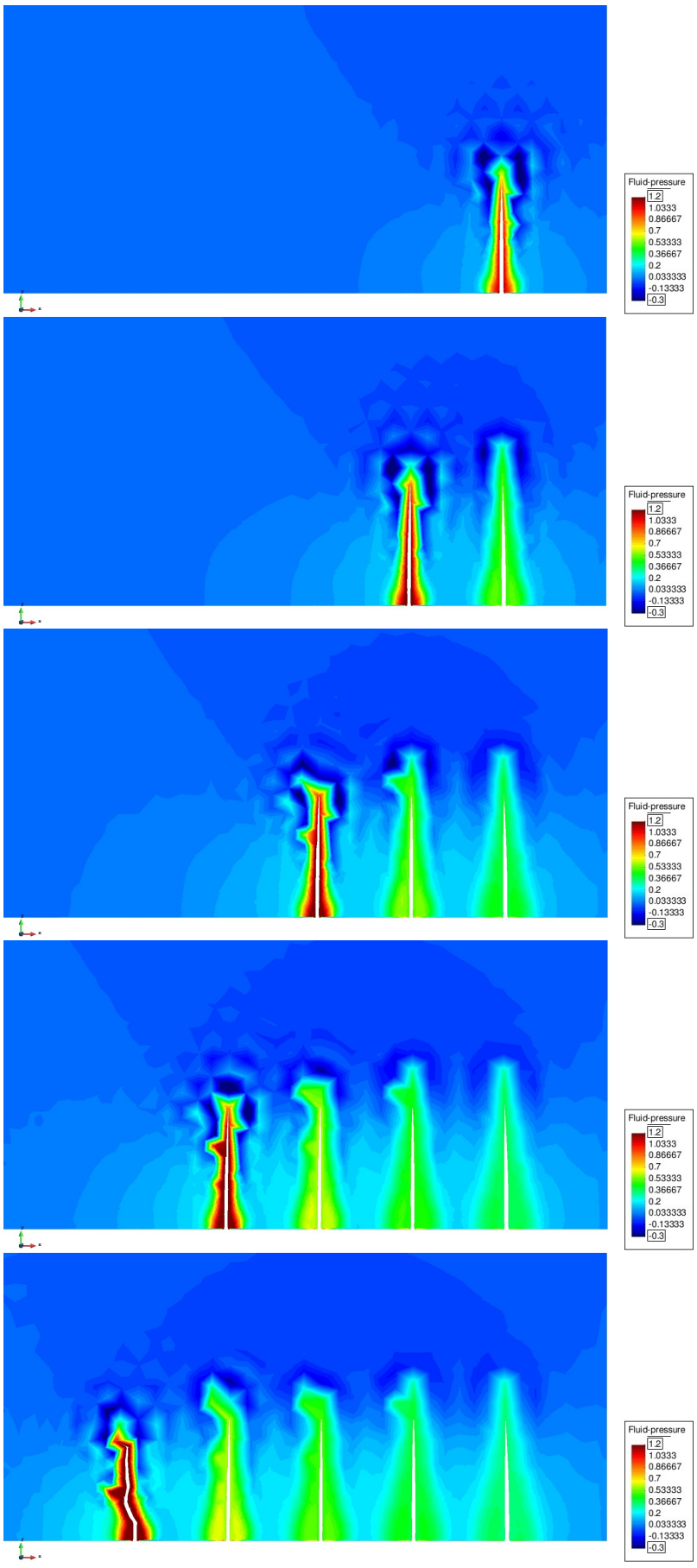

Figure 4.60: Fluid pressure distribution at the end of each fracture job in a five-stage fracturing case, for a horizontal stress ratio $\sigma_h/\sigma_H = 0.7$.

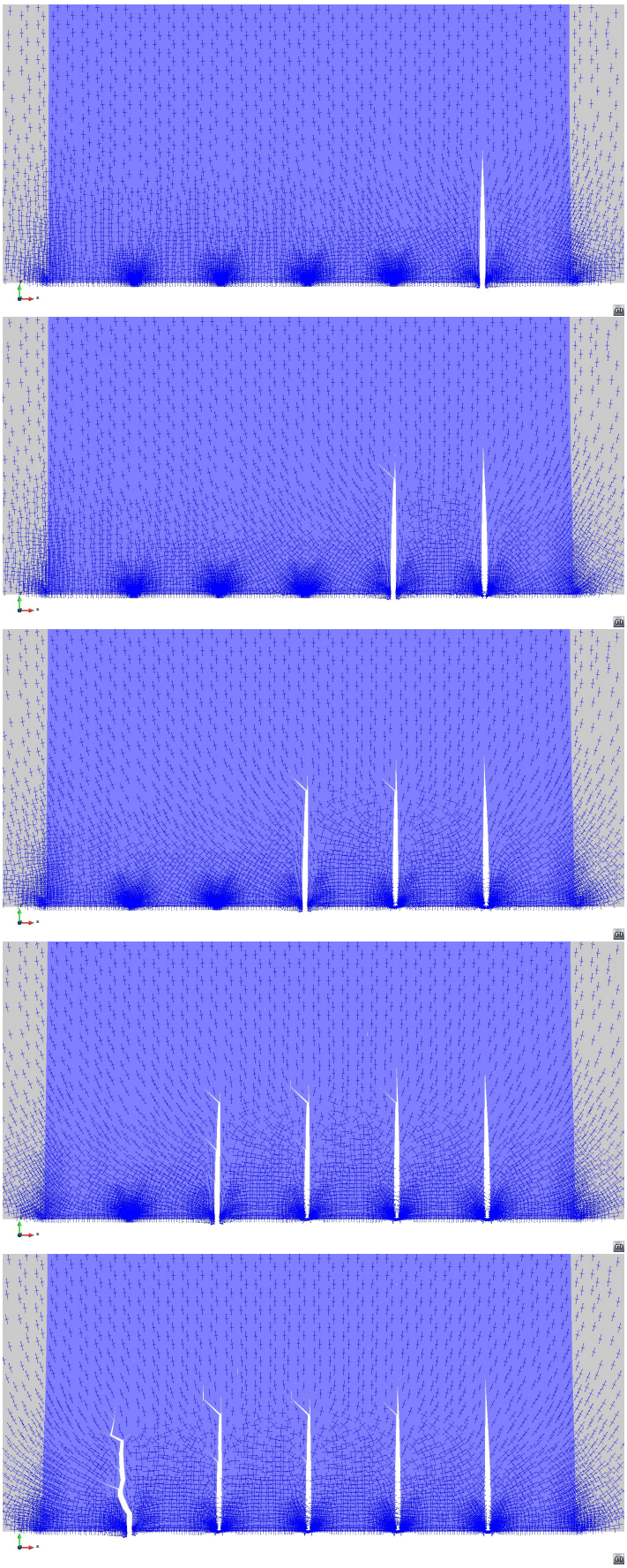

Step 1
Injection point 1

Step 2
Injection point 2

Step 3
Injection point 3

Step 4
Injection point 4

Step 5
Injection point 5

Figure 4.61: Principal stress directions at the end of each fracture job in a five-stage fracturing case, for a horizontal stress ratio $\sigma_h/\sigma_H = 0.7$.

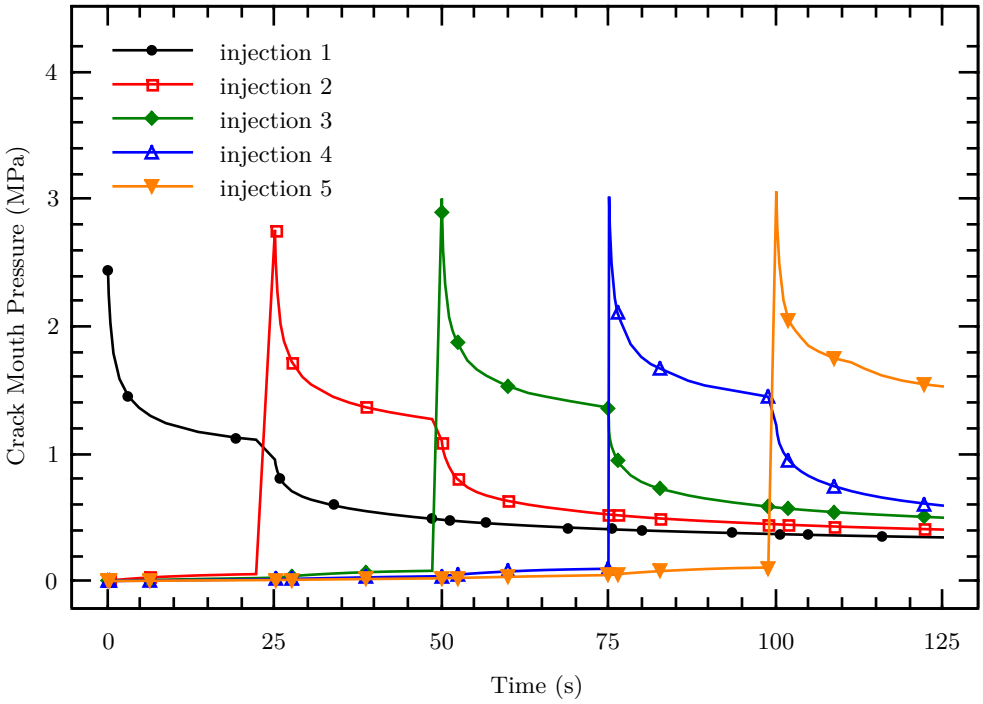

Figure 4.62: Crack mouth fluid pressure evolution after five fracture jobs, for a horizontal stress ratio $\sigma_h/\sigma_H = 0.7$.

The evolution of fluid pressure at the injection points (crack mouths) along the entire simulation is represented in Fig. 4.62. It is observed that the peak pressure for each injection is higher than the previous one, due to the increment of stress confinement after the previous fracture job. Therefore, the pressure necessary for opening the fracture increases progressively due to the interaction of jobs.

Sensitivity analysis respect to the initial stress In this subsection, the effect of stress anisotropy is investigated. For this purpose, different computations are run assuming the same maximum compression (σ_H) applied along y-axis (on top and bottom limits of the domain), and two additional different levels of minimum compression (σ_h) applied over x-axis: $0.5\sigma_H$, $0.7\sigma_H$ and $0.9\sigma_H$. The material properties used are the same as in Tables 4.11 and 4.12. The geometry, the material properties and de boundary conditions are identical to those presented for the base simulation (Section 4.3.2.a)

Figure 4.63 shows the fluid pressure distribution at the end of last fracture job, for the various σ_h/σ_H ratios. The results demonstrate that fracture interaction is clearly more pronounced as the difference between principal stresses is lower. For instance, the third injection in the case with ratio 0.9 shows a deviation not detected for ratios 0.7 and 0.5 until the fifth job and with much lower intensity.

Sensitivity analysis with respect to the material properties of the fractures In this subsection, the influence of the interface material parameters is investigated.

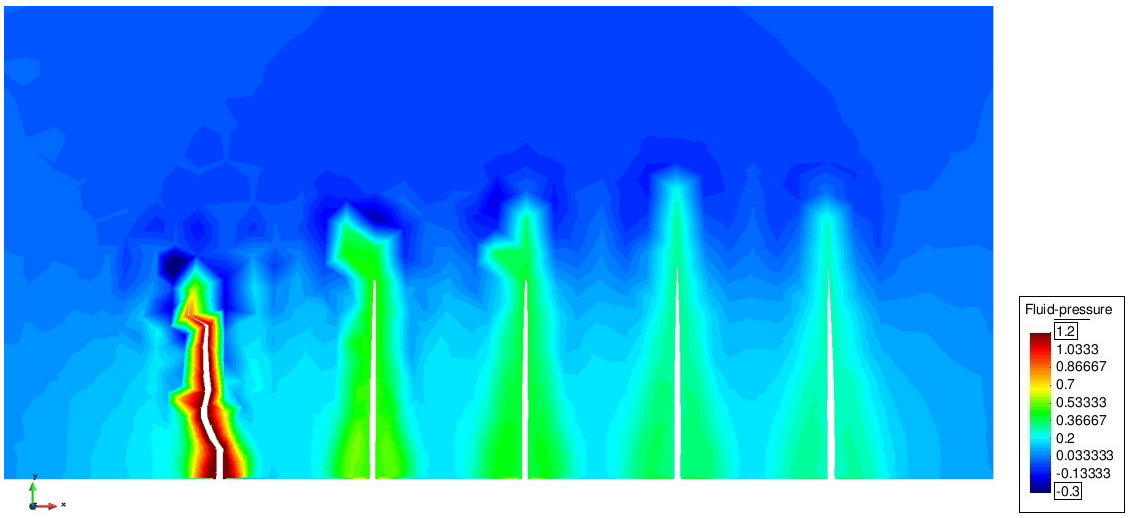

(a) $\sigma_h = 0.5 \times \sigma_H$

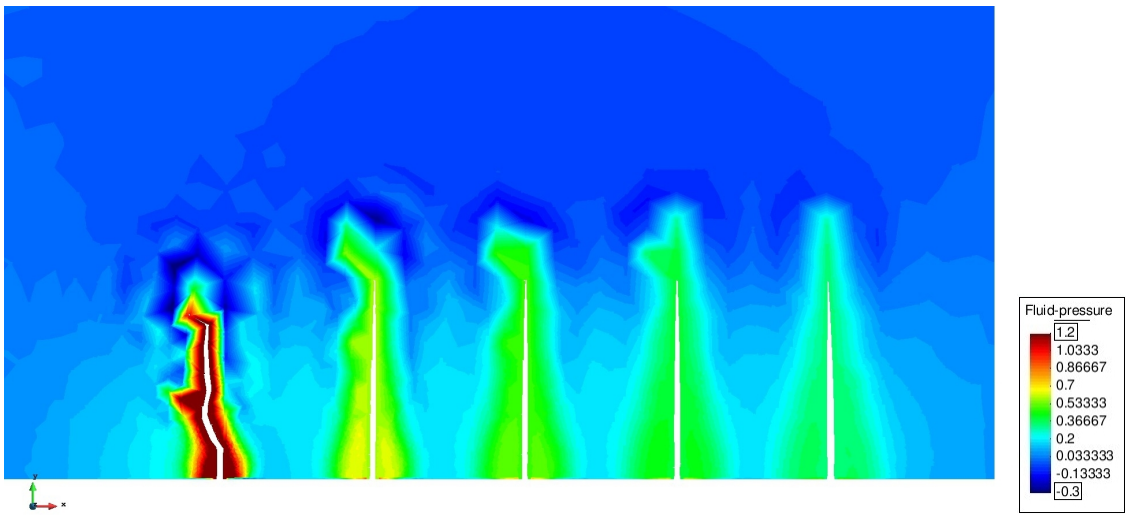

(b) $\sigma_h = 0.7 \times \sigma_H$

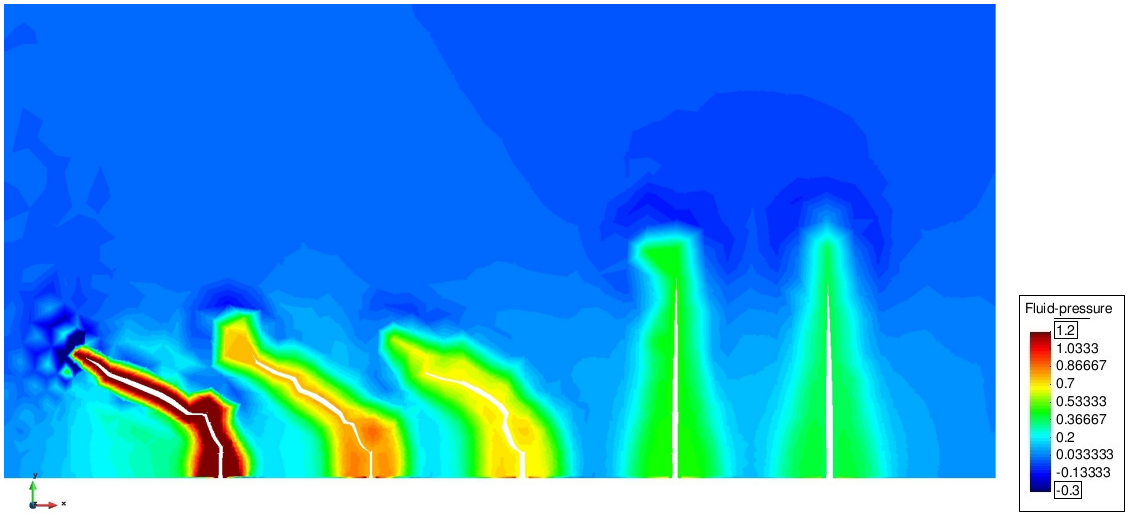

(c) $\sigma_h = 0.9 \times \sigma_H$

Figure 4.63: Effect of stress anisotropy on fracture interaction: fluid pressure distribution at time 125 s for σ_h/σ_H a) 0.5 b) 0.7 and c) 0.9.

Simulations are repeated with two sets of interface strength parameters (base case: $c_0 = 0.5\,\text{MPa}$ and $\chi_0 = 0.05\,\text{MPa}$; new case: $c_0 = 0.01\,\text{MPa}$ and $\chi_0 = 0.002\,\text{MPa}$), and also two different values of *in situ* stress anisotropy ratio ($\sigma_h/\sigma_H = 0.5$ and 0.9).

A summary of the results is depicted in Fig. 4.64, in which the fluid pressure distribution and the end of fifth injection is represented. The results show that the interaction between shots due to the change of material properties seems to be lower than the one observed with other factors such as *in situ* stress variation.

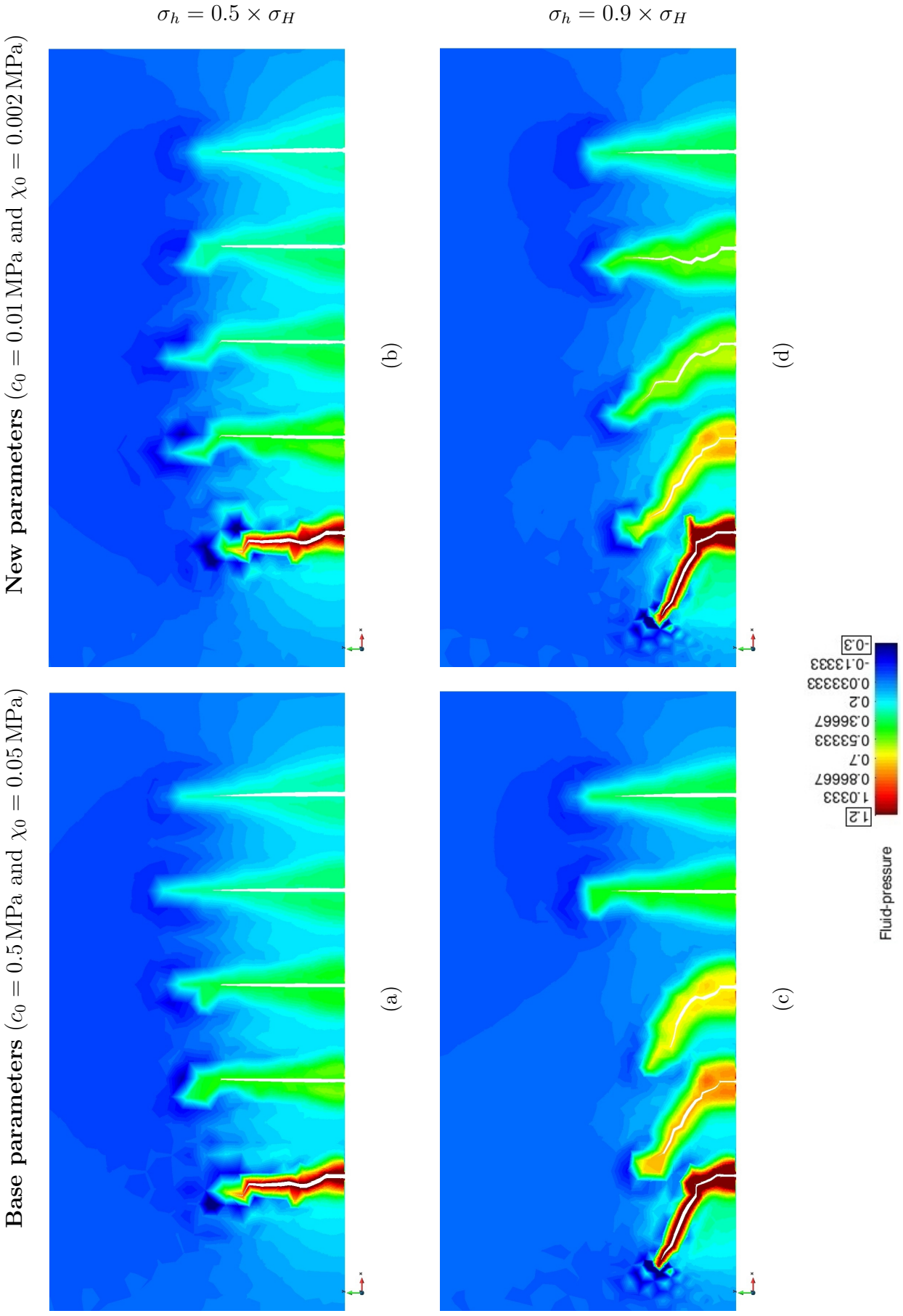

Figure 4.64: Comparison between different material properties and stress anisotropy ratios. Fluid pressure distribution at time 125 s.

4.4 Multistage fracture study in 3D

This section describes the application of the model to a realistic case of multistage hydraulic fracture of a deep unconventional reservoir, in which a real 3D model is required due to the lack of symmetry. As described in previous sections, the proposed model represents fracture propagation through a FEM model with zero-thickness interfaces (FEM+z). Additional to demonstrating the applicability of the model in 3D, more specific objectives of this example are: first, to evaluate whether fracture propagation may or may not be affecting undesired geological levels, and second, to analyze the effect of fracture interaction in order to optimize stage injections.

This case is presented in four subsections as follows: the geometry, parameters and initial conditions of the problem are presented in Section 4.4.1 and the results of the analysis are included in Sections 4.4.2 to 4.4.5.

4.4.1 General description of the case

4.4.1.a Geological settings

The area of interest consists of thirteen layers of sandstone ("target layers") of variable thickness, between metric and decametric order (3 m to 30 m), embedded into a detritic formation of sandstones, limestones and clays. The structure, schematized in Fig. 4.65, has a subhorizontal layout and it is located at great depth, the top layer is at 7870 m depth. The set has a total thickness of approximately 250 m.

The reservoir is located between two levels:

1. The top part is limited by a fault (z=7870 m depth), which should be avoided in order to minimize the risk of unstable propagation.
2. The lower part is limited by a water saturated aquifer (z=8188 m).

4.4.1.b Reservoir description

The exploitation of the reservoir is projected by means of an deviated borehole, in which three stages of fracture have been planned. The azimuth of the borehole is 15° with respect to the minimum horizontal compression stress direction (σ_h). The inclination of the borehole axis is 28° with respect to the vertical axis (z) (see Fig. 4.66). As a first approach, 3 stages of hydraulic fracture are planned at 7970 m, 8060 m and 8126 m depth (see Fig. 4.65).

Regarding the hydraulic parameters of the injection, an essential parameter is fluid viscosity. In this case, the fluid viscosity is variable in time. First, a fluid with a low viscosity ("slick water") is injected to facilitate the propagation of the fracture. Then, once the fracture is generated, the viscosity is increased in order to allow the transport

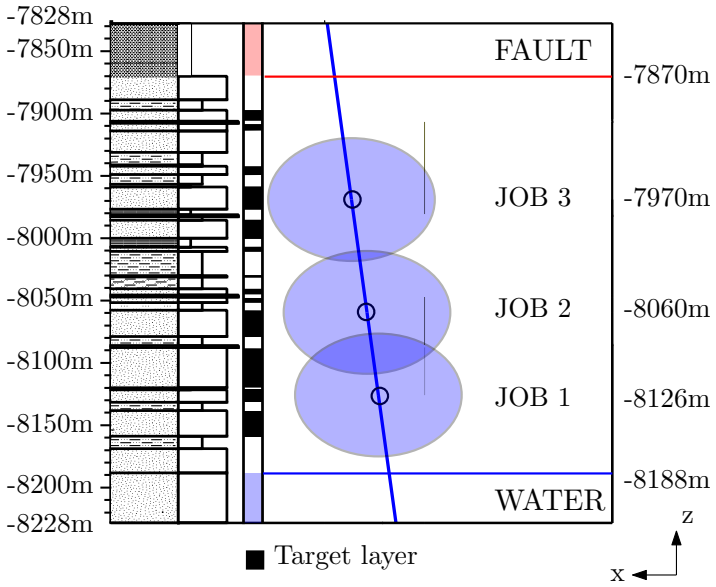

Figure 4.65: Scheme of geological layers, well trajectory and fracturing jobs considered in the analysis.

of the proppant. The real value of viscosity in the reservoir is difficult to determine, because it is the result of a mixture which is modified during the injection.

Due to the difficulty to model this behavior, the present analysis assumes a constant value of 400 cp, which is considered an average between the injected fluid (1400 cp) and the fluid contained in the fracture. From the modeling point of view, this value of viscosity is applied to the fluid flowing along the fracture. The fluid flowing to the medium has been specified with a much lower viscosity close to the water. This is due to the fact that a kind of screen or filter (a "cake") is formed on the walls of the fracture surface that only allows water molecules to flow into the medium. This screen also helps retaining proppant particles into the fracture.

4.4.1.c Model geometry

The area under study is a cube of 400 m side in which the borehole geometry and the geology settings are introduced following the description below. The vertical planes of hydraulic fracture are assumed and discretized with zero-thickness interface elements. Due to the 3D complexity of this case, a general widespread introduction of interfaces to allow non-pre-established fracture paths as presented in previous sections, is postponed to future studies. However, multiple fracture paths are still possible due to the introduction of interfaces along selected horizontal planes.

The possibility of inter-layer fractures is introduced with ten horizontal planes of interfaces, eight of them on top and bottom of the most rigid formations (cemented sands) and the other two at the limits of the reservoir (pay zone) with overburden and underburden layers. These additional planes are included in order to allow potential T-shape fracture propagation.

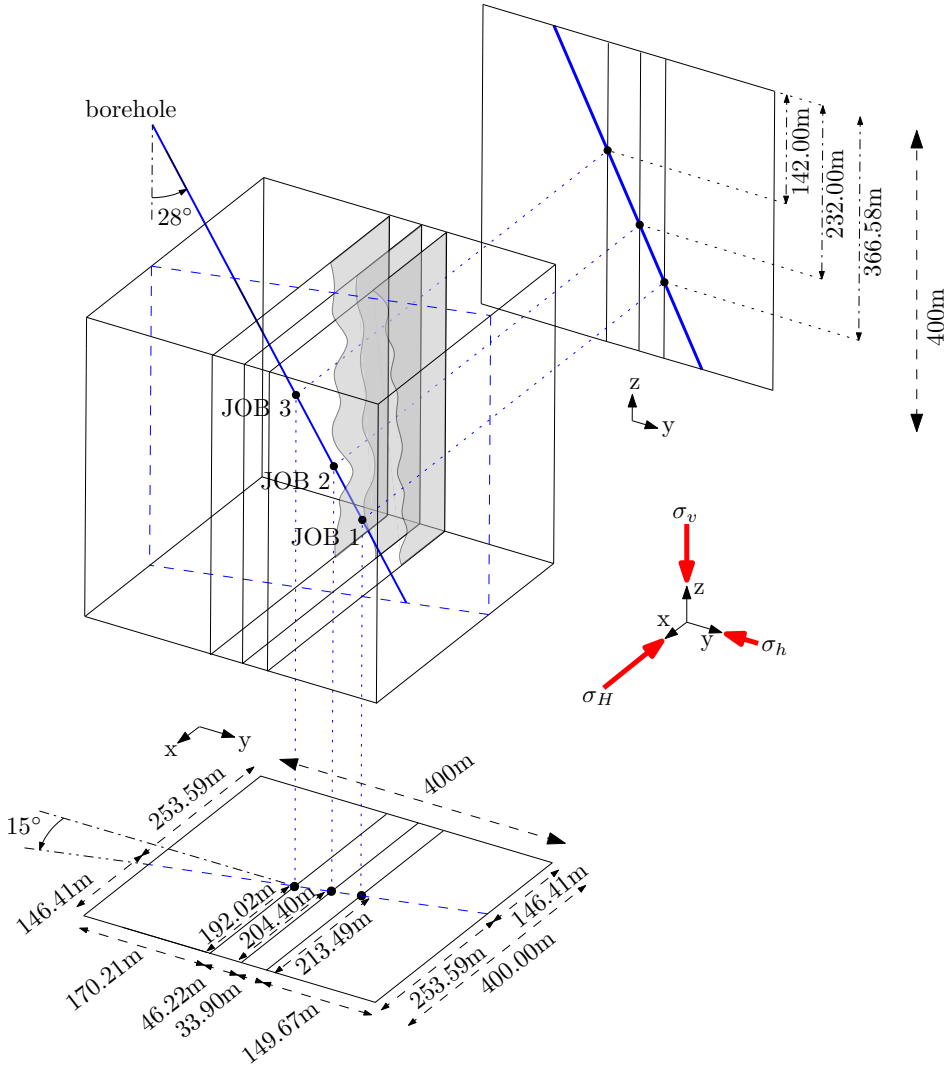

Figure 4.66: Geometry of the 3D model with the well trajectory and 3 stages of fracture: the central figure contains a 3D sketch of the cubical domain, with the three vertical planes related to the injections; the upper figure contains the "yz" projection of the model; and the lower figure is the projection "xy".

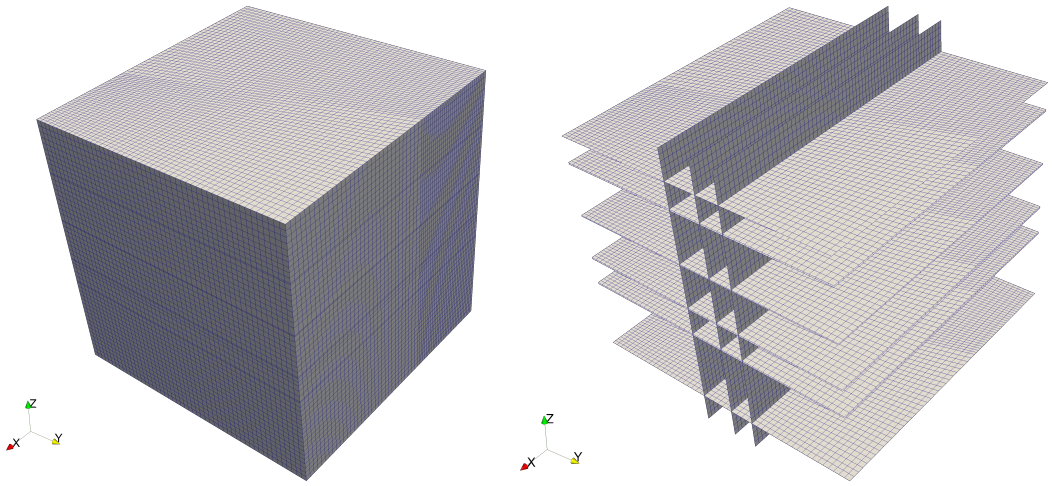

(a) Contimuum elements (b) Interface elements

Figure 4.67: Finite element mesh used in 3D model: a) hexahedral mesh of the continuum medium; and b) fracture planes discretized with zero-thickness interface elements.

The model has been discretized with a regular mesh of 232 375 nodes, the continuum is composed by 176 256 linear hexahedral elements, and the fractures by 43 008 rectangular zero-thickness interface elements (see Fig. 4.67).

4.4.1.d Material properties

Continuum

The physical model is composed of thirty-seven layers as described above (see Fig. 4.70(b)). For this analysis, due to the fact that the non-linearity is only related to fracture propagation, elastic material has been enough for the definition of the behavior of the continuum. A summary of the values used is depicted in Fig. 4.68, where a schematic stratigraphic column is related to the logs of *Young*'s modulus (E), *Poisson*'s ratio (ν), porosity (n) and horizontal permeability (k_x). The values had been obtained from indirect measurements (sonic logs, gamma logs, etc.).

The analysis of the registers show the existence of three layers with very high stiffness, which require a special discretization.

Transverse isotropy is assumed for the permeability ($k_x = k_y > k_z$), with the horizontal permeability 10 times larger than the vertical one. The value of the hydraulic conductivity ($K^f_{x,y,z}$) has been obtained assuming that the injection fluid is water. Therefore, fluid density (ρ^f) in consistent units is equal to $0.001\,\mathrm{Mt/m^3}$ and the dynamic fluid viscosity (μ) equal to $1 \cdot 10^{-9}\,\mathrm{MPa \cdot s}$. The value of conductivity is assumed to be constant for this simulation. More details about the parameters used may be found in Appendix B Table B.1

Interface

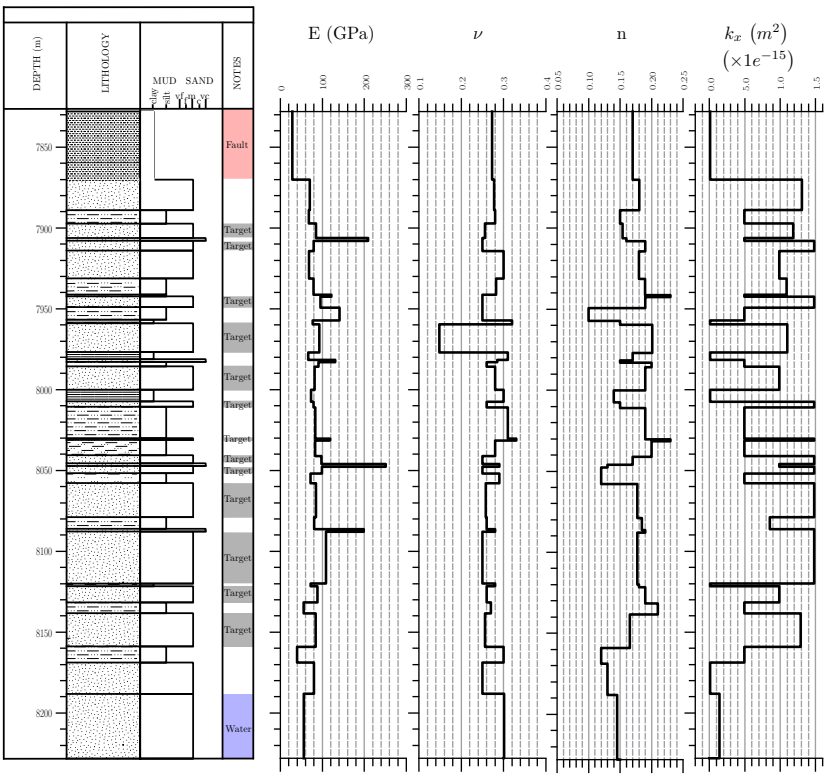

Figure 4.68: Description of the continuum properties of the 3D model: E, the Young's modulus; ν, the Poisson's ratio; n, the porosity; and k_x, the horizontal permeability.

This model assumes the same number of interface materials as the number of continuum materials (see Fig. 4.70(b)). In order to analyze fracture propagation the fracture-based elastoplastic constitutive law is considered for the interfaces.

The main parameters describing the model are depicted in Fig. 4.69. The values represented are the tangent of the friction angle ($\tan\phi$), the tensile strength (χ_0), the cohesion (c_0) and the fracture energy in mode I (G_f^I). The cohesion and the tensile strength are calculated from the value of Uniaxial Compression Strength (UCS), which were obtained from geophysical measurements.

Due to the lack of data, the fracture energy is obtained with the following procedure. First, for a pure tension loading case and assuming high values of stiffness modulus (K_n), expression (Eq. (4.19)) relates the dissipated energy (W^{cr}) to the normal relative displacement opening of the fracture (u_n^{cr}) Stankowski (1990). Then, the dissipated energy is imposed to be proportional to a certain percentage of the fracture energy in mode I (G_f^I), for instance 99%.

$$W^{cr} = G_F^I \left(1 - e^{\left(\frac{-\chi_0}{G_F^I} u_n^{cr} \right)} \right) \tag{4.19}$$

Finally, after some manipulations, (Eq. (4.20)) is obtained which relates the specific

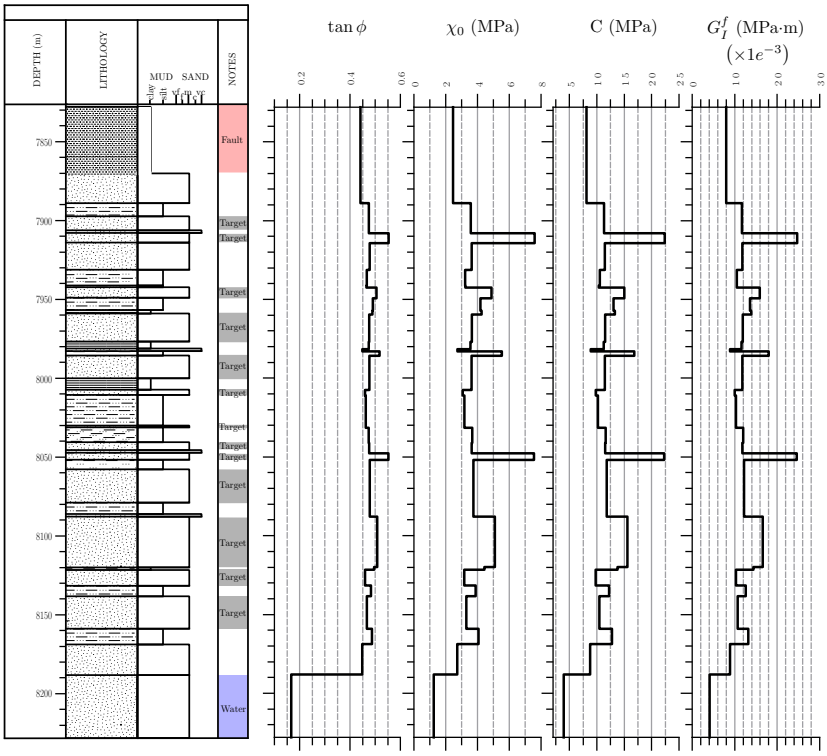

Figure 4.69: Description of the interface element properties of the 3D model with 3 stages: $\tan\phi$, the tangent of friction angle; χ_0, the tensile strength; C_0, the cohesion; and G_f^I , the fracture energy in mode I.

energy in mode I to a given normal crack opening and tensile strength. The energies used for the basic simulation are obtained considering 15 mm as the crack opening normal crack displacement. This value will be the object of a sensitivity analysis in Section 4.4.4.

$$G_I^F = \left(\frac{-\chi_0}{\ln(1-0.99)}\right) u_n^{cr} \tag{4.20}$$

The value of fracture energy in mode IIa is assumed to be ten times larger than fracture energy in mode I ($G_f^{IIa} = 10 \times G_f^I$). The value for which the dilatancy is vanished (σ_{dil}, another important parameter of the constitutive model) is taken equal to the UCS strength.

The hydraulic parameters of the joints are the longitudinal transmissivity and the transversal conductivity. Longitudinal transmissivity is given by the cubic law and the initial value is considered nearly zero. Transversal conductivity has little or no effect in this calculation, due to the low conductivity of the continuum material, and a constant value of $1\,\mathrm{s}^{-1}$ has been assumed for all interfaces.

As previously explained, the "screen effect" due to impermeabilization of the walls of the fracture has been overcome by the assumptions that the viscosity of the fluid inside the fracture is higher than that of the medium. For this purpose a viscosity of 400 cp ($4.0 \cdot 10^{-7}$ MPa · s) has been assumed for the joint elements.

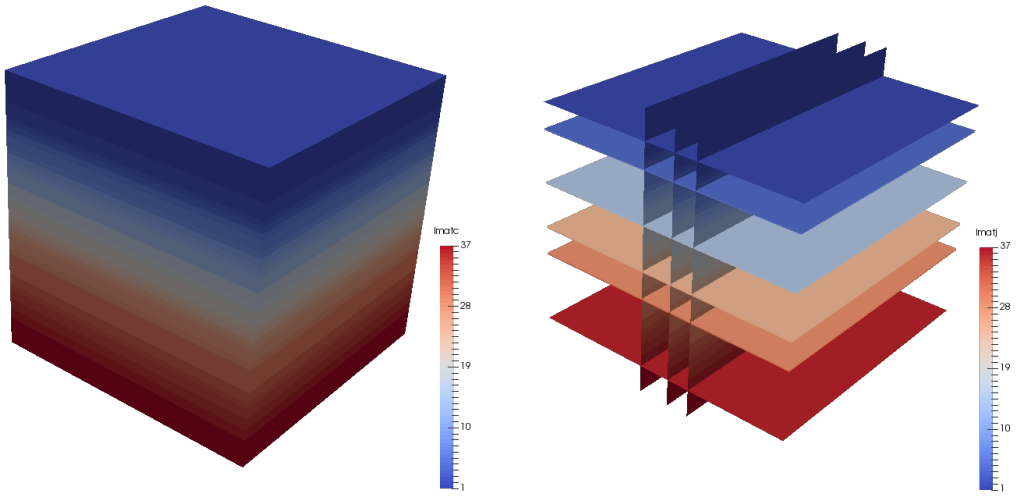

(a) Contimuum elements (b) Interface elements

Figure 4.70: Distribution of the material properties of the 3D model: a) continuum elements; and b) interface elements.

4.4.1.e Boundary conditions

The boundary conditions applied to the mechanical problem consist of "rollers" for all the faces of the cube. This condition is maintained for all steps of the simulation.

For the hydraulic calculations two steps are defined for each fracturing stage. The first one is an "injection" step of 2 h with a constant rate of 0.09 m^3/s (33.96 bbl/min), and the second one is a "dissipation" step of 22 h, simulating the time between each work of injection, (totally 1 day per job).

4.4.1.f Initial conditions

Although the method uses both mechanical and hydraulic variables, the definition of the initial state has been formulated in terms of effective stresses, and a constant fluid pressure has been assumed for the whole domain; in this case 137.89 MPa. Gravity effect has been neglected.

Figure 4.71 shows the profile of the effective stresses used for the simulation, showing that the maximum and minimum compression stresses are horizontal, while the vertical is the intermediate.

Note that, for convenience, the model geometry is aligned with the stress axis. The maximum horizontal stress (σ'_H) is parallel to the x-axis, the minimum horizontal stress (σ'_h) is parallel to y-axis, and the vertical component (σ'_v) is parallel to z-axis. The vertical stress has been obtained from the integration of the weight of the layers, which is a linear distribution in depth since the density was assumed constant.

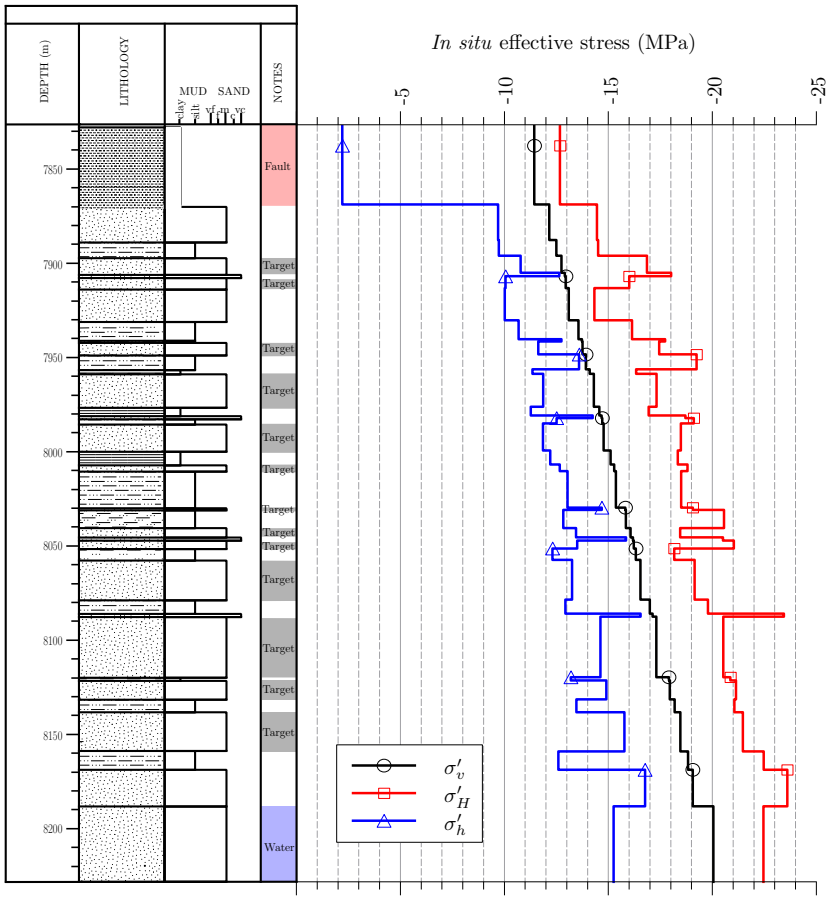

Figure 4.71: Profile of *in situ* effective stress, where σ'_v is the vertical component (z-axis), σ'_H is the maximum horizontal component (x-axis) and σ'_h is the minimum horizontal component (x-axis).

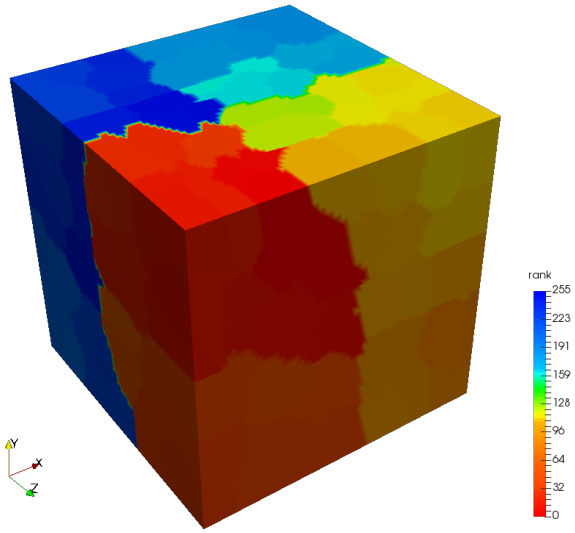

Figure 4.72: Domain decomposition of the 3D model.

4.4.2 Base case analysis

Numerical simulations have been run using the parallel capabilities of the code. For this purpose, the overall domain has been decomposed in 256 subdomains (see Fig. 4.72), and GMRES solver has been selected for the solution of the linear system at each iteration. The choice of GMRES is because iterative methods show a better performance in parallel calculations (scalability). Additionally, this method is well adapted to non-symmetric systems, as it will result from the non-associated constitutive law for interfaces, and the calculation of steady state conditions in the initialization step. In order to improve the numerical conditioning, a "Additive Schwarz Method" preconditioner (ASM) has been used too. The average "wall-clock" time was approximately 6 h for a complete computation (3 stages).

Additionally, a scalability analysis has been performed in order to study the degree of parallelization. For this purpose a simulation including only the initialization step, which is elastic, has been performed to determine the time necessary. For accessibility reasons, this analysis has been run in a different computer, Titani, which is a cluster server from the *Barcelona School of Civil Engineering*. The server is composed by 5 nodes of 2× Intel Xeon E52650L v3 (1.8 GHz) with 12 cores per unit. For system availability, the simulations were run with up to 96 CPUs. The results presented in Fig. 4.73 show a good performance. Due to several factors, among them memory requirements of the problem, kind of solver and Titani's architecture, a super-linear scalability[2] is observed up to 60 processors. Figure 4.73(a) shows the total amount of time necessary to complete the entire test, which includes the input data reading, element integrations, the solution of two iterations, and the output writings. Figure 4.73(b) shows

[2]the simulation scales better than the ideal or linear ratio

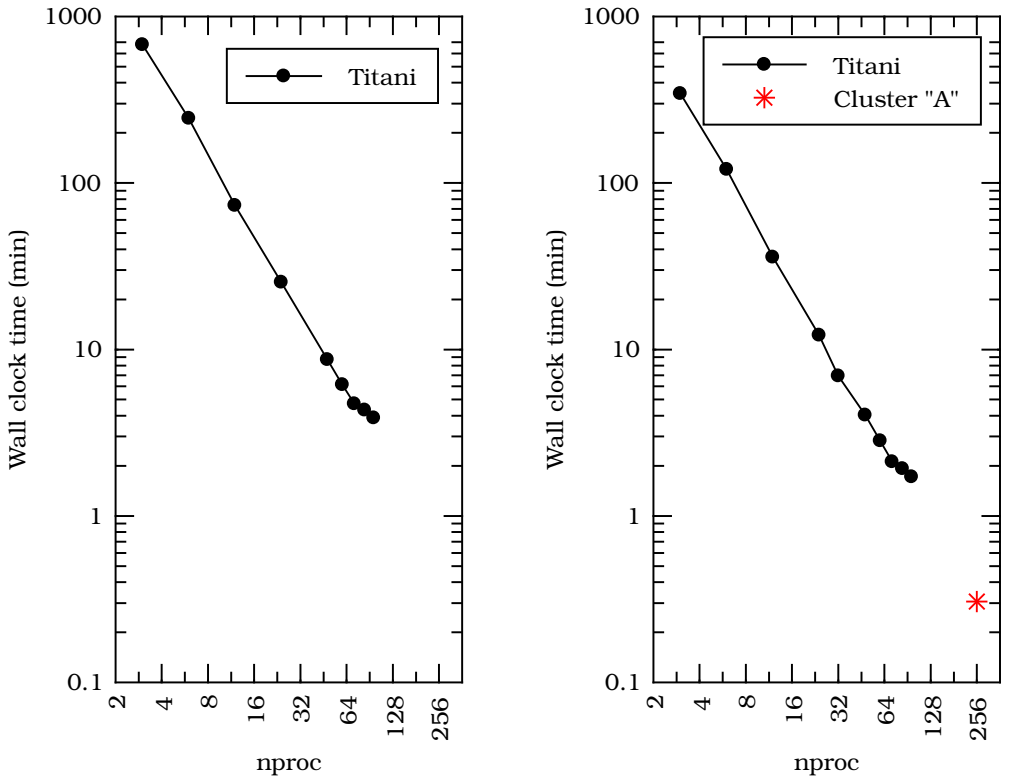

(a) Total time (b) Solver time (1 linear iteration)

Figure 4.73: Scalability analysis for 3D model case; a) Total time (wall clock), including i/o routines, element integrations and 2 linear solutions b) Solver time, single linear solution.

the isolated time for the solver. Although scalability tests and simulations have been performed on different machines, which in principle avoids their comparison, to get an idea of the performance achieved, both results are represented in the same figure. Assuming that all iterations require the same amount of time, results from Fig. 4.73(b) can be used to estimate the total amount of time requiered for complete simulation (around 1000 iterations). For example using only 3 CPU the estimated time would be around 8 months (1000 iter $\times$ 344 min/iteration).

Figure 4.74 shows the fracture energy spent (Wcr/G_f^I) after stopping each injection. In general, the fractures have an average diameter of 80 m. The first injection generates a fracture with a larger horizontal dimension of 80.8 m, as compared to vertical dimension of 77 m high (Fig. 4.74(a)). Probably because of the existence of limiting layers with higher levels of horizontal stress, and also more rigid, this first fracture propagates more downwards than upwards. In contrast, the second injection produces a fracture that extends less horizontally (75 m) than vertically (79.4 m) (Fig. 4.74(b)). Although injection is performed near a highly compressed and stiffer layer, the fracture seems to propagate without being affected, probably due to the low thickness of the layer. Finally the third injection has a horizontal elliptic shape, 93.5 m of width and 82.9 m of height (see Fig. 4.74(c)). The injection tends to propagate upwards, probably because

Table 4.13: Fracture shape.

	$\varnothing_{hz}$[1] m	$\varnothing_{v}$[2] m	*Aspect ratio*	*Area*[3] m^2
Job 1	80.5	77.0	1.05	4868.29
Job 2	75.0	79.4	0.94	4677.04
Job 3	93.5	82.9	1.13	6087.73

[1] $\varnothing_{hz}$, horizontal diameter
[2] $\varnothing_{v}$, vertical diameter
[3] Area surface, $A = \pi \times (d_{hz}/2) \times (d_{v}/2)$

the layers below the injection point have higher horizontal confinement. Table 4.13 summarizes the geometric dimensions of three fractures assuming an elliptical shape.

Figure 4.75 shows the evolution of the stresses of the continuum along the y-axis (stress that at most points is the minimum horizontal stress σ_h), and the evolution of the fracture aperture of the interfaces that have exceeded their strength and have started opening (u_n^{cr}). The stresses are represented on a vertical plane, oriented in such a way that it includes the straight line of the well.

It is observed that, in the injection steps, the effective stresses around the fracture decreases significantly. This phenomenon is related to the increase of the fluid pressure of the continuum due to the effects of leak-off. Once the injection is stopped and times goes by, horizontal effective stresses increase again until they reach a value that near the fracture turns out to be slightly higher than the *in situ* stress value. This effect is explained by the dissipation of the over-pressure generated by the injection and the opening of the fracture that, due to the type of constitutive model used does not recover even if stresses unload. Although this effect is numerical, this behavior has been accepted as a good first approximation for the modeling of the proppant.

Regarding the opening of the fracture, values ranging from 1 mm to 4 mm are observed. These low values might indicate an overestimation of the strength parameters as well as an overestimation of the fracture energy used, although no precise information is available about possible realistic opening values in this case.

Figure 4.76 depicts the curves of the fluid pressure evolution at each injection. Each curve (job 1, job 2 and job 3) is represented in terms of the time after the beginning of the corresponding injection. The results obtained follow in general terms the patterns described in the literature. First, a peak is observed (Breakdown point), associated to the beginning of the propagation. This peak is more pronounced in highly cohesive materials.

However the maximum value reached in this simulations seems unrealistically high. The reason may lie on the details of the numerical simulation used for the first seconds of injection. Since a constant flow is prescribed and the initial transmissivity of the fracture is nearly zero, this leads to high pressure values in order to allow the start of

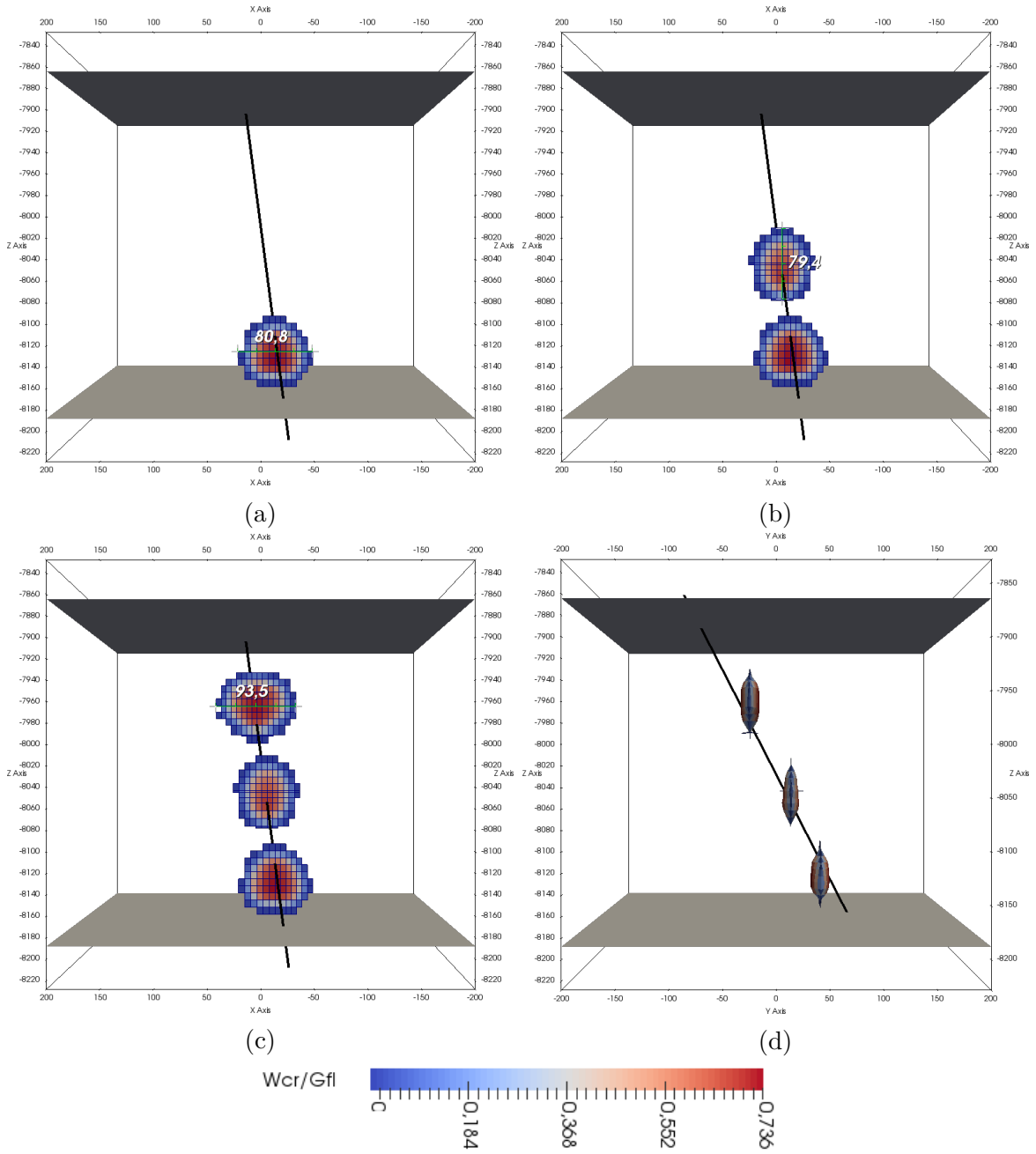

Figure 4.74: Evolution of W^{cr}/G_f^I (MPa · m) at the open interfaces at various times of the calculation: (a) frontal view after first injection, time 2 h; (b) frontal view after second injection, time 26 h; (c) frontal view after third injection, time 50 h ; and (d) lateral view after third injection with deformation. All contours represented on the deformed mesh (magnification ×5000). Figures on the front view reflect dimensions in m.

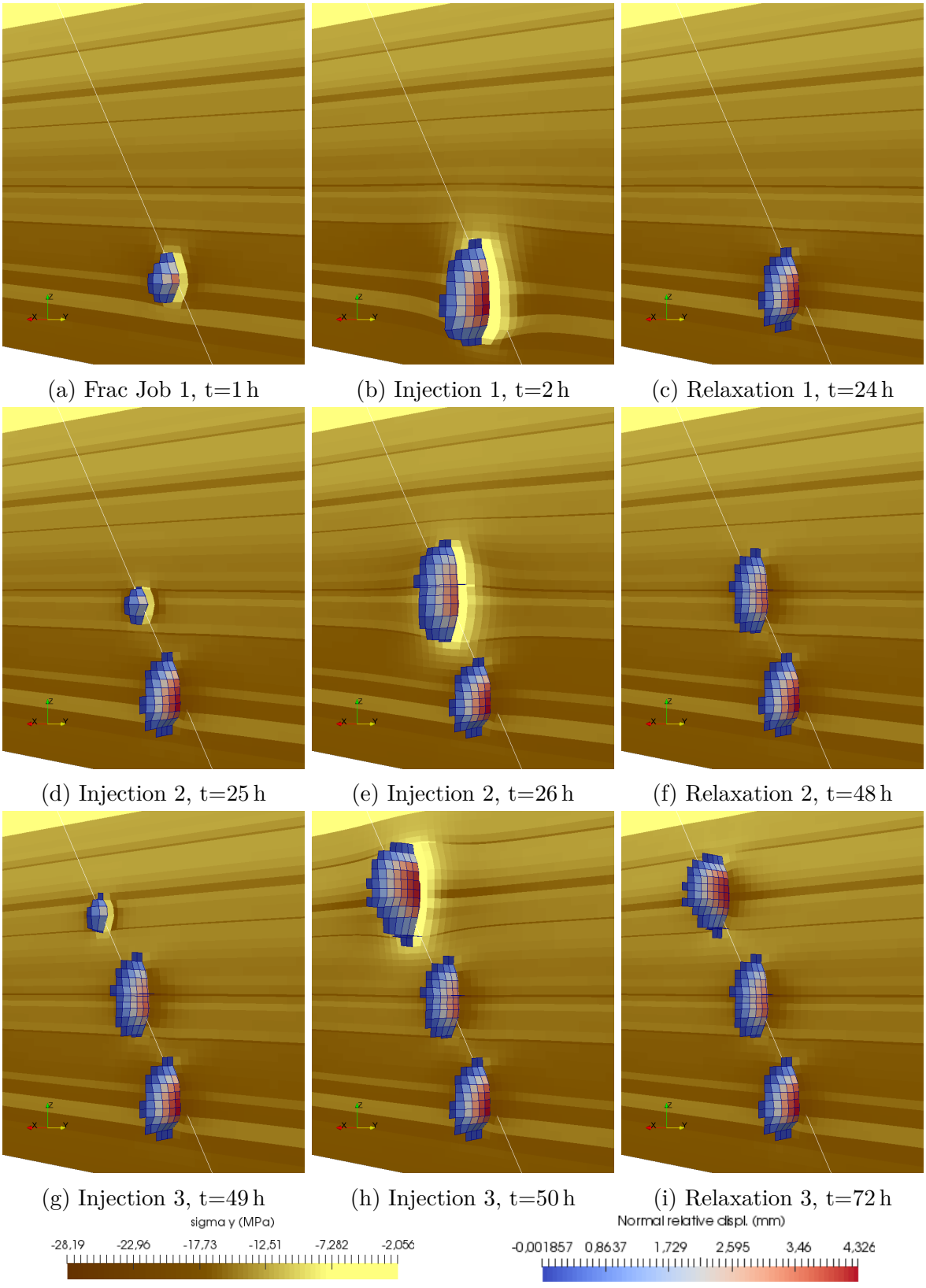

(a) Frac Job 1, t=1 h (b) Injection 1, t=2 h (c) Relaxation 1, t=24 h

(d) Injection 2, t=25 h (e) Injection 2, t=26 h (f) Relaxation 2, t=48 h

(g) Injection 3, t=49 h (h) Injection 3, t=50 h (i) Relaxation 3, t=72 h

Figure 4.75: Evolution of σ_y in the continuum (MPa), and normal relative opening displacement (r_n) on the open interfaces (mm). Contours plotted over deformed mesh (magnification $\times$5000).

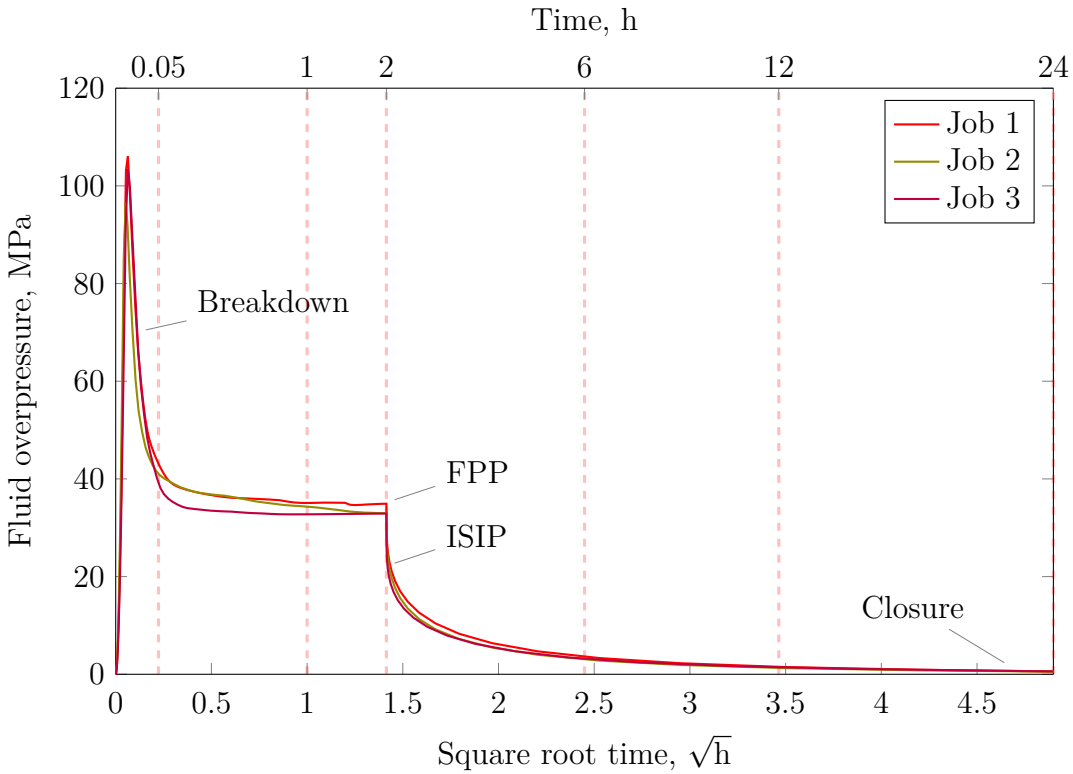

Figure 4.76: Fluid pressure evolution at the three injection points, represented with respect to time after each injection.

fluid flow along the interface. In addition, this behavior may be accentuated because the flow condition is imposed at a single point of zero dimension.

Then, in about 3 min the curve stabilizes to a constant value around (Fracture Propagation Pressure (FPP)) 38 MPa, which can be related to the stable propagation of the fracture. This value is held until the end of the injection (Δt=2 h). Then,when injection is stopped, a sudden drop of fluid pressure is observed, which corresponds to the Instantaneous Shut-In Pressure (ISIP), with an approximated value of 20 MPa. After that, pressure is dissipated ate rates progressively slower until the initial *in situ* pressure is recovered asymptotically After 22 h from the end of the injection closure is practically reached.

An interesting aspect observed is the interaction between injections, which can be seen in Fig. 4.77, where all curves are represented on the same time line. Although the results at the deformation level do not show a remarkable interaction, the pressure evolution curves do reflect it. In particular, at the second injection point there is a slight increase in pressure due to the dissipation wave of the first injection (Fig. 4.77-A). Similarly, the first injection point receives the dissipation wave from the second injection (Fig. 4.77-B). The third injection point seems not to be affected with previous injections.

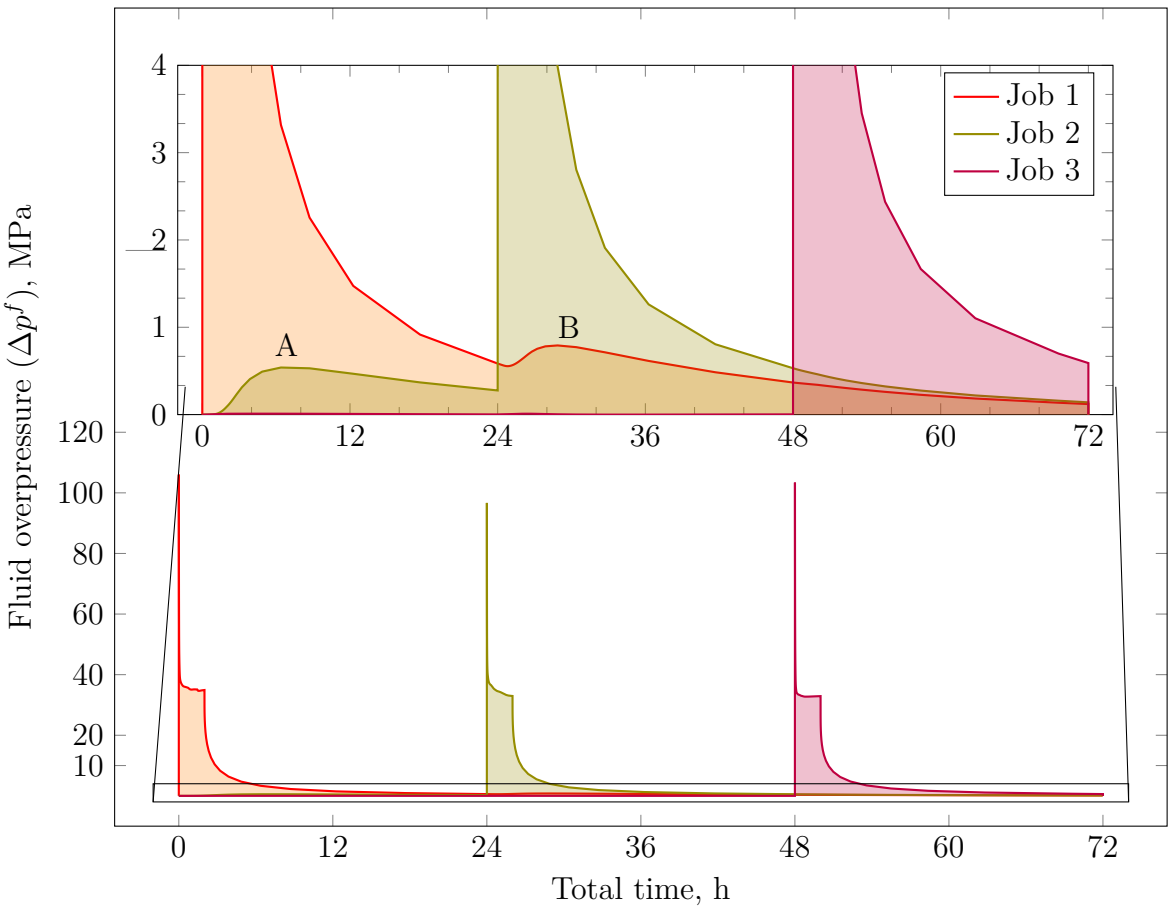

Figure 4.77: Fluid pressure evolution

4.4.3 Sensitivity to the fluid viscosity

This section explores the effect of the variation of viscosity on fracture propagation. As described in the introduction, due to the use of special additives to facilitate the transport of the proppant, the fluid injected has different values of viscosity at different times of injection. Furthermore, there are also differences between the viscosity of the fluid in the fracture and in the continuum. The exact values are difficult to determine, since they are the result of different components that are mixed during the injection. In this study (base case, §4.4.2) fluid viscosity has been assumed constant with an average value 400 cp. It remains for further study the use of more precise values or variable viscosity.

In this section the analysis of an extreme case has been carried out. The new analysis considers, for the viscosity of the fluid of the fracture, a value equal to the water viscosity ($\mu = 1\,\text{cp}$) . This case would be the most unfavorable, since the lower is viscosity, the higher is the propagation.

Figure 4.78 shows the final extension of the fractures, with contours corresponding to the fracture energy dissipated at the end of the third fracture stage. It is apparent that the fractured surface is significantly more extensive than the one shown previously, even reaching the limits of the pay zone. Due to this fact, although numerically correct, the results can only be evaluated in a qualitative way, since the imposed boundary conditions may have significantly affected the final solution.

An interesting observation in this limit case is the interaction effects between fractures. In Fig. 4.78 it is clearly seen how the second fracture modifies the shape of the third fracture. In subfigure b) a front-rear view shows a deviation to the right, of the third fracture.

4.4.4 Sensitivity to the fracture energy

This section describes a sensitivity analysis of the fracture propagation with respect to the value of the fracture energy. The constitutive law is controlled by an energy-type history variable (energy spent in fracture process, W^{cr}), which defines the evolution of the parameters that control the fracture surface. The constitutive model assumes a softening-type evolution, which requires two parameters, one defining the value of energy for which tensile strength vanishes (G_f^I), and another one defining the energy necessary to obtain a pure frictional model (G_f^{IIa}). These two parameters will be the object of the present sensitivity study.

For this purpose, two alternative pairs of energy values have been used. Using Eq. (4.20), which relates the value of G_f^I to a critical opening displacement, a lower additional value has been calculated using a u_{crit} of 10 mm, and an upper value using a u_{crit} of 20 mm. These values correspond to an increase or decrease of 33% respect to the base solution. Due to the lack of data, for the definition of the fracture energy

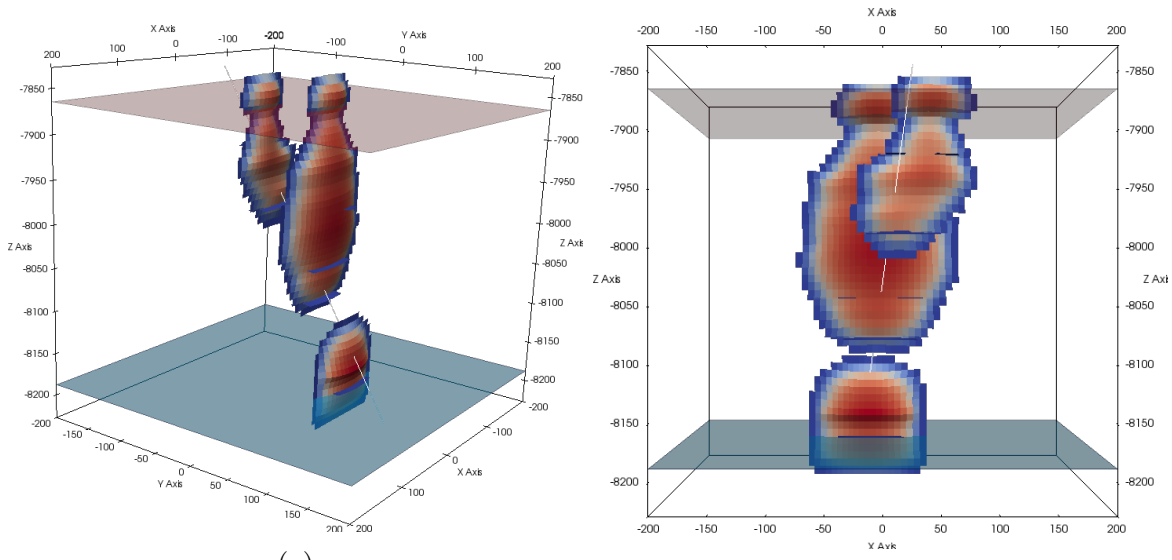

(a) (b)

Figure 4.78: W^{cr}/G_f^I (MPa · m) at the open interfaces after the last injection using water viscosity for the interfaces: (a) lateral view; and (b) frontal view. All contours represented on the deformed mesh (magnification ×5000).

in shear-compression (G_f^{IIa}), the common assumption has been made that G_f^{IIa} is ten times the fracture energy in tensile mode (G_f^I). Figure 4.79 shows a log with the energy parameter in mode I used for the study.

Table 4.14 includes a summary of the geometric dimensions of the fractures developed for each of three pairs of values of G_f^I and G_f^{IIa} . The results obtained show a a limited influence of fracture energy on fracture propagation. However a tendency that would be in line with the expected trends can be observed. For instance, the value of fractured area surface, depicted in Fig. 4.80-left, shows a tendency of decreasing fracture area surface due to the increase of the values of the fracture energy (increase of u_{crit}). Figure 4.80-right shows the maximum aperture reached for each job. It can be clearly seen as there is a decrease of fracture aperture by increasing the fracture energy of the fracture. Both results are related to the fact that by increasing the fracture energy, the softening slope of the resulting stress-opening curve of the fracture is decreased, and consequently for the same dissipated work, stress is higher.

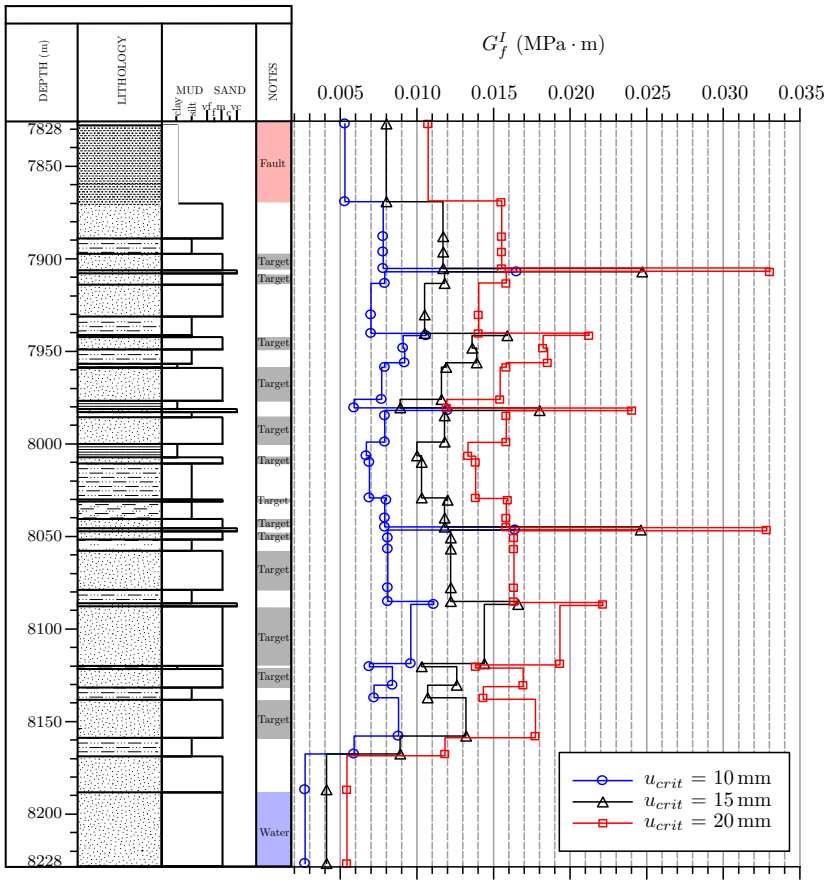

Figure 4.79: Energy parameters in mode I (G_f^I) used for the sensitivity analysis of fracture energy.

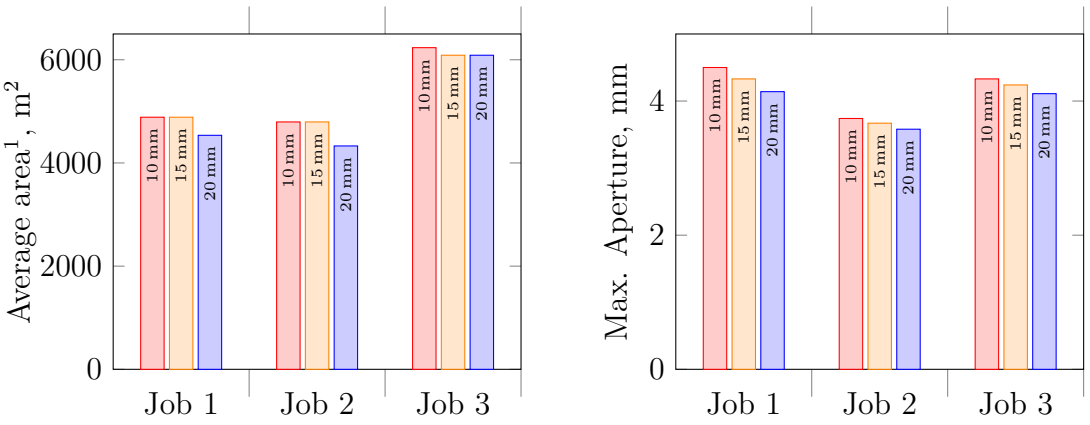

[1] Area of the idealized ellipse.

Figure 4.80: Comparison between different values of u_{critic}, grouped by hydraulic jobs: left) comparison of the idealized area surface of the fracture; and right) maximum fracture aperture.

Table 4.14: Fracture shape and dimensions of 3D 3-stage hydraulic fracture, with various fracture energy values (sensitivity analysis).

		$\varnothing_{hz}$	$\varnothing_v$	$\varnothing_{hz}/\varnothing_v$	A	u_{max}
		m	m		m^2	mm
$u_{crit} = 10\,mm$	*Job 1*	80.8	77	1.05	4886.43	4.50
	Job 2	75	81.4	0.92	4794.85	3.74
	Job 3	93.5	84.9	1.13	6234.61	4.33
$u_{crit} = 15\,mm$	*Job 1*	80.8	77	1.05	4886.43	4.33
	Job 2	75	81.4	0.92	4794.85	3.67
	Job 3	93.5	82.9	1.13	6087.74	4.23
$u_{crit} = 20\,mm$	*Job 1*	75	77	0.97	4535.67	4.14
	Job 2	75	73.5	1.02	4329.51	3.58
	Job 3	93.5	82.9	1.13	6087.74	4.11

$\varnothing_{hz}$, horizontal diameter

$\varnothing_v$, vertical diameter

$\varnothing_{hz}/\varnothing_v$, aspect ratio

A, geometric area, $A = \pi \times \varnothing_{hz}/2 \times \varnothing_v/2$

u_{max}, max. aperture

Similar results are observed in the evolution of pressure at the point of injection of each job (see Fig. 4.81). In the extended image of the fracture propagation zone, a slight variation of about 1 MPa is observed with respect to the base value, whereas the higher values are associated with higher fracture energies. Figure 4.82 depicts a

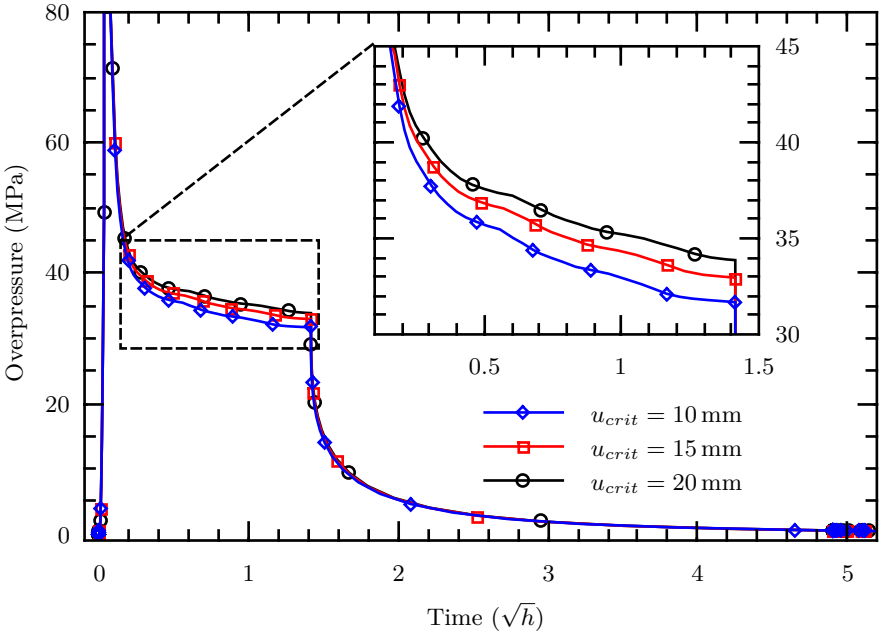

Figure 4.81: Fluid evolution

frontal view (parallel to the σ_h axis) with the footprints of the three fractures, showing no significant differences due to the variation of fracture energy values.

4.4.5 Sensitivity to the tensile strength

In order to evaluate the influence of considering or not the tensile strength of the fracture, a case has been run with zero tensile strength.

Table 4.15 shows a summary of the variables that describe the geometry of the fractures generated, assuming elliptic fracture shape. The results have been compared with those obtained considering non-zero tensile strength case (base case, Table 4.13). From the analysis of the results, it can be seen that the effect of tensile strength is remarkable; depending on the *in situ* stress, the increase of fracture area surface with respect to the base case was between 10% and 26% (see Fig. 4.83).

Another interesting point to note is the change in the aspect ratio: the results without tensile strength exhibited an inversion of this parameter with respect to the case with tensile strength. For jobs 1 and 3 the propagation of the fracture is mainly vertical, while the job 2 propagation is horizontal. These changes can probably be explained by the fact that in the absence of tensile strength, propagation is probably determined by the distribution of *in situ* stress and the permeability, while in the case with non-zero tensile strength, the tensile strength takes an important role.

The final shape of the fractures is observed in Fig. 4.84, where a comparison of

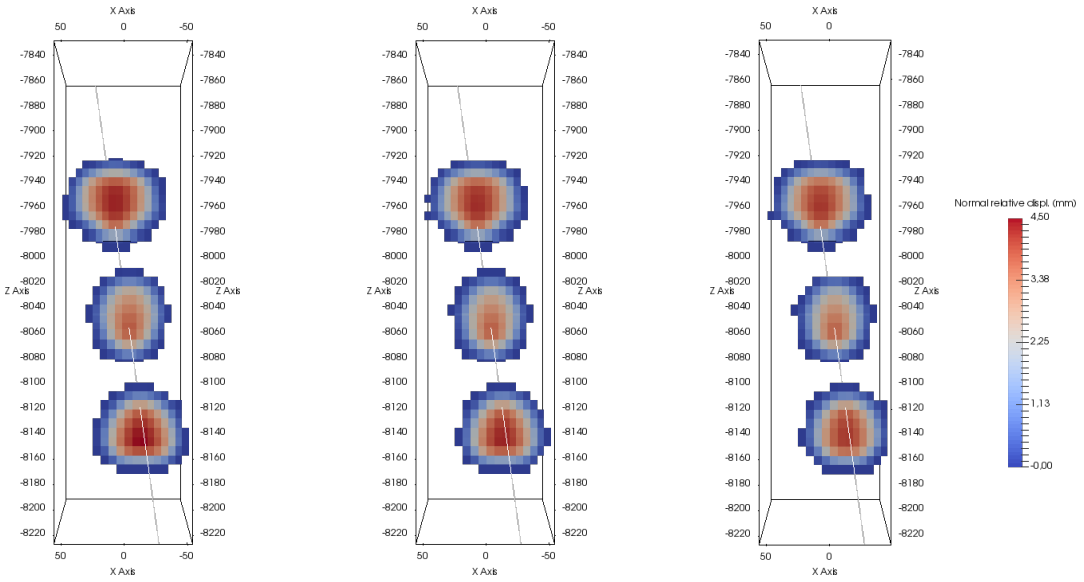

(a) u_{crit}=10 mm (b) u_{crit}=15 mm (c) u_{crit}=20 mm

Figure 4.82: Effect of fracture energy variation, comparison of normal relative displacements (mm) after 3 stages injections: (a) case with u_{crit}=10 mm; (b) case with u_{crit}=15 mm; and (c) case with u_{crit}=20 mm

Table 4.15: Fracture shape of 3D 3-stage analysis with/without tensile strength (sensitivity analysis).

	$\varnothing_{hz}$ m	$\varnothing_v$ m	$\varnothing_{hz}/\varnothing_v$	A m^2	ΔA %
Job 1	80.8	84.6	0.96	5368.73	10.28
Job 2	87.5	81.4	1.07	5593.99	19.61
Job 3	92.1	106.0	0.87	7667.52	25.95

$\varnothing_{hz}$, horizontal diameter
$\varnothing_v$, vertical diameter
$\varnothing_{hz}/\varnothing_v$, aspect ratio
A, geometric area, $A = \pi \times \varnothing_{hz}/2 \times \varnothing_v/2$
ΔA, increment respect to base case analysis (Table 4.13)

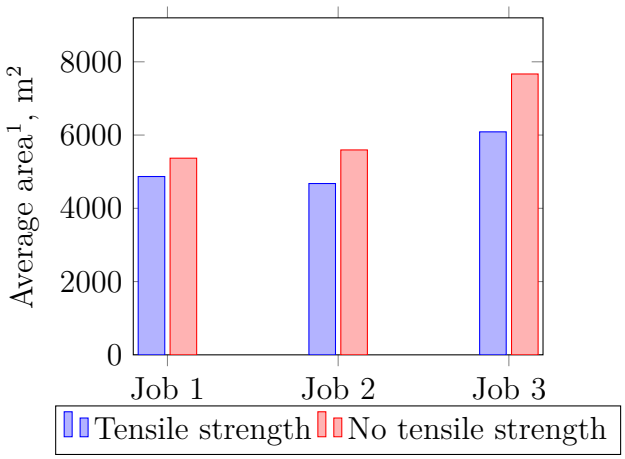

[1] Area of the idealized ellipse.

Figure 4.83: Average area surface (m^2), comparison between cases with/without tensile strength.

normal relative displacements between with/without tensile strength is presented. An interesting aspect that can be observed in this figure is the reduction of the normal relative displacement in the case without tensile strength. The maximum normal relative displacement observed is 3.83 mm while the maximum for tensile strength case is 4.33 mm. The reason for this difference can be explained with the type of boundary condition applied at the point of injection. As in both cases the injection rate is identical, the case without tensile strength which has more fracture surface, does not have to increase the thickness as much, in order to accommodate the same volume of injected fluid.

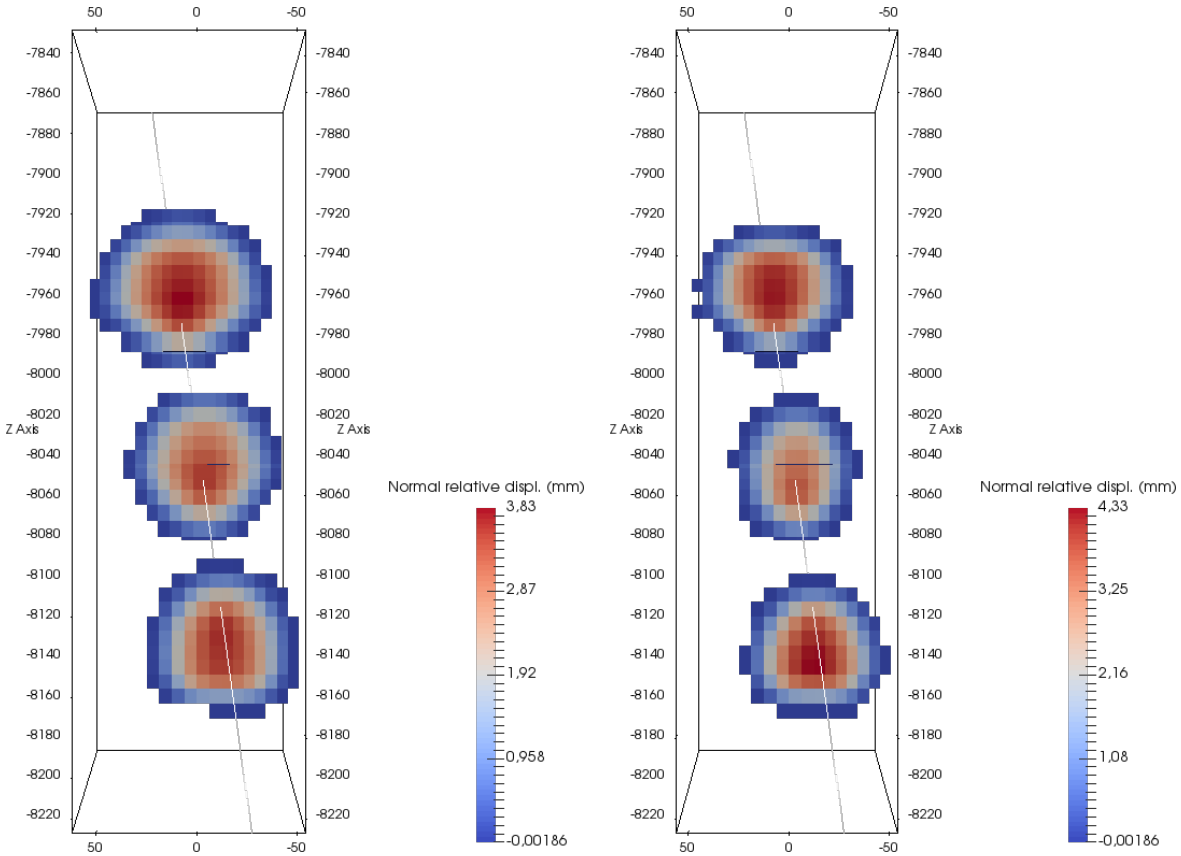

(a) No tensile case

(b) Tensile case

Figure 4.84: Normal relative displacements (mm) after 3-stage injections: (a)) case without tensile strength; and (b)) case with tensile strength

Chapter 5

Sand production modeling

Contents

The production of sand (also known as sand/rock production or sanding) is a phenomenon that occurs in oil wells. The wall of the oil well can not resist the state of stresses imposed during the drawdown process. The result is a disaggregation of the medium into sand grains.

Due to the scale of analysis (centimeter scale) the sand production modeling is strongly influenced by the effect of the rock microstructure. This influence may becomes crucial in perforation holes, where small diameters are used. Current methodologies, based on continuum strategies, solve microstructure effects by means of increasing the complexity of the model, for instance using *Cosserat* theory, gradient plasticity, etc. (Vardoulakis et al., 1996, Stavropoulou et al., 1998, Papamichos et al., 2001). Although

these procedures may lead to realistic results, they are not valid for all cases (i.e. tensile zones may not be well defined). Other methods based on discrete approach have also been developed, as for example the DEM. Discrete approaches produce interesting results from a mechanical point of view, because they are able to reproduce the discrete nature of rock and realistic failure kinematics on the basis of conceptually simple and physical model assumptions. However the main limitation of this approach is the modeling of the fluid flow, which is usually calculated by means of the FEM solved on a separate background mesh and then the fluid pressure is "injected" into the DEM model (Jensen et al., 2001, Li et al., 2006).

The main motivation of the present work is to provide a methodology that can overcome some of those limitations for the modeling of rock sand production. On the one hand, one objective is to avoid complex continuum formulations with unphysical parameters and that, being limited by the kinematics of deformation of continuum media, exhibit strong limitations to represent the right kinematics of failure, mostly due to the propagation of cracks and discontinuities. On the other hand it is also intended to provide a more satisfactory solution for the flow problem, in the sense that the domain can be the same and the open cracks and discontinuities may become preferential channels in the flow calculations. For this purpose, a new methodology is proposed based on a mesomechanical approach, successfully used in heterogeneous materials such as concrete (Carol et al., 2001). The application of this approach to rock sanding was first proposed in the context of the candidate's Graduation Thesis (Garolera, 2003), in order to obtain a realistic methodology for assessing the risk of sand production and a quantitative assessment of the problem.

This chapter has been divided into six sections. The first section contains a brief introduction of the problem to be modeled, followed in the second section by the corresponding state of the art. The third section deals with the description of the microstructure analysis in rock materials that will be used for material characterization in Sections 5.5 and 5.6. Section 5.4 is devoted to the methodology of sand production analysis The results are included in Sections 5.5 and 5.6. In this Thesis, two sets of hollow cylinder test simulations are presented. The first set (§5.5) consists of a set of simulations oriented to the validation of the method. The calculations were made using a prototype material using typical parameters for sandstones. The studies have been oriented to the study of the sensitivity of the method and to the study of the effect of size. The second set (§5.6) of simulations has consisted of reproducing real rock sanding data.

5.1 Introduction

The production of sand (also known as sand/rock production or sanding) is a phenomenon that occurs in the wells. The wall of the well can not withstand the state

of stress created during the drawdown process. The result is a disaggregation of the medium. In the case of oil wells, according to data from the *Society of Petroleum Engineering* (SPE), the problem affects more or less 70% of oil and gas reserves, due to the fact that most of these reserves are found in sandy materials (Fjaer et al., 2008).

The phenomenon is caused by the fracturing of the medium due to the change of stress that occurs during excavation, and the pressure gradient imposed during oil extraction. This fracturing involves a loss of cohesion between grains, their disaggregation and finally their removal by fluid flow, resulting in the production of solid particles. The final result of this process can vary from simple erosion of the wall of the drill to the collapse of the cavity. The factors that influence the production of sand can be classified into three groups: (i) factors related to the geologic formation; (ii) factors related to the kind of completion and (iii) factors related to the production strategies. See Table 5.2 (§5.2) for more details.

From the technological viewpoint, the problem of sand production has been approached with the use of variety of techniques to prevent sand disaggregation, generically called *sand control*. Aside from controlling the draw-down pressure production rate, basically two families of techniques are used to control sand production: (i) chemical consolidation, i.e. resin injection, precipitation of $CaCO_3$, etc.; and (ii) physical exclusion, i.e. gravel-pack, screen-filters, etc.

In spite of achieving the primary objective of reducing sand production, however sand control techniques may result in a loss of productivity that in some cases may not be affordable. For this reason, since two decades ago, efforts have been aimed at understanding the mechanisms of sanding in order to improve recovery techniques (Han, 2003). Nowadays it is well accepted that certain amount of sand production may be acceptable in order to enhance production. Therefore the objective is to develop the tools in order to be able to quantify the conditions to maximize the production of hydrocarbons while maintaining the production of sand within the acceptable limits. Poor management of this phenomenon can lead to problems of sand overproduction. Table 5.1 depicts a list of problems and benefits of not doing any sand control.

The production of sand is a matter concerning any kind of perforation in disaggregable materials, mainly sandstones but also present in calcareous rocks. Due to the wide range of cases, present work focuses on weak formations, and in particular on those cases in which perforated boreholes are used for completion. This technique is used when the casing is set and cemented to the formation. Then, to allow hydrocarbon production, the casing is perforated by means of charges that are fired from borehole into the formation using perforation guns. This method creates perforations perpendicular to the borehole axis, of 1 cm to 2 cm of diameter and 20 cm to 50 cm length (see Fig. 5.1-left). Note that, to avoid confusions in this thesis, the word perforation refers to small diameter lateral perforations generated with the gun technique.

From the numerical point of view, in the analysis of perforations one of the key

Table 5.1: List of pros and cons of no sanding control (Han, 2003, Dusseault and Santarelli, 1989).

Problems	Benefits
• Erosion of production equipment. • Well blocking, blockage of tubing assemblage and plugging of the surface facilities. • Increase workover operations to repair or replace equipment and clean wells. • Formation subsidence and casing collapse • Treatment problems of sand waste impregnated with oil.	• Porosity and permeability enhancement. • Increase oil mobility, due to reduction of resistance to liquid movement. • Foamy oil behavior, the exosolution and growth of gas bubbles in the soil.

aspects is the scale effect. Considering the order of centimeters of the perforation diameter, the formation microstructure may have a significant role. Standard continuum approaches can not take heterogeneities into account very easily. To remedy this limitation, alternative approaches have been proposed, the main ones of which: (i) the use of enriched continuum methods (i.e. *Cosserat* continuum, gradient plasticity, etc.); and (ii) the use of discrete approaches (i.e. DEM). However each of these technique have their own drawbacks.

The present study intends to overcome the main drawbacks of existing numerical simulation techniques. A mesoscopic (micromechanical) approach is proposed, in which the grain level is explicitly discretized by using the finite element method with zero-thickness interface elements. In particular, the present chapter focuses on the 2D analysis of a perforation cross-section. Figure 5.1 shows a schematic perforation including the 2D cross-section considered for the numerical analysis.

5.2 State-of-the-art of sand production

As mentioned in section 5.1, solid production is produced as the result of the effects of the change of stresses in the medium plus the drag force exerted by the fluid. The intensity of this process, in turn, depends on many factors. Several authors describe in detail all the factors that may affect the volume of sand obtained. In particular Veeken et al. (1991) arrange the factors in three groups: (i) factors inherent to the geological formation; (ii) factors related to the drilling/completion technology; and (iii) factors related to the production phase. A detailed list of factors is depicted in Table 5.2.

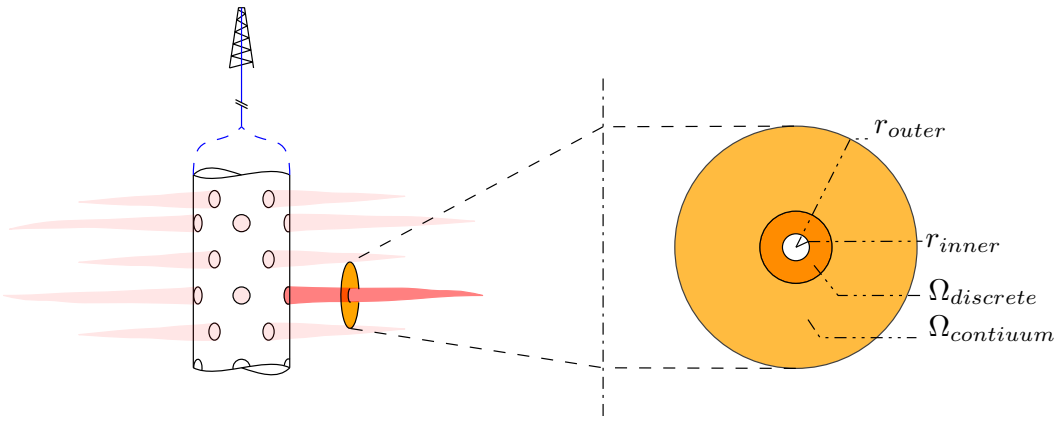

Figure 5.1: Schematic drawing of a borehole with horizontal drills generated through perforation guns. Study section is presented in orange.

Table 5.2: Parameters that influence the production of sand Veeken et al. (1991).

Geological formation		**Completion**	**Production**
Rock	**Reservoir**		
Strength	Pore pressure	Well dip and diameter	Flow rate
In situ stress	Permeability	Casing (open well, perforation guns,...)	Drawdown pressure
	Fluid composition (gas, oil, water)	Kind of well (production/injection)	Fluid velocity
	Drainage area	Sand control screens	Accumulated volume of sand
	Reservoir thickness	Completion and stimulation fluids	
	Homogeneity	Pipe diameter	

The state-of-the-art review is divided into two parts: first, Section 5.2.1 describes the basics about sand production, with emphasis in experimental observations; and second, Section 5.2.2 is devoted to the prediction tools, with special interest on numerical methods.

5.2.1 Understanding sand production

Sand production is a complex problem involving several disciplines, among them: 1. continuum mechanics; 2. fracture mechanics; and 3. fluid dynamics. Due to difficulty to isolate factors in field data, conceptual models and laboratory tests have been proposed to help understanding the basics of sand production. As an introduction to sand production, the conceptual model proposed by Morita (found in Fjaer et al. (2008)) will be discussed first. In spite of its simplicity, this model provides a simple way to understand the relative importance of stress state and fluid flow in sand production, and particularly that in general drag forces from the fluid are not enough to generate sand production, and therefore sand production in general will be the consequence of the change in effective stress state. Then, the section includes a brief review of experimental tests. Some conclusions obtained from existing literature are summarized.

5.2.1.a Conceptual model for drag forces

As an introduction, the conceptual model of forces from Morita (1994) is briefly described. This model considers the forces acting on a single rock particle or grain (see Fig. 5.2). Two kind of forces are considered: (i) the binding force (F_r), value necessary to break the inter-granular bonds, and (ii) the destabilizing force (F_h), which is the drag force exerted by the fluid.

The binding force is obtained assuming a frictional model such as Mohr-Coulomb, with cohesion C_0, tensile strength T_0 and a friction angle ϕ. As the consequence, the average force (F_r) necessary to remove a grain is equal to:

$$F_r = \pi \left(\frac{d_g}{2}\right)^2 \left[4C_0 + tan\left(\phi\right)\left(2\sigma'_r + 2\sigma'_\theta\right) + T_0\right] \tag{5.1}$$

where d_g is the average grain diameter; and σ'_r and σ'_θ are the radial and circumferential components of the effective stresses.

On the other side, an estimate of the drag forces is obtained considering that forces (F_h) are proportional to the fluid pressure difference between the two particles sides and that may be obtained from the pressure gradient and size of the particle, and substituting the Darcy expression $\left(q = \frac{k}{\eta_f}\nabla\phi\right)$ and the volume of one grain, $V_g =$

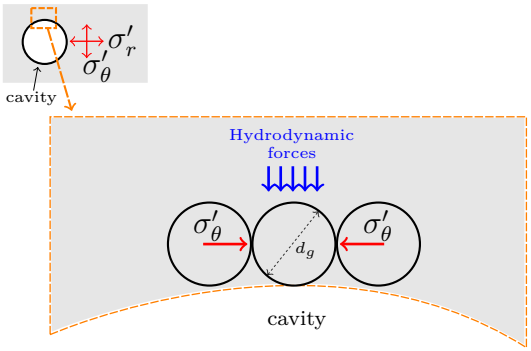

Figure 5.2: Sand grain at the wall of a cylindrical test (figure adapted from Fjaer et al. (2008)).

$\frac{1}{6}\pi d_g^3$, the final expression is obtained:

$$F_h = 30\pi\eta_f \left(\frac{1-\phi}{\phi^3}\right)\frac{Q}{A}d_g \tag{5.2}$$

where η_f is the dynamic viscosity; and ϕ the porosity.

Equations (5.1) and (5.2) will help us understanding the relative importance of the various factors for sand disaggregation. For this purpose, strength is assumed to be very low; friction angle is assumed zero and cohesion as the only term contributing to the stability. Additionally, a cohesion value of 1 MPa is considered, which corresponds to a poorly consolidated sandstone. The results obtained for Eqs. (5.1) and (5.2) for different grain sizes d_g 10 µm and 100 µm are presented in Fig. 5.3. As shown in the figure, destabilizing forces F_h are below resistance forces F_r in all the domain. Consequently, this simple case demonstrates that fluid flow in poorly consolidated sandstones is not sufficient for sand failure. Therefore, in general, sand production must be caused by the change in effective stresses that causes failure of the inter-particle bonds.

Surely, in loose sand samples, the fluid drag effect alone may be determinant. However this range of lowest strength is out of the scope of the present study.

5.2.1.b Laboratory tests

Laboratory experimental studies have been used since the first attempts to analyze the production of sand in oil wells. As a former objective, researchers have been focusing their attention on understanding the primary mechanisms controlling solid production.

One of the most common experimental tests generally accepted to reproduce closely the actual conditions of the well is the Hollow Cylinder Test (HCT). However a variety of HCT have been proposed depending on many details of setup and implementation. For instance, Cook et al. (1994) proposed a complex triaxial (axisymmetric) test in which both fluid and stress were controlled (Fig. 5.4). The stress is applied over outer and inner contours ($\sigma_{outer}, \sigma_{inner}$) and the fluid was divided in two components, an

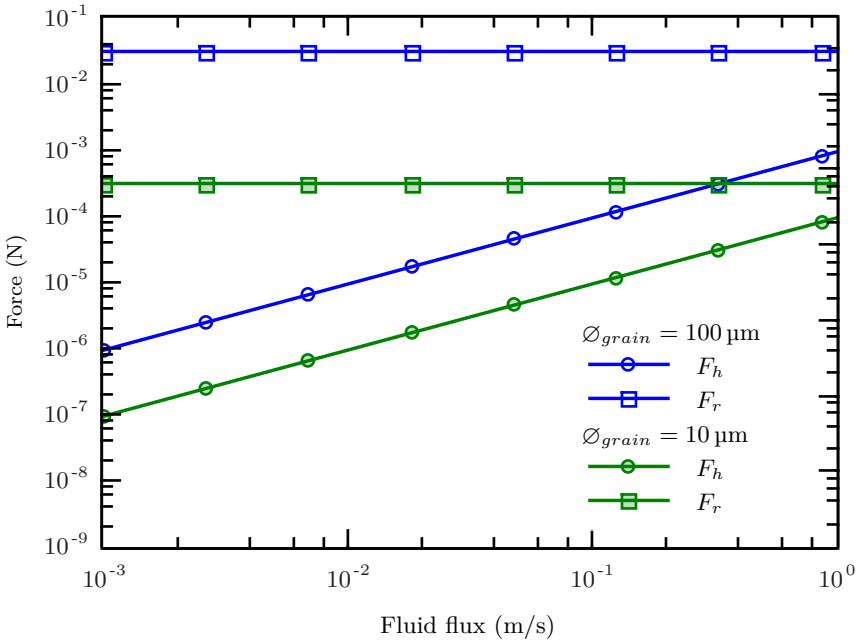

Figure 5.3: Forces involved in the equilibrium of a grain. On one hand the destabilizing force due to the fluid drag (F_h), and on the other hand the resistance forces between grains (F_r). The results are given for two grain diameters, which cover the common range of sandstone grain size d_g 10 µm and 100 µm (adapted from Fjaer et al. (2008)).

axial flow (q_{long}) (along inner hole) and a radial flow (q_{radial}) across rock sample (see Fig. 5.5). In addition, an optical device (endoscope) was installed inside the inner hole to study the mechanisms of cracking. Finally specifically for the study of sand production, a sand trap was installed in fluid system to allow the control of the amount of sand produced during testing process. Afterwards, similar experiment methodology have been conducted by van den Hoek et al. (2000), Nicholson et al. (1998), Tronvoll and Halleck (1994), Papamichos et al. (2001).

It is interesting to note that in the published experiments, the load is applied over outer boundary ($\sigma_{outer} > 0$), with no inner load ($\sigma_{inner} = 0$, atmospheric pressure). This procedure produces a failure that could differ from real borehole conditions. In real conditions, failure state is generally reached after a well decompression.

To ensure the reproducibility of the specimens, the first tests were made with artificial materials (Cook et al., 1994). The samples were made with composite material (sand and resin), which ensures the repeatability and it allows proper characterization. This first study focused on the analysis of materials in a low range of resistance of approximately 1 MPa to 3 MPa under compression stress. This kind of experiments were oriented to determine the basic factors controlling sand production: the contribution of fluid flow and the variation of stresses.

The study also included tests conducted on samples of rock, with results given in different publications, such as Nicholson et al. (1998), Papanastasiou et al. (1998).

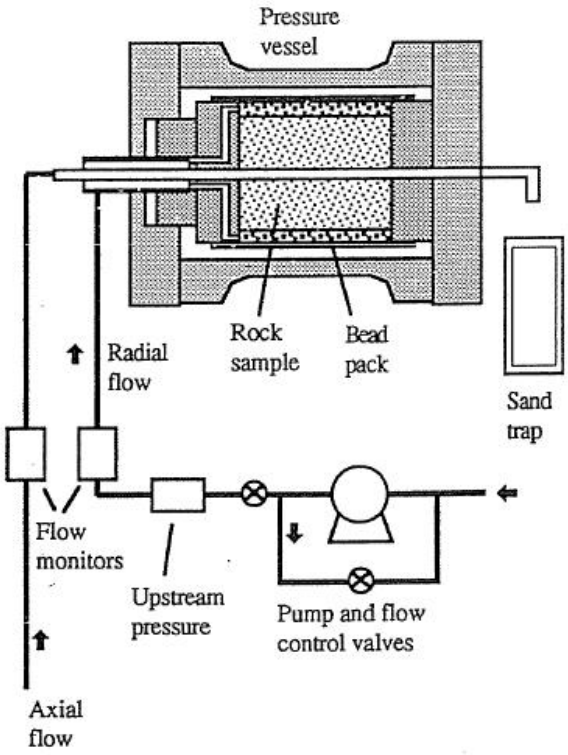

Figure 5.4: Initial test setup for sand production. Test setup consisting of a hollow cylindrical specimen with flow along inner hole, and independent radial and axial stresses (Cook et al., 1994).

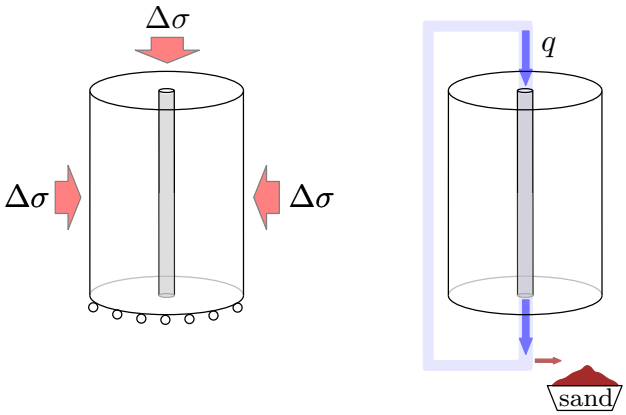

a) Mechanical conditions b) Hydraulic conditions

Figure 5.5: Hollow cylinder test scheme.

Table 5.3: Values of sand failure for specimens of different rock type (Veeken et al., 1991).

	Average strength (MPa)	Average sanding pressure (MPa)
Jurassic	6.1 (5.2 to 7)	5.2 (4.9 to 5.5)
Saltwash South	25.25	19.4 (6.6 to 28)
Red Wildmoor	30.1	32.7 (32 to 33.2)

The analysis used three types of materials, all within the range of weakly[1] cohesive sandstones with high permeability. These tests allowed the authors to contrast the results with those obtained from synthetic samples. Regarding the initiation of sand production (onset), it was noted that the value of the applied load to start the process is not too different from the strength value of the material obtained by compressive tests Nicholson et al. (1998). This is reflected in Table 5.3, where the second column shows the values of compressive strength and the third column includes the pressure threshold value for the initiation of sand production. This result confirmed the importance of applied stress in the process of sand production.

According to the experimental observations, the role of the main agents may be summarized as follows:

Stress state The rock, which owns its initial strength due to cementation between grains, was mechanically damaged by the application of stress. This damage is mainly in the form of inter-granular cracks which cause the rock grains near the inner hole surface to become loose and detach for the material.

Fluid Once the fluid flow established along the inner hole, the fluid drags along the loose particles and this starts the process of sand production.

Laboratory testing of weakly cohesive materials have determined that sand production is extremely linked to the variation of stresses. The stress variation is caused by several factors, the main ones being the release of stresses due to hole excavation, and the variation of effective stresses caused by the change of pore pressure around the hole. Figure 5.6 shows how sand production varies depending on the mechanical stress and fluid pressure gradient (drag forces).

Another important factor is the effect of axial fluid, which acts as a transport agent once started the cracking in the case of weak materials. This factor becomes more important as the rock resistance is reduced, in rocks without any cohesion it may become the main factor.

Finally, we should mention the importance of microstructure in the case of rocks with some cohesion, because size effect is observed in the tests with this kind of specimens.

Flow effect

[1]Uniaxial compressive stress range: 2 MPa to 25 MPa.

An interesting study of the flow effect was presented by Cook et al. (1994). The work, carried out with synthetic samples of low resistance, evaluates the effect of radial flow (transversal flow into the perforation) and the effect of axial flow (flow along the inner hole). In turn, the effect of radial flow was split into two different effects: (i) the effect of the variation of effective stresses due to the gradient of pore pressures; and (ii) the effect of drag forces due to fluid flow. This subsubsection refers only to the second effect.

Cook et al. (1994) found little influence of the drag forces due to radial flow on sand production (see Fig. 5.6). This result, obtained from indirect measurements because it was impossible isolate the effect due to radial flow only, was subsequently confirmed in other studies such as Nicholson et al. (1998). Therefore, it was determined that in the case of low cohesion materials, only the axial component of the flow influences the production of sand. This result was explained on the basis of two factors: the effect of the fluid as a transport agent; and the effect of erosion that results from the impacts of the sand grains carried by the fluid on the surface of the inner hole (wall perforation).

In the specimens tested it was found that, for increased axial flow, sand production was increased significantly. It was found that for speeds less than $0.2\,\mathrm{m}\cdot\mathrm{s}^{-1}$ transport did not occur because the flow did not have enough energy for sand transportation.

Later, Tronvoll et al. (1997), got slightly different results using synthetic samples of lower resistance (0 MPa to 2 MPa). From tests with ultra-weak samples, the radial flow seemed to influence the production of sand. This was attributed to internal erosion exerted by the flow at microstructural level. They reported that this effect accelerated by 50% the initiation of sand production.

Stress effect

The tests conducted by Cook et al. (1994) showed that the most important factor of sand production was the effective stress. In lab experiments, effective stress variations depend on: 1. load applied over external domain; 2. the redistribution of stresses due to the opening of the hole; and 3. the gradient of fluid pressure. According to observations, the stress state is the responsible of generating the initial cracking. Therefore the agent that controls the first step of sand production.

In the case of artificial materials, it was found that sand production began only after a certain stress value, independent of the axial flow, which confirmed the dominant effect of stresses on the initiation of the process (Fig. 5.6(c)).

Another interesting observation was that the maximum production of sand occurred on opposite sides of the perforation, and at 90°with the axis of maximum compression. This is reasonable since these are the areas with maximum shear due to stress concentration effect of the perforation.

Failure mode

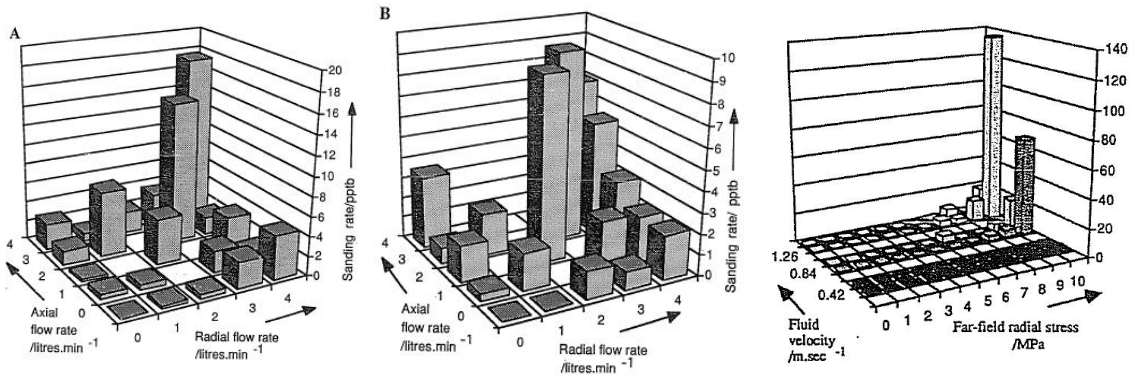

(a) (b) (c)

Figure 5.6: Sand production (vertical axis) versus : (a) radial and axial flow $2\,\mathrm{mm}\cdot\mathrm{s}^{-1}$; (b) radial and axial flow $4\,\mathrm{mm}\cdot\mathrm{s}^{-1}$; and (c) external stress and fluid velocity (Cook et al., 1994).

Another remarkable aspect observed was that the different failure mode obtained for different materials. The samples with intermediate strength properties exhibited a quasi-brittle behavior. Shear failures, breakouts, were observed around the perforation, which tended to enlarge the hole. In contrast, the weaker samples showed compaction behavior. Phenomena of disaggregation and collapse occurred at the same time until failure due to the perforation closure. The experiments also observed the emergence of spiral fractures around the perforation (Fig. 5.7).

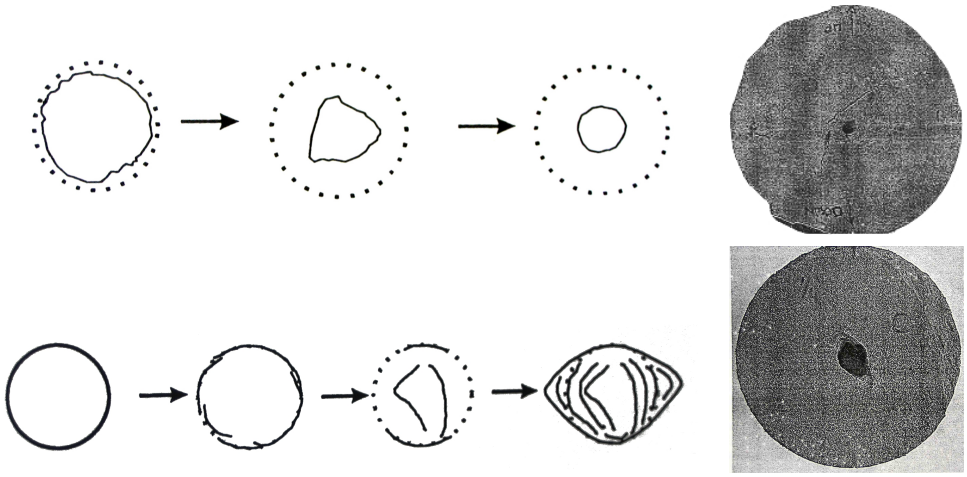

Figure 5.7: Change in diameter on the perforation. Schematic drawings and micro-photographs of the final section. At the top, results for a sample of very weakly cemented rock. Bottom shows results for a moderately cemented rock Nicholson et al. (1998).

The same phenomenon has also been described by other authors, for example in the work of van den Hoek et al. (2000). In this case it was observed how the type of rupture in large diameter boreholes was always under shear-compression conditions, while for small diameters, tensile conditions were also possible (Fig. 5.8). This difference could be explained from the interaction of micro-defects on the stability of the hole, with one

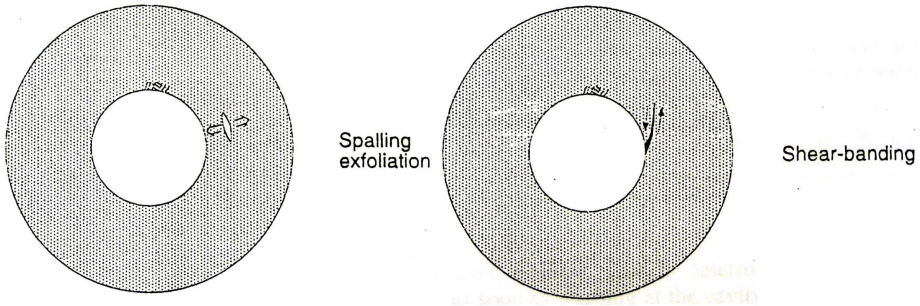

Figure 5.8: Failure mode in the perforations: a) Tensile stress (spalling, exfoliation), b) shear-compression stress (shear bands) van den Hoek et al. (2000).

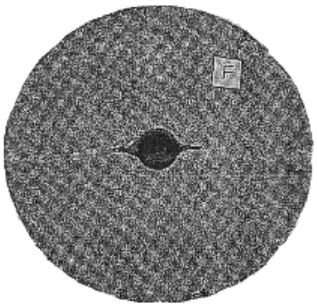

Figure 5.9: Micro-photograph of a cross-section where the fracture has propagated along the plane of stratification (Nicholson et al., 1998).

or the other mechanisms being more likely depending on drilling diameter.

In terms of deformation, it was noted how strain increases upon initiation of sand production (onset). In turn, it became evident how the anisotropy of the material changed the geometry of the rupture, since it tended to evolve according to planes of weaker stratification or fractures (Fig. 5.9).

Figure 5.10 describes the mechanics of borehole failure in sandstone (Cuss et al., 2003), including spalling, breakouts and block detachments.

Scale effect

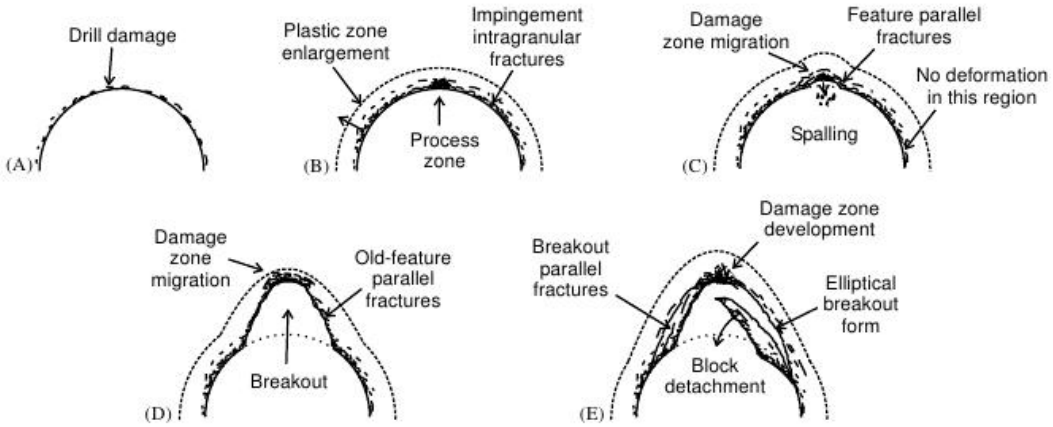

Figure 5.10: Progressive breakout development in Tennessee sandstone (taken from Cuss et al. (2003)).

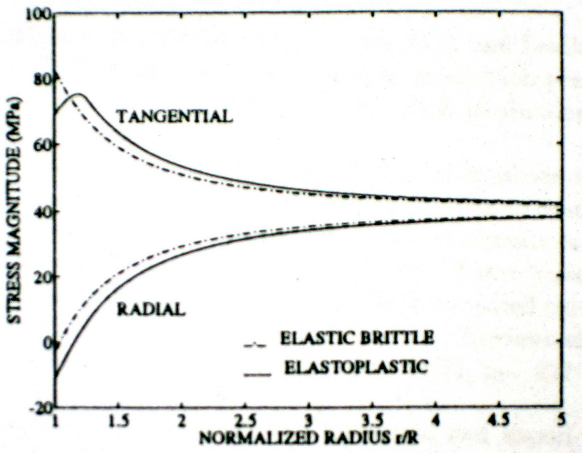

Figure 5.11: Stress distribution for a *Castlegate* sandstone (Bradford and Cook, 1994).

The samples with intermediate strength properties also showed size effect. According to Papanastasiou et al. (1998), for this type of material, perforations of larger diameter were less stable than those of smaller diameter. On the other side, in weaker samples (with a collapsible behavior) the size effect observed was not significant.

5.2.2 Prediction models

The prediction of sand production (rock sanding initiation and rate of sand production) has been attempted with different analytical and numerical approaches, which can be classified into three categories: 1. closed-form formulas, 2. continuum-based models (FEM) and 3. discrete models (DEM).

5.2.2.a Closed-form solutions

In the literature, different analytical models have been proposed to determine sand production. Early models, such as the ones proposed by Morita (1994), Bradford and Cook (1994) or van den Hoek et al. (1994), focused on the determination of the rock sanding initiation (onset), looking at the problem from a mechanical standpoint. For example, Bradford and Cook (1994) use a combination of the classical continuum formulation with the effect of pore pressure and effective stresses. In this way, they obtain an estimate of the minimum pressure inside the hole to prevent breakage. Figure 5.11 illustrates the results obtained.

Later, authors such as Papamichos et al. (2001), Fjaer et al. (2004) proposed an analytical method for assessing not only initiation but also to quantify sand production after that. This result is obtained by relating the accumulated volume of solid particles (m_s) with the increasing porosity (ϕ), being ρ_s the density of the solid particles (Eq. (5.3)):

$$\frac{\partial m_s}{\partial t} = \rho_s \frac{\partial \phi}{\partial t} \tag{5.3}$$

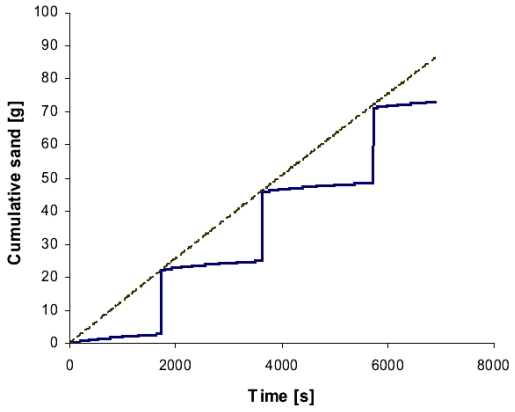

(a)

Q	0.00015 m^3/s	q_o	0.001 m/s
$(D - D_c)/C_o$	0.04	λ_c	500 s/m^3
ϕ_o	0.2	ϕ_{cr}	0.3
ρ_s	2650 kg/m^3	η	1 cP
R	0.01 m	L	0.4 m

(b)

Figure 5.12: Cumulative production curve of sand at constant extraction pressure. Analytical model prediction (dashed line) versus experimental result (continuos line) (Fjaer et al., 2004).

The authors get, after a several considerations (Fjaer et al. (2004)), an expression that provides the amount of sand produced according to a given extraction pressure (Eq. (5.4)):

$$\dot{M}_s = \eta R P_s \frac{D - D_C}{C_0} (Q - S_c q_0) \tag{5.4}$$

where $\dot{M}_s$ corresponds to the average rate of sand production; η is the viscosity of the fluid; R the radius of the cavity; P_s parameter dependent on porosity; D and D_c the extraction pressure and the critical extraction pressure; C_0 the uniaxial compressive strength; Q the longitudinal flow; S_c the surface area; and q_0 the initial Darcy velocity. Figure 5.12 shows an example application of this method.

5.2.2.b Continuum models

This section includes the approaches that consider the rock as a homogeneous continuum medium, without explicit consideration of microstructural geometry of the rock. This methodology considers the rock from a macroscopic point of view, stress and deformations are those of a continuum, and hardening and/or softening are defined by continuum state variables. The most common way to implement this approach via the FEM.

Several FEM-based methodologies have been developed. Initially the focus was to predict the initiation of sand production (onset). Later, continuum formulations were oriented to quantify sand production.

Sand failure, initiation of sand production

The numerical studies of sand production began with the determination of the conditions of rock sand initiation by using different constitutive models as summarized by Rahmati et al. (2013):

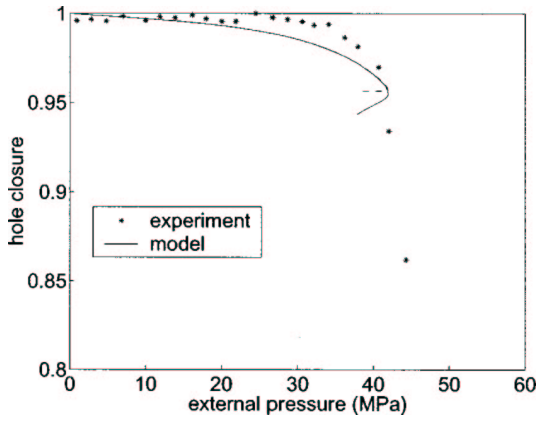

(a)

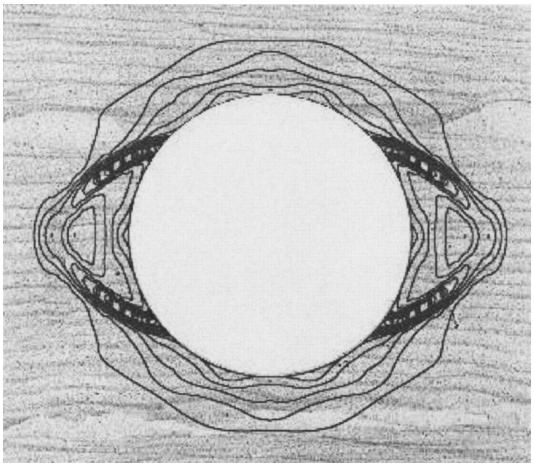

(b)

Figure 5.13: Analysis of the closure of a perforation using of Cosserat continuum. a) Closure of the perforation versus external pressure. b) Shear component of plastic strain after localization (Papanastasiou and Zervos, 2004).

- Models based on Cosserat theory: initially proposed by Muhlhauss and Vardoulakis (1987), Vardoulakis and Sulem (1996), these models use additional degrees of freedom (micro-rotations), which incorporate the properties of the microstructure. Figure 5.13 shows the results obtained by Papanastasiou and Vardoulakis (1992) using this technique.

- Continuum damage models Cheng and Dusseault (2002): they store the effects of previous loading history in an internal variable called damage variable.

- Models based on the theory of gradients, Zervos et al. (2001a,b). These models incorporate strain gradients in the laws of evolution of state variables, which may be interpreted as bringing in an internal length scale. The characteristic length may be related to physical dimension such as grain size, fracture or variable length features, etc. (Papanastasiou and Zervos, 2004).

At the same time, research has also been developed on the application of multiple-phase flow codes. Using the concepts of poro-elasticity (*Biot*), authors like Wang (2001) have applied models with coupling between solid, liquid and gas phases.

Rate of sand production

Once the conditions for initiation of sand production were established, research turned into developing models to predict the amount of particles detached from the rock. Vardoulakis et al. (1996) and Stavropoulou et al. (1998) proposed a study of the problem using a hydro-mechanical analysis in which an additional phase was introduced to evaluate the volume of fluidized grains, V_{fs}. The total volume is:

$$V = V_s + V_f + V_{fs} \tag{5.5}$$

where, V_s is the of solid volume and V_f the fluid volume.

The solution process involves first solving the equations that define the mechanical behavior of the solid skeleton, and then the fluid transport problem including the terms associated with hydraulic (flow) and the terms that define the erosion (fluidized solid). The coupling is achieved by using as common variable the porosity (ϕ), because according to the authors, erosion increases porosity. Then, solid deformations induce changes of porosity, which in turn affects permeability as described by *Kozemy-Carman* equation:

$$k = k_c \frac{\phi^3}{(1-\phi)^2} \tag{5.6}$$

where, k is the current permeability and k_c the initial permeability.

Changes in porosity additionally modify the mechanical behavior of rock including deformations and strength parameters. These changes cause a readjustment of the equilibrium conditions and also in turn cause further changes in porosity. Integrating the equations for all those phenomena, one can finally obtain a time-dependent system of partial differential equations, the mass balances for solid phase, the fluidized solid and the fluid itself, expressed as follows:

$$\frac{\partial \phi}{\partial t} = \frac{\dot{m}}{\rho_s} \tag{5.7}$$

$$\frac{\partial c\phi}{\partial t} + \nabla \cdot (c\bar{q}_i) = \frac{\dot{m}}{\rho_s} \tag{5.8}$$

$$\nabla \cdot \bar{q}_i = 0 \tag{5.9}$$

where, $\dot{m}$ is the solid mass rate; ρ_s the solid density; c the fluidified solid particles; and $\bar{q}_i$ the fluid velocity.

This system may be solved by adding a forth equation, that of the solid mass rate (constitutive equation for erosion):

$$\frac{\dot{m}}{\rho_s} = \lambda (1-\phi) \left(c - \frac{c^2}{c_{cr}} \right) |\bar{q}_i| \tag{5.10}$$

where, λ is a model coefficient and c_{cr} is the critical value for c in which erosion and deposition are balanced. Papamichos et al. (2001) proposed an alternative equation to 5.10. In that case, it is considered that the porosity variation is directly proportional to the flow parameter (Eq. (5.11)), in this way avoiding the coupling with c (Papamichos, 2004).

$$\frac{\partial \phi}{\partial t} = (1-\phi) |\bar{q}_r| \tag{5.11}$$

For the numerical solution of the equations of equilibrium and balance, Galerkin weighted residual technique may be used. The temporal discretization is solved using finite differences.

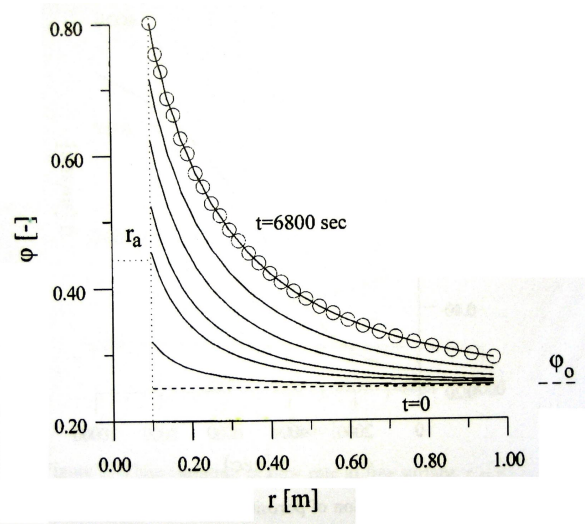

Figure 5.14: Profiles of porosity according to distance from the center of the perforation and withtimeStavropoulou et al. (1998)

The main results by Stavropoulou et al. (1998) are:

- The erosion is concentrated around the hole and decreases very fast with the radius (Fig. 5.14). The same occurs with the permeability, because it is linked to the porosity, which in this case is related to erosion.

- The time of initiation of sand production can be easily determined because it is related to the porosity and it produces a drastic reduction in the strength of the rock.

Subsequently, this approach was used by other authors, like Wan and Wang (2002) to study two-dimensional perforations. In Fig. 5.15, results are presented to illustrate a break in the form of fluidized sand around the perforation, which is consistent with the experimental observations.

Finally, note that this group of methods are able to quantify the amount of sand produced; however they involves a large number of parameters difficult to calibrate (Han, 2003).

5.2.2.c Models of discrete cracking

In this type of numerical models the domain is decomposed in "particles" that can move independently form each other, although they are subject to the forces exerted by the other particles nearby which are in contact. Within this family of methods the most popular is the Discrete Element Method DEM originally developed by Cundall (1971), Cundall and Strack (1979).

The DEM approaches the problem from the microstructure, characterizing each material "grain" as an independent particle. Then the idea is to analyze the problem as a dynamic system, in which each particle is subjected to a net force equal to the sum of the forces from surrounding particles. If the net force is not zero, the particle will

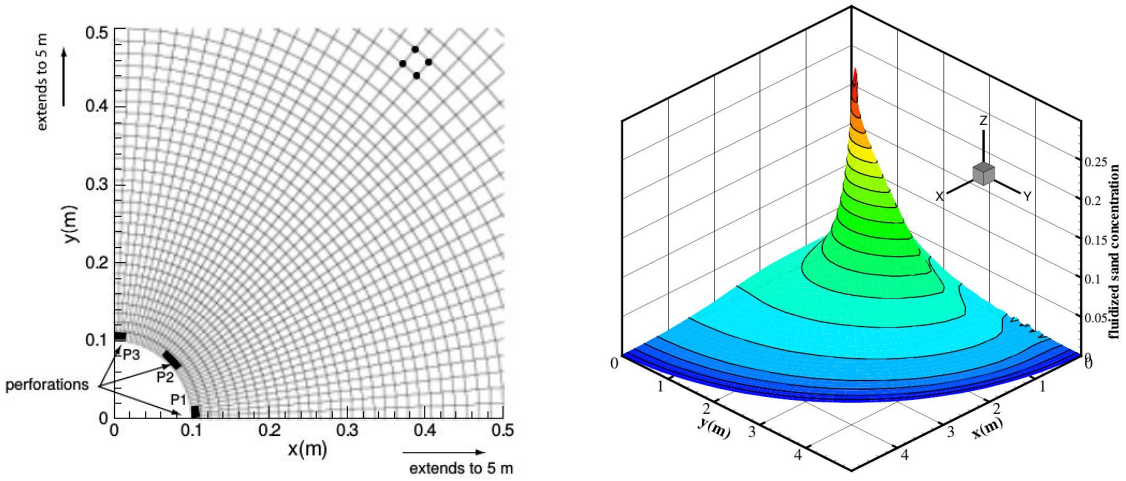

(a) (b)

Figure 5.15: Example with erosion coupling. a) Details of the drilling of the mesh used, b) fluidized sand concentration after 3 days in the drilling environment (Wan and Wang, 2002).

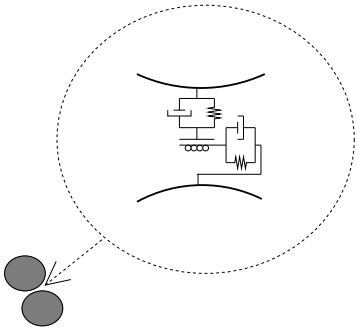

Figure 5.16: Conceptual diagram of the contact between two DEM particles (Jensen et al., 2001).

experience the corresponding acceleration, will change position, and interaction forces will change.

The shape of the particles is assumed to correspond to simple geometries (ellipses, rectangles, etc.). The contacts between particles are simulated as a system of elastic springs and frictional elements (Fig. 5.16). The magnitude of the force is calculated from the distance between centers of particles (overlap). Several authors like Jensen et al. (1999, 2001), Zhang and Dusseault (2000), Cook et al. (2004), Fjaer et al. (2004), Climent et al. (2014), have developed their models within this framework.

Some authors have coupled the DEM with the flow problem. Jensen et al. (1999) considers an additional finite element mesh in the same domain to solve the flow equation (Laplace). The differences in porosity due to the motion of particles, are introduced as changes in the permeability of the continuum as predicted by a cubic law (Eq. (5.12)), where k is the permeability, C is a constant and e is the porosity:

$$k = C\frac{e^3}{1+e} \tag{5.12}$$

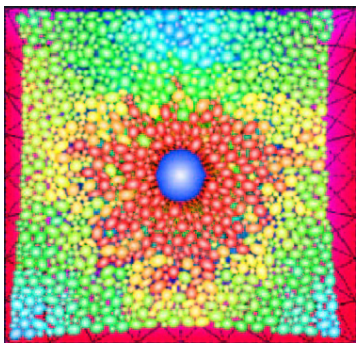

Figure 5.17: DEM simulation in a cross-section of a perforation (Jensen et al., 2001).

With this model, Jensen et al. (1999), run three comparative studies with different strength parameters but same grain geometry. The results, even if only qualitative, have demonstrated the potential of the procedure. However, the authors found some restrictions to apply this methodology. The main difficulties were the high computational cost and the difficulty to reproduce experimental results. This is why, to reduce the number of particles, model particles had to be interpreted as groups of physical particles. Discrepancies were also found in the predictions of Darcy's law, possibly caused by limitations due to the combination of discrete elements and continuum finite elements.

A similar analysis was also developed by Fjaer et al. (2004). These authors analyzed a region of the perforation using grain size values close to the real values, reaching similar results to those seen in experimental models and analytical models (Fig. 5.18).

Finally, it should be noted that, according to Han (2003), this family of methods, although closer to the real problem than other existing methods, has some important limitations. In addition to the limiting computational cost, they exhibit the limitation of the shape of the particles. The rock fabric is no easy to simulate because the particles are reduced to spheres or ellipses.

5.3 Microstructural analysis

In this section, a micromechanical approach based on the FEM+z (§2.2) is described for the analysis of cemented granular materials such as sandstone rock, including the effects of inter-granular and intra-granular cracking and fracture. Instead of the phenomenological parameters used in the traditional continuum-based formulation of the FEM, the proposed methodology is capable of reproducing complex behavior using only a few physical parameters, although this is at the expense of discretizing the grain microstructure explicitly. In previous studies this approach has been used very successfully to represent the mechanical behavior of concrete and other quasi-brittle materials under a variety of loading scenarios Carol et al. (2001), López et al. (2008), Caballero

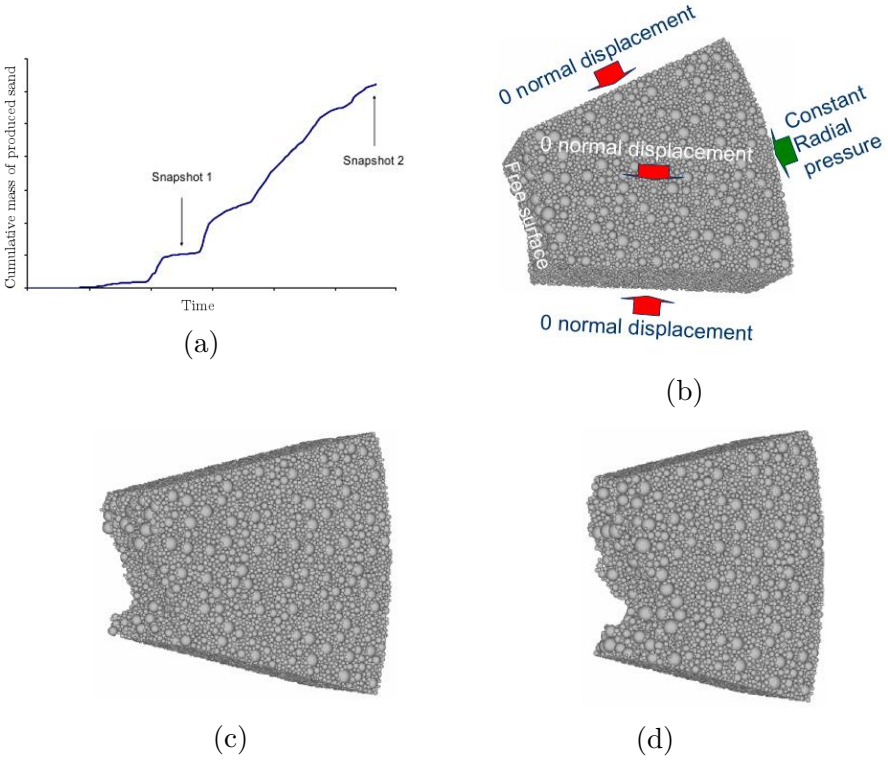

Figure 5.18: Example of a sector of 30° corresponding to the rock around a perforation (Fjaer et al., 2004): a) Cumulative production curve of sand respect time, for a given stress and flow; b) Initial conditions; c) simulation at t_1; d) simulation at t_2.

Microscopic level Mesoscopic level Macroscopic level

Figure 5.19: Levels of analysis as proposed by Wittmann (1983).

et al. (2006).

This section describes several aspects related to the analysis of the microstructure, with special interest in the generation of microstructures.

5.3.1 Extension of microstructural analysis to rock materials.

In the study of physical phenomena, and in particular in mechanics, a key factor is the level of observation. The behavior observed in experiments may be very complex, and attempts to described it with continuum-type models may lead to complex formulations including many non-physical parameters. However, changing the scale of observation, and representing explicitly the various material components, such complex behavior may be obtained as the result of overall composite behavior, even if the behavior of each component individually is much simpler.

The homogeneous continuum assumption traditionally used in engineering studies may lead to acceptable results in simple cases, in which the microstructural studies may add insight and information. However, when material behavior becomes complex, microstructural studies may become the only way to reproduce such behavior and provide a realistic reliable model.

For example, in the numerical modeling of concrete mechanical behavior, which has many similarities to rock behavior, three basic levels of observation were originally proposed (Wittmann, 1983):

1. Macroscopic level: the medium is considered a homogeneous continuum.

2. Mesoscopic level: the medium is considered heterogeneous, consisting of several phases including the largest heterogeneities (aggregate particles) and a matrix (mortar including smaller aggregates).

3. Microscopic level: the internal structure of cement paste and the interfaces between those phases are explicitly represented.

Experience available in concrete analysis (López, 1999, Caballero et al., 2006, López et al., 2008) demonstrate that the intermediate level (mesoscopic level) is enough to explain most aspects of the observed mechanical behavior of such kind of quasi-brittle

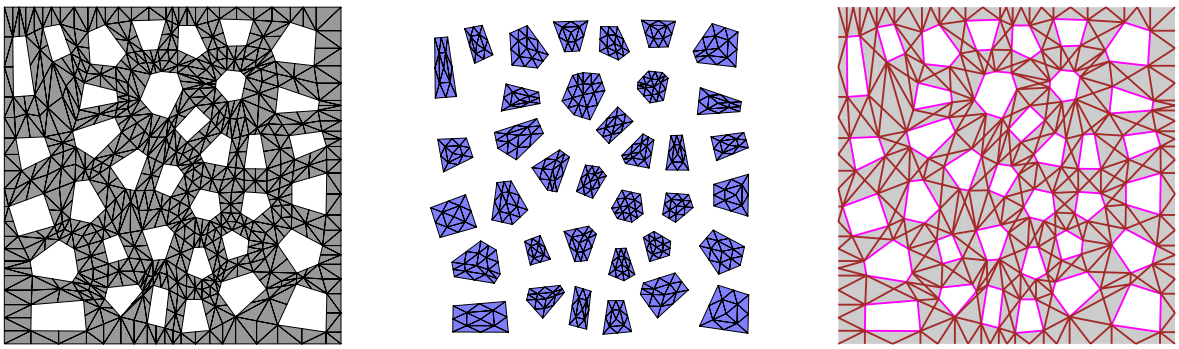

a) Matrix elements b) Aggregate elements c) Interface elements

Figure 5.20: Microstructural mesh used in the study of propagation of cracks in concrete. a) Discretization of the matrix; b) Discretization of aggregates; and c) Interface elements used López (1999).

material. This level of analysis makes it possible to observe the aggregate-matrix interaction, and to explain the mechanisms of failure as well as the phenomenon of size effect. Following the proposal from López (1999), concrete is simulated with two continuum material phases, the aggregates and the matrix, and with two types of interfaces, aggregate-matrix and matrix-matrix. The two phases are discretized with continuum elements (triangles and squares, in 2D), and the interfaces with zero-thickness interface elements. An example of a mesh used in the study of the propagation of cracks in concrete can be seen in Fig. 5.20.

Following the terminology commonly used in the geomechanical literature, although the level of study is mesostructural, this kind of modeling from now on will be refereed to as *microstructural modeling*. Microstructural analysis has been shown to be especially suitable for the study of materials with quasi-brittle behavior.

A qualitative representation of quasi-brittle behavior is depicted in Fig. 5.21, where the strain-stress relationship of an ideal uniaxial compression test is presented. The beginning of the curve is characterized by an initial elastic load (until A), followed by a loss of elasticity due to micro-cracking starting before reaching the peak (B). The peak occurs when coalescence of micro-cracks into a macro-cracks starts taking place. After reaching the peak, the coalescence of micro-cracks into macro-cracks continues (C) until reaching a residual state (D), that corresponds to blocs sliding with friction and tensile or cohesion strength remaining.

Due to the similarity between the observed mechanical behavior of concrete and rock, the microstructural approach has been applied to the analysis of sandstone rock specimens. Both materials are composed of similar phases, the aggregates correspond to the grains of sand, and the matrix, the cement between particles.

Due to the small grain size, average diameter between 0.1 mm to 1.0 mm, the initial microstructural geometry has been simplified in order to reduce the number of elements and nodes. For this reason, the continuum elements belonging to the matrix phase have

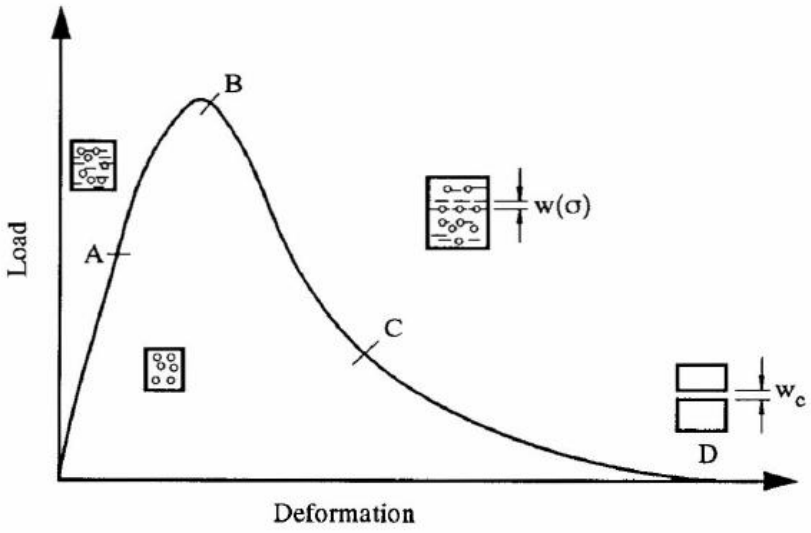

Figure 5.21: Schematic of a tension-strain curve with softening for a quasi-fragile material Karihaloo et al. (1993).

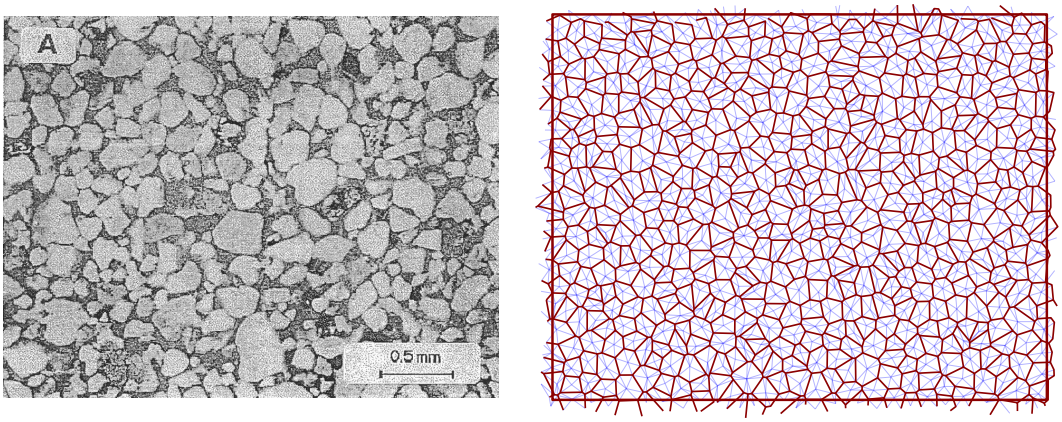

a) Real rock microstructure b) Idealized microstruture

Figure 5.22: Comparison between a real sample: a) Micro-photograph from a sandstone sample (provided by Papanastasiou (2001)); and b) the interface layout of idealized model with FEM+z. In dark, contacts between grains and, in pale, intragranular cracks.

been replaced by an appropriate contact behavior between grains, which includes the behavior of the matrix phase (see Fig. 5.22). This simplification may be reviewed in future studies, depending on the available computational resources.

The microstructural study used in this thesis uses a mixed (or hybrid) procedure. The rock behavior is approximated by a continuum medium containing a grid of zero-thickness interface elements, which make it possible the localization of deformations when approaching material failure thanks to the displacement and stress jumps provided by the interfaces.

One of the main advantages of this type of modeling is the intrinsic incorporation of a characteristic length. Due to the use of relative displacements and the appropriate constitutive law including fracture energy parameters G_f^I and G_f^{IIa} for the mechanical

formulation of the interface, the method naturally exhibits an intrinsic size scale effect.

5.3.2 Microstructure generator

An important aspect of the work described in this chapter is the generation of micro-geometries and the corresponding FE meshes. efforts have been aimed at obtaining an automatic mesh generation procedure with the following requirements:

- Grains of approximately equal size distributed randomly.
- Intergranular phases idealized as a contact between grains.

The mesh generator is based on the version developed by Roa (2004). The process can be summarized in the following steps (see Fig. 5.23):

1. Generation of a initial grid of points with random distribution.
2. A network of triangles is generated using a *Dealunay* triangulation, where the vertices are the random points generated in step 1.
3. A *Voronoi* tessellation is obtained from the *Dealunay* triangulation of step 2. At this point, a filter is introduced to remove the small sides and therefore avoid elements with poor geometric conditioning.
4. Discretization of polygons in triangular elements and introduction of interface elements of zero thickness between each pair of continuum elements.

5.3.3 Micromechanical testing

This section describes the 2D numerical simulation of a triaxial test. The domain considered consists of a square specimen with approximately 40x40 grains. The values of the specimen dimensions (l_0) and grain size ($\varnothing_{grain}$) used in the examples, are specified in Fig. 5.24

In order to include the possibility of intra-granular cracking, zero-thickness interface elements have been inserted, not only along the inter-granular boundaries, but also across grains, as already described in Section 5.3.2.

Boundary conditions

The boundary conditions applied to the triaxial compression test are described in Fig. 5.25. Two loading steps are applied; first, a confining step with a hydrostatic load of value σ_0; and second, a deviatoric step consisting of a prescribed displacement on the upper side of the specimen. Due to the expected softening behavior, an arc-length strategy was employed in the numerical analysis in order to control post-peak response.

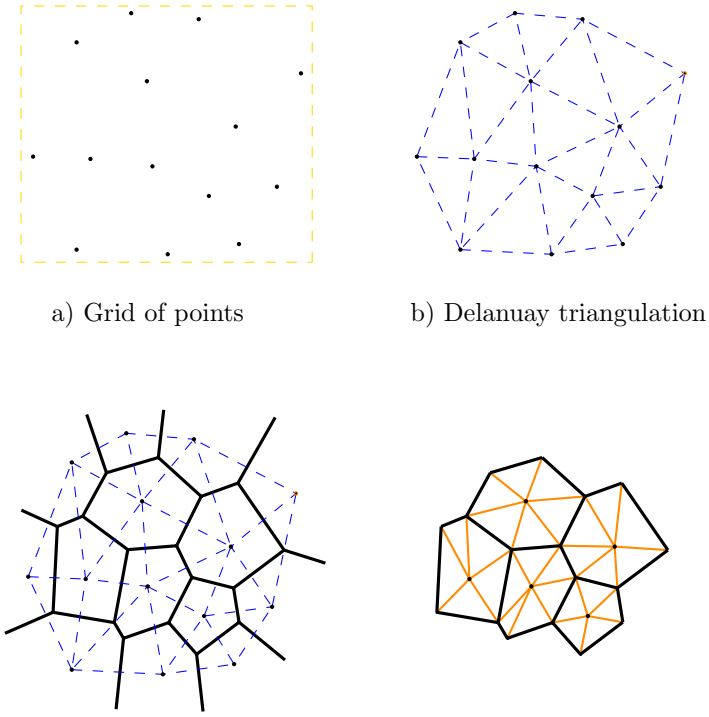

a) Grid of points b) Delanuay triangulation

c) Voronoi tessellation d) Element discretization

Figure 5.23: *Delaunay-Voronoi* based mesh generation method: a) Random node distribution, Delaunay vertices; b) *Delaunay*'s triangulation; c) *Voronoi* tessellation; and d) element discretization; black thicker lines correspond to the intergranular zero-thickness interfaces, and orange thiner lines to intragranular zero-thickness interfaces.

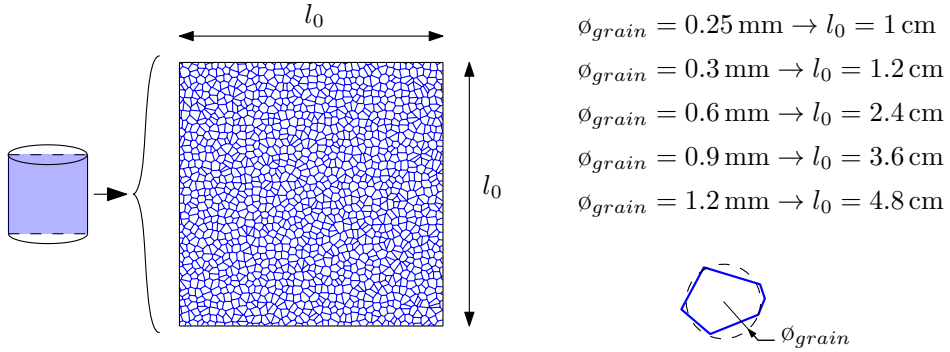

Figure 5.24: Model geometry of the "triaxial" compression test considering rock microstructure.

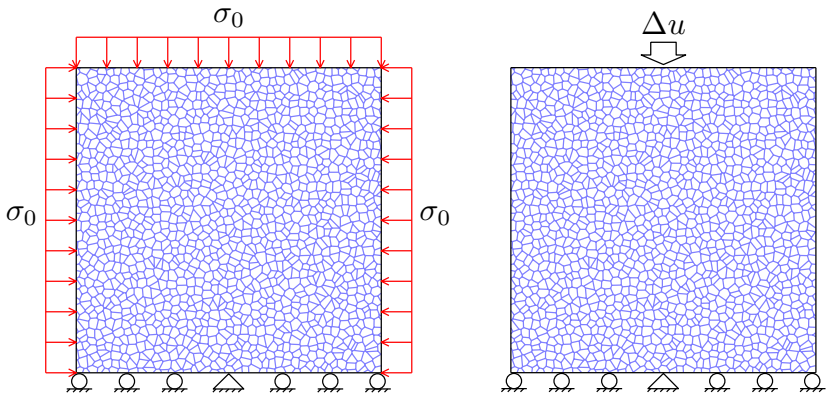

a) Confining step b) Deviatoric step

Figure 5.25: Boundary conditions of the TCT: left) Confining step; and right) deviatoric step.

Table 5.4: Material properties of continuum.

Parameter		*Value*	*Units*
E	Young's modulus	34.0	GPa
ν	Poisson's ratio	0.27	-

Material properties

The micromechanical testing has been performed using typical parameter values based on the *Red Wildmoor* sandstone (Papamichos et al., 2000).

A summary of the main parameters are presented in Tables 5.4 and 5.5. The first table (5.4) shows the material parameters that define the continuum behavior, which have been assumed equal to the typical values for quartz grains.

The values of the interface material parameters have been adjusted to fit to the *Red Wildmoor* biaxial tests (Table 5.5). Note the use of relatively high interface stiffness coefficients (K_n, K_t), in order to ensure small elastic deformation of the interfaces. This aspect is discussed in more detail in Section 5.3.4. Also note the relatively low fracture energy values (G_f^I and G_f^{IIa}), which are necessary to reproduce the low resistance range exhibited by this type of rock.

5.3.4 "Triaxial" Compression Test

The first analysis assumes a fixed grain size of 0.6 mm and intra-grain interfaces with "double" value of strength parameters with respect to inter-grain interfaces.

The evolution of crack propagation for the case of 1 MPa confinement is represented in Fig. 5.26. In the figure, one can clearly identify the qualitative steps of fracture propagation described in Section 5.3.1: micro-cracking, coalescence into macro-cracks, and localized state.

Figure 5.27 shows the triaxial strain-stress curves obtained for different values of

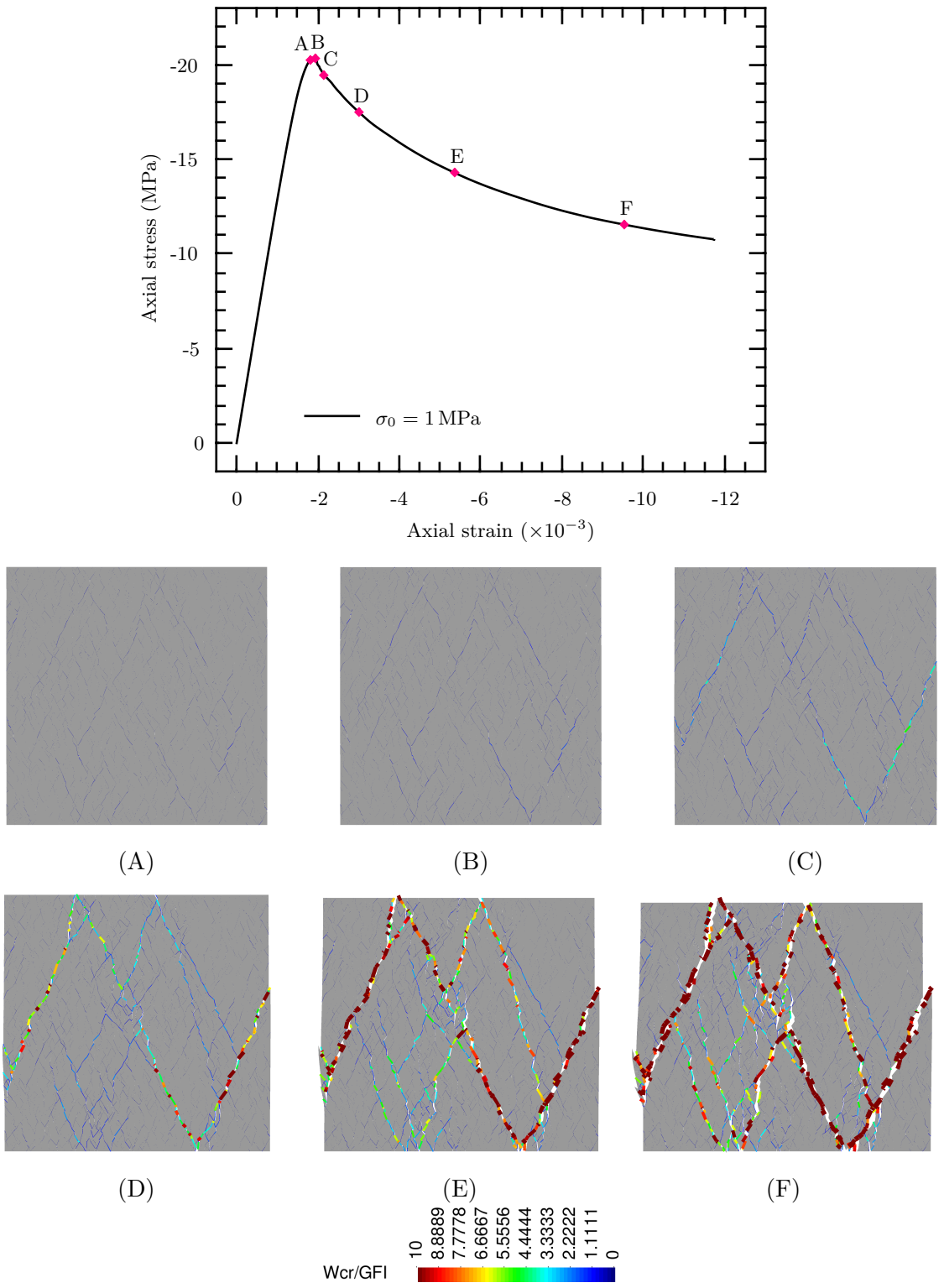

Figure 5.26: Evolution of fracture propagation for 1 MPa confinement case: Top, average stress-strain curve obtained for triaxial compression in 2D; and bottom, Normalized energy spent along interfaces (Wcr/G_f^I). Results plotted on the deformed mesh (magnification $\times 5$).

Table 5.5: Material properties of interfaces.

Parameter		*Value*		*Units*
		Inter-Grain	Intra-Grain	
K_n	Normal stiffness	$1 \cdot 10^8$	$1 \cdot 10^8$	$\mathrm{MPa} \cdot \mathrm{m}^{-1}$
K_t	Tangential stiffness	$1 \cdot 10^8$	$1 \cdot 10^8$	$\mathrm{MPa} \cdot \mathrm{m}^{-1}$
χ_0	Tensile strength	0.4	0.8	MPa
$\tan(\phi)$	Friction angle	0.5773 (30.0°)	0.5773 (30.0°)	
c_0	Cohesion	4.0	8.0	MPa
G_f^I	Energy mode I	0.006	0.026	$\mathrm{MPa} \cdot \mathrm{m}$
G_f^{IIa}	Energy mode IIa	0.1	0.4	$\mathrm{MPa} \cdot \mathrm{m}$
σ_{dil}	Sigma dilatation	10.0	10.0	$\mathrm{MPa} \cdot \mathrm{m}$

confinement: 0 MPa, 1 MPa, 5 MPa, 10 MPa, 20 MPa and 40 MPa. Figure 5.28 represents the crack pattern obtained at the end of each triaxial simulation with different confinement pressures. It is clearly observed that, as confinement is increased, more damage (understood as energy dissipation) is observed and less clear localization is produced. The results show that the approach is able to represent brittle-ductile transition without introducing additional ingredients.

5.3.5 Sensitivity to microstructure

The sensitivity to microstructure is analyzed by means of two kinds of simulations: the analysis of the effect of intragranular strength; and the analysis of the size of the grain.

5.3.5.a Intra-grain strength

Figure 5.29 shows the average strain-stress curves obtained for the three scenarios of intragranular strength: 1) infinite, 2) double than inter-granular strength and 3) same as intergranular strength. It can be observed that intra-granular strength values influence dramatically the resulting behavior of the overall material. Not allowing intra-granular cracking leads to an upper bound of the mechanical behavior for which failure under uniaxial compression is never reached. On the other end, case c) approaches the behavior of a quasi-brittle material without the granular structure considered (since cracks can develop equally through grains as in between grains), which leads to a lower bound of the overall strength; and finally option b) with the right parameters should represent a more realistic intermediate case.

As it can be also seen in Fig. 5.29, the material post-peak response is also greatly influenced by grain strength; as intra-grain resistance is increased, the overall model behavior becomes more brittle.

In Fig. 5.30, the general crack pattern obtained and some enlarged details of a section of a main macro-crack, are depicted for the three assumptions of intra-granular

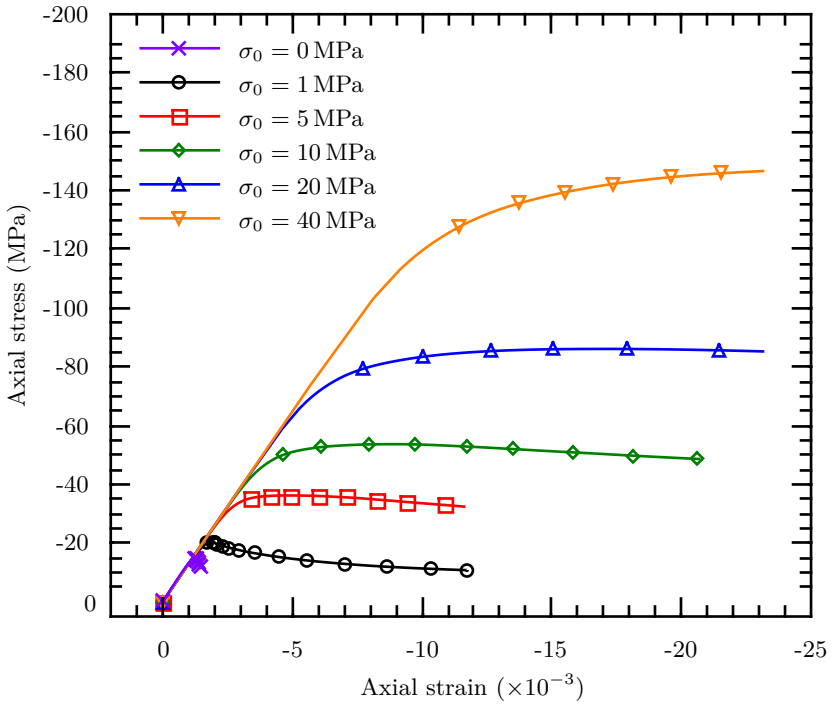

Figure 5.27: Stress-strain curves for different levels of confinement.

strength. For case b) with double strength, it may be clearly observed that cracks are basically opening/sliding around grains except at certain very specific points where grains crack due to the high stress concentration, while for case c) this happens systematically, and for case a) this does not happen at all. These details of micromechanical cracking may help understanding the resulting overall stress-strain curves of Fig. 5.29. A first conclusion of these results is that the direct uniaxial compression test is very sensitive to grain strength, and that some form of intra-granular cracking must be allowed for a realistic description of the direct uniaxial compression test of a granular material using Voronoi-generated grain geometry.

5.3.5.b Grain size

The effect of the size of the grain is analyzed using the size values depicted in Fig. 5.24, that is: $\varnothing_{grain} = 0.25\,\text{mm}, 0.3\,\text{mm}, 0.6\,\text{mm}, 0.9\,\text{mm}$ and $1.2\,\text{mm}$. For this purpose, the coordinates of the original mesh are transformed (scaled) in order to obtain a mesh with the desired grain size. The material parameters remain equal to the previous example (Tables 5.4 and 5.5), and the boundary conditions similar to the unconfined compression test from previous analysis.

Figure 5.31 shows the change in the strain-stress relationship at the macroscopic level, which are obtained for the different grain sizes. It is observed that as the size of the grains is reduced, the initial elastic stiffness of the overall system decreases as well. This may be explained because as the size of the grain is reduced, the number of

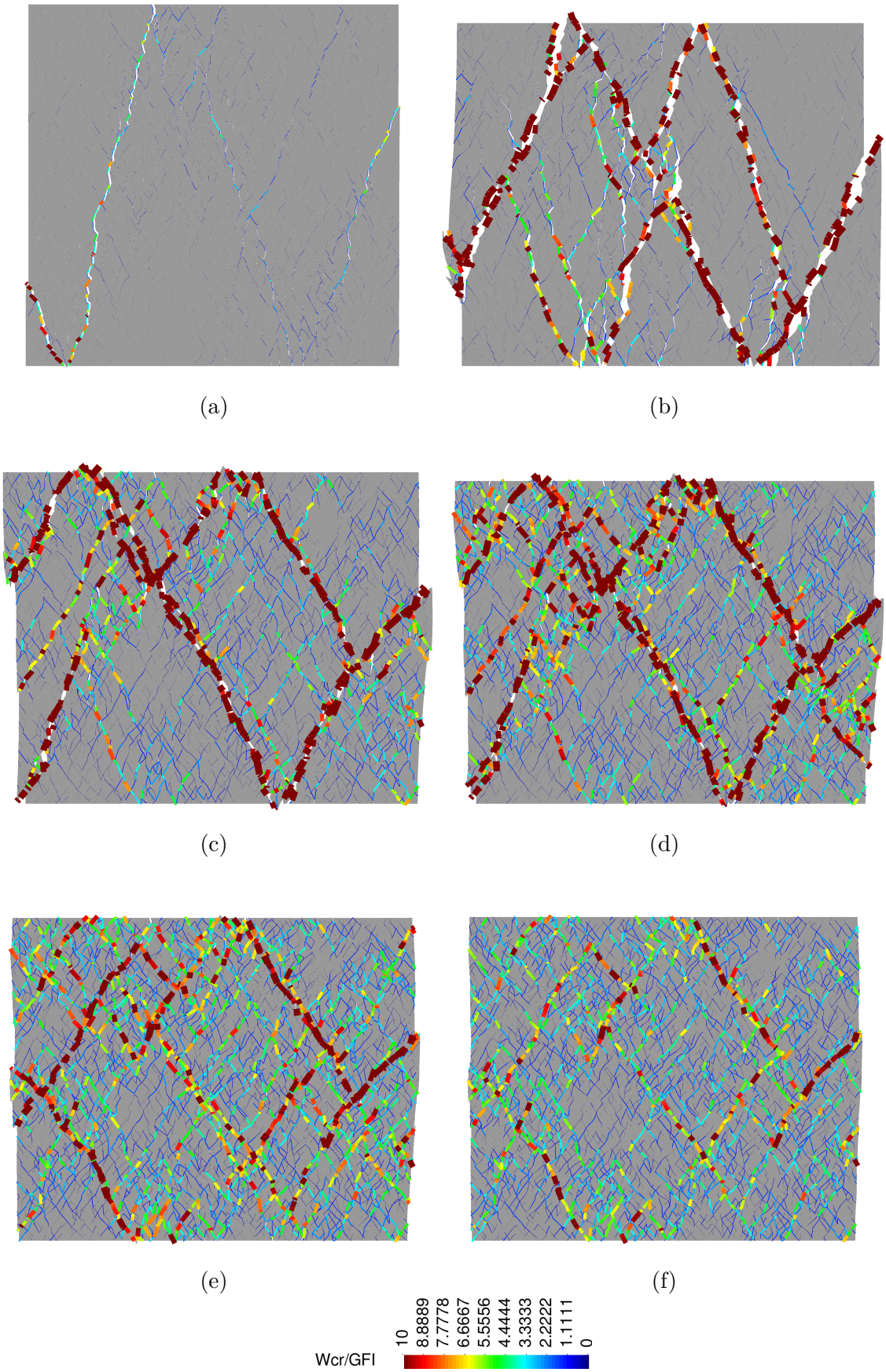

Figure 5.28: Results of the 2D "triaxial" compression test at various confinement pressures. Normalized energy spent (Wcr/G_f^I) at: a) No confinement; b) 1 MPa; c) 5 MPa; d) 10 MPa; e) 20 MPa; and f) 40 MPa. Results plotted on the deformed mesh (magnification ×5) for the final state reached in each simulation.

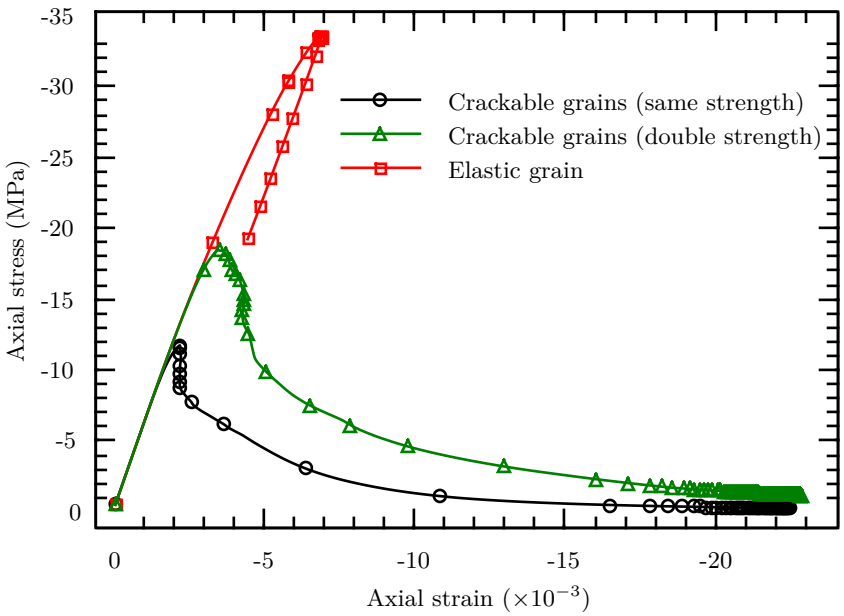

Figure 5.29: Average strain-stress curves for the uniaxial compression simulations, with three different assumptions for intragranular cracking: 1) grains are elastic an can not crack, 2) grains can crack but strength parameters are double than those for inter-granular fractures, and 3) grains can crack, and strength is the same.

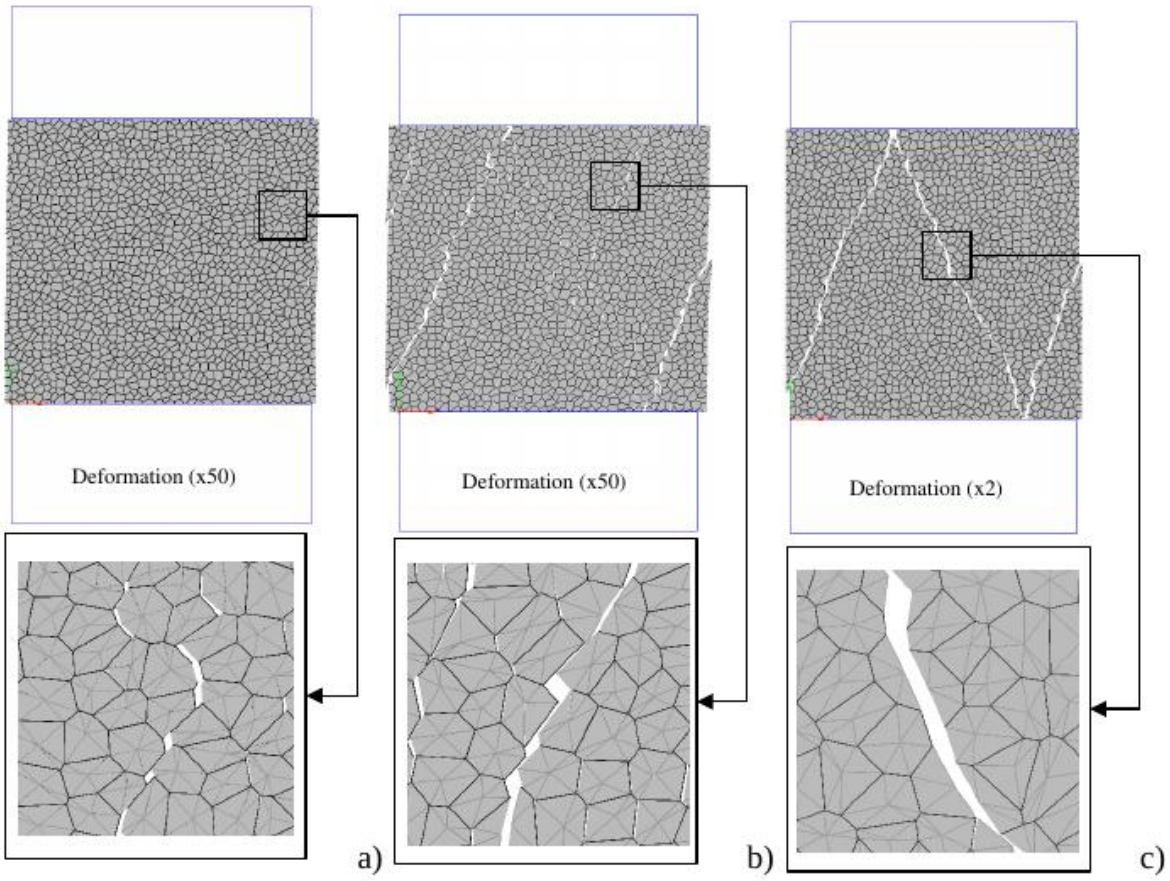

Figure 5.30: Mesh deformations for UCT at different values of grain resistance: a) elastic grains; b) fracture grains (double resistance) and c) fracture grains (single resistance).

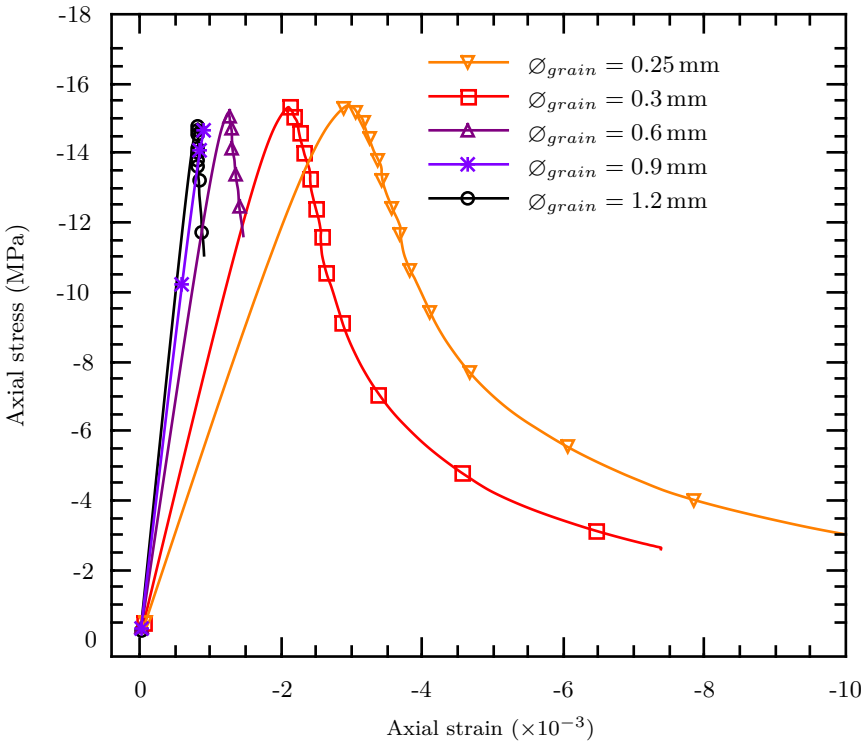

Figure 5.31: Stress-strain curve for uniaxial compression test for different average grain size.

interfaces per unit thickness of material is increased. Assuming as a first approximation that the equivalent stiffness of the system (E_{eq}) may be expressed as a series system composed by continuum and interfaces, the overall equivalent elastic modulus may be expressed as:

$$\frac{1}{E_{eq}} = \frac{1}{E} + \frac{n}{K_n} \tag{5.13}$$

where n is the number of interfaces per unit length. Note that, as the result of the above expression, as the number of interfaces per unit thickness is increased, the equivalent elastic modulus decreases, as observed in the FE calculations depicted in Fig. 5.31.

The equivalent values of Young's modulus and Poisson's ratio as obtained from numerical tests are presented in Table 5.6. Note that increasing the number of interfaces per meter (as it happens when ϕ_{grain} is reduced) leads to lower elastic modulus and to "dilution" of Poisson's ratio. Then, values of Table 5.6 are successfully compared with the analytical solution provided by Eq. (5.13) (case $K_n = 1.0 \cdot 10^5\,\mathrm{GPa \cdot m^{-1}}$) (see Fig. 5.32).

Figure 5.32 shows the value of E_{eq} as a function of grain size for different values of interface stiffness coefficient. The results are obtained with analytical expression 5.13

Table 5.6: Equivalent parameters from micromechanical analysis.

Parameter		$\varnothing_{grain}$(mm)			*Units*
		0.6	0.9	1.2	
E	Young's modulus	13.66	17.25	19.8	GPa
ν	Poisson's ratio	0.15	0.18	0.21	-

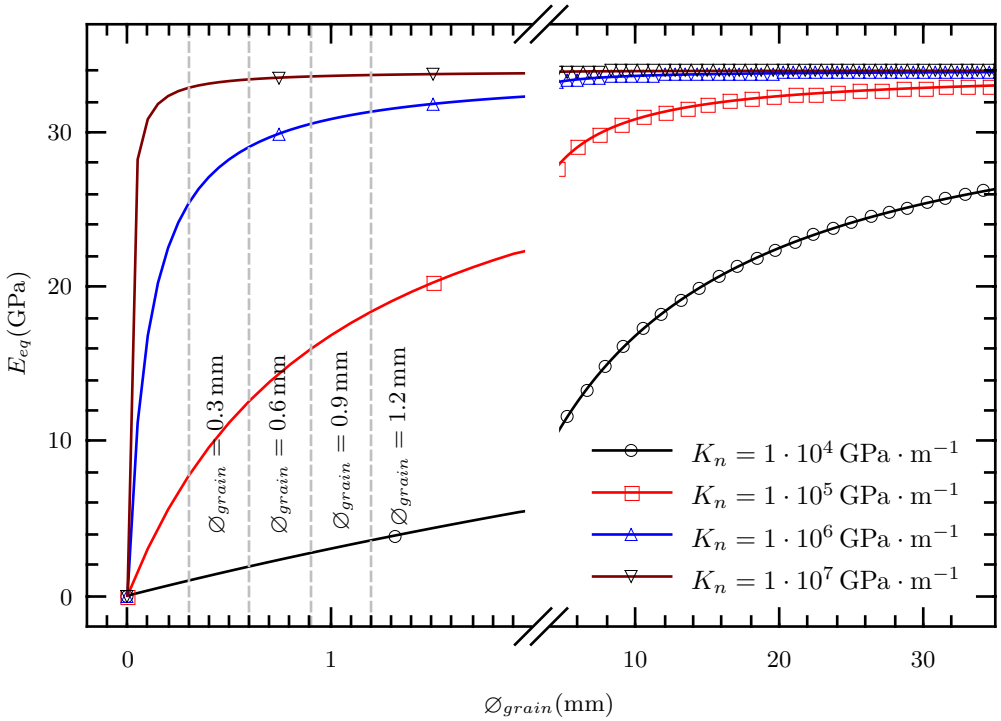

Figure 5.32: Equivalent elastic modulus for different grain sizes and interface stiffness.

assuming that the number of interfaces per unit length may be expressed as:

$$n = 3\left(\frac{1}{\varnothing_{grain}}\right) \tag{5.14}$$

where $\varnothing_{grain}$ is in m.

The curves of Fig. 5.32 indicate that, if one would want overall stiffness to approach the grain stiffness, for the range of grain sizes considered this would require interface stiffness of the order of $1 \cdot 10^7$ GPa · m^{-1} or more, which means at least two orders of magnitude higher than the values considered ($1 \cdot 10^5$ GPa · m^{-1}). The convenience or not of such condition is a separate discussion, which has to do with whether the interface stiffness has physical meaning (that of stiffness of the cementing materials) or it is considered a more numerical artifact (penalty coefficient).

5.4 Methodology of sand production analysis

The methodology which has been implemented for sand production analysis is based on the simulation of 2D micromechanical models of hollow cylinder cross-sections. This section describes the main aspects related to model generation and numerical techniques used for such analysis.

5.4.1 Main assumptions

The methodology implemented is based on the following assumptions:

1. The calculation is made with the theory of small deformations.
2. Cracks totally open in between and inside grains will be identified and an automatic criterion will detect the cases in which the crack trajectory is closed and isolates a grain or group of grains.
3. The effects of the axial fluid are not explicitly taken into account since the study is two-dimensional. However, it is considered that indirectly, the elimination of the grains or groups of grains detached from the rest, is the result of this agent.
4. Due to computational limitations, the minimum grain size considered for the analysis has been 0.6 mm.
5. Although damage is present due the perforation procedure (eg. due to the effects of the explosion Cuss et al. (2003)), this effect is not considered in the initial simulations.

5.4.2 Generation of the sand production model

As already indicated, the simulation of sand production is based on the analysis of 2D cross-sections. In order to reduce the number of discretization elements, the model has been split into two subdomains: an inner discrete domain around the perforation hole, in which the microstructure is explicitly represented; and an outer continuum domain extending to a sufficiently distant boundary, in order to ensure boundary conditions.

The generation of the above geometric sand models is carried out into three consecutive steps:

1. **Generation of the discrete domain** The initial microstructural mesh is generated using the *Delaunay-Voronoi* procedure for an initial square domain (§5.3.2), from which all elements are removed which are inside the desired inner radius (r_{inner}) and outside the desired outer radius (r_{outer}^{discr}). In this way, a domain in the form of a circular ring is obtained (see Fig. 5.33b). In the cases analyzed, the ring thickness has been taken as approximately the radius of the perforation, with a

minimum thickness of 10 grains in order to ensure that the relevant normal and shear stress gradients are located in the inner discrete domain near the hole.

2. **Generation of continuum domain** In order to ensure that the boundary conditions are correctly represented, an extension of the mesh has been carried out with conventional continuum elements, to the limits of a domain (Fig. 5.33c-d). The outer domain is defined with a inner radius (r_{inner}^{cont}), which is the same as the outer radius of the discrete domain (r_{outer}^{discre}), and an outer radius (r_{outer}) where boundary conditions will be applied.

3. **Domain assembly and generation of input data** The final mesh consists of the union of both domains, inner and outer. In order to join the meshes, first the common nodes have been detected and then the nodes and elements of the mesh coming from the outer domain have been renumbered. Additionally, the elaboration of a perimeter set of joints just along the boundary between inner and outer domains has been generated in order to ensure the transition between the mesh in the inner domain and the continuum in the outer domain. This is because the zero-thickness interfaces elements have to end in "T" intersections with other interface elements. During this stage a number of utility files for later post-processing stresses, etc. are also generated. Figure 5.33e-f) shows some details of one of the discretizations performed.

5.4.3 Solid Production simulation

One of the most sensitive developments in the sand production study has been the grain extraction criterion. The methodology implemented for this purpose was based on: (i) definition of the crack failure criterion (zero-thickness interface element failure), and (ii) definition of a criterion for removing a grain or set of grains.

Crack failure criterion

The criterion of crack failure has been developed using the internal variable of the interface constitutive model which consists of the energy dissipated in fracture process (W_{cr}). This energy normalized with respect to G_f^I is compared to a threshold value, typically fixed as 0.7, which is indicative of severe tensile degradation of the interface. Note that for an interface element to be marked as totally cracked, the condition (Eq. (5.15)) must be fulfilled at all its Gauss points.

$$\frac{W_{cr}}{G_f^I} \geq 0.7 \quad \Rightarrow \quad failure \tag{5.15}$$

Sanding algorithm (removing algorithm)

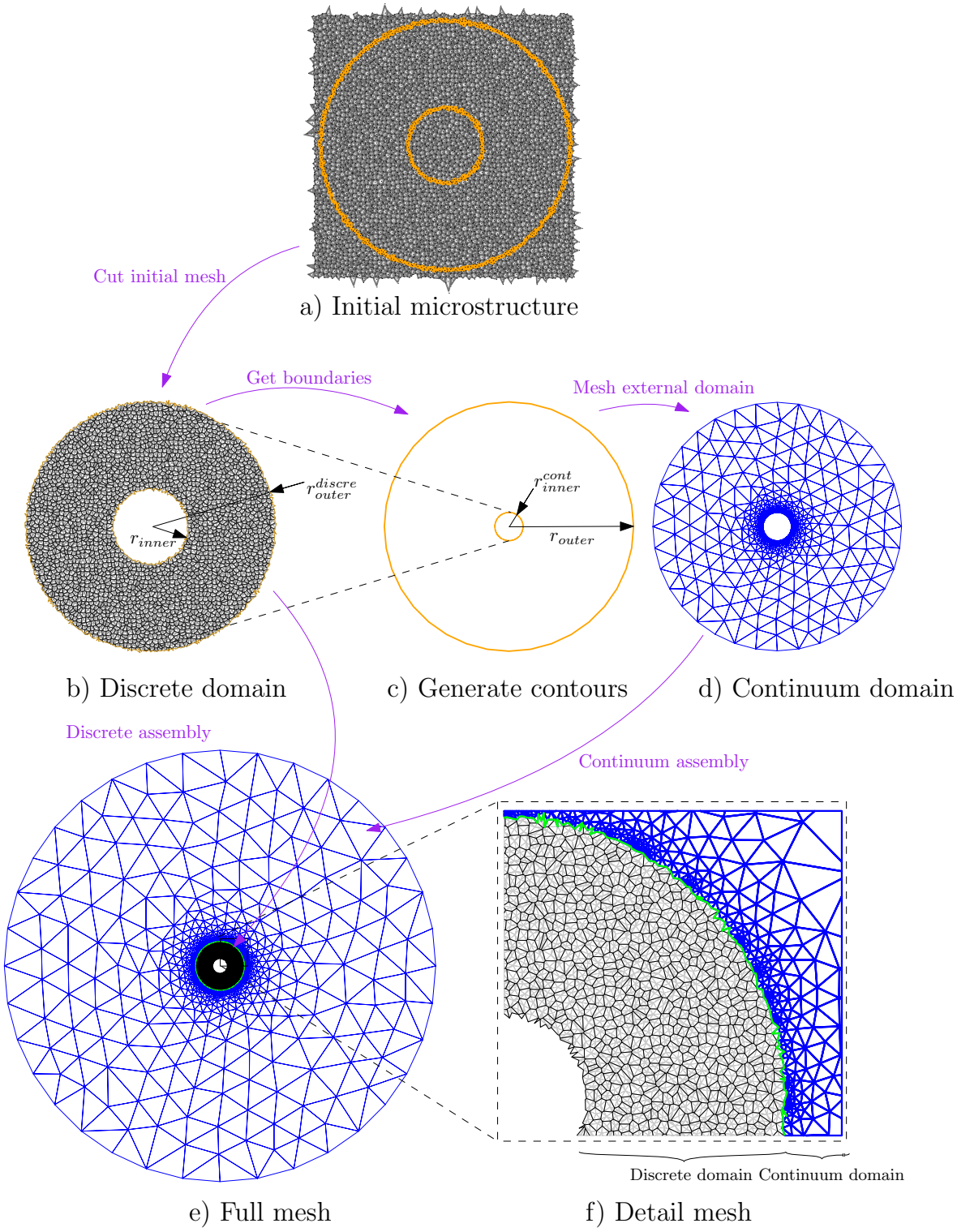

Figure 5.33: Generation of the sand production model: a) initial mesh generated via Delaunay-Voronoi; b) ring-type inner domain; c) geometry of the outer perimeter; d) continuum outer domain; e) complete mesh; and f) detailed view of the inner domain, showing mesh distribution of grains.

Once the cracked interfaces have been identified, a criterion for grain extraction has been defined. This method consists of extracting the grains or groups of grains that are isolated from the medium by a concatenation of fractured interface elements that starts and ends at the free surface of the inner perforation. This procedure has been automated with the inclusion of a module in the DRAC code that checks, at the end of each increment step, the criterion previously explained. The implementation can be summarized in the following points:

1. **Tree algorithm** over failed interfaces. This algorithm looks for any path of cracked interfaces that isolates a part of the discrete domain from the rest of the domain. First, the interfaces with nodes on the inner perforation boundary are checked to detect if they are cracked. Once this is satisfied, a tree algorithm is used to check for any path of cracked fractures that leads to another node of the inner surface, different from the initial one (Fig. 5.34b). In the case of finding a fracture that isolates a part of the domain, then an algorithm is activated to detect the grains to be eliminated. If several paths are found which are one inside the other, the algorithm selects the maximum envelope.

2. **Elimination of grains**. In case that any crack path exists that isolates a grain or group of grains, the removal algorithm is started (Fig. 5.34c). This automatic algorithm is based on the excavation procedure already existing in DRAC which can be divided in two steps:

   (i) Evaluation of excavation forces (F_{exc}). The excavation forces are computed using the appropriate integral of stress over the removed (excavated) domain (Ω_r) (Eq. (5.16)). The computation of equivalent nodal forces (F_{exc}) due to excavation is only applied to existing nodes. Due to the fact that from the viewpoint of flow the excavation procedure takes place in steady state conditions, the evaluation of internal forces can be carried out directly in terms of the effective stress.

$$F_{exc} = \int_{\Omega_r} B^{\mathsf{T}} \boldsymbol{\sigma}' \, d\Omega \tag{5.16}$$

   (ii) Application of excavation forces. The excavation forces are assembled into the load vector (or Right Hand Side vector (RHS)) and are applied in small increments.

3. **Generation of data files** for the subsequent calculations. These are the files indicating which elements have to be removed in the excavation process, and what forces have to be applied on the remaining nodes.

In order to improve the performance of the procedure, a hierarchical model of the mesh geometry including grains and interfaces is generated at the beginning of the

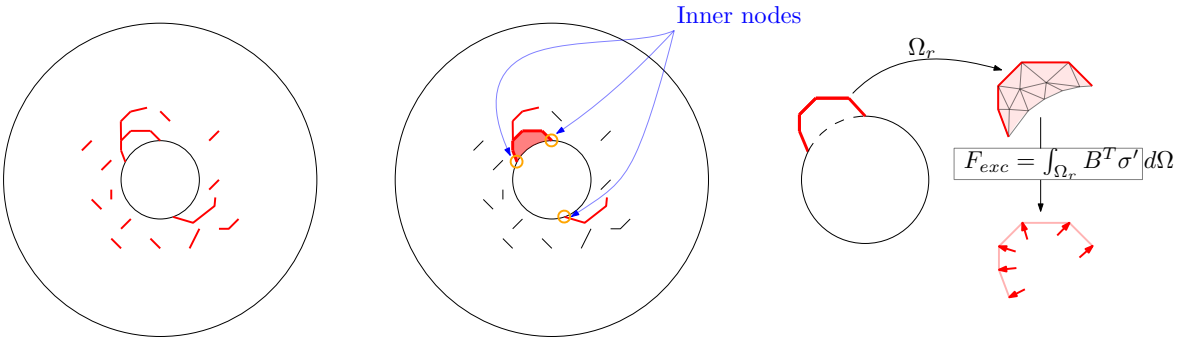

a) Detect failed interfaces b) Tree algorithm c) Removal algorithm

Figure 5.34: Simplified scheme of the sand production methodology.

calculation, which contains the list of connectivities of joints and grains.

Figure 5.34 summarizes the different steps involved in the sanding algorithm.

5.5 Hollow Cylinder Test (HCT) modeling

As already indicated in Section 5.2.1.b (Laboratory tests) one of the most common tests to evaluate and quantify the risk of sand production in real rock samples is the Hollow Cylinder Test (HCT). Therefore, after proposing a new numerical model for sand production, it seems the logical first step to verify it and try to calibrate its parameters with experimental results of this test.

Consequently, this section describes the application of the proposed approach for sand production, to the study of the HCT, using, for a first verification, the prototype material already described in Section 5.3.3 (parameter values depicted in Tables 5.4 and 5.5).

5.5.1 Sensitivity of HCT calculation to the perforation diameter

The objective of this section is to show the potential of the methodology developed to capture the scale effect due to variation of internal diameter of the perforation. For this purpose, calculations of HCT test have been carried out with three different perforation diameters. In all cases the material parameters and the microstructure geometry ($\varnothing_{grain} = 0.6\,\text{mm}$) have been fixed, and only the inner hole radius has been changed. Three internal radius sizes have been tested: $r_{inner} = 0.25\,\text{cm}, 0.5\,\text{cm}$ and $1.0\,\text{cm}$ (see Fig. 5.35).

The results clearly show a size effect due to variation of perforation radius. It can be seen how the external collapse load increases as the internal radius decreases (see Fig. 5.36). It should be noted that this result is obtained naturally from the proposed method, even if material parameters are given exactly the same values in the three calculations. This is due to the fact of using interface elements of zero-thickness to represent cracks, and also to the way in which the constitutive law is formulated, and

Table 5.7: Model geometries of internal radius sensitivity analysis.

Geometry dimensions	Very small	Small	Common
Inner radius (r_{inner})	0.25 cm	0.5 cm	1.0 cm
Intermediate radius (r_{outer}^{discr})	1.4 cm	1.8 cm	2.1 cm
Outer radius (r_{outer})	10 cm	10 cm	10 cm
Grain diameter ($\varnothing_{grain}$)	0.6 mm	0.6 mm	0.6 mm
Mesh dimensions			
n. nodes	22 649	38 120	38 822
n. continuum	9340	14 767	15 369
n. zero-thickness	10 810	18 455	18 647

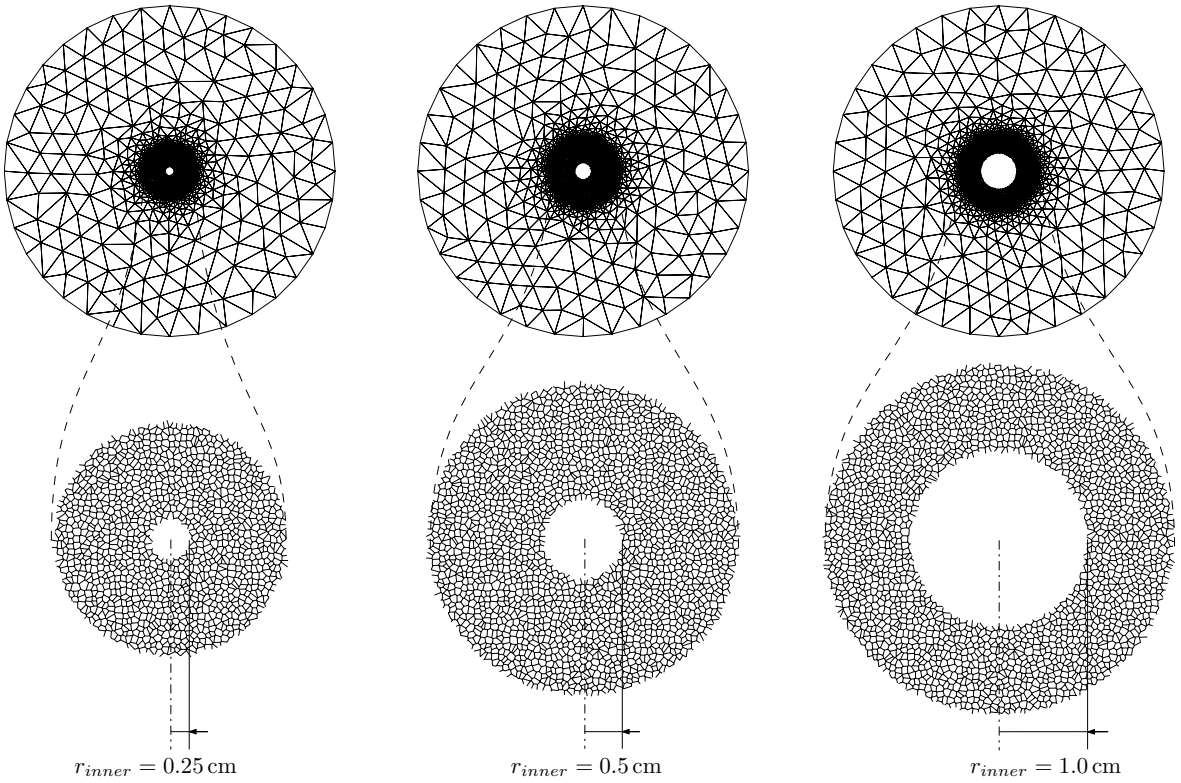

Figure 5.35: Model geometries of internal radius sensitivity analysis. Internal radius (r_{inner}) from left to right: 0.25 cm, 0.5 cm and 1.0 cm. In top, full model; and bottom, detail of the discrete domain (only inter-grain interfaces are represented).

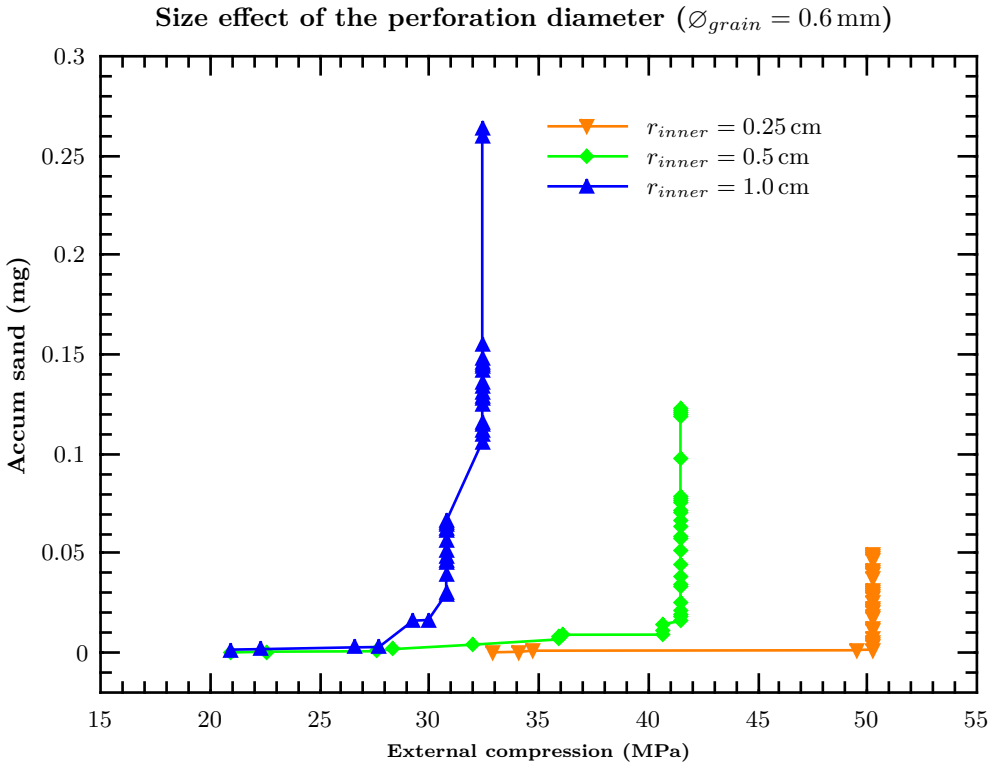

Figure 5.36: Accumulated sand production with increasing load, for the HCT with three different perforation diameters.

in particular the way in which the evolution (softening) of the strength parameters of the interface is postulated. As already explained in Section 2.5.4, the constitutive law of the interfaces uses as a history variable the dissipated fracture energy, with the fracture energies G_f^I and G_f^{IIa} as parameters of the model. This implies that the energy consumed by the model to create a certain crack extension will be proportional to the area created (in contrast to continuum models, in which even if the constitutive law would have similar parameters, dissipation would be per unit volume, therefore require more complex regularization techniques to ensure the proper energy dissipation). A direct consequence of a correct energy dissipation per unit of new crack area created is that the model will also automatically exhibit size effects (see extensive discussion in Bažant and Planas (1998))

Table 5.8 summarizes the results related to the onset of sand production and the collapse pressure of the three calculations. Figure 5.37 shows resulting geometry with the energy spent over the remaining interfaces after 50 stages of excavation. It can be clearly observed, that, from a qualitative point of view, the damage is higher for larger perforations diameters.

Table 5.8: Onset pressure and collapse pressure for different perforation diameters.

Perforation (r_{inner})	0.25 cm	0.5 cm	1.0 cm
Onset pressure	33 MPa	21 MPa	21 MPa
Collapse pressure	50.5 MPa	41.7 MPa	32.7 MPa

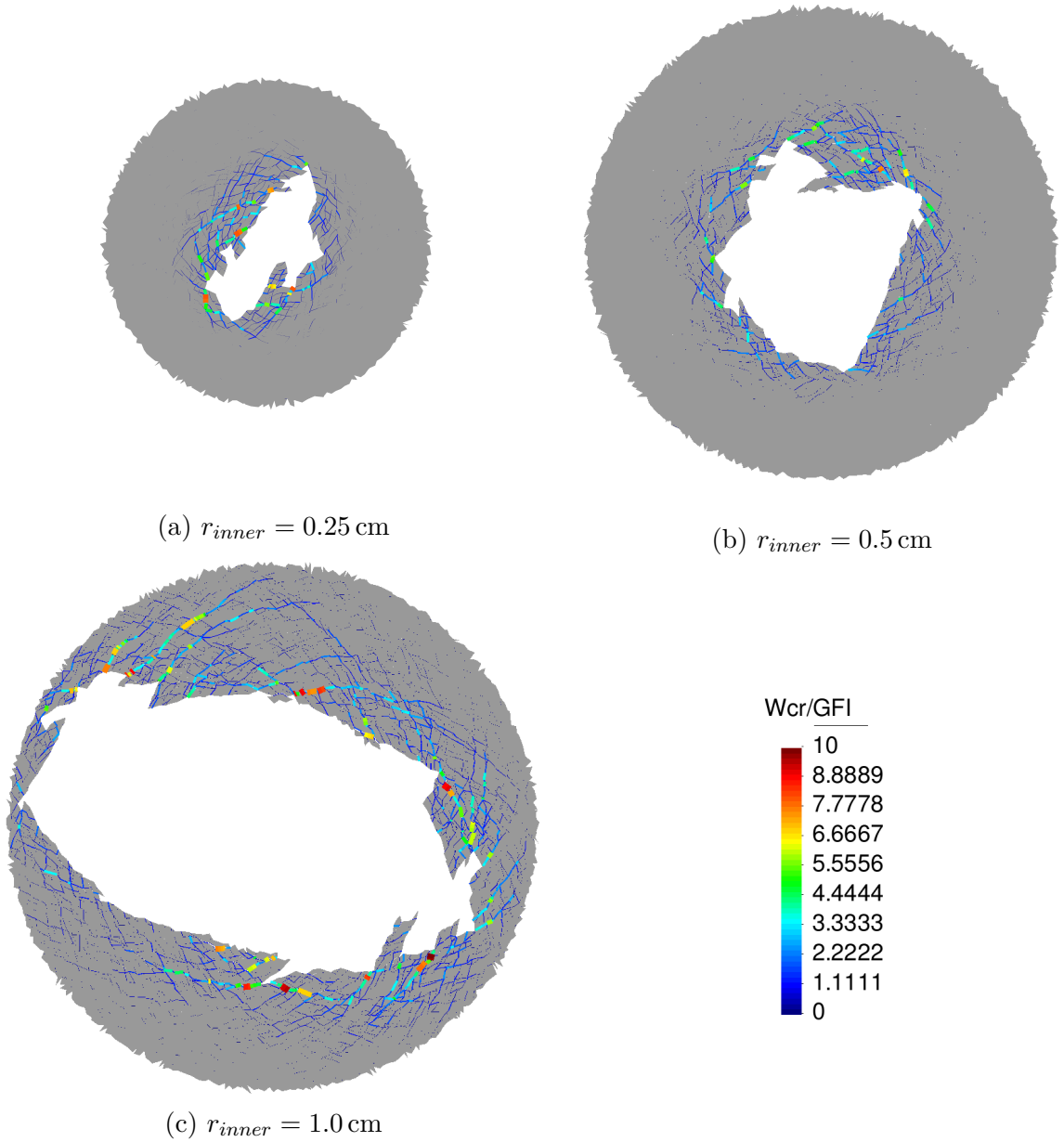

(a) $r_{inner} = 0.25\,\text{cm}$

(b) $r_{inner} = 0.5\,\text{cm}$

(c) $r_{inner} = 1.0\,\text{cm}$

Figure 5.37: Fracture energy spent (W^{cr}) along interface elements the HCT with three perforation diameters, after 50 grain removal excavation stages: a) $r_{inner} = 0.25\,\text{cm}$; b) $r_{inner} = 0.5\,\text{cm}$; and c) $r_{inner} = 1.0\,\text{cm}$. Results plotted on the deformed meshes of discrete domain (magnification $\times 5$).

5.5.2 Sensitivity to grain size and to microstructural parameter values

5.5.2.a Intra-grain strength

Sensitivity to intra-grain strength is evaluated with two additional simulations assuming a grain size ($\varnothing_{grain}$) of 0.6 mm and an internal radius (r_{inner}) of 1 cm. The first additional simulation assumes elasticity (that is, infinite strength) for intra-grain interfaces. This simulation could be understood as a lower bound analysis in terms of the amount of cracking, because if grains are not allowed to crack, for an equal level of external load, cracking will be lower. On the other hand, in terms of strength this case is an upper bound, since higher external load will be needed to overcome the additional friction due to the microstructural geometry, since cracks have to develop around grains, resulting in much higher shear loads.

The other case assumes the same strength for both intra-grain and inter-grain interfaces. Again this case could be understood as an upper limit from a production point of view, and a lower limit from the viewpoint of overall strength.

The results shown in Fig. 5.38 exhibit a clear effect of intra-grain strength on sand production. Sand production is triggered at lowest load of 20 MPa in the case of same strength in all interfaces, and about 50% higher (30 MPa) for the case of double strength in intra-granular interfaces. The elastic case reaches an external load of up to 95 MPa without showing evidences of collapsing and with a small rate of sand accumulation. This simulation ended unsuccessfully due to numerical problems, probably related to highly brittle behavior. Figure 5.39 shows a the energy dissipated along remaining interfaces at the end of each test. It is interesting to observe how the internal strength of the grains may affect the crack pattern. The figures show that, as the intra-grain strength decreases, the tendency increases to localization and to larger breakout failures.

5.5.2.b Grain size

The sensitivity to grain diameter has been investigated by analyzing three cases with grain diameter of 0.6 mm, 0.9 mm and 1.2 mm (see Fig. 5.40).

The results depicted in Fig. 5.41 do not show a clear effect of the grain diameter on sand production. Figure 5.42 shows the energy dissipated along the remaining interfaces at the end of each test.

5.6 Real case application

This section includes the application of the approach developed to real data of hollow cylinder tests. For this purpose, courtesy of *Repsol*, data was available from samples

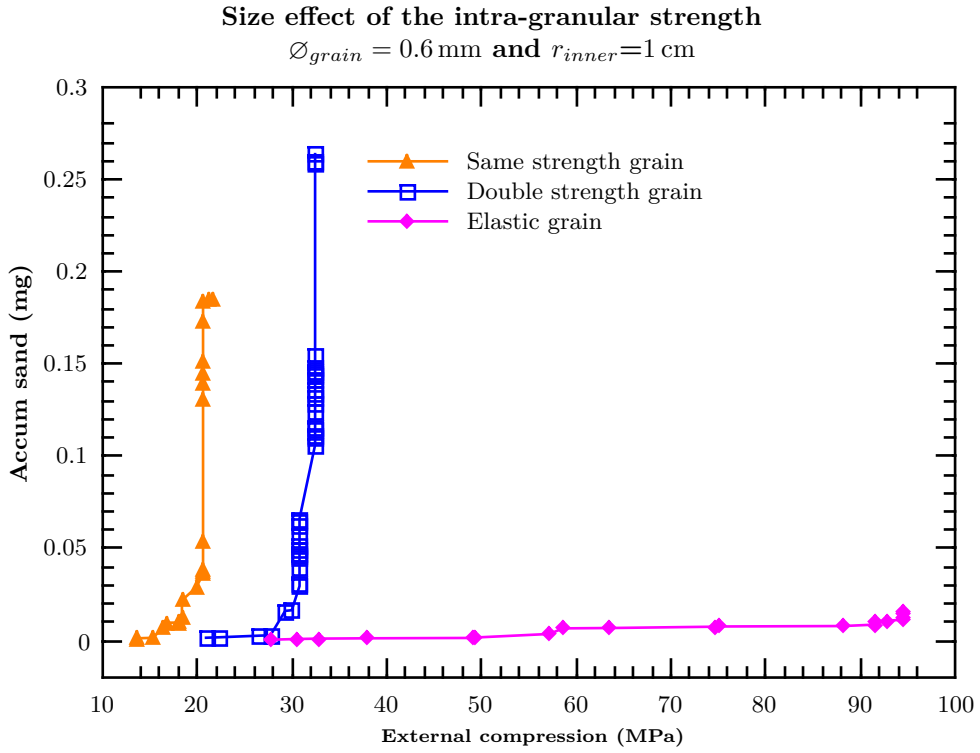

Figure 5.38: Curves of accumulated sand production for various assumptions of inter-granular strength.

from a well with potential sand management problems. The material to be modeled is a cemented granular material with calcareous matrix. Three hollow cylinder test (HCT) were performed as well as several characterization tests. This study has focused on the simulation of two HCT tests (the third one collapsed without showing sand production until failure). For the calibration of the model, this analysis has been focused on the results of two triaxial test performed with samples from the same well and depths close to those of the samples used for the HCTs.

The simulation consists of two parts: first a calibration test is performed in order to reproduce as close as possible the macroscopic behavior shown in triaxial tests (§5.6.1). Second, with the parameters obtained above, a simulation of sand production is performed, and is compared with the experimental data (§5.6.2).

5.6.1 Material characterization

An important point of the analysis is the material calibration due to the fact that microstructural parameters have to be inferred from the macroscopic behavior. For this purpose a similar test to the one that was used in Section 5.3.3 is performed.

The first assumption has been the grain size, which was fixed to be 0.6 mm as a first attempt. Results already presented in Section 5.5.2.b show that the proposed approach does not seem very sensitive to grain size. Then, the second assumption was the elastic

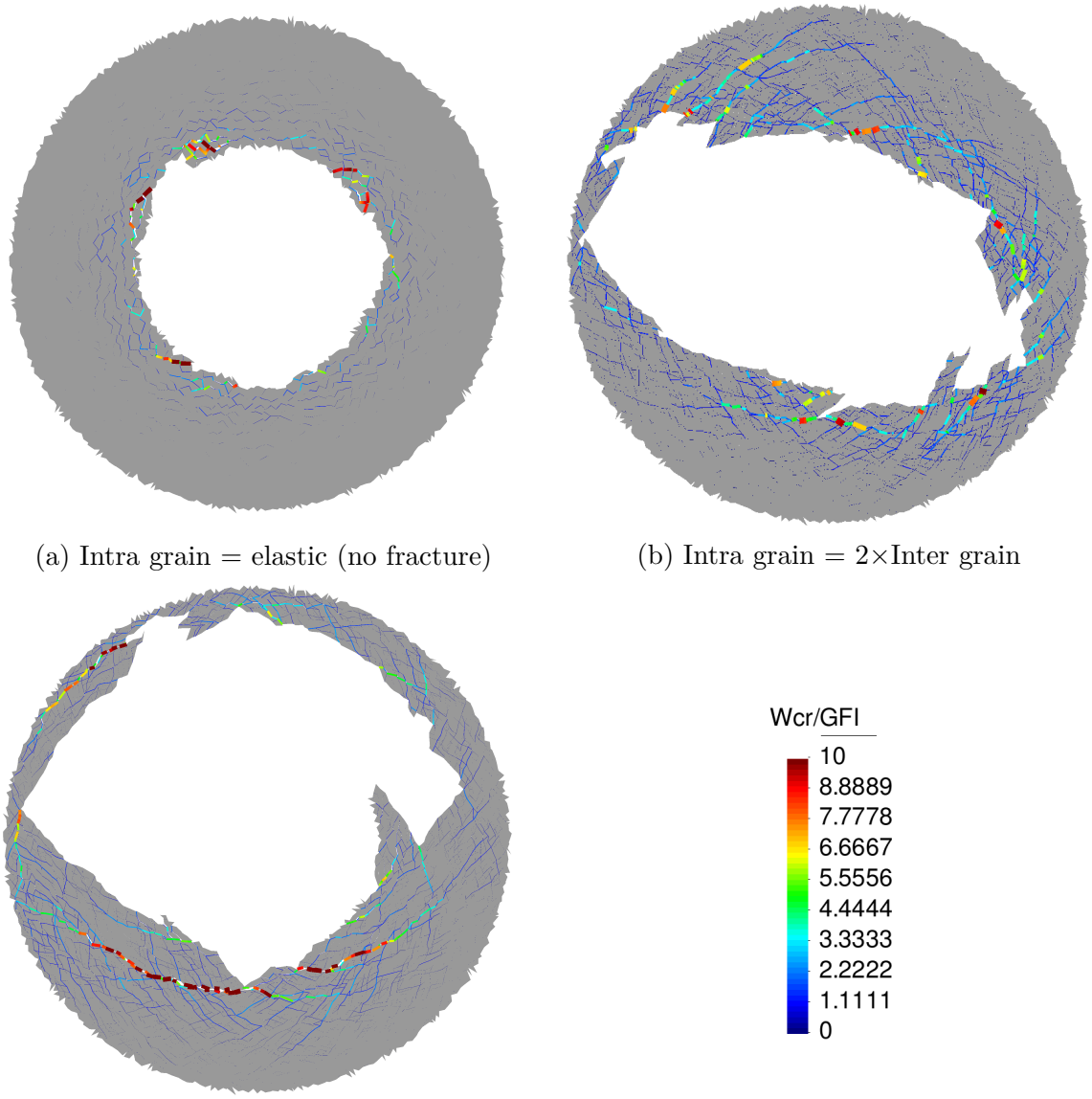

(a) Intra grain = elastic (no fracture)

(b) Intra grain = 2×Inter grain

(c) Intra grain = Inter grain

Figure 5.39: Fracture energy spent (W^{cr}) along remaining interfaces for different values of intra-grain strength at the end of test: a) Elastic interface, no failure is possible inside grain ; b) The resistance o intra-grains is greater (cohesion and tensile strength double); and c) Same strength between intra and inter grain interfaces. Results plotted on deformed meshes of discrete domain (magnification ×5).

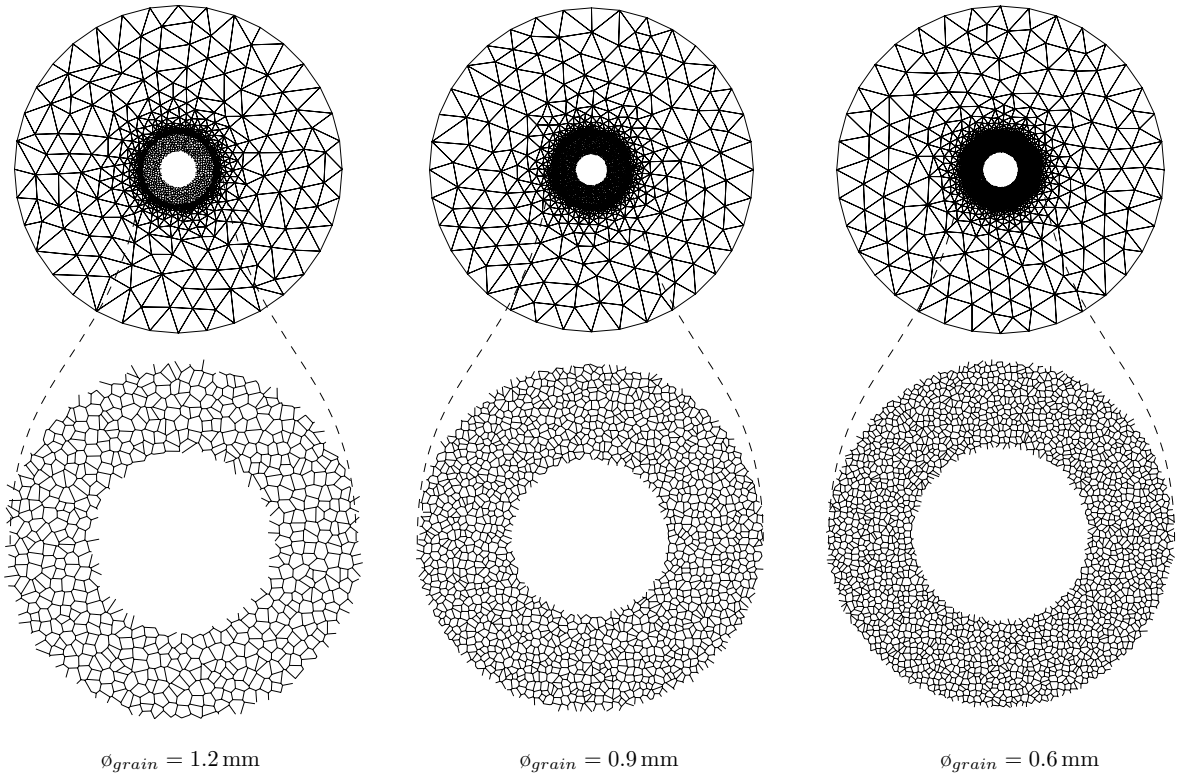

Figure 5.40: Model geometries of grain size sensitivity analysis. Grain size ($\varnothing_{grain}$) from left to right: 1.2 mm, 0.9 mm and 0.6 mm. In top, full model; and bottom, detail of the discrete domain (only inter-grain interfaces are represented).

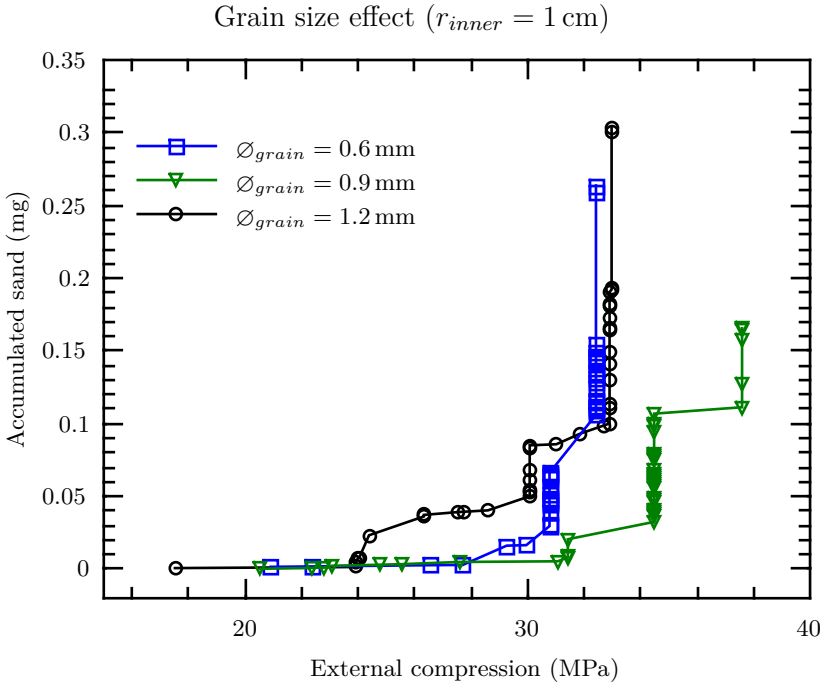

Figure 5.41: Curves of accumulated sand production for various assumptions of the grain diameter.

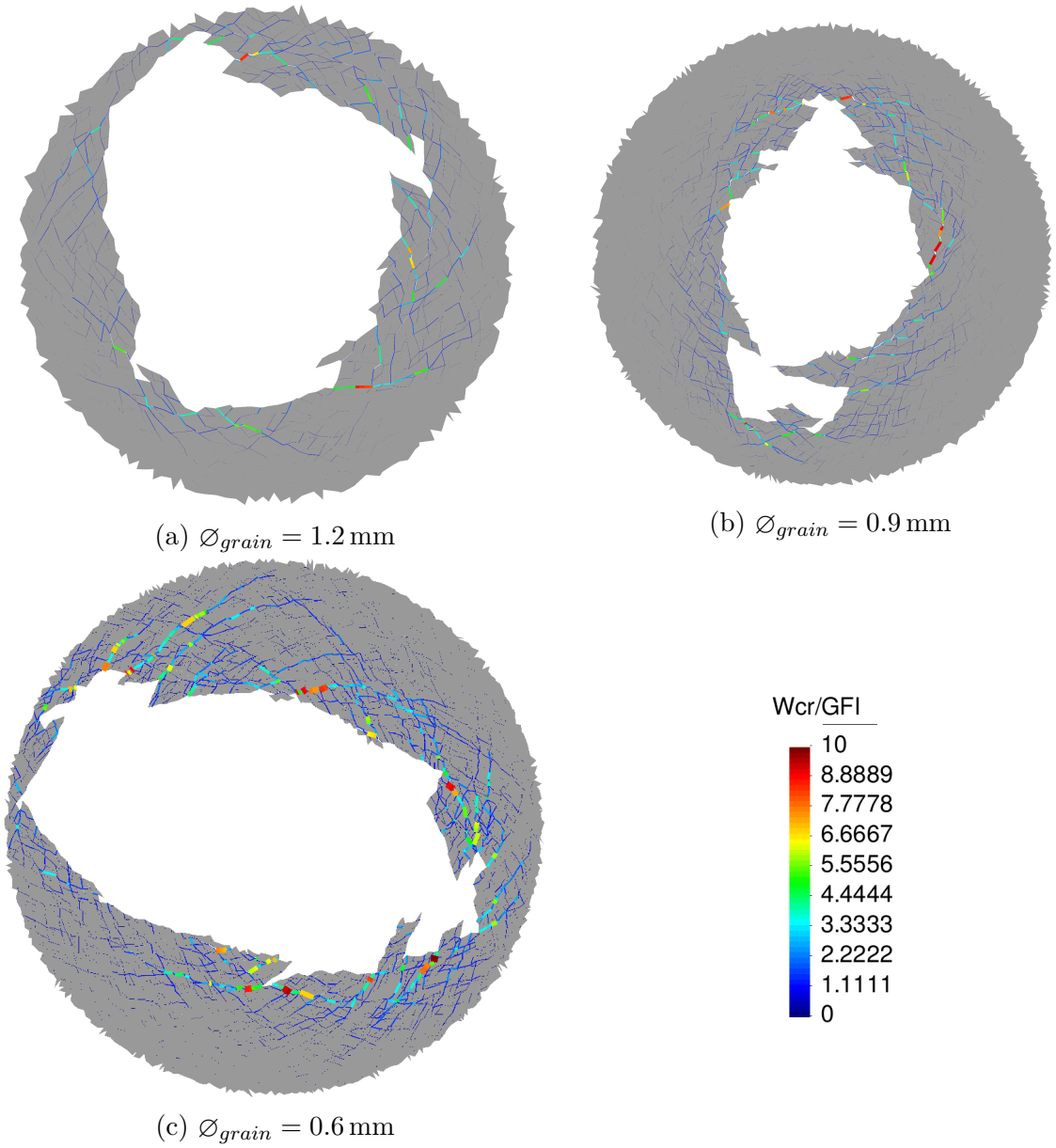

(a) $\varnothing_{grain} = 1.2\,\text{mm}$

(b) $\varnothing_{grain} = 0.9\,\text{mm}$

(c) $\varnothing_{grain} = 0.6\,\text{mm}$

Figure 5.42: Fracture energy spent (W^{cr}) along remaining interfaces for different values of grain diameter at the end of test: a) $\varnothing_{grain} = 1.2\,\text{mm}$; b) $\varnothing_{grain} = 0.9\,\text{mm}$; and c) $\varnothing_{grain} = 0.6\,\text{mm}$. Results plotted on deformed meshes of discrete domain (magnification $\times 5$).

Table 5.9: Material properties of continuum.

Parameter		*Value*		*Units*
		Grains	Equiv. Continuum	
E	Young's modulus	34.0	13.66	GPa
ν	Poisson's ratio	0.27	0.15	-

Table 5.10: Material properties of interfaces.

Parameter		*Value*			*Units*
		Inter-Grain	Intra-Grain	Contact	
K_n	Normal stiffness	$1 \cdot 10^8$	$1 \cdot 10^8$	$1 \cdot 10^8$	$\text{MPa} \cdot \text{m}^{-1}$
K_t	Tangential stiffness	$1 \cdot 10^8$	$1 \cdot 10^8$	$1 \cdot 10^8$	$\text{MPa} \cdot \text{m}^{-1}$
χ_0	Tensile strength	0.4	0.8		MPa
$\tan(\phi)$	Friction angle	0.5773 (30.0°)	0.5773 (30.0°)		
c_0	Cohesion	6.0	12.0		MPa
G_f^I	Energy mode I	0.01	0.04		$\text{MPa} \cdot \text{m}$
G_f^{IIa}	Energy mode IIa	0.1	0.4		$\text{MPa} \cdot \text{m}$
σ_{dil}	Sigma dilatation	10.0	10.0		$\text{MPa} \cdot \text{m}$

isotropic behavior of the continuum elements, that due to the lack of data, were taken equal to the ones used in previous section (see Table 5.9).

Regarding the mechanical parameters of the interface elements, stiffness coefficients have been assigned relatively high values. However, in this case these parameters have not been interpreted as penalty coefficients; a certain elastic deformation is accepted to correspond to the deformation of the cementing matrix material which is represented by the interface behavior. Another assumption has been the difference between strength parameters of the inter/intra-granular interfaces. In the absence of specific information, tensile strength (χ_0) and cohesion (c_0) values for intra-granular interfaces have been assumed double with respect to those used for intergranular interfaces. The energies have been also assumed different in this case with $\times 4$ values in intra-granular interfaces with respect to inter-granular ones.

The elastic parameters values are displayed in Table 5.9. In the same table are also shown the values of elastic parameters for the overall equivalent material (macroscopic values) which have been obtained numerically from the calibration calculations, these values will be used for the outer domain in the HCT analysis, as described in next subsection.

The best fitting parameters regarding interface elements are given in Table 5.10. Note that, for completeness, the table includes also the interface parameters from the contact between the inner discrete domain and the outer continuum domain.

Figure 5.43 shows the two triaxial strain-stress curves obtained for the best fitting set of parameters, together with the experimental curves. In spite of the random

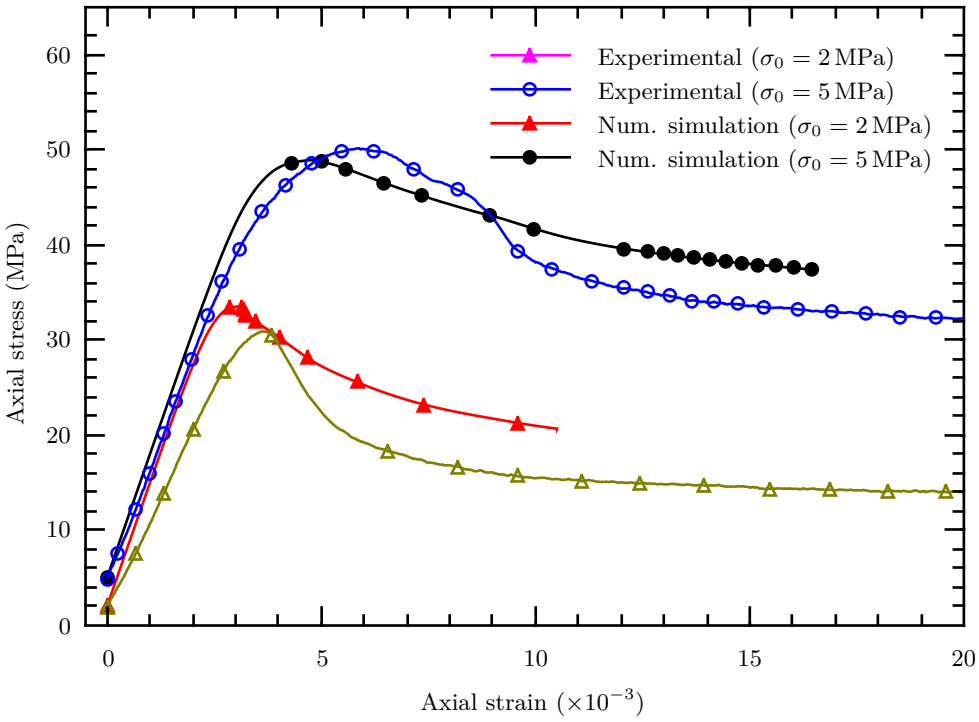

Figure 5.43: Biaxial Compression Test for real material.

nature of the samples, the results obtained with the microstructural model show a remarkably good fit. Both results are obtained with exactly the same set of model parameters, only the initial boundary conditions have been changed between the two cases ($\sigma_0 = 2$ MPa and 5 MPa).

Figures 5.44 and 5.45 show the displacement filed and the energy dissipated along interfaces for the last computed increment of each of the two triaxial tests for 2 MPa and 5 MPa confinement. The figures show relatively different localization modes: more brittle behavior is observed in the lower confinement case, where clear shear bands are observed; while more ductile behavior is observed in the higher confinement case, where the localization in the center of the specimen is more diffuse and expands across a zone or "thick band" of shear failure.

5.6.2 Hollow cylinder test simulation

The simulation of HCT follows the same methodology as depicted in previous section (§5.5). In this case however, the geometry has been generated according to the real test dimensions (inner radius of 0.6 cm and outer radius of 1.8 cm). The mesh has 46 721 nodes, 18 097 continuum elements and 22 613 zero-thickness interface elements. (see Fig. 5.46)

The results of sand production in hollow cylinder test are presented in Fig. 5.47, together with the experimental data of two tests carried out with similar samples. The onset of sanding in the calculation seems to start at a load (28 MPa) which is lower

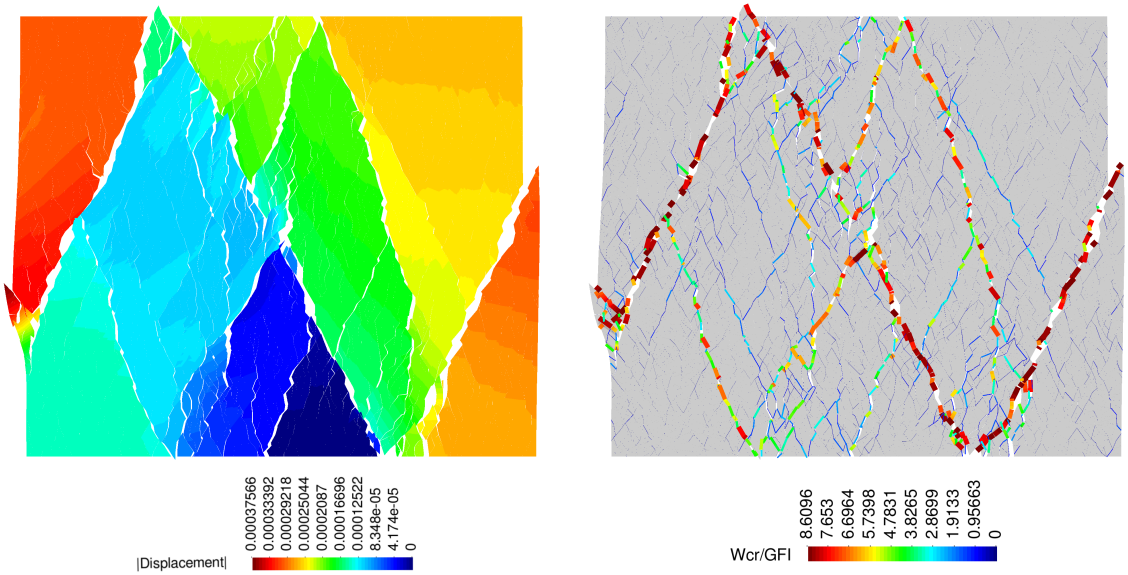

(a) Displacement modulus (m).

(b) Normalized energy spent ($W^c r/G_f^I$).

Figure 5.44: Material characterization: results from triaxial compression test at 2 MPa confinement: a) Displacement modulus (m); and b) Normalized energy spent along interface elements ($W^c r/G_f^I$). Results plotted over deformed mesh (magnification $\times 5$).

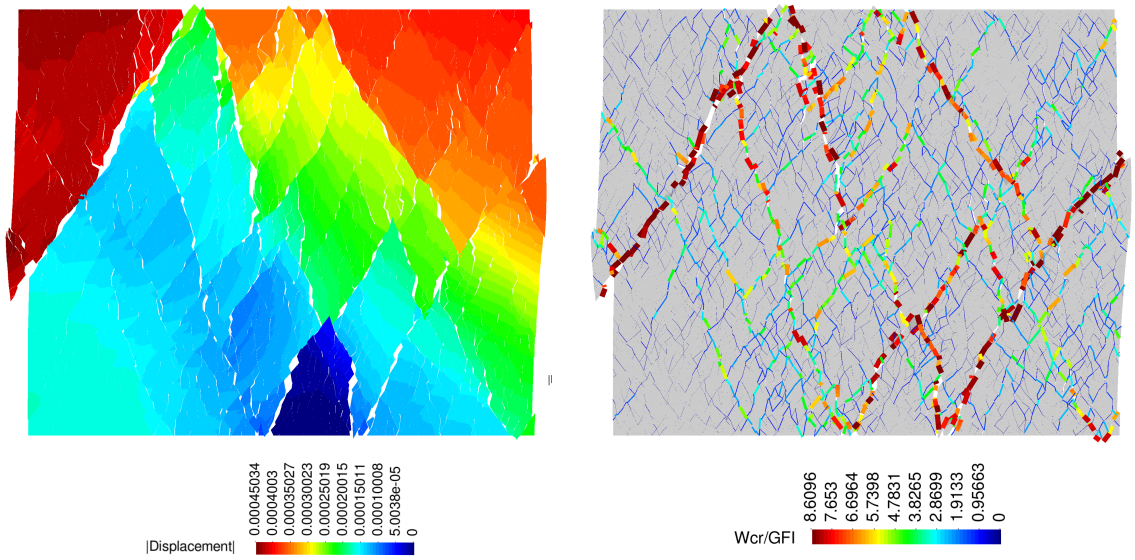

(a) Displacement modulus (m).

(b) Normalized energy spent ($W^c r/G_f^I$).

Figure 5.45: Material characterization: results from triaxial compression test at 5 MPa confinement: a) Displacement modulus (m); and b) Normalized energy spent along interface elements ($W^c r/G_f^I$). Results plotted on deformed mesh (magnification $\times 5$).

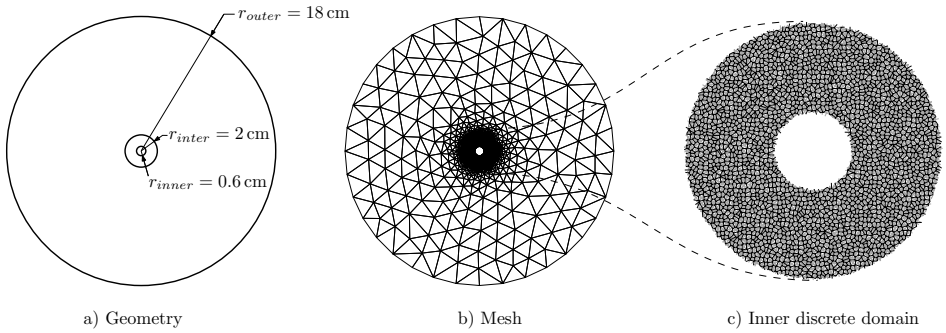

Figure 5.46: Geometry used to model the real test data.

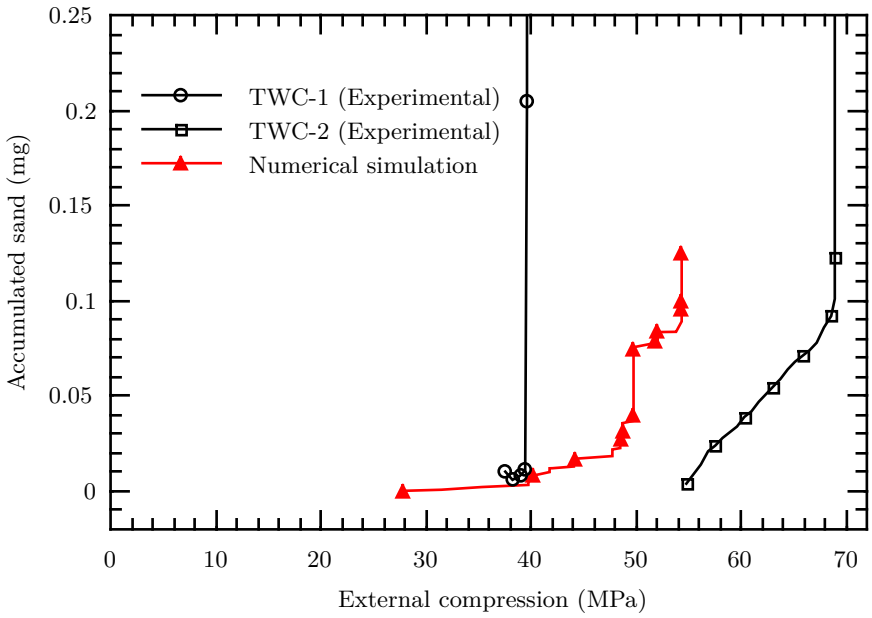

Figure 5.47: Accumulated sand in the HCT. Comparison between numerical results and experimental data.

that both experimental tests (38 MPa and 55 MPa). A possible explanation for this phenomenon could be related to the discretization, whether the grain size is not adequate or local effects of the discretization. With respect to sand production, one of the experiments (TWC-1) seems to collapse immediately without a measurable production of sand, while the other (TWC-2) is more progressive. The curve obtained numerically exhibits a behavior in between the two experiments, with a gradual onset of production, similar to that observed in the TWC-2 test, but rapidly alternates with phases of collapse.

Figures 5.48 and 5.49 depict the geometry evolution of the sanding process, as well as the fracture energy along remaining discontinuities at each stage and the maximum compressive stress, respectively.

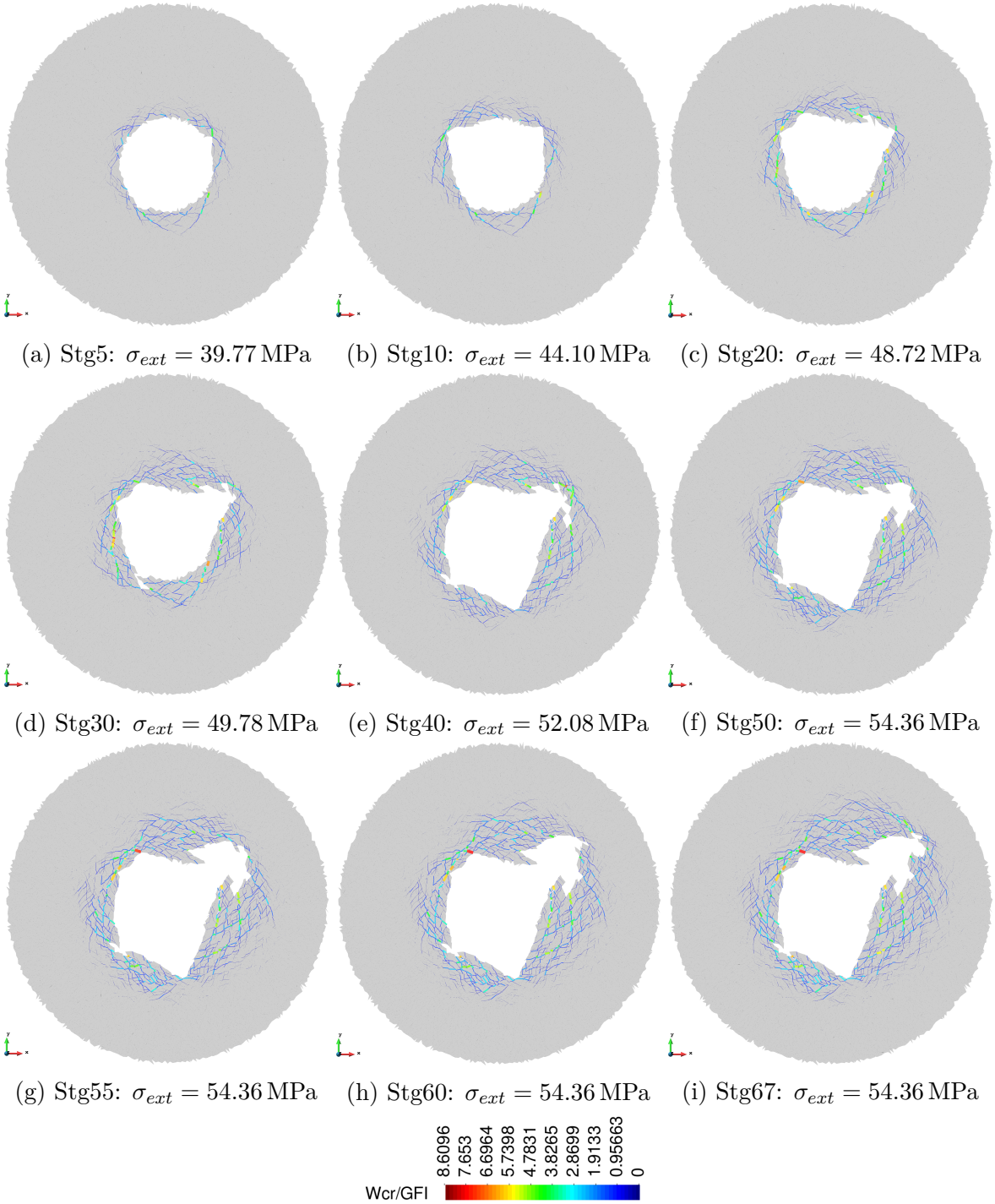

(a) Stg5: $\sigma_{ext} = 39.77\,\text{MPa}$ (b) Stg10: $\sigma_{ext} = 44.10\,\text{MPa}$ (c) Stg20: $\sigma_{ext} = 48.72\,\text{MPa}$

(d) Stg30: $\sigma_{ext} = 49.78\,\text{MPa}$ (e) Stg40: $\sigma_{ext} = 52.08\,\text{MPa}$ (f) Stg50: $\sigma_{ext} = 54.36\,\text{MPa}$

(g) Stg55: $\sigma_{ext} = 54.36\,\text{MPa}$ (h) Stg60: $\sigma_{ext} = 54.36\,\text{MPa}$ (i) Stg67: $\sigma_{ext} = 54.36\,\text{MPa}$

Figure 5.48: Evolution of geometry and of W^{cr}/G_f^I along the remaining interface elements. Line diagram plotted on deformed mesh of discrete domain (magnification $\times 5$).

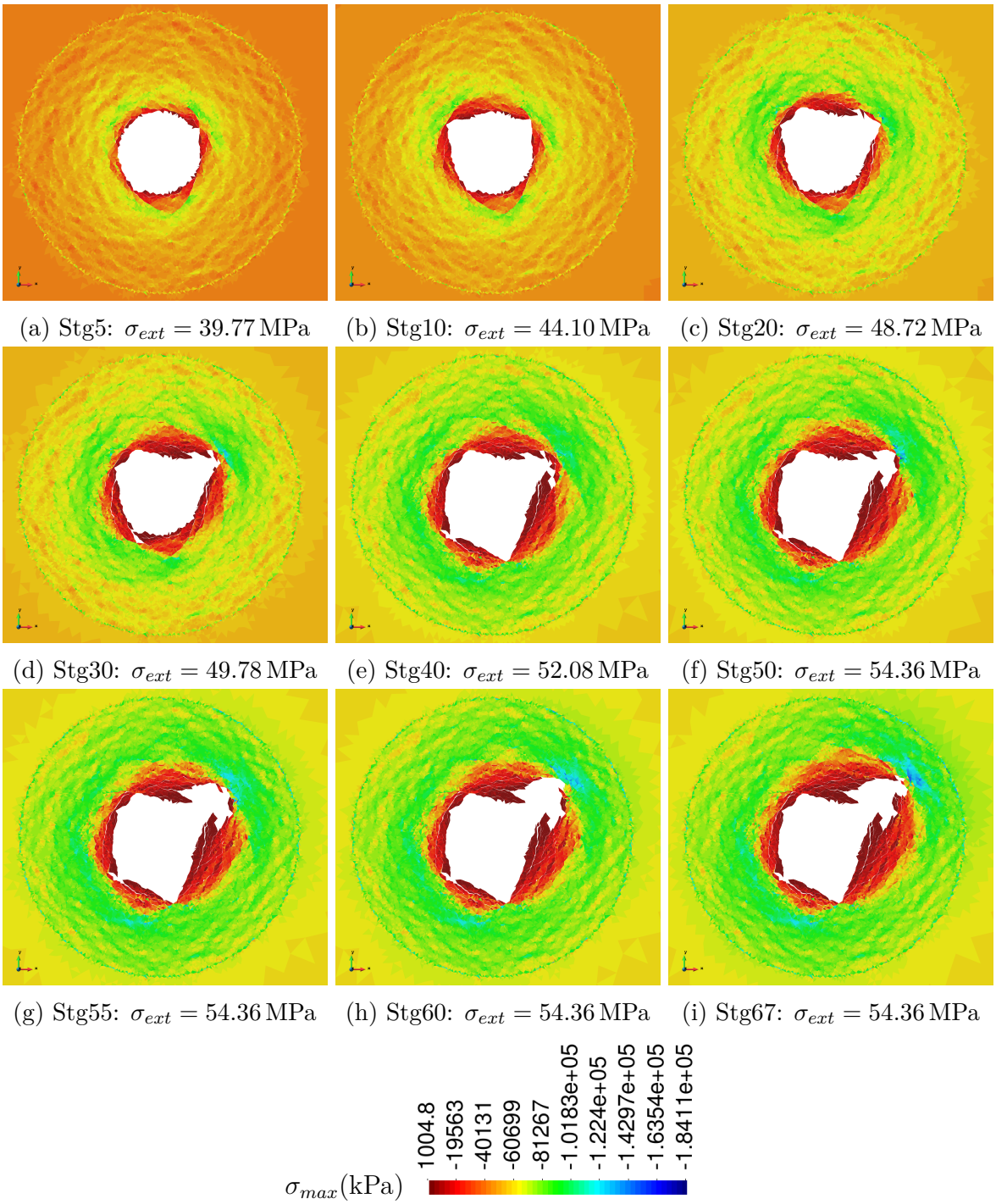

(a) Stg5: $\sigma_{ext} = 39.77\,\text{MPa}$ (b) Stg10: $\sigma_{ext} = 44.10\,\text{MPa}$ (c) Stg20: $\sigma_{ext} = 48.72\,\text{MPa}$

(d) Stg30: $\sigma_{ext} = 49.78\,\text{MPa}$ (e) Stg40: $\sigma_{ext} = 52.08\,\text{MPa}$ (f) Stg50: $\sigma_{ext} = 54.36\,\text{MPa}$

(g) Stg55: $\sigma_{ext} = 54.36\,\text{MPa}$ (h) Stg60: $\sigma_{ext} = 54.36\,\text{MPa}$ (i) Stg67: $\sigma_{ext} = 54.36\,\text{MPa}$

Figure 5.49: Evolution of σ_{max}(kPa) in the continuum elements around the perforation. Contour fill plotted over deformed mesh (magnification $\times 5$).

Chapter 6

Summary, conclusions and future work

Contents

6.1 Summary and conclusions

The general objective of this thesis is to extend the range of applicability of the Finite Element Method with zero thickness interface elements (FEM+z) to 3D, large and complex problems in geomaterials, with special interest in petroleum geomechanics. This general objective has led to specific developments and applications such as the 3D code implementations and parallelization, and to specific petroleum geomechanics studies, both at the macroscale (hydraulic fracture) and microscale (sand production).

The modeling of hydraulic fracture shows that both, zero-thickness interfaces and a coupled hydro-mechanical formulation may lead to an accurate representation of one or multiple interacting fractures in tight reservoirs. On the other hand, the study of sand production, demonstrates the potentiality of the microstructural analysis with fractured-based interfaces elements, for the complex processes in geo-materials involving micro-cracking, coalescence, branchings, grain detachment, etc.

Some specific conclusions for each chapter of the thesis are presented below:

Hydro-Mechanical formulation in 3D The extension to 3D of the hydro-mechanical formulation of the double node zero-thickness interface elements proposed by Segura (2007) has been developed and implemented in a computer code, with satisfactory results in the verification examples. From the theoretical viewpoint, the formulation is generalized via the definition of "transport" matrices for both mechanical and hydraulic formulations, so that the two levels of the formulation can be clearly separated: the nodal variables of the interface element, and the mid-plane variables. Additionally, geometric aspects of the definitions of local axis and their derivatives are clearly described. All those concepts are key ingredients for the accurate definition of the integral form of force vectors and stiffness matrices. The formulation described is successfully validated with benchmarking

examples based on analytical expressions of a single hydraulic fracture, that are presented in Chapter 4.

Parallelization The parallelization of the code DRAC is achieved through the implementation of the public domain library PETSc. The new code structure is conceived to perform a correct subdivision of tasks associated to each processor. For this purpose, a domain decomposition strategy has been implemented, which is crucial for an efficient matrix generation and assembly. The results obtained show a good degree of parallelization, demonstrated with a cube benchmark test. Afterwards, the parallel code has been used successfully in demanding cases such as multiple hydraulic fracture modeling, presented in Chapter 4.

Hydraulic fracture The applications to hydraulic fracture have served a dual purpose. First, the examples of a single fracture have been used to validate the proposed formulation, since it has been possible to compare the results with the predictions of analytical expressions such as GDK or PKN, and to other numerical results from the literature. And second, the examples of multiple interacting fractures have shown the capabilities to analyze large and complex cases. The studies performed have shown a number of relevant aspects of multiple fracturing such as the effect of geometry (distance between injections) and the effect of *in situ* stresses.

Sand production The last chapter of the thesis is devoted to the micromechanical analysis of sand production, including the generation and testing of micromechanical models based on the use of zero-thickness interface elements. Micromechanical (mesoscopic level) analysis with FEM+z has been successfully used to model the mechanical behavior of rock materials, using a similar approach as used previously for other heterogeneous materials (López, 1999, Caballero et al., 2006). The rock grains are modeled as a group of continuum elastic elements and the cement (or matrix) is modeled with zero-thickness interfaces. This kind of modeling has been successfully used in uniaxial and triaxial compression test simulations presented in this Thesis. These numerical tests have been used for calibration purposes, comparing the macroscopic results obtained with the existing laboratory data.

Due to the availability of experimental data, the simulation of sand production has been focused on the modeling of the hollow cylinder test. The simulations have been divided into two parts. First, using a prototype material, the sensitivity of the method to geometric and microstructural variations has been analyzed, and the effect of the perforation size is clearly observed. The second part deals with the analysis of a real case of sanding, that includes micromechanical tests for parameter calibration and the simulation of sand production. The results, despite the intrinsic variability of the samples, have shown a satisfactory agreement with

average experimental results, both in terms of initiation and production of sand.

6.2 Future research work

The work presented in this doctoral thesis has covered a wide range of topics related to numerical methods, ranging from the theoretical formulation of the models, to some aspects of the implementation or the advanced modeling of large-scale geo-material problems. From work developed and results obtained, a number of possible enhancements have been identified that would extend the applicability and would make more efficient the numerical calculation.

Some of these possible further developments are listed below:

Enhancement of zero-thickness interface elements

Fracture development along non-pre-established paths In the current version of the code, fractures can only propagate along pre-established paths along which interface elements have been pre-inserted. If those have been pre-inserted in sufficient number, the fracture can develop with relative freedom, but at the expense of significant computational effort. Therefore, one possible improvement would be that the fracture does not necessarily follow those lines, but can open along an entirely new path. Two options are envisaged for this new formulation: the use of zero-thickness interfaces with node relocation, or the use of a hybrid zero-thickness/XFEM formulation.

Development of rigid plastic interfaces Classical interface elements with double nodes are convenient, but may cause the total number of nodes in the mesh to increase dramatically if pre-inserted in the mesh in large numbers. Also micromechanical simulations show that, although using high values of stiffness coefficients reduces unphysical elastic deformations, high stiffness has a limit for numerical reasons, and the presence of large number of interfaces per unit length, may lead to a non-negligible additional deformability as well as to dilution of Poisson's ratio (see Eq. (5.13)). To avoid these effects, an alternative that has been suggested is the development of a rigid-plastic interface element without stiffness coefficient as proposed by Ciancio et al. (2007, 2013).

Constitutive law with partial closure effect Development of an advanced fracture energy-based constitutive law for zero-thickness interfaces with partial closure effect. Current constitutive models available for fracture opening/sliding, consider either full closure upon unloading or no closure at all. A model combining damage mechanics and plasticity could reproduce partial closure as representing

a more realistic effect as for instance takes place if proppant/acid techniques are used in the context of hydraulic fracture.

Temperature effects and multiphase Temperature effects and multiphase extensions of the FEM+z formulation. The addition of temperature, and subsequent couplings with the current H-M formulation, together with multiphase flow oriented to petroleum engineering, would widen the range of applications of the code in this field.

Further possible developments in the code

MPI-OpenMPI The implementation of a mixed system, including a first level with a shared memory paradigm (parallelism via *OpenMP*), and a second level with a distributed memory paradigm (*MPI*) could take better advantage of the local resources of the system.

Load balancing The simulations performed are not taking into account the load associated to each processor (subdomain), for example if the non-linear behavior is concentrated in a single subdomain the speed of the entire calculation is penalized by the speed of this particular subdomain. Performance could be improved by implementing load-balancing algorithms, which consists in distributing some elements belonging to overloaded subdomains to neighboring subdomains.

Further possible developments in hydraulic fracture

Variable fluid The possibility to change the fluid properties during the injection history would make it possible to represent more realistically this type of processes.

Proppant modeling The option to include more realistically proppant effects would also improve the code capabilities. One option is adding a convective transport model in terms of proppant concentration, although this would add one more coupled field to the formulation.

Further possible developments for sand production

Enhanced microstruture The analysis developed in the present thesis uses as a first approximation a simplified model of microstructure consisting of elastic grains plus zero-thickness interfaces. As already mentioned in Section 5.3.1, one possible enhancement could be to model the matrix phase with a non-zero thickness layer, by using a similar discretization approach as previously used in concrete analysis. Introduction of grain elongation could extend the range of the model to anisotropic rocks

Tree algorithm parallelization Due to the complexity of the routines related to the tree algorithm, this part of the code, and consequently all simulations of sand production are performed in a sequential version of the DRAC code. Therefore, the parallelization of the sand production subroutines would clearly improve numerical efficiency in this type of calculations.

Coupled modeling of drawdown process The sand production calculation carried out so far have been aimed at the hollow cylinder test, which can be modeled in terms of the effective stress, therefore using a purely mechanical calculation. Future work could be directed to simulate the real drawdown process taking place at a well perforation, that should involve fully coupled HM micromechanical analysis.

3D modeling of sand production The simulations developed in this thesis are based on the analysis of 2D cross-section of a hollow cylinder test. A natural and challenging improvement would be the extension to 3D of this type of analysis.

References

Aadnoy, B. S. (2003). Introduction to special issue on borehole stability. *Journal of Petroleum Science and Engineering*, 38(3-4):79–82.

Adachi, J., Siebrits, E., Peirce, A., and Desroches, J. (2007). Computer simulation of hydraulic fractures. *International Journal of Rock Mechanics and Mining Sciences*, 44(5):739–757.

Amadei, B., Sture, S., Saeb, S., and Atkinson, R. (1989). An evaluation of masonry joint shear strength in existing buildings. Report to NSF, Dept. of Civil, Environmental and Architectural Engrg., University of Colorado, Boulder.

Ayachit, U. (2015). *The ParaView Guide: A Parallel Visualization Application*. Kitware, paraview 4.3 edition.

Balay, S., Abhyankar, S., Adams, M. F., Brown, J., Brune, P., Buschelman, K., Dalcin, L., Eijkhout, V., Gropp, W. D., Kaushik, D., Knepley, M. G., McInnes, L. C., Rupp, K., Smith, B. F., Zampini, S., and Zhang, H. (2016). PETSc Web page. http://www.mcs.anl.gov/petsc.

Barree, R. (2009). Principles of hydraulic fracturing. web.

Bažant, Z. P. and Planas, J. (1998). *Fracture and Size Effect in Concrete and Other Quasibrittle Materials*. CRC Press.

Boone, T. J. and Ingraffea, A. R. (1990). A numerical procedure for simulation of hydraulically-driven fracture propagation in poroelastic media. *International Journal for Numerical and Analytical Methods in Geomechanics*, 14(1):27–47.

Bradford, I. and Cook, J. (1994). A semi-analytic elastoplastic model for wellbore stability with applications to sanding. In *Eurock'94*, page 347–354, Rotterdam. Balkema.

Bradley, W. B. (1979). Mathematical concept-stress cloud can predict borehole failure. 77(8):92–101.

Caballero, A. (2005). *3D meso-mechanical numerical analysis of concrete fracture using interface elements*. PhD thesis, UPC. Departament d'Enginyeria del Terreny, Cartogràfica i Geofísica.

Caballero, A., Carol, I., and López, C. M. (2006). A meso-level approach to the 3d numerical analysis of cracking and fracture of concrete materials. *Fatigue and Fracture of Engineering Materials and Structures*, 29(12):979–991.

Caballero, A., Willam, K., and Carol, I. (2008). Consistent tangent formulation for 3d interface modeling of cracking/fracture in quasi-brittle materials. *Computer Methods in Applied Mechanics and Engineering*, 197(33–40):2804 – 2822.

Carol, I., López, C. M., and Roa, O. (2001). Micromechanical analysis of quasi-brittle materials using fracture-based interface elements. *International Journal for Numerical Methods in Engineering*, 52:193–215.

Carol, I. and Prat, P. C. (1990). A statically constrained microplane model for the smeared analysis of concrete cracking. In *Computer-Aided Analysis and Design of Concrete Structures*, volume 2, pages 919–930. Pineridge Press.

Carol, I. and Prat, P. C. (1995). A multicrack model based on the theory of multisurface plasticity and two fracture energies. In *Computational Plasticity, COMPLAS IV*, volume 2, pages 1583–1594. Pineridge Press.

Carol, I., Prat, P. C., and López, C. M. (1997). Normal/shear cracking model: application to discrete crack analysis. *Journal of engineering mechanics*, 123(8):765–773.

Cerfontaine, B., Dieudonné, A., Radu, J., Collin, F., and Charlier, R. (2015). 3d zero-thickness coupled interface finite element: Formulation and application. *Computers and Geotechnics*, 69:124 – 140.

Cheng, H. and Dusseault, M. (2002). Continuum damage theories and petroleum geomechanics. In *SPE/ISRM Rock mechanics conference*, number SPE 78198, Irving, TX, USA.

Ciancio, D., Carol, I., and Cuomo, M. (2007). Crack opening conditions at 'corner nodes' in fe analysis with cracking along mesh lines. *Engineering Fracture Mechanics*, 74(13):1963 – 1982.

Ciancio, D., Carol, I., and Cuomo, M. (2013). A method for the calculation of inter-element stresses in 3d. *Computer Methods in Applied Mechanics and Engineering*, 254:222 – 237.

Climent, N., Arroyo, M., O'Sullivan, C., and Gens, A. (2014). Sand production simulation coupling dem with cfd. *European Journal of Environmental and Civil Engineering*, 18(9):983–1008.

Cook, B., Lee, M., DiGiovanni, A., Bronowski, D., Perkins, E., and Williams, J. (2004). Discrete element modeling applied to laboratory simulation of near-wellbore mechanics. *International Journal of Geomechanics*, page 19–27.

Cook, J., Bradford, I., and Plumb, R. (1994). A study of the physical mechanisms of sanding and application to sand production prediction. In *European Petroleum Conference , 25-27 October , London, United Kingdom*, number SPE paper no. 28852, pages 473–480. Society of Petroleum Engineers, Society of Petroleum Engineers.

Cundall, P. (1971). A computer method for simulating progressive, large-scale movements in blocky rock systems. In *Symp. of the Int. Society for Rock Mechanincs*, volume 1.

Cundall, P. and Strack, O. (1979). A discrete numerical model for granular assemblies. *Geotechnique*, 29(1):47–65.

Cuss, R., Rutter, E., and Holloway, R. (2003). Experimental observations of the mechanics of borehole failure in porous sandstone. *International Journal of Rock Mechanics and Mining Sciences*, 40(5):747 – 761.

Detournay, E. and Carbonell, R. (1997). Fracture-mechanics analysis of the breakdown process in minifracture or leakoff test. *SPE Production and Facilities*, 12(3):195–199.

Dusseault, M., Maury, V., Sanfilippo, F., and Santarelli, F. (2004). Drilling Around Salt: Risks, Stresses, And Uncertainties. In *Gulf Rocks 2004, the 6th North America Rock Mechanics Symposium*, number 04-647, Houston, Texas. American Rock Mechanics Association.

Dusseault, M. and Santarelli, F. (1989). A conceptual model for massive solids production in poorly-consolidated sandstones. *Rock at Great Depth. Proceedings ISRM/SPE*, 2:789–797.

Fjaer, E., Cerasi, P., Li, L., and Papamichos, E. (2004). Modeling the rate of sand production. In *Gulf rocks 2004, the* 6^{th} *North America rock mechanics Symposium (NARMS): Rock mechanics across borders ans disciplines*, number ARMA/NARMS 04-588, Houston, Texas. American rock mechanics association.

Fjaer, E., Holt, R. M., Horsrud, P., Raaen, A. M., and Risnes, R. (2008). *Petroleum related rock mechanics*. Elsevier, 2nd edition.

Gambolati, G., Ferronato, M., Teatini, P., Deidda, R., and Lecca, G. (2001). Finite element analysis of land subsidence above depleted reservoirs with pore pressure gradient and total stress formulations. *International Journal for Numerical and Analytical Methods in Geomechanics*, 25(4):307–327.

Garolera, D. (2003). Estudio microestructural del rock sanding. Master's thesis, Escola tècnica superior d'enginyers de camins, canals i ports de Barcelona, Universitat Politècnica de Catalunya, Barcelona. (in spanish).

Garolera, D., Aliguer, I., Carol, I., Segura, J., Lakshmikantha, R., and Alvarellos, J. (2014). Hydro-mechanical coupling in zero-thickness interface elements, formulation and applications in geomechanics. In *ISRM International Congress on Rock Mechanics*, pages 1379–1384. CRC Press.

Garolera, D., Aliguer, I., Segura, J., Carol, I., Lakshmikantha, R., and Alvarellos, J. (2013). Zero-thickness interface elements with h-m coupling, formulation and applications in geomechanics. In *International Conference on Computational Plasticity*, pages 1372–1383.

Geertsma J. and De Klerk F. (1969). A Rapid Method of Predicting Width and Extent of Hydraulically Induced Fractures. *J. Pet. Tech.*, 246:1571–1581.

Goodman, R. E., Taylor, R. L., and Brekke, T. L. (1968). A model for the mechanics of jointed rock. *Journal of the Soil Mechanics and Foundation Division*, 94(SM3):637–659.

Hadri, B. (2011). Introduction to parallel I/O. https://www.olcf.ornl.gov/wp-content/uploads/2011/10/Fall_IO.pdf.

Han, G. (2003). *Rock Stability under Different Fluid Flow Conditions*. PhD thesis, Departament of Chemical Engineering, University of Waterloo, Canada.

Heroux, M. A., Bartlett, R. A., Howle, V. E., Hoekstra, R. J., Hu, J. J., Kolda, T. G., Lehoucq, R. B., Long, K. R., Pawlowski, R. P., Phipps, E. T., Salinger, A. G., Thornquist, H. K., Tuminaro, R. S., Willenbring, J. M., Williams, A., and Stanley, K. S. (2005). An overview of the Trilinos project. *ACM Trans. Math. Softw.*, 31(3):397–423.

Jensen, R., Preece, D., Cook, B., and Williams, J. (2001). Modeling sand production with darcy coupled with discrete elements. In et al. Desai, editor, *Comp. Meth. And Adv. In Geomech*, page 819–822. Balkema, Rotterdam.

Jensen, R., Preece, D., Perkins, E., and Williams, J. (1999). Sand production modeling using superquadratic discrete elements and coupling of fluid flow and particle motion. In Amadei, Kranz, Scott, and Smeallie, editors, *Rock Mech. for Industry*, page 209–216. Balkema, Rotterdam.

Jérémie Gaidamour and Pascal Hénon and Yousef Saad (2010). HIPS (Hierarchical Iterative Parallel Solver) is a scientific library that provides an efficient parallel iterative solver for very large sparse linear systems. http://hips.gforge.inria.fr.

Karihaloo, B., Carpinteri, A., and Elices, M. (1993). Fracture mechanics of cement mortar and plain concrete. *Advn. Cem. Bas. Mat.*, 1(2):92–105.

Karypis, G. and Kumar, V. (1998). *METIS: A Software Package for Partitioning Unstructured Graphs, Partitioning Meshes, and Computing Fill-Reducing Orderings of Sparse Matrices.*

la Cruz, R. D., Calmet, H., and Houzeaux, G. (2011). Implementing a XDMF/HDF5 parallel file system in Alya.

Lewis, R. and Schrefler, B. (1998). *The finite element method in the static and dynamic deformation and consolidation of porous media.* Second edition.

Li, L., Papamichos, E., and Cerasi, P. (2006). Investigation of sand production mechanisms using dem with fluid flow. In van Cotthem, A., Charlier, R., Thimus, J.-F., and Tshibangu, J.-P., editors, *Eurock 2006: Multiphysics Coupling and Long Term Behaviour in Rock Mechanics*, page 241–247. International Society for Rock Mechanics, Taylor & Francis.

Li, L., Tang, C., Li, G., Wang, S., Liang, Z., and Zhang, Y. (2012). Numerical Simulation of 3D Hydraulic Fracturing Based on an Improved Flow-Stress-Damage Model and a Parallel FEM Technique. *Rock Mechanics and Rock Engineering*, 45(5):801–818.

López, C. M. (1999). *Análisis microestructural de la fractura del hormigón utilizando elementos finitos tipo junta. Aplicación a diferentes hormigones.* PhD thesis, Escola tècnica superior d'enginyers de camins, canals i ports . Universitat Politècnica de Catalunya, Barcelona.

López, C. M., Carol, I., and Aguado, A. (2008). Meso-structural study of concrete fracture using interface elements. i: numerical model and tensile behavior. *Materials and Structures*, 41(3):583–599.

Mack, M. and Warpinski, N. (2000). *Reservoir Stimulation*, chapter Mechanics of Hydraulic Fracturing,. Number Chap. 6. John Wiley & Sons, West Sussex, UK, third edition edition.

Mira, P. and Pastor, M. (2002a). Non linear problems: Introduction. *Revue française de génie civil*, 6 - Numerical Modelling in Geomechanics.

Mira, P. and Pastor, M. (2002b). Nonlinear problems: Advanced techniques. *Revue française de génie civil*, 6 - Numerical Modelling in Geomechanics.

Morita, N. (1994). Field and laboratory verification of sand-production prediction models. *SPE drilling and completion*, (9):227–235.

Mühlhaus, H.-B. (1993). Continuum models for layered and blocky rock. *Comprehensive rock engineering*, Invited Chapter for Vol. II: Analysis and Design Methods:209–231.

Muhlhauss, H. and Vardoulakis, I. (1987). The thickness of shear bands in granular materials. *Géotechnique*, 37(3):271–283.

Nicholson, E., Goldsmith, G., and Cook, J. (1998). Direct observation and modeling of sand production processes in weak sandstone. In *SPE/ISRM Eurock 98 Conference*, number SPE paper no. 47328, Trondheim, Noruega.

Nordgren, R. (1972). Propagation of a Vertical Hydraulic Fracture. *Society of Petroleum Engineers*.

Oron, A. P. and Berkowitz, B. (1998). Flow in rock fractures: The local cubic law assumption reexamined. *Water Resources Research*, 34(11):2811–2825.

Ortiz, M. and Popov, E. (1985). Accuracy and stability of integration algorithms for elastoplastic constitutive relations. *Int. J. Numer. Methods Engrg*, 21:1561–1576.

Pande, G. N., Beer, G. G., and Williams, J. R. (John R.), . (1990). *Numerical methods in rock mechanics*. John Wiley & Sons.

Papamichos, E. (2004). Hydro-mechanical coupling for erosion. In *Revue français de genie civil*, volume 8 -Failure, Degradation and Instabilities-, chapter Failure in rocks, page 709–734.

Papamichos, E., Tronvoll, J., Vardoulakis, I., Labuz, J. F., Skjaerstein, A., Unander, T. E., and Sulem, J. (2000). Constitutive testing of red wildmoor sandstone. *Mechanics of Cohesive-frictional Materials*, 5(1):1–40.

Papamichos, E., Vardoulakis, I., Tronvoll, J., and Skjaerstein, A. (2001). Volumetric sand production model and experiment. *Int. J. Numer. Anal. Meth. Geomech.*, 25:789–808.

Papanastasiou, P. (2001). Colección de micro-fotografias de las texturas de rocas.

Papanastasiou, P., Nicholson, E., Goldsmith, G., and Cook, J. (1998). Sanding prediction: Experimental results and numerical modeling. In et al., T., editor, *Poromechanics*, page 457–462. Balkema, Rotterdam.

Papanastasiou, P. and Zervos, A. (2004). Wellbore stability analysis: From linear elasticity to postbifurcation modeling. *International Journal of Geomechanics*, 4(1):2–12.

Papanastasiou, P. C. and Vardoulakis, I. G. (1992). Numerical treatment of progressive localization in relation to borehole stability. *International Journal for Numerical and Analytical Methods in Geomechanics*, 16(6):389–424.

Pérez-Foguet, A., Rodríguez-Ferran, A., and Huerta, A. (2001). Consistent tangent matrices for substepping schemes. *Computer Methods in Applied Mechanics and Engineering*, 190(35–36):4627–4647.

Perkins, T. and Kern, L. (1961). Widths of Hydraulic Fractures.

Potts, D. M. and Zdravković, L. (1999). *Finite element analysis in geotechnical engineering : theory*. Thomas Telford, London.

Prabhat and Koziol, Q. (2014). *High Performance Parallel I/O*. Chapman and Hall/CRC.

Prat, P., Gens, A., Carol, I., Ledesma, A., and Gili, J. (1993). DRAC:A computer software for the analysis of rock mechanics problems. In Liu, H., editor, *Application of Computer Methods in Rock Mechanics*, pages 1361–1368. Shaanxi Science and Technology Press.

Rahmati, H., Jafarpour, M., Azadbakht, S., Nouri, A., Vaziri, H., Chan, D., and Xiao, Y. (2013). Review of sand production prediction models.

Roa, O. (2004). *Análisis microestructural del comportamiento mecánico del hueso trabecular*. PhD thesis, Escola tècnica superior d'enginyers de camins, canals i ports . Universitat Politècnica de Catalunya, Barcelona. (in spanish).

Rutqvist, J. (2012). The geomechanics of co2 storage in deep sedimentary formations. *Geotechnical and Geological Engineering*, 30(3):525–551.

Sarris, E. and Papanastasiou, P. (2012). Modeling of hydraulic fracturing in a poroelastic cohesive formation. *International Journal of Geomechanics*, 12(2):160–167.

Secchi, S. and Schrefler, B. (2012). A method for 3-D hydraulic fracturing simulation. *International Journal of Fracture*, 178(1-2):245–258.

Segura, J. M. (2007). *Coupled HM analysis using zero-thickness interface elements with double nodes*. PhD thesis, UPC. Departament d'Enginyeria del Terreny, Cartogràfica i Geofísica.

Segura, J. M. and Carol, I. (2004). On zero-thickness interface elements for diffusion problems. *International Journal for Numerical and Analytical Methods in Geomechanics*, 28(9):947–962.

Segura, J. M. and Carol, I. (2008a). Coupled hm analysis using zero-thickness interface elements with double nodes. part i: Theoretical model. *International Journal for Numerical and Analytical Methods in Geomechanics*, 32(18):2083–2101.

Segura, J. M. and Carol, I. (2008b). Coupled hm analysis using zero-thickness interface elements with double nodes—part ii: Verification and application. *International Journal for Numerical and Analytical Methods in Geomechanics*, 32(18):2103–2123.

Smith, I. and Giffiths, D. (2004). *Programming the finite element method*. John Wiley and Sons, cop, 4 edition.

Smith, M., Montgomery, C., and Roegiers, J.-C. (2012). 3D Fracture Geometry Modeling, Real or Pseudo? web.

Sneddon, I. (1946). The Distribution of Stress in the Neighbourhood of a Crack in an Elastic Solid. In *Series A. Mathematical and Physical Sciences*, volume 187, pages 229–260. Royal Society of London.

Stankowski, T. (1990). *Numerical Simulation of Progressive Failure in Particle Composites*. Ph.d. thesis, University of Colorado, Boulder, CO, USA.

Stavropoulou, M., Papanastasiou, P., and Vardoulakis, I. (1998). Coupled well bore erosion and stability analysi. *Int. J. for Numer. and Anal. Meth. Geomech*, 22:749–769.

Thakur, R., Gropp, W., and Lusk, E. (1999). On implementing MPI-IO portably and with high performance. In editor, editor, *Proc. the Sixth Workshop on I/O in Parallel and Distributed Systems*, pages 23–32.

The HDF Group (2000-2017). Hierarchical Data Format version 5. http://www.hdfgroup.org/HDF5.

Tronvoll, J. and Halleck, P.-M. (1994). Observations of sand production and perforation cleanup in weak sandstone. In *Eurock'94*, pages 355–360, Rotterdam. Balkema.

Tronvoll, J., Skjaerstein, A., and Papamichos, E. (1997). Sand production: mechanical failure or hydrodynamic erosion? *International Journal of Rock Mechanics and Mining Sciences*, 34(3-4):291.e1–291–e17. ISRM International Symposium 36th U.S. Rock MechanicsSymposium.

van den Hoek, P., Hertogh, G., de Bree, P., Kenter, C., and Papamichos, E. (2000). A new concept of sand production prediction: theory and laboratory experiments. *SPE Drilling & Completion*, 15(4):261–273.

van den Hoek, P., Smit, D.-J., Kooijman, A., de Bree, P., Kenter, C., and Khodaverdian, M. (1994). Size dependency of hollow-cylinder stability. In *Eurock'94*, page 191–197, Rotterdam. Balkema.

Vardoulakis, I., Stavropoulou, M., and Papanastasiou, P. (1996). Hydromechanical aspects of sand production problem. *Transport in Porous Media*, 22:225–244.

Vardoulakis, I. and Sulem, J. (1996). *Bifurcation analysis in geomechanics*. Blackie academic an professional.

Vaziri, H., Xiao, Y., Islam, R., and Nouri, A. (2002). Numerical modeling of seepage-induced sand production in oil and gas reservoirs. *Journal of Petroleum Science and Engineering*, 36(1–2):71 – 86.

Veeken, C., Davies, D., and C.J.Kenter (1991). Sand production prediction review: developing an integrated aproach. Technical Report 22792, SPE.

Vilarrasa, V., Bolster, D., Olivella, S., and Carrera, J. (2010). Coupled hydromechanical modeling of CO2 sequestration in deep saline aquifers. *International Journal of Greenhouse Gas Control*, 4(6):910 – 919. CO2 Storage at the EGU General Assembly 2009.

Wan, R. and Wang, J. (2002). A coupled erosion-stress deformation model for sand production using streamline upwind finite elements. In Pande, P., editor, *Num. Models in Geomech*, page 301–308. Swets & Zeitlinger, Lisse.

Wang, Y. (2001). A coupled reservoir-geomechanics model and applications to well bore stability and sand prediction. In *SPE International Thermal Operations and Heavy Oil Symposium*, number SPE paper no. 69718, Margarita, Venezuela.

Warpinski, N., Abou-Sayed, I., Moschovidis, Z., and Parker, C. (1994). Comparison Study of Hydraulic Fracturing Models-Test Case: GRI Staged Field Experiment No. 3. *SPE Production & Facilities*, 9(01):7–16.

Witherspoon, P. A., Wang, J. S. Y., Iwai, K., and Gale, J. E. (1980). Validity of cubic law for fluid flow in a deformable rock fracture. *Water Resources Research*, 16(6):1016–1024.

Wittmann, F. (1983). Structure of concrete with respect to crack formation. In Wittmann, F., editor, *Fracture mechanics of concrete*, page 43–74. Elsevier.

Yew, C. (1997). *Mechanics of Hydraulic Fracturing*. Elsevier Science.

Zervos, A., Papanastasiou, P., and Vardoulakis, I. (2001a). A finite element displacement formulation for gradient elastoplasticity. *Int. J. Numer. methods Eng.*, 50:1369–1388.

Zervos, A., Papanastasiou, P., and Vardoulakis, I. (2001b). Modelling of localization and scale effect in thick-walled cylinders with gradient elastoplasticity. *Int. J. Solids Struct.*, 38:5081–5095.

Zhang, L. and Dusseault, M. (2000). Sand production simulation in heavy oil reservoir. In *The SPE international oil and gas conference an exhibition*, number SPE 64747, Beijing, China. SPE.

Zienkiewicz, O. and Taylor, R. (2000a). *The Finite element method*, volume 1 - The basis. Butterworth Heinemann, Oxford, 5 edition.

Zienkiewicz, O. and Taylor, R. (2000b). *The Finite element method*, volume 2 - Solid mechanics. Butterworth Heinemann, Oxford, 5 edition.

Zienkiewicz, O. C. and Pande, G. N. (1977). Time-dependent multilaminate model of rocks—a numerical study of deformation and failure of rock masses. *International Journal for Numerical and Analytical Methods in Geomechanics*, 1(3):219–247.

Appendix A

Acronyms

BVP Boundary Value Problem (BVP)

CMOD The Crack Mouth Opening Displacement

CMP The Crack Mouth fluid Pressure

UCS The Uniaxial Compression Strength

DEM The Distinct Element Method

FDM The Finite Difference Method

FEM The Finite Element Method

FPP The Fracture Propagation Pressure

GDK The Geertsma de-Klerk Khristianovich analytical model

HCT Hollow Cylinder Test

ISIP The Instantaneous Shut-In Pressure

LEFM The Linear Elastic Fracture Mechanics

PKN The Perkins Kern Nordgren analytical model

PVW Principle of Virtual Work

SPE The Society of Petroleum Engineering

XFEM The Extended Finite Element Method

Appendix B

Data multistage fracture study in 3D

Table B.1: Material properties for both continuum and interface elements

Depth (m)	Type	E (GPa)	ν	n	K_x^f ($\mathrm{m \cdot s^{-1}}$)	K_z^f ($\mathrm{m \cdot s^{-1}}$)
7839.00	Fault	28.4927	0.2728	0.1700	9.8692E-10	9.8692E-11
7870.10	Sand	70.0353	0.2776	0.1805	1.3071E-07	3.8952E-08
7888.90	Silty	67.8397	0.2800	0.1500	4.9346E-08	4.9346E-09
7897.20	Target Sand	84.8658	0.2560	0.1540	1.1843E-07	3.1582E-08
7906.20	Sand Cement Lime	208.9112	0.2500	0.1600	4.9346E-08	4.9346E-09
7908.00	Target Sand	79.2997	0.2500	0.1900	1.4804E-07	4.9346E-08
7914.30	Sand	68.2441	0.3000	0.1800	9.8692E-08	1.9738E-08
7931.30	Silty	78.9704	0.2823	0.1897	1.0906E-07	2.7733E-08
7941.30	Silty	121.4666	0.2500	0.2300	4.9346E-08	4.9346E-09
7942.50	Target Sand	95.4415	0.2500	0.1900	1.4804E-07	4.9346E-08
7949.30	Silty	140.9202	0.2500	0.1000	4.9346E-08	4.9346E-09
7957.20	Shale	76.9634	0.3200	0.1500	9.8692E-10	9.8692E-11
7959.60	Target Sand	92.7734	0.1483	0.2011	1.1004E-07	2.9182E-08
7977.00	Shale	66.3790	0.3100	0.1700	9.8692E-10	9.8692E-11
7981.60	Sand Cement Lime	130.6027	0.0000	0.1500	4.9346E-08	4.9346E-09
7983.00	Silty	90.7629	0.2600	0.2000	4.9346E-08	4.9346E-09
7985.80	Target Sand	81.5438	0.0000	0.1900	9.8692E-08	1.9738E-08
8000.10	Shale	73.0125	0.3000	0.1400	9.8692E-10	9.8692E-11
8007.50	Target Sand	78.9669	0.2600	0.1500	1.4804E-07	4.9346E-08
8011.00	Silty	83.1758	0.3100	0.1900	4.9346E-08	4.9346E-09
8030.30	Target Sand	118.5913	0.3300	0.2300	1.4804E-07	4.9346E-08
8031.50	Silty	82.8126	0.2800	0.2000	4.9346E-08	4.9346E-09
8041.10	Target Sand	97.7848	0.2500	0.1700	1.4804E-07	4.9346E-08
8046.00	Sand Cement Lime	250.9693	0.2900	0.1300	9.8692E-08	1.9738E-08
8047.70	Target Sand	98.9446	0.2500	0.1200	1.4804E-07	4.9346E-08
8051.90	Silty	71.8111	0.2900	0.1200	4.9346E-08	4.9346E-09
8057.90	Target Sand	84.7718	0.2579	0.1774	1.4804E-07	4.9346E-08
8078.90	Silty	80.4495	0.2600	0.1846	8.5356E-08	2.1139E-08
8086.30	Sand Cement Lime	198.5691	0.2800	0.1900	1.4804E-07	4.9346E-08
8087.90	Target Sand	108.6662	0.2500	0.1774	1.4804E-07	4.9346E-08
8119.90	Shale	72.0478	0.2800	0.1800	9.8692E-10	9.8692E-11
8121.60	Sand	88.3273	0.2600	0.1900	9.8692E-08	1.9738E-08
8131.60	Silty	55.4299	0.2700	0.2100	4.9346E-08	4.9346E-09
8138.40	Sand	84.0454	0.2561	0.1655	1.2897E-07	3.7904E-08
8159.10	Silty	39.7775	0.3000	0.1200	4.9346E-08	4.9346E-09
8168.80	Sand	79.9792	0.2500	0.1300	9.8692E-10	9.8692E-11
8188.10	Water	55.7706	0.3012	0.1454	1.4215E-08	1.4215E-09

Table B.2: Material properties for both continuum and interface elements

Depth (m)	Type	$\tan\phi$	χ (MPa)	C (MPa)	G_f^I (MPa · m)
7839.00	Fault	0.4415	2.4612	8.1050	0.0080
7870.10	Sand	0.4415	2.4612	8.1050	0.0080
7888.90	Silty	0.4749	3.5779	11.3081	0.0117
7897.20	Target Sand	0.4749	3.5779	11.3081	0.0117
7906.20	Sand Cement Lime	0.4749	3.5779	11.3081	0.0117
7908.00	Target Sand	0.5534	7.5969	22.3922	0.0247
7914.30	Sand	0.4782	3.6347	11.4538	0.0118
7931.30	Silty	0.4667	3.2226	10.5399	0.0105
7941.30	Silty	0.4652	3.2348	10.3567	0.0105
7942.50	Target Sand	0.5052	4.8804	15.0114	0.0159
7949.30	Silty	0.4907	4.1845	13.0396	0.0136
7957.20	Shale	0.4890	4.2576	13.2872	0.0139
7959.60	Target Sand	0.4763	3.6451	11.5074	0.0119
7977.00	Shale	0.4745	3.5564	11.2498	0.0116
7981.60	Sand Cement Lime	0.4490	2.7364	8.8779	0.0089
7983.00	Silty	0.5174	5.5323	16.8325	0.0180
7985.80	Target Sand	0.4770	3.6271	11.4548	0.0118
8000.10	Shale	0.4770	3.6271	11.4548	0.0118
8007.50	Target Sand	0.4597	3.0703	9.7973	0.0100
8011.00	Silty	0.4626	3.1759	10.1936	0.0103
8030.30	Target Sand	0.4626	3.1759	10.1936	0.0103
8031.50	Silty	0.4743	3.6703	11.6075	0.0120
8041.10	Target Sand	0.4761	3.6334	11.5149	0.0118
8046.00	Sand Cement Lime	0.4761	3.6334	11.5149	0.0118
8047.70	Target Sand	0.5526	7.5553	22.2861	0.0246
8051.90	Silty	0.4785	3.7426	11.7976	0.0122
8057.90	Target Sand	0.4785	3.7426	11.7976	0.0122
8078.90	Silty	0.4785	3.7426	11.7976	0.0122
8086.30	Sand Cement Lime	0.4785	3.7426	11.7976	0.0122
8087.90	Target Sand	0.5081	5.0937	15.5784	0.0166
8119.90	Shale	0.4958	4.4341	13.7695	0.0144
8121.60	Sand	0.4598	3.1681	9.7781	0.0103
8131.60	Silty	0.4833	3.8832	12.2287	0.0126
8138.40	Sand	0.4670	3.2975	10.4566	0.0107
8159.10	Silty	0.4872	4.0652	12.7568	0.0132
8168.80	Sand	0.4486	2.7261	8.7677	0.0089
8188.10	Water	0.1668	1.2465	3.9474	0.0041

Table B.3: *In situ* stress

Depth (m)	Type	σ_v (MPa)	σ_H (MPa)	σ_h (MPa)
7839.00	Fault	-11.4374	-12.6709	-2.2081
7870.10	Sand	-12.1585	-14.4515	-9.6983
7888.90	Silty	-12.4990	-14.5068	-9.7333
7897.20	Target Sand	-12.7447	-16.8554	-10.7812
7906.20	Sand Cement Lime	-12.9054	-18.0178	-12.6395
7908.00	Target Sand	-12.9477	-16.0027	-10.0560
7914.30	Sand	-13.0958	-14.3273	-10.0188
7931.30	Silty	-13.5623	-16.1373	-10.6838
7941.30	Silty	-13.7295	-17.7285	-12.7436
7942.50	Target Sand	-13.7577	-17.4426	-11.6301
7949.30	Silty	-13.9172	-19.2416	-13.5896
7957.20	Shale	-14.1025	-16.3342	-11.3502
7959.60	Target Sand	-14.3016	-17.3169	-11.8660
7977.00	Shale	-14.5659	-16.9374	-11.2695
7981.60	Sand Cement Lime	-14.6735	-18.7023	-14.2446
7983.00	Silty	-14.7063	-19.1072	-12.5105
7985.80	Target Sand	-14.7718	-18.4856	-11.8555
8000.10	Shale	-15.1066	-18.3380	-12.2051
8007.50	Target Sand	-15.2798	-18.8046	-12.6629
8011.00	Silty	-15.3617	-18.4995	-13.0366
8030.30	Target Sand	-15.8137	-19.0602	-14.6810
8031.50	Silty	-15.8418	-20.5598	-12.8325
8041.10	Target Sand	-16.0668	-18.4511	-13.4455
8046.00	Sand Cement Lime	-16.1816	-20.5092	-15.8483
8047.70	Target Sand	-16.2215	-21.0328	-13.5013
8051.90	Silty	-16.3199	-18.1658	-12.3113
8057.90	Target Sand	-16.5420	-19.1470	-13.2545
8078.90	Silty	-16.9925	-19.7875	-12.9337
8086.30	Sand Cement Lime	-17.1256	-23.4394	-16.5474
8087.90	Target Sand	-17.3060	-20.5251	-14.6183
8119.90	Shale	-17.9128	-20.8638	-13.1938
8121.60	Sand	-17.9526	-21.1361	-14.9023
8131.60	Silty	-18.1868	-21.0584	-13.4627
8138.40	Sand	-18.4610	-21.4663	-15.7717
8159.10	Silty	-18.8309	-22.4681	-12.5960
8168.80	Sand	-19.0580	-23.6040	-16.7653
8188.10	Water	-20.0483	-22.4557	-15.2520